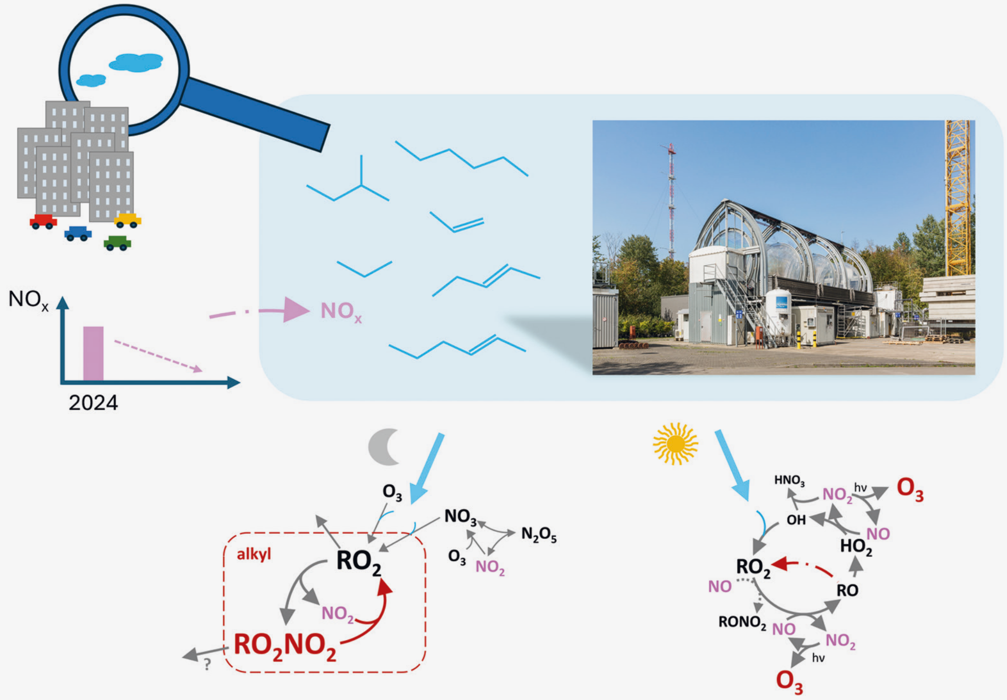

Investigation of current and future anthropogenic chemical regimes in simulation chamber experiments

Michelle Färber

Energie & Umwelt / Energy & Environment
Band / Volume 657
ISBN 978-3-95806-809-4

Mitglied der Helmholtz-Gemeinschaft

JÜLICH
Forschungszentrum

Schriften des Forschungszentrums Jülich
Reihe Energie & Umwelt / Energy & Environment Band / Volume 657

Forschungszentrum Jülich GmbH
Institute of Climate and Energy Systems (ICE)
Troposphäre (ICE-3)

Investigation of current and future anthropogenic chemical regimes in simulation chamber experiments

Michelle Färber

Schriften des Forschungszentrums Jülich
Reihe Energie & Umwelt / Energy & Environment Band / Volume 657

ISSN 1866-1793 ISBN 978-3-95806-809-4

Bibliografische Information der Deutschen Nationalbibliothek.
Die Deutsche Nationalbibliothek verzeichnet diese Publikation in der
Deutschen Nationalbibliografie; detaillierte Bibliografische Daten
sind im Internet über http://dnb.d-nb.de abrufbar.

Herausgeber und Vertrieb:
Forschungszentrum Jülich GmbH
Zentralbibliothek, Verlag
52425 Jülich
Tel.: +49 2461 61-5368
Fax: +49 2461 61-6103
zb-publikation@fz-juelich.de
www.fz-juelich.de/zb

Umschlaggestaltung: Grafische Medien, Forschungszentrum Jülich GmbH

Titelbild: SAPHIR-Kammer: Forschungszentrum Jülich – Sascha Kreklau
Stadt-Skizze: Färber et al., ACS EST Air 2024, 1, 9, 1096-1111

Druck: Grafische Medien, Forschungszentrum Jülich GmbH

Schriften des Forschungszentrums Jülich
Reihe Energie & Umwelt / Energy & Environment, Band / Volume 657

D 38 (Diss. Köln, Univ., 2024)

ISSN 1866-1793
ISBN 978-3-95806-809-4

Vollständig frei verfügbar über das Publikationsportal des Forschungszentrums Jülich (JuSER)
unter www.fz-juelich.de/zb/openaccess.

Abstract

Air pollution is a societal challenge, affecting millions of people world-wide living in urban conglomerates. In cities, emissions are mostly from anthropogenic activities such as traffic, industry, cooking, and use of volatile care products. These emissions are not only hazardous for human health, they also undergo chemical degradation driven by oxidants, forming secondary pollutants such as ozone (O) and particles.

Main tropospheric oxidants are the hydroxyl radical (OH), dominating oxidation processes during the day, the nitrate radical (NO), predominantly available during the night, and ozone. In the reaction chain of the atmospheric oxidation of volatile organic compounds (VOCs), peroxy (RO_2) and hydroperoxy (HO_2) radicals are formed, which oxidise nitric oxide (NO) to nitrogen dioxide (NO_2), the latter being the main tropospheric source of ozone following its photolysis. Understanding atmospheric oxidation processes is crucial for mitigating air pollution and tackling current and future air quality challenges.

In many different field studies, performed in or close to urban areas, measured HO_2 and/or RO_2 radical concentrations could not be reproduced by chemical model calculations, which represent the current understanding of the atmospheric chemistry. Even though chemical models carry uncertainties, the observed discrepancies in particular for RO radicals often exceeded a factor of three, making air quality prediction challenging. Data collected during field campaigns are very valuable in highlighting where our gap of knowledge for atmospheric chemical processes lies. Laboratory studies and experiments in atmospheric simulation chambers can then focus on investigating such processes in a confined and controlled environment.

In this thesis, first the performance and comparability of several different atmospheric simulation chambers were studied. Oxidation experiments of -pinene were performed in nine different simulation chambers, which are part of the EUROCHAMP-2020 consortium. Chamber effects, such as the release of small oxygenated compounds from the chamber wall or the loss of trace gases or particles on the chamber wall were characterised. Furthermore, yields of pinonaldehyde, formaldehyde, and acetone, which are products from the oxidation of -pinene by OH, could be derived for experiments in five different chambers. A high variability of the yields of pinonaldehyde and formaldehyde was observed, which is also reflected in the available data from the literature. In contrast, obtained acetone yields agree within the combined uncertainties for the different chambers and within the uncertainties with reported literature values.

Overall, well-characterised simulation chambers offer a great opportunity to investigate atmospheric chemistry in a controlled environment. The goal is to simplify the complexity of field studies while still keeping the conditions comparable to the real atmosphere.

The main part of the thesis is on the investigation of the daytime and nighttime oxidation of anthropogenic VOCs in the atmospheric simulation chamber SAPHIR at Forschungszentrum Jülich, Germany. Measured trace gas and radical concentrations were compared to zero-dimensional box model calculations, based on the Master Chemical Mechanism (MCM) and complemented by an updated ozonolysis scheme for alkenes, and by state-of-the-art peroxy and alkoxy chemistry from structure-activity relationships (SAR).

Photooxidation experiments were performed for a variety of anthropogenic VOCs at different levels of NO, mimicking current (high NO) and future (low NO) chemical regimes. The VOCs investigated were chosen according to their alkoxy chemistry, forming HO_2 either in a single-step reaction (propane, propene, trans-2-hexene) or in a multi-step reaction involving the regeneration of RO_2 (iso-pentane, n-hexane), which results in a different number of ozone

molecules produced per oxidised VOC molecule. A comparison between measured trace gases and radicals with results from the the MCM showed overall a good agreement (within 17 %) for most VOCs. An improved agreement of HO_2 and RO_2 radical concentrations, in experiments with n-hexane, was found for the MCM complemented by SAR, assuming a factor of higher organic nitrate yields for first-generation RO_2 and RO_2 isomerisation reactions.
HO_2/RO_2 ratios were derived from measured and modelled radical concentrations, showing a % smaller ratio for the VOCs forming HO_2 in a multi-step reaction compared to VOCs forming HO_2 in a single-step reaction. The production of odd oxygen (O_x O_3 NO_2) was calculated from modelled radical concentrations and from measured O_x for 3 < NO < ppbv and for NO < ppbv, where the O_x formation could additionally be determined from measured radical concentrations. Overall, a good agreement was found for the different approaches. In agreement with the observations of the HO_2/RO_2 ratio, a % higher O_x production was observed for species, regenerating another RO_2 radical before eventually forming HO_2. Overall, the model-measurement discrepancies of the O_x production rates, as found in urban areas, were not observed in the performed chamber experiments.
The nighttime oxidation of cis-2-butene and trans-2-hexene was tested in the presence of NO_2 at different temperatures (from C to C). At low temperatures, time profiles of measured RO_2 radical concentrations were significantly delayed and lower peak concentrations were reached than observed in the modelled RO_2 radical time series. The model-measurement agreement could be significantly improved by including the formation of non-acyl peroxynitrates (RO_2NO_2) from the reaction of RO_2 with NO_2 in the chemical model for all formed non-acyl peroxy radicals. The formation of non-acyl RO_2NO_2, with the exception of methyl peroxynitrate, is not implemented in commonly used chemical mechanisms, such as the MCM, as it is thought to be negligible due to the short lifetime of alkyl (non-acyl) RO_2NO_2 of less than s at K. This study suggests that at C, % of RO_2 radicals are stored as corresponding peroxynitrates in the presence of only few ppbv of NO_2, which may impact ambient RO_2 and NO_x (NO NO_2) concentrations. In addition, a recent model study found an increase of NO_x of up to % on the ground, when including the formation of non-acyl RO_2NO_2. This suggests that these reactions should be included in chemical mechanisms for a better representation of the underlying chemistry.

Zusammenfassung

Luftverschmutzung ist eine gesellschaftliche Herausforderung, die insbesondere in Ballungsgebieten eine große Rolle spielt und Millionen von Menschen weltweit betrifft. Emissionen in Städten sind von anthropogenen Aktivitäten, wie zum Beispiel Verkehr, Industrie, Kochaktivitäten und der Benutzung flüchtiger Pflegeprodukte, geprägt. Abgesehen von der gesundheitsschädlichen Wirkung werden Emissionen durch die Reaktion mit Oxidationsmitteln chemisch abgebaut, wobei Sekundärschadstoffe, wie zum Beispiel Ozon und Partikel, entstehen.

Die wichtigsten Oxidationsmittel der Troposphäre sind das Hydroxylradikal (OH), das tagsüber Oxidationsprozesse dominiert, das Nitratradikal (NO_3), das insbesondere in der Nacht von Bedeutung ist, und Ozon. Im Verlauf der atmosphärischen Oxidation von flüchtigen organischen Verbindungen (VOCs) werden Peroxy- (RO_2) und Hydroperoxy-Radikale (HO_2) gebildet, die Stickstoffmonoxid (NO) zu Stickstoffdioxid (NO_2) oxidieren. Stickstoffdioxid stellt die Hauptquelle tropopshärischen Ozons dar, das durch die Photolyse von NO_2 gebildet wird. Das Verständnis atmosphärischer Oxidationsprozesse ist von entscheidender Bedeutung für die Eindämmung der Luftverschmutzung und für die Bewältigung aktueller und künftiger Herausforderungen in Hinsicht auf die Luftqualität.

In verschiedenen Feldstudien, die in oder in der Nähe von urbanen Räumen durchgeführt wurden, konnten gemessene HO_2- und/oder RO_2-Radikalkonzentrationen nicht durch chemische Modellrechnungen reproduziert werden, die das gegenwärtige Verständnis atmosphärischer Chemie widerspiegeln. Auch wenn chemische Modelle eine gewisse Unsicherheit haben, so wurden, insbesondere für RO_2-Radikale, oftmals Diskrepanzen von mehr als einem Faktor drei beobachtet, was eine Vorhersage von Luftqualität erschwert. Die Durchführung von Feldstudien ist allgemein sehr wichtig, um Wissenslücken in Bezug auf atmosphärische Oxidationsprozesse aufzudecken, die dann in Laborexperimenten, wie zum Beispiel in Atmosphärensimulationskammern, in kontrollierten Rahmenbedingungen untersucht werden können.

Diese Arbeit behandelt die Untersuchung von atmosphärischen Oxidationsprozessen in Simulationskammern. Zuerst wurde die Performance und die Vergleichbarkeit verschiedener Atmosphärensimulationskammern untersucht. Dafür wurden Oxidationsexperimente mit -Pinen in neun verschiedenen Simulationskammern, die Teil des EUROCHAMP-2020-Konsortiums sind, durchgeführt. Kammereffekte, wie zum Beispiel die Freisetzung von kurzkettigen, sauerstoffhaltigen Verbindungen von der Kammerwand oder der Verlust von Spurengasen oder Partikeln an der Kammerwand, wurden charakterisiert. Des Weiteren konnten die Ausbeuten an Pinonaldehyd, Formaldehyd und Aceton, die Produkte der Oxidation von -Pinen durch OH sind, in Experimenten in fünf verschiedenen Kammern bestimmt werden. Eine hohe Variabilität der Pinonaldehyd- und Formaldehydausbeuten wurde beobachtet, die sich auch in den Literaturwerten widerspiegelt. Aus den Experimenten abgeleitete Acetonausbeuten stimmen insgesamt innerhalb der kombinierten Fehler überein. Dies gilt auch für den Vergleich mit Literaturwerten.

Generell bieten Atmosphärensimulationskammern eine gute Möglichkeit, die Chemie der Atmosphäre in einer kontrollierten Umgebung zu untersuchen. Das Ziel ist es dabei, die Komplexität von Feldstudien zu vereinfachen und dennoch vergleichbare Bedingungen mit der realen Atmosphäre zu schaffen.

Der Hauptteil der Arbeit befasst sich mit der Untersuchung der Oxidation von anthropogenen VOCs am Tag und in der Nacht in der Atmosphärensimulationskammer SAPHIR am Forschungszentrum Jülich, Deutschland. Gemessene Spurengas- und Radikalkonzentrationen wurden mit 0-dimensionalen Boxmodellrechnungen verglichen, die auf dem Master Chemical Mechanism (MCM) basieren, das durch ein neues Ozonolyseschema für Alkene sowie aktueller Peroxy- und Alkoxychemie aus Struktur-Wirkungsbeziehungen (SAR) komplementiert wurde. Photooxidationsexperimente wurden für verschiedene anthropogene VOCs bei unterschiedlichen NO-Konzentrationen durchgeführt, die die derzeitigen (hohes NO) und zukünftigen (niedriges NO) chemischen Bedingungen simulieren. Die untersuchten VOCs wurden gemäß ihrer Alkoxychemie ausgewählt, wobei HO_2 entweder in einer einfachen Reaktion (Propan, Propen, trans-2-Hexen) oder in einer Mehrfachreaktion (iso-Pentan, n-Hexan) gebildet wird. Da bei der Mehrfachreaktion ein zusätzliches RO_2-Radikal gebildet wird, werden in der Einfach- und Mehrfachreaktion unterschiedlich viele Ozonmoleküle pro oxidiertem VOC erwartet. Eine gute Übereinstimmung (innerhalb von %) ergab der Vergleich der gemessenen Spurengase und Radikale mit den Ergebnissen des MCMs. Die Ergänzung des MCM durch SAR führte zu einer verbesserten Übereinstimmung der HO_2- und RO_2-Radikalkonzentrationen bei Experimenten mit n-Hexan, insbesondere wegen höheren Ausbeuten an organischen Nitraten sowie zusätzlichen RO_2-Isomerisierungsreaktionen. Die HO_2/RO_2-Konzentrationsverhältnisse wurden aus gemessenen und modellierten Radikalkonzentrationen bestimmt, wobei ein % kleineres HO_2/RO_2-Verhältnis beobachtet wurde für die VOCs, die zusätzliche RO_2-Radikale bilden. Die Produktion von Ozon und NO_2 ($O_x = O_3 + NO_2$) wurde aus modellierten Radikalkonzentrationen und gemessenem O_x-Konzentrationen für chemische Bedingungen mit NO Konzentrationen von $3 < \mathrm{NO} <$ ppbv und NO < ppbv berechnet. Für NO < ppbv konnte die O_x-Bildung zusätzlich aus gemessenen Radikalkonzentrationen bestimmt werden. Insgesamt wurde eine gute Übereinstimmung zwischen den verschiedenen Berechnungen gefunden. In Übereinstimmung mit den beobachteten HO_2/RO_2-Konzentrationsverhältnissen wurde eine % höhere O_x-Produktion für VOCs beobachtet, die HO_2 in einer Mehrfachreaktion mit NO bilden. Insgesamt wurden die Diskrepanzen zwischen gemessenen und aus Modellrechnungen bestimmten O_x-Produktionsraten, wie sie aus Feldstudien abgeleitet wurden, in den durchgeführten Kammerversuchen nicht beobachtet.

Die nächtliche Oxidation von cis-2-Buten und trans-2-Hexen wurde in Gegenwart von NO_2 bei verschiedenen Temperaturen (C bis C) untersucht. Bei niedrigen Temperaturen waren die gemessenen Konzentrationszeitreihen von RO_2-Radikalen deutlich verzögert und es wurden niedrigere Spitzenkonzentrationen erreicht als in den von den Boxmodellrechnungen erwarteten RO_2-Konzentrationszeitreihen. Die Übereinstimmung zwischen modellierten und gemessenen RO_2-Radikalkonzentrationen konnte deutlich verbessert werden, wenn die Bildung von Alkylperoxynitraten (RO_2NO_2) aus der Reaktion von RO_2 mit NO_2 im Modell inkludiert wurde. In den oft genutzten chemischen Mechanismen, wie zum Beispiel dem MCM, wird die Bildung von Alkyl-RO_2NO_2, mit Ausnahme vom Methylperoxynitrat, nicht berücksichtigt, da sie aufgrund der kurzen Lebensdauer der Alkylperoxynitrate von weniger als 1 s bei 298 K als vernachlässigbar angesehen wird. Diese Arbeit zeigt, dass % der Alkyl-RO_2-Radikale bei C in den entsprechenden Peroxynitraten gespeichert sind, was sich auf die RO_2- und $NO_x(= NO + NO_2)$-Umgebungskonzentrationen auswirken könnte. Darüber hinaus wurde in einer kürzlich durchgeführten Modellstudie ein Anstieg der NO_x-Konzentration um bis zu 25 % berechnet, wenn man die Bildung von Alkyl-RO_2NO_2 berücksichtigt. In Kombination mit den Ergebnissen dieser Arbeit legt dies nahe, dass diese Reaktionen in die chemischen Mechanismen einbezogen werden sollten, um die zugrundeliegende Chemie besser zu repräsentieren.

Contents

1 | Introduction

Air pollution in urban environments and its impact on human health have already been reported since the 12 century (Goodhill, 1971; Finlayson-Pitts and Pitts, 2000). Most prominent examples are the volcanic eruptions of the Huaynaputina and Tambora volcanos in Peru and Indonesia in 1600 and 1815, respectively, which led to a significant cooling of the atmosphere due to the formation of sunlight-reflecting sulfate aerosol from the oxidation of emitted sulfur dioxide (SO). As a consequence and also due to the high amount of dust particles which were transported over the entire globe, crop failures were reported worldwide leading to famines and economic crises as well as a high death rate (Stothers, 1984; Briffa et al., 1998; Verosub and Lippman, 2008; Fei et al., 2016). Since the industrial revolution, air pollution and climate changed gradually on regional and global scales (Finlayson-Pitts and Pitts, 2000; Seinfield and Pandis, 2006). In addition to biogenic emissions (predominantly isoprene and monoterpenes such as -pinene), anthropogenic (human made) emissions started contributing to the amount of volatile organic compounds (VOCs) in the air and tremendously increased over the last hundred years (Fig. 1.1) (Lamarque et al., 2010; Hoesly et al., 2018; Skeie et al., 2023), impacting not only regional air quality but also global climate (Intergovernmental Panel On Climate Change, 2023). Famous air pollution events were for example the London and Los Angeles smogs. While the London smog with the most severe event in 1952 was driven by high amounts of SO and particles, the Los Angeles smog, with the first appearance

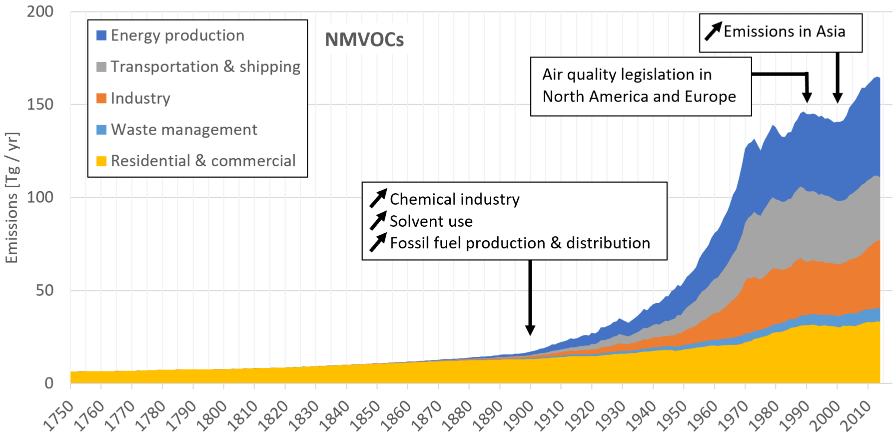

Figure 1.1: Emission trend of non-methane volatile organic compounds (NMVOCs) from 1750 to 2014, categorised into different sectors. The data are adopted from the Community Emissions Data System (CEDS) and Hoesly et al. (2018). Comments are based on the 6 IPCC Report (Intergovernmental Panel On Climate Change, 2023).

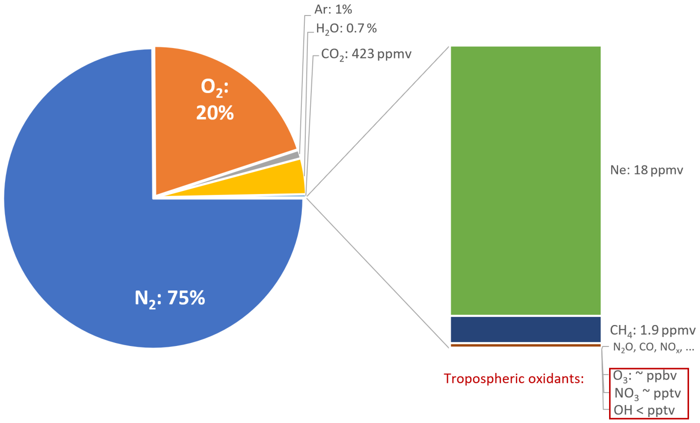

Figure 1.2: Chemical composition of the lower troposphere. The data are taken from Visconti (2016), with the exception of the CO_2 mixing ratio, which is an updated value measured at the monitoring station at Mauna Loa in the week of the 21 of January, 2024 (US Department of Commerce, 2024). The water vapour mixing ratio is variable. The given value was measured in Lauder, New Zealand, on the 25 of November, 2023 (US Department of Commerce, 2024).

in Los Angeles in the late 1940's, was driven by the photochemical degradation of VOCs in the presence of nitrogen oxides, which led to large amounts of hazardous ozone, up to ppbv (parts per billion) in Mexico city (Finlayson-Pitts and Pitts, 2000). The photochemical smog is still a world-wide problem in areas with high emissions of VOCs and nitrogen oxides and unfavourable weather conditions (Finlayson-Pitts and Pitts, 2000). Anthropogenic emissions are predominantly caused by the production and distribution of fossil fuel as well as their use for industry, transportation, cooking, and heating (Fig. 1.1) (Hoesly et al., 2018; Intergovernmental Panel On Climate Change, 2023). Most of the emitted non-methane hydrocarbons are removed from the troposphere (km altitude) on a timescale of hours to months (Seinfield and Pandis, 2006; Intergovernmental Panel On Climate Change, 2023) and therefore play a major role in regional air quality. Methane (CH), however, has a relatively long atmospheric lifetime of yr (Seinfield and Pandis, 2006) and is the most abundant VOC in the troposphere with a global mean mixing ratio of ppmv (status: September 2023, US Department of Commerce (2024)) which increased by % over the last years due to the continuously increasing emissions. Beside carbon dioxide (CO), water vapour (H O), and ozone (O), methane is a greenhouse gas, absorbing infrared radiation, and thus contributes to the global warming due to its high abundance (Finlayson-Pitts and Pitts, 2000).

Before being ultimately removed from the atmosphere by deposition, VOCs typically undergo a variety of gaseous and heterogeneous reactions. The tropospheric oxidation of chemical compounds initiating the chemical degradation of trace gases in the troposphere is mainly driven by three species: ozone, the nitrate radical (NO), and the hydroxyl radical (OH), with tropospheric surface concentrations in the ppbv to low-pptv (parts per trillion) range (Fig. 1.2) (Finlayson-Pitts and Pitts, 2000; Seinfield and Pandis, 2006). While the oxidation of VOCs is dominated by the OH radical during the day and by the nitrate radical during the night, ozone contributes to oxidation processes during both, the day and the night, (Finlayson-Pitts and Pitts, 2000; Seinfield and Pandis, 2006). Even though tropospheric oxidation significantly reduces primary pollutants such as toxic CO, secondary pollutants including ozone, nitrous acid (HNO), and particulate matter (PM) are produced in the chemical degradation of VOCs. Both ozone and PM are not only harmful for human health but also lead to environmental impacts such as a decreased visibility or damage of crops (Finlayson-Pitts and Pitts, 2000; Gaffney and Marley, 2020). Therefore, it is crucial to understand the formation of these secondary pollutants from their precursors. Since the concentrations of the precursor and the secondary pollutants are not linearly correlated, predictions of secondary pollutants are challenging (Finlayson-Pitts and Pitts, 2000).

The relationship between the secondary pollutants and their precursors can be investigated with atmospheric simulation chambers which allow to study the atmospheric oxidation of single VOCs and the resulting formation of secondary pollutants without perturbations by emissions or meteorology (Finlayson-Pitts and Pitts, 2000; Doussin et al., 2023). These chamber studies help developing and evaluating atmospheric chemical models which are used to understand pollutant levels observed in the real troposphere (Doussin et al., 2023). By improving the understanding of the production of secondary pollutants such as O , future air quality can be better predicted and thus controlled via fitted emission protocols.

1.1 Anthropogenic emissions in urban areas

In the past, ozone and particle pollution in urban regions were in particular associated to emissions of nitrogen oxides, namely nitric oxide (NO) and nitrogen dioxide (NO), and volatile organic compounds (VOC) from motor vehicles (McDonald et al., 2018). Therefore, emission regulations were introduced reducing and controlling tailpipe emissions which led to a reduction of NO_x (NO NO_2) and petrochemical VOCs from transportation and to a decrease of high surface ozone pollution events (Warneke et al., 2012; Pollack et al., 2013; Ehlers et al., 2016; Wallington et al., 2022; Wu et al., 2023). However, a stagnation of the decreasing trend of urban ozone concentrations was observed in the last decade (Jiang et al., 2018; Li et al., 2019a; Sicard et al., 2020; McHugh et al., 2023; Wu et al., 2023). Several explanations were suggested such as unfavourable meteorological conditions (Gaudel et al., 2020; Wu et al., 2023), a changing chemical regime (Laughner and Cohen, 2019; Sicard et al., 2020; Kim et al., 2022), a decrease in particulate matter and consequently of the aerosol sink of hydroperoxy radicals and NO_x (Li et al., 2019a,b), as well as the increasing importance of non-combustion sources to the urban VOC mixture (Jiang et al., 2018; McDonald et al., 2018). McDonald et al. (2018) identified a so far unknown source of VOCs called volatile chemical products (VCP) in

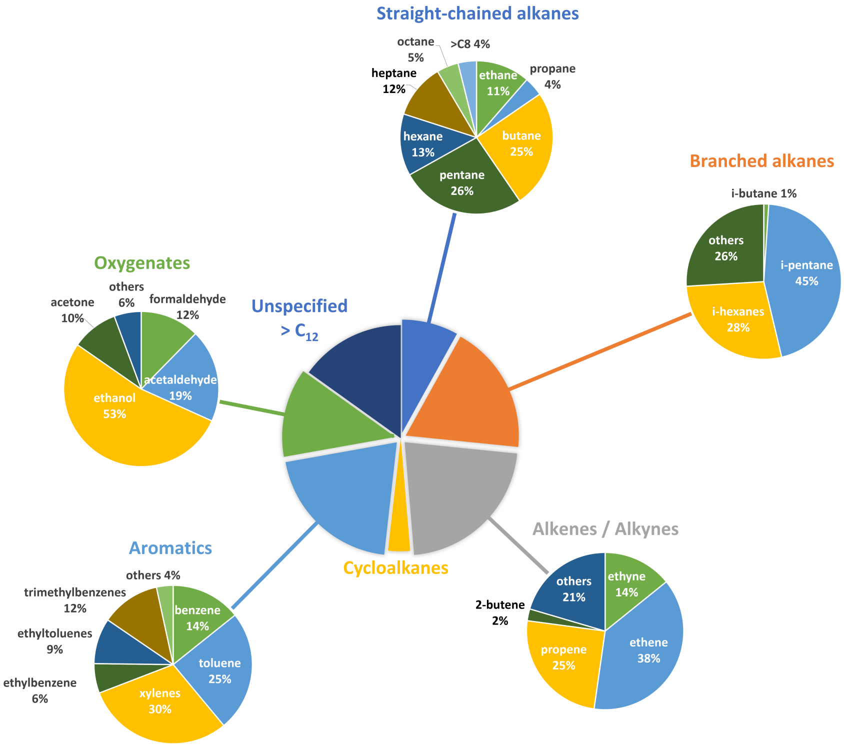

Figure 1.3: Chemical composition of gasoline exhaust, with values taken from McDonald et al. (2018).

Los Angeles, US, which contributes about % to petrochemical VOC emissions (McDonald et al., 2018; Gkatzelis et al., 2021; Asif et al., 2023) and also contributes significantly to VOC emissions in smaller cities (Coggon et al., 2018). Examples for VCPs are cleaning agents, personal care products, printing inks, coatings, adhesives, and pesticides (McDonald et al., 2018). Thus, petrochemical VOCs are found to not only be emitted by transportation and shipping, as assumed in the past, but also by VCPs, such that these types of VOCs still contribute significantly to urban air mixtures nowadays (Ehlers et al., 2016; McDonald et al., 2018; Wang et al., 2023) and represent about % of the total amount of non-methane VOCs in the troposphere (Fig. 1.1) (Hoesly et al., 2018). As shown in Fig. 1.3 for gasoline exhaust, petrochemical VOCs span a large variety of hydrocarbons, with a large fraction of the VOC pool constituted by alkanes, alkenes, and aromatics. While the photochemical oxidation of aromatics is still poorly understood, the tropospheric gas-phase chemistry of alkanes and alkenes is well investigated (Akimoto and Hirokawa, 2020). The abundance of the VOCs is controlled by both, their emission sources and sinks. In the tropospheric oxidation of

VOCs, peroxy (RO) and hydroperoxy (HO) radicals are formed. During the day when OH predominantly initiates the oxidation process, RO and HO radicals contribute to the air pollution by converting nitric oxide into hazardous nitrogen dioxide, which forms ozone by its photolysis. This is the only relevant source of surface ozone. Furthermore, OH radicals can be regenerated by the reaction of RO and HO with NO. Thus, the tropospheric radical chemistry does not only control the OH radical concentration in the troposphere and thus the oxidation capacity, but also the formation of hazardous secondary pollutants such as ozone. Beside O , oxygenated VOCs are formed in the day- and nighttime oxidation which can act as precursors for secondary organic aerosol (SOA) (Finlayson-Pitts and Pitts, 2000; Seinfield and Pandis, 2006).

1.2 Tropospheric daytime and nighttime chemistry

The formation of secondary pollutants such as ozone and particulate matter is strongly coupled to the chemistry of the free radicals RO (organic peroxy radical) and HO (hydroperoxy radical). In this section, the tropospheric oxidation of organic VOCs (hydrocarbons) is introduced for polluted and clean environments with a focus on the formation of ozone.

Oxidation of hydrocarbons by OH

The tropospheric daytime oxidation of pollutants is dominated by the OH radical, which is the most important tropospheric oxidant due to its high reactivity (0.01 s <lifetime < 1 s) (Ren, 2003; Isaksen and Dalsøren, 2011; Nölscher et al., 2012; Gligorovski et al., 2015; Brune et al., 2016; Griffith et al., 2016; Tan et al., 2017, 2018; Whalley et al., 2018; Tan et al., 2019; Slater et al., 2020; Whalley et al., 2021) and its abundance in the sub-pptv range (typical average, daytime concentration = cm , Finlayson-Pitts and Pitts (2000)). The OH radical reacts both with saturated and unsaturated hydrocarbons such as alkanes and alkenes, respectively (Tab. 1.1). In the following, alkanes are denoted as RH where R denotes the moiety which is the methyl group (CH_3) in case of methane (CH). For CH , the hydroxyl radical is the only significant reactant and thus controls their abundances in the atmosphere. In the chemical degradation of *e.g.*, CH ($R = CH_3$), organic peroxy radicals (RO) such as the hydroperoxy radical (HO) are formed (Finlayson-Pitts and Pitts, 2000; Seinfield and Pandis, 2006):

$$\mathrm{OH} \quad \mathrm{RH} \quad \mathrm{R} \quad \mathrm{H_2O} \tag{R1.1}$$

$$\mathrm{R} \quad \mathrm{O_2} \quad \mathrm{RO_2} \tag{R1.2}$$

where saturated VOCs are oxidised by OH via a hydrogen (H) abstraction reaction. The reaction of alkyl radicals R with O forming a peroxy radical happens on a timescale of tens to hundreds of nanoseconds such that RO radicals are immediately formed (Reaction (R1.2))

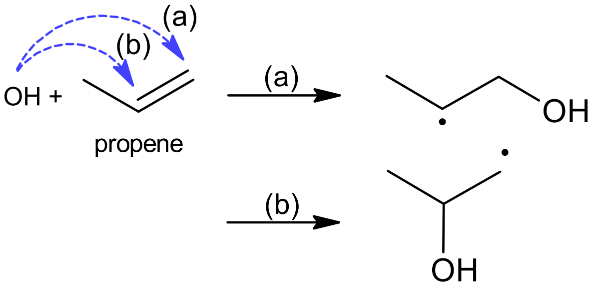

Figure 1.4: Schematic of the OH addition reaction with propene.

(Finlayson-Pitts and Pitts, 2000; Atkinson et al., 2006). In contrast, the OH radical preferably adds to a double bond in its reaction with unsaturated compounds such as alkenes, as shown in Fig. 1.4 for propene. The branching ratio of the OH addition to either sides of the double bond follows Markovnikov addition rules, stating that the stability is highest for formed tertiary radicals and lowest for primary radicals (Gaffney and Marley, 2020). Since a radical is also formed in the OH addition reaction (Fig. 1.4), a peroxy radical is generated as well (Reaction (R1.2)).

Fate of peroxy radicals in polluted environments

The fate of peroxy radicals depends on the presence (or absence) of nitric oxide (NO). In polluted environments, characterised by the the presence of NO (Seinfield and Pandis, 2006), the main reactant of RO is NO (Finlayson-Pitts and Pitts, 2000; Seinfield and Pandis, 2006):

$$RO_2 \quad NO \quad RO \quad NO_2 \tag{R1.3}$$

$$RO_2 \quad NO \qquad RONO_2 \tag{R1.4}$$

In contrast to Reaction (R1.4) in which an organic nitrate (RONO) is formed, Reaction (R1.3) does not terminate the radical cycle (Fig. 1.5). The formed alkoxy radical (RO) in Reaction (R1.3) can undergo different reactions: an H abstraction reaction (Reaction (R1.5)), decomposition (Reaction (R1.6)), or an isomerisation reaction (Reaction (R1.7)) (Finlayson-Pitts and Pitts, 2000; Orlando et al., 2003):

$$O_2 \quad RO \quad R^1CHO \quad HO_2 \tag{R1.5}$$

$$RO \quad R^2 \quad R^3CHO \tag{R1.6}$$

$$RO \quad HOR^4 \tag{R1.7}$$

where R, R^1, R^2, R^3, and R^4 denote different moieties. While the pseudo-first order rate coefficient of the H-abstraction reaction ($_{R1\,5}$ O_2) is typically on the order of s , the rate coefficients of the decomposition and isomerisation reactions can vary over orders

Table 1.1: Overview of typical atmospheric lifetimes of selected anthropogenic VOCs towards their reaction with OH, NO , and O . Concentrations of cm , pptv, and ppbv were assumed for OH, NO , and O , respectively. The values are based on reaction rate coefficients taken from Atkinson et al. (2004, 2006), if not noted differently. The lifetimes can then be calculated via $_{\mathrm{X}\ \mathrm{VOC}}$ $_{\mathrm{X}\ \mathrm{VOC}}\,\mathrm{X}$ with X = OH, NO , O .

VOC	OH	NO	O
methane	5 yr		
propane	1.1 d		
propene	1.1 h [a]	1 d	23 h
iso-pentane [a]	3.1 d		
cis-2-butene [a]	5 h	40 min	1.8 h
n-hexane [a]	2.1 d		
trans-2-hexene	4.6 h	37 min [b]	1.4 h [b]

[a] Based on reaction rate coefficients taken from Atkinson (1997).

[b] Based on reaction rate coefficients taken from Atkinson and Arey (2003).

of magnitude and are highly dependent on the structure of the alkoxy radical (Somnitz and Zellner, 2000; Peeters et al., 2004; Atkinson et al., 2006; Atkinson, 2007; Vereecken and Peeters, 2009, 2010). Depending on R^2 and R^4, Reactions (R1.6) and (R1.7) may either lead to the formation of another RO radical, undergoing another reaction step with NO (Reaction (R1.3)) in a polluted environment, or produce an HO radical after an H-abstraction reaction. The HO radicals then react with NO, regenerating the hydroxyl radical and thus closing the radical cycle (Fig. 1.5) (Finlayson-Pitts and Pitts, 2000; Seinfield and Pandis, 2006):

$$\mathrm{HO_2} \quad \mathrm{NO} \quad \mathrm{OH} \quad \mathrm{NO_2} \qquad \text{(R1.8)}$$

In contrast, termination reactions of the radical cycle such as Reaction (R1.4) do not lead to the regeneration of the OH radical. The organic nitrate yield ($_{\mathrm{RONO_2}}$), which is equivalent to the branching ratio of Reaction (R1.4), depends on the structure and the size of the peroxy radical (Carter and Atkinson, 1989; Arey et al., 2001; Teng et al., 2015; Jenkin et al., 2019). Another predominant termination reaction is due to the reaction of OH with NO producing HNO (Fig. 1.5):

$$\mathrm{OH} \quad \mathrm{NO_2} \qquad \mathrm{HNO_3} \qquad \text{(R1.9)}$$

This is typically the main radical termination reaction at high NO (Finlayson-Pitts and Pitts, 2000). The deposition of HNO contributes significantly to the removal of NO_x from the atmosphere which was estimated to be % in the Los Angeles basin (Russell et al., 1993; Finlayson-Pitts and Pitts, 2000).

The formation of NO molecules in the reaction of RO and HO with NO (Reactions (R1.3) and (R1.8)) leads to the formation of ozone (Fig. 1.5) (Finlayson-Pitts and Pitts, 2000;

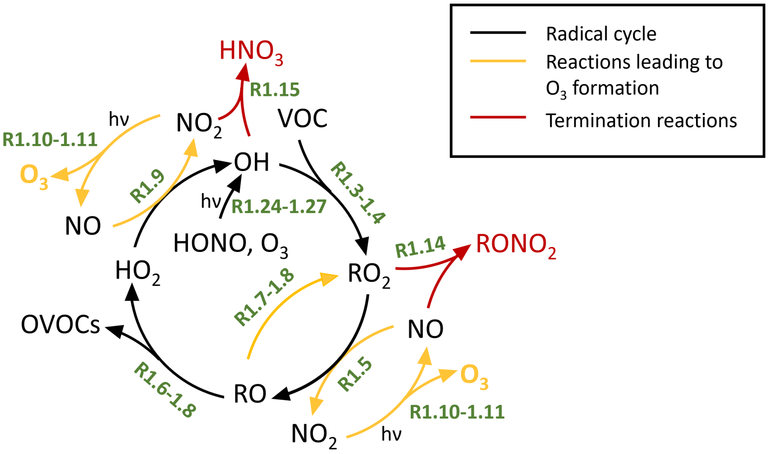

Figure 1.5: Schematic of the radical chemistry dominated by the presence of NO (polluted environment) and its impact on the ozone formation.

Seinfield and Pandis, 2006):

$$NO_2 \quad h \qquad nm \quad NO \quad O \quad P \qquad \text{(R1.10)}$$

$$O \quad P \quad O_2 \qquad O_3 \qquad \text{(R1.11)}$$

where O P denotes the oxygen atom in its ground state. The chemical degradation of VOCs is the only source of O during the day. In environments impacted by emissions from combustion processes, surface O concentrations can exceed ppbv (Seinfield and Pandis, 2006). In the presence of NO, NO is regenerated by the reaction of NO with O (Finlayson-Pitts and Pitts, 2000; Seinfield and Pandis, 2006):

$$NO \quad O_3 \quad NO_2 \quad O_2 \qquad \text{(R1.12)}$$

Via Reactions (R1.10)-(R1.12), NO, NO , and O are photochemically coupled and a photostationary state is established, characterised by equal production and destruction rates of NO (Seinfield and Pandis, 2006):

$$\frac{d\,NO_2}{d} \qquad {}_{NO_2}\,NO_2 \qquad {}_{(R1.12)}\,O_3\;NO \qquad (1.1)$$

where ${}_{NO_2}$ denotes the photolysis frequency of NO . Since O and NO concentrations are in a photostationary state (Eq. (1.1)), both together are often summarised as odd oxygen ($O_x \quad O_3 \quad NO_2$) (Seinfield and Pandis, 2006). The net production of odd oxygen

(Reactions (R1.3) and (R1.8)) can then be calculated from (Seinfield and Pandis, 2006):

$$O_x \qquad {}_{R1\,3}\ RO_2\ NO \qquad {}_{RONO_2} \qquad {}_{R1\,8}\ HO_2\ NO \qquad {}_{O_x} \tag{1.2}$$

where ${}_{R1\,3}$ and ${}_{R1\,8}$ refer to the rate coefficients of the reaction of RO and HO with NO (Reactions (R1.3) and (R1.8)), respectively. Furthermore, ${}_{RONO_2}$ and ${}_{O_x}$ denote the organic nitrate yield (Reaction (R1.4)) and loss reactions of O_x, respectively, which are further discussed below. Since the O_x production rate is sensitive to the reaction of peroxy radicals with NO, the fate of the formed alkoxy radicals (Reactions (R1.5)-(R1.7)) impacts the O_x formation significantly. Two O_x molecules are expected to be formed from the reaction of one VOC with OH, if the uni- or bimolecular reaction of the alkoxy radical yields an HO_2 radical (Fig. 1.5). If another RO radical is formed instead of an HO radical, a second RO_2 NO reaction takes place within one radical cycle, yielding another NO and thus O molecule (Fig. 1.5). Beside their reaction with NO, peroxy radicals can also react with NO leading to the formation of reservoir peroxynitrate species (RO NO) such as peroxynitric acid (HO NO):

$$HO_2 \quad NO_2 \qquad HO_2NO_2 \tag{R1.13}$$

$$RO_2 \quad NO_2 \qquad RO_2NO_2 \tag{R1.14}$$

Both, HO NO and alkyl peroxynitrate compounds are thermally unstable and regenerate NO and HO or RO after the thermal decomposition. Due to the short lifetimes of HO NO and of alkyl-RO NO (s and s at K, respectively), they are thought to be irrelevant with regard to radical chemistry in the lower troposphere. Therefore, the formation of alkyl-RO NO (Reaction (R1.14)) is not implemented in atmospheric chemical models with the exception of methyl peroxynitrate due to its abundance (Atkinson et al., 2004; Jenkin et al., 2019). Other exceptions are peroxyacetyl nitrate compounds (PANs) formed from acyl peroxy radicals (R(=O)O). Due to their elongated lifetime of min to min at K and atm, acyl peroxyacetyl nitrates act as reservoir species for RO and NO and can be transported over long distances before releasing RO and NO_x (NO NO_2) again (Finlayson-Pitts and Pitts, 2000; Atkinson et al., 2006; Jenkin et al., 2019).

Fate of peroxy radicals in remote environments

In pristine environments, characterised by low NO_x concentrations (pptv, Seinfield and Pandis (2006)), other loss reactions of peroxy radicals become competitive with the reaction of RO with NO such as (Finlayson-Pitts and Pitts, 2000; Seinfield and Pandis, 2006):

$$\mathrm{RO_2}\quad \mathrm{HO_2}\quad \mathrm{ROOH}\quad \mathrm{O_2} \tag{R1.15}$$

$$\mathrm{ROH}\quad \mathrm{O_3} \tag{R1.16}$$

$$\mathrm{RO}\quad \mathrm{OH}\quad \mathrm{O_2} \tag{R1.17}$$

$$\mathrm{RO_2}\quad \mathrm{R\,O_2}\quad \mathrm{RO}\quad \mathrm{R\,O}\quad \mathrm{O_2} \tag{R1.18}$$

$$\mathrm{R}_{\ \mathrm{H}}\quad \mathrm{O}\quad \mathrm{R\,OH}\quad \mathrm{O_2} \tag{R1.19}$$

$$\mathrm{ROOR}\quad \mathrm{O_2} \tag{R1.20}$$

For aliphatic peroxy radicals, consisting only of carbon and hydrogen atoms, the reactions of RO with HO proceed via Reaction (R1.15). Non-zero branching ratios of Reactions (R1.16) and (R1.17) are expected for acyl-RO and for RO with specific functional groups (Jenkin et al., 2019). For the permutation reactions of RO (Reactions (R1.18)-(R1.20)), including self-reactions (R'=R) and cross-reactions (R' R), the branching ratios of the different reaction channels depend on the predominant type of RO in the air. Typically, Reaction (R1.18) is the predominant pathway with a branching ratio of more than % (Jenkin et al., 2019).

Apart from Reactions (R1.15)-(R1.20), the isomerisation of RO radicals can also play a role in remote areas (Vereecken and Nozière, 2020). A schematic of a 1,6 H-migration reaction, which eventually leads to the formation of a new RO radical (HOOR O), containing a hydroperoxide (OOH) group, is shown in Fig. 1.6. Chain reactions of several RO isomerisation reactions lead to the formation of low-volatility oxygenated compounds and highly oxygenated molecules (HOMs), which play a crucial role in the secondary aerosol formation (Hallquist et al., 2009; Jokinen et al., 2014; Ehn et al., 2017; Bianchi et al., 2019; Rissanen, 2021). Depending on the size and the structure of the newly formed peroxy radical, it can undergo either several isomerisation reactions, yielding either another higher oxidised RO radical (HOO) R O , before stable products containing a high ratio of oxygen to carbon atoms are formed. Another reaction pathway after an isomerisation reaction can be the formation of a carbonyl together with an OH radical (Fig. 1.6). The latter reaction pathway is the result from an -OOH H-migration which leads to the formation of an -OOH radical that decomposes spontaneously (Vereecken et al., 2004; Vereecken and Nozière, 2020). If possible, the OOH substituted RO radical can undergo rapid scrambling, shifting the hydrogen atom between the peroxy and the hydroperoxy group (HOOR O ' O R OOH) (Vereecken and Nozière, 2020) and therefore, leading to different products. With reaction rate coefficients larger than s , the scrambling reaction is dominant over reactions of RO with HO and even with NO under most atmospheric conditions (Miyoshi, 2012; Jørgensen et al., 2016; Nozière and Vereecken,

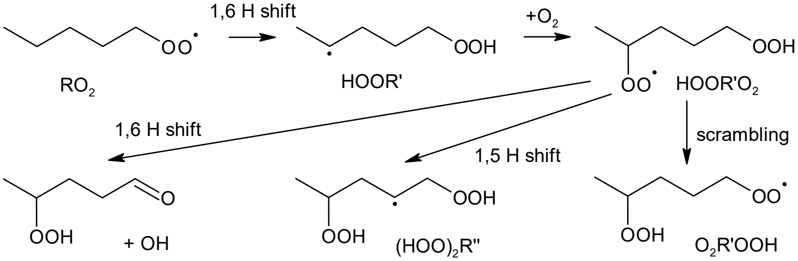

Figure 1.6: Schematic displaying the RO isomerisation reaction as well as secondary reactions. The reaction scheme is adopted from the open access publication by Vereecken and Nozière (2020) under the Creative Commons Attribution 4.0 License (https://creativecommons.org/licenses/by/4.0).

2019). Typically, the isomerisation reaction rates are faster for higher oxidised compounds (Vereecken and Nozière, 2020; Rissanen, 2021) and the reaction rate coefficients highly depend on the functional groups around the involved hydrogen atom and the peroxy group as well as on the span of the migration (Vereecken and Nozière, 2020).

In remote areas, the HO reaction with itself, forming the reservoir species hydrogen peroxide (H O), can play a role for the atmospheric fate of HO (Finlayson-Pitts and Pitts, 2000):

$$\mathrm{HO_2 \quad HO_2 \quad\quad H_2O_2 \quad O_2} \tag{R1.21}$$

H_2O_2 either releases one HO molecule in its reaction with OH or forms two OH radicals in its photolysis.

OH production

Apart from the OH recycling in the presence of VOCs and NO, the OH radical is produced photolytically which limits its abundance to mainly daytime hours. The major source of OH is the photolysis of ozone, which can yield an electronically excited oxygen atom O(D), which reacts with water vapour (H O) forming eventually two OH radicals (Finlayson-Pitts and Pitts, 2000; Seinfield and Pandis, 2006):

$$\mathrm{O_3 \quad h \qquad\quad nm \qquad O_2 \quad O \;\; D} \tag{R1.22}$$

$$\mathrm{O \;\; D \quad H_2O \qquad OH} \tag{R1.23}$$

$$\mathrm{O \;\; D \qquad\qquad O \;\; P} \tag{R1.24}$$

Beside its reaction with water vapour, O D is predominantly deactivated by collisions *e.g.*, with N (Finlayson-Pitts and Pitts, 2000). Due to the high amount of H O and a strong actinic flux, highest OH radical concentrations can be found in the tropics (Seinfield and Pandis, 2006). Another source, especially in urban areas is the photolysis of nitrous acid (HONO), which often accumulates during nighttime. It photolyses at longer wavelengths than ozone, yielding a NO molecule in addition to an OH radical. As long wavelengths penetrate the atmosphere already in the early morning hours, HONO photolysis can be the major OH source at that time of the day before ozone photolysis gains in importance (Finlayson-Pitts and Pitts, 2000; Atkinson et al., 2004; Seinfield and Pandis, 2006):

$$\mathrm{HONO} \quad h \qquad\qquad \mathrm{nm} \quad \mathrm{OH} \quad \mathrm{NO} \tag{R1.25}$$

In rural areas, OH radicals are also formed from the reaction of HO with O (Finlayson-Pitts and Pitts, 2000; Gligorovski et al., 2015):

$$\mathrm{HO_2} \quad \mathrm{O_3} \quad \mathrm{OH} \quad \mathrm{O_2} \tag{R1.26}$$

Beside the primary radical production by photolytic reactions, hydroperoxy radicals are also photolytically produced by the photolysis of formaldehyde (Finlayson-Pitts and Pitts, 2000):

$$\mathrm{HCHO} \quad h \qquad\qquad \mathrm{nm} \quad \mathrm{H} \quad \mathrm{HCO} \tag{R1.27}$$

$$\mathrm{HCO} \quad \mathrm{O_2} \quad \mathrm{HO_2} \quad \mathrm{CO} \tag{R1.28}$$

$$\mathrm{H} \quad \mathrm{O_2} \quad \mathrm{HO_2} \tag{R1.29}$$

being the major primary source of HO during the day (Finlayson-Pitts and Pitts, 2000).

Oxidation of hydrocarbons by O

The relatively high ozone concentrations, which are typically more than three orders of magnitude larger than OH radical concentrations in the troposphere, facilitate the oxidation of unsaturated VOCs by ozone even though the reaction rate coefficients are orders of magnitudes smaller than the reactions with OH (Tab. 1.1) (Finlayson-Pitts and Pitts, 2000). Ozone can only react with unsaturated VOCs (ozonolysis), which contain minimum one double bond, and adds to their double bond, forming a short-lived primary ozonide (POZ), which decomposes producing carbonyls and chemically activated Criegee intermediates (CI , Fig. 1.7). The fate of the formed Criegee intermediates has been a subject of mechanistic studies for decades (Finlayson-Pitts and Pitts, 2000; Taatjes et al., 2014; Vereecken et al., 2014; Vereecken, 2017; Vereecken et al., 2017; Newland et al., 2020, 2022). The branching ratios of the two different pairs of carbonyls and Criegee intermediates, and ( ) in Fig. 1.7, are typically assumed to be similar (Seinfield and Pandis, 2006). However, a recent study by Newland et al. (2022) suggests a dependency of the branching ratio on the moieties R -R , highlighting the ongoing research on this topic. Structure-activity relationships for the rates of reactions of Criegee intermediates have been recently developed by Vereecken et al. (2017) and Newland et al.

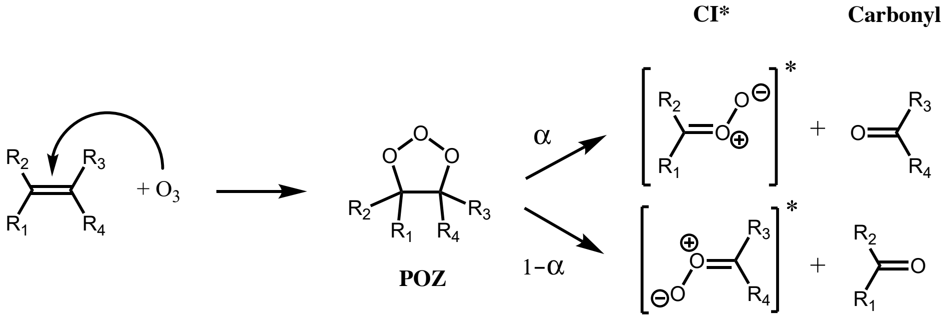

Figure 1.7: Simplified schematic of the reaction of ozone with an unsaturated compound forming a primary ozonide (POZ) which decomposes forming carbonyls in addition to excited and stabilised Criegee intermediates. The figure is adopted from the open access publication by Newland et al. (2022) under the Creative Commons Attribution 4.0 License (https://creativecommons.org/licenses/by/4.0).

(2022). Generally, excited Criegee intermediates can decompose or be collisionally stabilised before undergoing subsequent unimolecular and bimolecular reactions (Finlayson-Pitts and Pitts, 2000; Seinfield and Pandis, 2006; Taatjes et al., 2014; Newland et al., 2022). If strong UV radiation is not available like during the night, in winter, or in higher latitudes, a significant fraction of the total OH production is from ozonolysis reactions (Taatjes et al., 2014). Similarly, ozonolysis may also contribute to the OH formation during the night and during dusk, when photolytic formation is suppressed (Finlayson-Pitts and Pitts, 2000).

Oxidation of hydrocarbons by NO

Beside ozone and the hydroxyl radical, the nitrate radical (NO) is a tropospheric oxidant, produced in the reaction of ozone with NO (Finlayson-Pitts and Pitts, 2000; Seinfield and Pandis, 2006):

$$NO_2 \quad O_3 \quad NO_3 \quad O_2 \tag{R1.30}$$

During the day, NO is rapidly lost by photolysis, regenerating NO and O , and by its reaction with NO forming NO :

$$NO_3 \quad h \qquad nm \quad NO_2 \quad O \;\; P \tag{R1.31}$$

$$NO_3 \quad NO \quad NO_2 \tag{R1.32}$$

Therefore, the NO radical typically plays a minor role for tropospheric daytime oxidation (Finlayson-Pitts and Pitts, 2000). In boreal forests however, the oxidation of biogenic volatile organic compounds by NO can also be competitive with the loss of NO by photolysis and the reaction with NO (Reactions (R1.31) and (R1.32)) during the day (Liebmann et al., 2018). During the night, NO can exist in sufficient concentrations to contribute to the tropospheric nighttime oxidation. NO and NO are then in a thermal equilibrium with the reservoir species dinitrogen pentoxide (N O) (Finlayson-Pitts and Pitts, 2000; Seinfield and Pandis, 2006):

$$NO_3 \quad NO_2 \qquad\qquad N_2O_5 \tag{R1.33}$$

The major loss of N O is its heterogeneous loss on aqueous aerosol forming HNO , which leads to an effective removal of tropospheric O_x. This loss pathway of N_2O_5 can be one major source of atmospheric HNO (Finlayson-Pitts and Pitts, 2000), which can also be formed from the reaction of NO radicals with hydrocarbons in the night (Finlayson-Pitts and Pitts, 2000):

$$NO_3 \quad RH \quad HNO_3 \quad R \tag{R1.34}$$

Like the OH radical, the NO radical reacts with saturated as well as unsaturated compounds via an H-abstraction reaction or a NO -addition reaction, respectively (Finlayson-Pitts and Pitts, 2000). Though the reaction of NO with alkanes is not expected to be a significant loss path of VOCs due to the small reaction rate coefficients between cm s to cm s (Finlayson-Pitts and Pitts, 2000). In the NO -addition reaction with alkenes, a -nitrate-alkyl RO (>C(ONO)-C(O)<) is formed.
In the presence of NO concentrations, RO radicals can also undergo a reaction with NO forming an alkoxy radical (RO) and NO (Finlayson-Pitts and Pitts, 2000; Seinfield and Pandis, 2006):

$$RO_2 \quad NO_3 \quad RO \quad NO_2 \quad O_2 \tag{R1.35}$$

with RO further reacting according to Reactions (R1.5)-(R1.7). At night, Reaction (R1.35) can be a major loss of RO_2 (Finlayson-Pitts and Pitts, 2000).
Generally, nighttime chemistry affects the chemical conditions on the next day (Brown and Stutz, 2012). As NO is efficiently photolysed at sunrise, releasing NO and ozone (Reactions (R1.31) and (R1.11)), NO acts as a nighttime reservoir for nitrogen oxides available for photochemistry. In addition, heterogeneous reactions of NO contribute significantly to the HONO formation at night, which photolyses in the morning producing OH radicals via Reaction (R1.25) (Wong et al., 2011).

1.3 Atmospheric radical measurement by laser-induced fluorescence

The detection of the atmospheric OH radical is challenging due to its low concentration (cm). To measure these low concentrations highly sensitive instrumentation utilising techniques, such as the laser-induced fluorescence (LIF), is required. The concept of laser-induced fluorescence is the excitation of molecules, such as the OH radical, via pulsed laser radiation and the detection of the subsequent deactivation of the molecule by spontaneous emission of a photon (fluorescence).
First attempts of measuring ambient OH radical concentrations with the LIF technique have

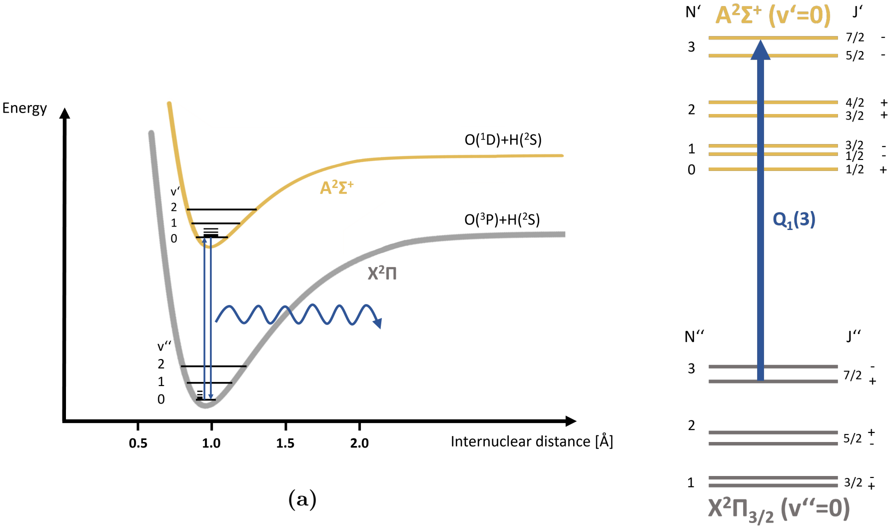

(a)

(b)

Figure 1.8: Jablonski diagram for the excitation and subsequent fluorescence of of the OH radical, inspired by Stauffer et al. (2012) (a), together with the rotational energy levels in and , inspired by McGee and McIlrath (1984) (b) and highlighting the transition, which is commonly used for the excitation of the OH radical. Vibrational and rotational quantum numbers are defined as v', v" and as N', N", respectively. Furthermore, , denote the total electronic angular momentum.

been made in the early 1970s by focusing a laser beam of nm onto a mm spot in air (Wang and Davis, 1974). However, the fluorescence efficiency was small (Tab. 1.2) and in addition, large interference signals were caused by the OH production from the photolysis of ozone (ozone-water interference, Reactions (R1.22) and (R1.23)) along the path of the laser beam (Crosley, 1995). An improvement of the instrumental design was pioneered by Hard et al. (1979, 1984), who measured the laser-induced fluorescence of OH in a low-pressure detector system by sampling air through a nozzle with an inner diameter of mm (Fluorescence Assay by Gas Expansion, FAGE). In this way, the background signal, interferences, as well as the non-radiative quenching of excited OH radicals could be reduced and the fluorescence efficiency improved (Hard et al., 1984).

Figure 1.8a displays the vibrational energy level scheme for the electronic ground state and for the first excited electronic state of the OH radical, which can be described by the Morse potential. For each electronic state there is a set of vibrational levels, characterised by the vibrational quantum number , and rotational states build upon each vibrational state (Finlayson-Pitts and Pitts, 2000; Diem, 2021).

In the early versions of the LIF instruments, OH radicals were excited in the

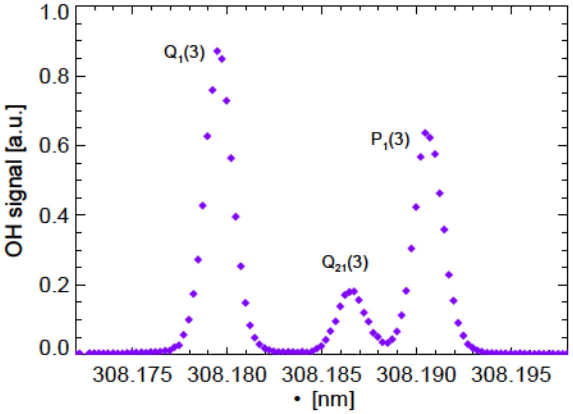

Figure 1.9: Excitation spectrum of OH radicals of the $X^2\Pi_{3/2}(v'' = 0) \rightarrow A^2\Sigma^+(v' = 0)$ transition between 308.17 nm and 308.2 nm, measured with the ROxLIF instrument using a calibration source (Section 3.1.2). Shown are the $Q_1(3) - Q_{21}(3) - P_1(1)$ absorptions.

1) vibrational level by laser light with a wavelength of 282 nm while fluorescence of the $A^2\Sigma^+(v' = 0) \rightarrow X^2\Pi(v'' = 0)$ band was measured, so that scattered and fluorescence photons can be easily discriminated. Further developments of the instrument in the 1990s made use of the excitation in the vibrational ground state of $A^2\Sigma^+(v' = 0)$ with $\lambda = 308$ nm due to the higher OH absorption cross section and the ~ 30 times smaller ozone absorption cross section than at 282 nm, leading to less interference from the photolysis of ozone and thus a better sensitivity of the instruments (Chan et al., 1990; Hofzumahaus et al., 1990; Brune et al., 1993; Hofzumahaus and Holland, 1993). After excitation, the excited radical undergoes rotational relaxation, caused by collisions with other molecules (Lengel and Crosley, 1977). As a consequence, fluorescence light in the wavelength range between 307 and 311 nm can be observed (Holland et al., 1995). Due to its large absorption cross section (Dorn et al., 1995), the $Q_1(3)$ transition of the $X^2\Pi_{3/2}(v'' = 0) \rightarrow A^2\Sigma^+(v' = 0)$ band is often used for excitation (Fig. 1.8b), where $X^2\Pi_{3/2}$ is one of the two fine structure states of the electronic ground state. Furthermore, the unique excitation spectrum of the $Q_1(3)$-$Q_{21}(3)$-$P_1(1)$ absorptions is easy identifiable (Fig. 1.9).

In the competition with the fluorescence, the excited OH($A^2\Sigma^+, v' = 0$) radicals can also be collisionally deactived by other air molecules such as N_2 or O_2, also called fluorescence quenching (Lengel and Crosley, 1978). The lifetime of the excited OH radicals can be written in terms of the natural radiative lifetime τ_{rad}, which is equivalent to the reciprocal Einstein coefficient for the spontaneous emission and equals 688 ns, and a quenching term (Tab. 1.2)

Table 1.2: Overview of the lifetime of excited OH radicals $_{\mathrm{OH}}$ at different pressures (Eq. (1.3)). The lifetime of excited OH radicals towards quenching through collisions with air molecules M is given by . Calculations here consider a water vapour mixing ratio of %.

[hPa]	[ns]	$_{\mathrm{OH}}$ [ns]
4	188	148
10	75	68
1013.25	0.7	0.7

(Atkins and de Paula, 2020):

$$_{\mathrm{OH}} \qquad \frac{\quad}{\quad} \tag{1.3}$$

In Eq. (1.3) denotes the quenching rates from collisions of OH with air molecules (=N , O , H O) and [ ] the concentration of the collisional partner . The time-dependent intensity of the fluorescence of OH radicals excited by a laser pulse can then be expressed as follows (Atkins and de Paula, 2020):

$$\exp \frac{\quad}{_{\mathrm{OH}}} \tag{1.4}$$

Due to the similar wavelength of the laser light and the fluorescence light the fluorescence is measured via gated photon counting. A detailed description of the gated photon counting, as applied for the SAPHIR ROxLIF instrument, can be found in Section 3.1.2.

1.4 Objectives of this thesis

In several field campaigns (Brune et al., 2016; Tan et al., 2017; Whalley et al., 2018; Tan et al., 2019; Slater et al., 2020; Whalley et al., 2021; Woodward-Massey et al., 2023), urban air was studied focusing on the radical chemistry during daytime and nighttime. Comparisons with atmospheric chemical model calculations revealed discrepancies between measured and modelled HO and RO radical concentrations, especially for NO mixing ratios larger than ppbv during the day (Brune et al., 2016; Griffith et al., 2016; Tan et al., 2017, 2018; Whalley et al., 2018; Slater et al., 2020; Whalley et al., 2021; Woodward-Massey et al., 2023). As a consequence, also a discrepancy of up to a factor of 10 in London (Whalley et al., 2018) and 100 in Beijing (Whalley et al., 2021) was observed for the ozone production rates (Brune et al., 2016; Griffith et al., 2016; Tan et al., 2017, 2018; Whalley et al., 2018; Slater et al., 2020; Whalley et al., 2021; Woodward-Massey et al., 2023) determined from measured and modelled radical concentrations in field studies according to Eq. (1.2) (Martinez, 2003; Ren et al., 2013; Brune et al., 2016). In addition, model-measurement discrepancies of particularly RO_2 radical concentrations were observed during the night in the presence of high NO mixing ratios (up to ppbv) (Tan et al., 2017, 2018; Whalley et al., 2018; Slater et al., 2020). The observed disagreements between chemical models and observations indicate an incomplete understanding of the radical chemistry driving the chemical degradation of VOCs and thus uncertainties for the formation of secondary pollutants such as ozone or secondary organic aerosol (Section 1.2). Solving this knowledge gap is crucial for mitigating air pollution and understanding processes affecting regional air quality for setting proper future emission regulations.

Different possibilities/suggestions have been tested to improve the model-measurement agreement during the day such as additional radical production from the photolysis of nitryl chloride (ClNO) or chlorine compounds (Tan et al., 2018; Slater et al., 2020), a decreased rate coefficient of the RO_2 NO reaction (Tan et al., 2017), or a lowered RO -to-HO conversion efficiency (Whalley et al., 2018, 2021).

Observed model-measurement discrepancies found for RO radical concentrations during the night (Tan et al., 2018; Whalley et al., 2018; Slater et al., 2020) may be partly explainable by a reduced detectability of specific nitrate-RO_2 radicals. Recent chamber studies revealed that a large fraction of RO_2 formed in the reaction of NO_3 with isoprene (Vereecken et al., 2021) and of nitrate-RO from short-chain alkenes (Novelli et al., 2021) cannot be detected by the laser-induced fluorescence technique, as this technique requires the formation of OH or HO from the alkoxy unimolecular reactions for the RO measurement. A good model-measurement agreement was found for RO_2 formed in the nighttime oxidation of cis-2-butene, considering the limited detectability of the major RO_2 species and an updated ozonolysis and radical scheme (Novelli et al., 2021). However, model-measurement discrepancies remain for *e.g.*, the nighttime RO chemistry of trans-2-hexene (Novelli et al., 2021). Furthermore, a recent global model study by Khan et al. (2020) showed that non-acyl peroxynitrates, formed in the reaction of RO_2 with NO_2, affect tropospheric oxidant concentrations. Alkyl peroxynitrates are typically not included in chemical models with the exception of methyl peroxynitrate, due to their short lifetime (s) at 298 K (Jenkin et al., 2019). They are assumed to be relevant at cold temperatures found in polar regions (Browne et al., 2011; Orlando and Tyndall, 2012) or in the upper troposphere (Browne et al., 2011).

Simulation chambers are excellent tools to test atmospheric oxidation processes in an isolated, well-known environment, allowing to simplify the chemistry of the complex air mixture, found in field studies, by studying the oxidation of single VOCs. Therefore, simulation chambers are important for refining chemical models by uncovering possible shortcomings in the current knowledge of atmospheric oxidation.

In Europe, the infrastructure ACTRIS is being implemented, comprising seventeen European simulation chambers and providing an access to simulation chambers and high quality experimental data, facilitating atmospheric research. As simulation chambers are confined by walls made of Teflon or metal chamber-related chemical and physical processes need to be well characterised and considered in the design of the experiments and the subsequent data analysis. One of the chambers within the ACTRIS infrastructure is the SAPHIR chamber at Forschungszentrum Jülich, Germany. In this work, a multi-chamber study, involving nine different simulation chambers, was performed. The largest part of this thesis focuses on experiments conducted in the SAPHIR chamber, aiming to better understand the gap between measured and modelled radical concentrations, observed in the different field studies. The following key questions are investigated:

- Do experiments from simulation chambers, evaluated as part of the EUROCHAMP-2020 multi-chamber study, deliver consistent results?
- Are zero-dimensional box model calculations, representing state-of-the-art chemical models, able to reproduce measured radical concentrations in simulation chamber experiments, mimicking daytime and nighttime conditions?
- Is the ozone production determined from observed odd oxygen (O_x O_3 NO_2) concentrations in agreement with the ozone production determined from measured and modelled radical concentrations, specifically during the oxidation chain of anthropogenic VOCs, for which a higher-than-usual number of NO-to-NO oxidation reactions play a role?
- Is there an increased disagreement in the simulation chamber experiments between modelled and measured O_x production as observed in field experiments for increasing levels of NO_x?
- Do non-acyl (alkyl) peroxynitrates affect the radical concentrations in the chamber oxidation experiments at ambient temperatures?

A multi-chamber study (Chapter 2) including nine different chambers was performed within the EUROCHAMP-2020 project, using the oxidation of -pinene to determine potential shortcomings of chamber effects which need to be considered in future experimental procedures of oxidation experiments. Furthermore, yields of gaseous products (pinonaldehyde, acetone, and formaldehyde) are derived to test the comparability of experiments performed in different chambers.

In addition, two sets of experiments were performed in the atmospheric simulation chamber SAPHIR, mimicking daytime and nighttime conditions observed in urban areas (Chapter 3). Measured trace gas and radical concentrations were compared to zero-dimensional box model calculations, based on mechanistic and kinetic information from the Master Chemical Mechanism (MCM) which was complemented by state-of-the-art radical chemistry and ozonolysis schemes. Photooxidation experiments of anthropogenic VOCs (propane, propene, iso-pentane, n-hexane, and trans-2-hexene), found in urban air mixtures (Fig. 1.3), were conducted at different NO_x concentrations (Section 3.2), representative for current (high NO) and future (low NO) chemical regimes. The investigated VOCs exhibit two different sorts of alkoxy chemistry, forming HO_2 either in one or two NO reaction steps. The impact of the different alkoxy chemistry on the ozone production was assessed by studying the HO /RO ratio and the O_x production, derived from measured and modelled radical concentrations. In addition,

atmospheric simulation chambers allow to determine the ozone production rate directly from the measured O_x concentration, which is not possible in field studies due to the influences of transport and a variety of ozone sources and sinks that are not easy to quantify.
The second set of experiments was performed in the dark, investigating the nighttime RO radical chemistry of trans-2-hexene and cis-2-butene at different temperatures to study the role of non-acyl peroxynitrates and their impact on the nighttime radical chemistry (Section 3.3).
In the realisation of the chamber experiments, a team of people was involved. Information about individual contributions and about data storage can be found in the individual chapters and is summarised in Chapter B.1.

2 | Investigation of chamber effects and gas-phase product yields in different simulation chambers

The content of this chapter is based on an unpublished report of “Work Package 2” of the EUROCHAMP-2020 project with the title “Report -pinene multi-chamber experiment” by M. Färber, H. Fuchs, D. Bell, H. Herrmann, G. McFiggans, W. Mellouki, A. Munoz, S. Pandis, B. Picquet-Varrault, H. Saathoff, A. Virtanen and was entirely rewritten. Data from the experiments in this work are stored on servers at the Institute for Energy and Climate Research, IEK-8: Troposphere at Forschungszentrum Jülich and are accessible on request.
The authors contributed to the original report as follows:
HF and MF wrote the report. HF provided MF scripts for the data processing of the individual chamber data. MF analysed the data. DB, HH, GM, WM, AM, SP, BP-V, HS, AV were responsible for chamber experiments performed in the PACS-C3, LEAK, MAC, HELIOS, EUPHORE, FORTH, CESAM, AIDA, and ILMARI chambers, respectively.

2.1 Introduction

There is a variety of atmospheric simulation chambers worldwide. In Europe, seventeen atmospheric simulation chambers are going to be part of the pan-European distributed infrastructure ACTRIS. The collaboration of chambers was funded in several projects, of which the last was the EUROCHAMP-2020 project (Doussin et al., 2023; Eurochamp, 2023). Each chamber is different in its size, wall material, radiation source, as well as in the available instrumentation, and is often designed for specific research questions, such as cloud formation or gas-phase chemistry (Doussin et al., 2023; Eurochamp, 2023). Depending on the material and the surface-to-volume ratio of the chamber, interactions of the air with the chamber wall can affect the results and need to be taken into account in the interpretation of experiments. One example is the release of chemical compounds from the chamber wall, as observed in the presence of light and water vapour (Rohrer et al., 2005; Zádor et al., 2006; Doussin et al., 2023). The characterisation of these chamber-specific properties is essential for studying atmospheric processes in the simulation chamber. Typically, chamber-specific processes are quantified in reference experiments, using atmospherically-relevant compounds, which chemistry is well investigated such as -pinene (Doussin et al., 2023).

The species -pinene belongs to the group of monoterpenes (sum formula $C_{10}H_{16}$), which constitutes the second highest fraction of non-methane organic compounds emitted by plants (Guenther et al., 2012). Due to its high emission rates, -pinene is the most abundant monoterpene in the atmosphere (Guenther et al., 2012).

The tropospheric oxidation of -pinene can be initiated by multiple chemical species like the hydroxyl radical (OH), ozone (O), and the nitrate radical (NO), where the latter is most important at night (Section 1.2) (Finlayson-Pitts and Pitts, 2000; Seinfield and Pandis, 2006). In the ozonolysis reaction of -pinene, a significant amount of OH radicals is produced, as the OH yield is of (Atkinson et al., 2006). Therefore, even in the dark, oxidation by the OH radical can become significant, so that often OH scavengers, such as cyclohexane, are used in chamber experiments for studying the oxidation of -pinene by O in the absence of OH. In the chemical degradation of -pinene, peroxy (RO) and hydroperoxy (HO) radicals are formed. The fate of RO radicals highly depends on the availability of nitric oxide (NO). In the absence of NO, RO radicals can undergo either bimolecular reactions with *e.g.*, HO or other RO radicals, or unimolecular reactions (Section 1.2) (Finlayson-Pitts and Pitts, 2000; Seinfield and Pandis, 2006). Beside formaldehyde (HCHO), acetone, and acetic acid, pinonaldehyde is a prominent gas-phase product, formed in the oxidation of -pinene by both, OH and O (Larsen et al., 2001). Low-volatility compounds can often condense on particles or even lead to the formation of new particles (Hakola et al., 1994; Kanakidou et al., 2000; Larsen et al., 2001; Ng et al., 2006; Mutzel et al., 2021).

The photooxidation of -pinene has been investigated in many gas phase and aerosol studies, most of them conducted in simulation chambers. The first oxidation step of the photooxidation of -pinene was, for example, investigated by Rolletter et al. (2019), who performed OH oxidation experiments in the outdoor simulation chamber SAPHIR at Forschungszentrum Jülich, Germany, under atmospheric conditions. Measured time series of radicals (OH, HO , RO) and organic products (HCHO, acetone, pinonaldehyde) were compared to results of zero-dimensional box model calculations based on the Master Chemical Mechanism (MCM v3.3.1, http://mcm.leeds.ac.uk) (Jenkin et al., 1997; Saunders et al., 2003) and an updated RO chemistry calculated in Vereecken et al. (2007). A model-measurement comparison involving the GECKO-A mechansim (Aumont et al., 2005; Camredon et al., 2007) was performed by McVay et al. (2016), who studied the SOA formation in photooxidation experiments in the environmental chambers at Caltech, US, at different levels of seed aerosol and OH radicals. Model-measurement discrepancies were found, which were assumed to either be due to a rapid vapour loss to the chamber walls or due to the autoxidation of products in the photooxidation and ozonolysis pathways. Mechanistic studies of the photooxidation of -pinene at low and high levels of NO were also performed in the chambers at Caltech, US, by Eddingsaas et al. (2012a,b), focusing on the gas-phase chemistry (Eddingsaas et al., 2012b) and the formation of SOA (Eddingsaas et al., 2012a). The effect of NO_x (NO NO_2) (Ng et al., 2007; Zhao et al., 2018) and of SO (Zhao et al., 2018) on the formation of secondary organic aerosol (SOA) was investigated as well, while the formation of highly oxygenated molecules (HOMs) from the oxidation of -pinene by OH was investigated by Lee et al. (2023). A first multi-chamber approach (MUCHACHAS) was performed by Donahue et al. (2012), where similar experiments investigating the ageing of SOA from the photooxidation of -pinene were carried out in four different chambers, three of which are also part of EUROCHAMP. Furthermore, the measured organic mass in particles formed during the experiments was compared to calculations based on the 2D volatility basis set (2D-VBS) framework and chamber loss mechanisms. Beside experimental studies, theoretical studies have been performed, focusing on the OH-initiated peroxy radical chemistry *e.g.*, by Piletic and Kleindienst (2022) and by Vereecken et al. (2007). The ozonolysis of -pinene (Hakola et al., 1994; Shilling et al., 2008; Saathoff et al., 2009; Tillmann et al., 2010; Ehn et al., 2014, 2017; Berndt, 2022; Skyttä et al., 2022) and the oxidation of -pinene by NO (Mutzel et al., 2021) has also been investigated. The influence of temperature and relative humidity on the production of pinonaldehyde and the SOA yield was studied by Saathoff et al. (2009) and Tillmann et al. (2010). Ehn et al. (2014) investigated the formation of HOMs and eventually of SOA from the ozonolysis of -pinene, studied in the Jülich Plant Atmosphere Chamber at Forschungszentrum Jülich, Germany.

Within the EUROCHAMP-2020 project, the photooxidation of -pinene was investigated in nine different atmospheric simulation chambers. The aim of this study is to test the consistency between results obtained in the different chambers. This was assessed by comparing gas-phase product yields. In total, 32 chamber experiments were evaluated. Concentrations of trace gases, involved in the yield analysis, were corrected for secondary chemistry and for chamber-specific wall losses and sources. In this chapter, chamber-specific properties, regarding chamber-related emissions and loss processes, are discussed and gas-phase product yields are compared.

2.2 Methods

2.2.1 Properties of the simulation chambers

Nine simulation chambers participated in the multi-chamber study, providing data from -pinene oxidation experiments (Fig. 2.1). Three chambers are outdoor chambers, confined by a Fluorinated Ethylene Propylene (FEP) film, which is chemically inert and has a high transmission of more than % for the solar spectrum (Bohn et al., 2005). The large volume (m) of the outdoor chambers results in a low surface-to-volume of maximum 1.2. Since outdoor chambers are exposed to all kind of weather conditions, the FEP films can be protected by a mobile housing in case of the HELIOS chamber, or by a shutter system as installed at the EUPHORE and SAPHIR chambers. This also allows measurements in the dark to simulate nighttime conditions. Replenishment flows of air causing a dilution of trace gases with rates on the order of s to s were active during the experiments, compensating the air consumption from instrumentation and possible small leakages.

In comparison to the outdoor simulation chambers, the indoor chambers are smaller, with volumes ranging between m and m , resulting in surface-to-volume ratios between 4.3 and 1.2. Most indoor chambers, participating in the multi-chamber study, are made of FEP films, except of the CESAM and AIDA chambers, whose walls consist of stainless steel and aluminium (AlMg), respectively. Dilution does not play a role in the MAC, LEAK, and ILMARI chambers, as the chambers are operated, such that the FEP bag collapses with time. In the FORTH chamber, dilution also does not contribute to the loss of trace gases and particles, however, the reason is unclear. Since sunlight cannot be used in indoor chambers, artificial light sources like blacklight lamps or xenon arc lamps are used.

In the outdoor chambers, OH radicals are mostly produced from the photolysis of HONO (Reaction (R1.25)), emitted from the Teflon chamber walls. In the PACS-C3 chamber, HONO was also injected. Interactions of the chamber wall with NO can also lead to the formation of HONO and thus of OH in the presence of light. This is the case in the CESAM, PACS-C3, and ILMARI chambers. Hydrogen peroxide (H_2O_2), forming two OH radicals in its photolysis, was injected in the HELIOS and ILMARI chambers. In the CESAM, FORTH, and MAC chambers, NO is added to the chamber air, leading to the production of OH from ozone photolysis, as a photochemical equilibrium between NO , O and NO concentration is established (Reactions (R1.10) and (R1.11)).

Emissions of trace gases, such as nitrous acid (HONO) and HCHO, are commonly observed in chambers made of Teflon. The emission strengths of trace gases from the wall are typically determined in reference experiments (Doussin et al., 2023). Particles are typically lost on the chamber wall with rates that depend on the wall material and the particle's properties. Further information about the individual chambers and chamber-related loss and production processes are summarised in Tabs. A.1 and A.2.

Figure 2.1: Simulation chambers, which are part of EUROCHAMP and which participated in the presented multi-chamber study, and their location. The pictures and the map (map tiles by CartoDB under the Creative Commons Attribution 3.0 License (https://creativecommons.org/licenses/by/3.0), map data from © OpenStreetMap contributors under ODbL) are taken from the EUROCHAMP webpage (Eurochamp, 2023).

2.2.2 Instrumentation

The volatile organic compounds -pinene, pinonaldehyde, formaldehyde, and acetone were detected by proton transfer mass spectrometers (PTR-ToF-MS) or by Fourier-transform infrared gas analysers (FT-IR) in most experiments. In the case of the experiments performed in the MAC and the SAPHIR chambers, -pinene was also measured by gas chromatography combined with a flame ionisation detector (GC-FID) and formaldehyde was detected by a Hantzsch monitor. In the SAPHIR chamber, HCHO was also measured by differential optical absorption spectrometer (DOAS) instrument.

OH radicals were measured with the laser-induced fluorescence (LIF) method and DOAS in the experiments performed in the SAPHIR chamber. Ozone concentrations were mostly detected via UV absorption. Only in the EUPHORE chamber, ozone was also measured with a FTIR gas analyser.

The OH precursor HONO was measured in the outdoor simulation chambers (HELIOS, EUPHORE, SAPHIR) via a Long Path Absorption Photometer (LOPAP) instruments and additionally with a FTIR gas analyser in the EUPHORE chamber. Time series of H_2O_2 were measured with a FTIR gas analyser in the experiments performed in the HELIOS chamber. In all chambers except of the HELIOS and the SAPHIR chambers, particles were detected. Particle size distributions were measured with scanning mobility particle sizers (SMPS) in most experiments, and with a differential mobility particle sizer (DMPS) in the MAC chamber. For most experiments, only total number concentrations were provided, together with total mass concentrations, derived from the integration of the number size distributions. The particle density was partly different in the calculations. For example, a particle density of µg m was assumed in experiments performed in the MAC and ILMARI chambers, while in the experiments conducted in the FORTH chamber, particle densities of µg m (experiment F1s) and µg m (experiment F2s) could be determined from comparing the AMS and the SMPS measurements. In the EUPHORE, CESAM, LEAK, and PACS-C3 chambers, total mass concentrations were directly provided. Mean particle diameters were provided for the experiments in the EUPHORE and the PACS-C3 chambers and otherwise derived from the total particle number concentrations. In addition, total number concentrations were measured with a condensation particle counter (CPC) in the PACS-C3 chamber (experiment P4, Tab. A.3). The chemical composition of aerosol was measured in the FORTH and in the ILMARI (experiments I2 and I3, Tab. A.3) chambers, where for the latter only organic mass concentrations were provided.

Photolysis frequencies in the outdoor simulation chambers are derived from actinic flux measurements inside (HELIOS, EUPHORE) or outside (SAPHIR) of the chamber. Photolysis frequencies which are needed for the yield analysis, such as of NO ($_{\mathrm{NO_2}}$), formaldehyde ($_{\mathrm{HCHO}}$), ozone ($_{\mathrm{O^1D}}$), and pinonaldehyde ($_{\mathrm{PINAL}}$), were provided for experiments conducted in the HELIOS and SAPHIR chambers. For experiments performed in the EUPHORE chamber, only photolysis frequencies of NO were available. Other photolysis frequencies were determined according to the clear-sky parametrisation, introduced by Saunders et al. (2003), which takes the solar zenith angle into account. To account for cloud conditions, the calculated photolysis frequencies were scaled by the ratio of the measured and calculated (clear sky) NO photolysis frequencies. In addition, the photolysis frequency of pinonaldehyde was scaled by a factor of 3.5 according to a recent finding by Rolletter et al. (2020) for the evaluation of all experiments. In contrast, photolysis frequencies in the indoor simulation chambers were derived from the individual lamp spectra.

2.2.3 Experimental conditions and procedures

Different chemical conditions were present in the experiments (Tab. A.3). Initial mixing ratios of -pinene were either below ppbv or above ppbv with a maximum mixing ratio of ppbv. Similarly, $\mathrm{NO_x}$ mixing ratios reached values of less than 15 ppbv or around 200 ppbv. Experiments were either performed at dry conditions with relative humidities below % or at humid conditions with relative humidities between % and %.

In most experiments, -pinene was oxidised by OH and O . In the oxidation experiments with

OH, OH radical concentrations were between cm and cm , dominating the oxidation of -pinene in most experiments. Ozone, which was either injected or produced by chemical reactions, reached mixing ratios between 10 and ppbv at the end of the experiments and contributed up to 70 % to the oxidation of -pinene.

Even though the nitrate radical does typically not play a role in the daytime oxidation chemistry due to its fast photolysis and its fast reaction with NO, production rates can be high in the presence of high concentrations of ozone and NO . This was the case in the experiments performed in the FORTH chamber and consequently, NO is expected to have contributed to the oxidation of -pinene in these experiments (Tab. A.3).

Particles were either formed in the experiments from the nucleation of gas-phase oxidation products or seed aerosol was present, on which organic compounds can condense (Doussin et al., 2023). Ammonium sulfate ($(NH_4)_2SO_4$) was used as seed aerosol and initial mass concentrations were around 30 µg m to µg m .

The experiments typically started with the injection of -pinene in the dark chamber, with the exception of the experiments in the SAPHIR chamber, where -pinene was injected in the sunlit chamber. NO was added either in the dark or during the photooxidation part of the experiment. If ammonium sulfate was added as seed aerosol or d -butanol as OH tracer, they were added in the dark chamber as well. In addition, OH precursors, such as HONO (PACS-C3), H_2O_2 (HELIOS, ILMARI), NO_2 (FORTH, MAC, CESAM), or O_3 (SAPHIR) were injected before the chambers were illuminated. In the experiments performed in the ILMARI chamber, H_2O_2 was injected after the lamps had been switched on.

As soon as the air in the chamber was exposed to light, the photooxidation of -pinene started, which was then studied for a couple of hours. In some experiments, -pinene was injected several times.

Also the release of HONO or HCHO from the chamber wall, was triggered by the illumination of the chamber. In the experiments in the SAPHIR chamber and in one of the experiments in the HELIOS chamber, the chamber was illuminated in the absence of -pinene to determine wall emission rates of HONO, formaldehyde, and acetone.

2.2.4 Analysis of the experiments

Chamber-specific processes

In the chamber studies, chamber sources and wall losses need to be accounted for in the calculation of product yields. In this work, wall emission rates as well as wall loss rates were either determined from periods of the experiments, when the chemical production was negligible, or they were calculated from the auxiliary mechanisms provided by the chamber providers (Tab. 2.1, Eurochamp (2023)). The wall loss of X, which can be either a gas-phase

Table 2.1: Auxiliary mechanisms provided by the chamber providers (Eurochamp, 2023). The wall emission rates refer to the photolytic production of trace gases, if not otherwise noted.

Chamber	Wall emission rate				Wall loss rate [s]		
	HONO [cm s]	HCHO	NO_2 [s]	HONO^a	HCHO	-pinene	Aerosol
HELIOS							
EUPHORE	^{b}	^{b}					^{c}
SAPHIR	^{b}	^{b}					
CESAM			14^d, 140				^{c}
FORTH-ASC							
MAC							^{c}
LEAK							^{c}
PACS-C3	91	50		^{d}, 0.84			
ILMARI			^{d},				^{c}

[a] Heterogeneous reactions of NO_2 forming HONO. In the case of the CESAM chamber, NO_2 referes to molecules deposited on the chamber wall. Beside HONO, NO (CESAM) or HNO_3 (FORTH, PACS-C3) is formed. If the yield of HONO was not 1, the rate was corrected accordingly; [b] See text for details; [c] For a particle diameter of 200 nm; [d] Dark reaction.

species or particles, can be described by a first-order loss process:

$$\frac{\mathrm{d\,X}}{\mathrm{d}} \qquad \mathrm{X} \tag{2.1}$$

where is the first-order loss rate of the species X on the wall and [X] is its concentration. The parametrisations of the chamber-related production of HONO and small oxygenated compounds, such as formaldehyde, are available from the published auxiliary mechanisms for the SAPHIR and EUPHORE chambers (Eurochamp, 2023). In the SAPHIR chamber, the emission strength of HONO ($_{\mathrm{HONO}}$) and of small oxygenated compounds ($_{\mathrm{OVOC}}$) were characterised by Rohrer et al. (2005) and can be described by the following formulas:

$$_{\mathrm{HONO}} \qquad \frac{}{} \quad \exp \quad \frac{\mathrm{K}}{} \qquad _{\mathrm{NO_2}} \tag{2.2}$$

$$_{\mathrm{OVOC}} \qquad \exp \quad \frac{\mathrm{K}}{} \qquad _{\mathrm{NO_2}} \tag{2.3}$$

where is the relative humidity and is a scaling factor which needs to be determined for each experiment, as the emission strength depends on the history of previous experiments. A parametrisation for the emission strengths of HONO and HCHO from the chamber wall is also provided for the EUPHORE chamber (Zádor et al., 2006):

$$ {}_{\mathrm{HONO}} \qquad {}_{\mathrm{NO_2}} \ \exp \quad \frac{\mathrm{K}}{} \qquad {}_{\mathrm{NO_2}} \tag{2.4} $$

$$ {}_{\mathrm{HCHO}} \qquad {}_{\mathrm{NO_2}} \ \exp \quad \frac{\mathrm{K}}{} \tag{2.5} $$

Product yields

In this work, product yields of pinonaldehyde, formaldehyde, and acetone were determined, if corresponding trace gas concentrations were measured. The product concentration [X] increases linearly with the amount of oxidised -pinene:

$$ \mathrm{X} \qquad {}_{\mathrm{X}} \tag{2.6} $$

The product yield ${}_{\mathrm{X}}$ is the slope of the linear function. However, product as well as -pinene concentrations need to be corrected for secondary chemistry (Section A.1.3). The formation of gas-phase products was determined for the oxidation of -pinene by OH. Therefore, other contributions to the loss of -pinene, such as its oxidation by ozone, its loss to the chamber wall, or its loss by dilution, need to be taken into account (Kaminski et al., 2017). Furthermore, in few experiments $\mathrm{NO_3}$ contributed to the loss of -pinene. Overall, the change in the -pinene concentration in the chamber experiments can be described as (Galloway et al., 2011; Kaminski et al., 2017):

$$ \frac{\mathrm{d}}{\mathrm{d}} \qquad {}_{\mathrm{O_3}} \ \mathrm{O_3} \qquad {}_{\mathrm{NO_3}} \ \mathrm{NO_3} \qquad {}_{\mathrm{OH}} \ \mathrm{OH} \tag{2.7} $$

denotes the first-order rate constant for dilution. The rate coefficients for the reaction of -pinene with OH, O , and NO are ${}_{\mathrm{OH}}$, ${}_{\mathrm{O_3}}$, and ${}_{\mathrm{NO_3}}$, respectively.

The oxidation products pinonaldehyde, acetone, and formaldehyde were also corrected for loss or production path other than their formation from the OH oxidation of -pinene (Section A.1.3). Concentrations of pinonaldehyde were not corrected for contributions from the ozonolysis of -pinene, therefore obtained yields are an upper limit for pinonaldehyde yields from the OH oxidation of -pinene.

For the determination of product yields, OH radical concentrations are needed. Only in the SAPHIR chamber, concentrations of the OH radical were measured. In experiments in some other chambers such as the FORTH, PACS-C3, and ILMARI chambers, d -butanol was injected for tracing the OH radical concentration from its observed loss. Alternatively, the decay of -pinene (Eq. (2.7)) can be used to determine the OH radical concentration. In both cases, the OH radical concentration is determined from (Galloway et al., 2011; Barmet et al., 2012):

$$ \mathrm{OH} \qquad \frac{}{{}_{\mathrm{OH} \ \mathrm{tracer}}} \quad \frac{\mathrm{tracer} \qquad \mathrm{tracer}}{\mathrm{tracer}} \tag{2.8} $$

where $_{\mathrm{OH}\quad\mathrm{tracer}}$ is the rate coefficient for the reaction of OH with the tracer. For the reaction rate of OH with -pinene, the value from Atkinson et al. (2006) is used while the reaction rate of OH with d -butanol is taken from Barmet et al. (2012). The tracer concentration needs to be corrected for other loss processes than the reaction with OH before calculating the OH radical concentration using a similar procedure as for correcting product concentrations in the yield calculations (Section A.1.3). For consistency, the OH radical concentration, determined from the decay of -pinene concentrations (Eq. (2.7)) were used in the yield analysis.

2.3 Results and discussion

2.3.1 Observations in the experiments

Measured time series of trace gases, calculated OH radical concentrations (Eq. (2.8)), and information about formed particles are shown in Figs. 2.2-2.10 and A.1-A.23 for each experiment (Tab. A.3). In all photooxidation experiments, -pinene is mainly consumed by OH, with contributions of ozone being typically less than %. In the presence of NO_x, the peroxy radicals preferably react with NO, forming NO_2 which photolyses producing ozone (Reactions (R1.10)-(R1.11)). NO , NO, and ozone are in a photostationary state shortly after the photooxidation has started. In the EUPHORE (Figs. 2.4, A.2-A.6) and CESAM (Figs. 2.7, A.9-A.10) chambers, at low -pinene and/or NO concentrations, the wall loss of ozone competes with its production from the photooxidation of -pinene.
At high NO_x, higher OH radical concentration are generally observed due to the efficient regeneration of OH from the reactions of NO with RO and HO (Fig. 1.5). At low OH radical concentrations, connected to low NO_x concentrations, the loss of -pinene by OH oxidation is small compared to the loss by dilution and wall loss in some experiments in specific chambers (HELIOS: Fig. A.1, EUPHORE: Figs. 2.4, A.2-A.4, CESAM: Figs. 2.7, A.9).
As soon as the -pinene concentration in the experiments is consumed, also the pinonaldehyde concentrations and particles decline due to their loss processes, such as the reaction with OH or the loss to the chamber wall. Since formaldehyde and acetone are also formed in secondary processes, they tend to still increase after -pinene has been entirely consumed.
An increase in the organic aerosol mass is observed in most experiments. In the photooxidation of -pinene, low and semivolatile compounds are formed, which can nucleate, leading to an increase in the total aerosol number and mass concentration. Typically one to two hours after the photooxidation started, the total particle number concentration reaches its maximum, while the total aerosol mass concentration and the mean particle diameter keep increasing due to coagulation of particles and the continuous condensation of gas-phase products on the particles (Mentel et al., 2009). This is also observed in the presence of seed aerosol. A small or delayed particle formation is observed in the experiments in the EUPHORE (Figs. A.2, A.3) and the MAC (Figs. 2.9, A.12-A.15) chambers performed at initial NO mixing ratios larger than ppbv. At low NO concentrations, RO recombination reactions are important, leading to the formation of low volatile organic compounds. At high NO, often more volatile organic compounds are formed (Presto et al., 2005; Ng et al., 2007; Pathak et al., 2007; Eddingsaas et al., 2012a; Zhao et al., 2018).

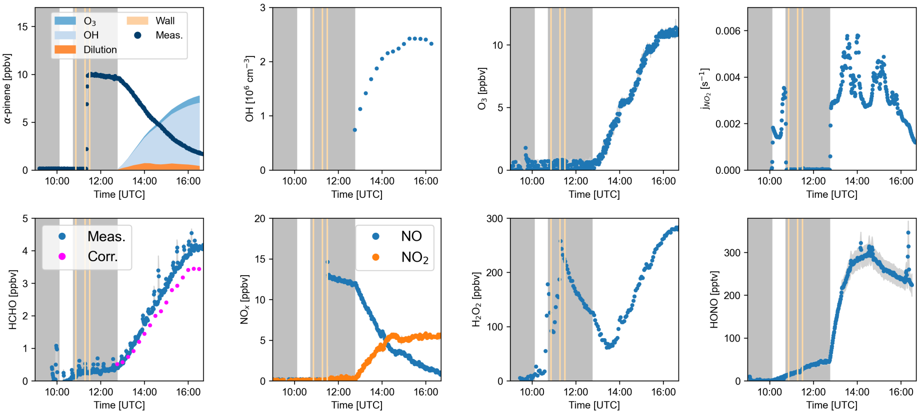

Figure 2.2: Time series of trace gas concentrations measured in the experiment H2 (Tab. A.3) performed in the HELIOS chamber. Different contributions to the loss paths of -pinene are shown by coloured areas together with the time series of the -pinene concentrations. OH radical concentrations are derived from the time series of the -pinene concentrations corrected according to Eq. (2.8). Injections of -pinene into the chamber are marked by yellow, vertical lines and dark conditions are indicated by grey areas. Temperatures between C to C were observed during the first illumination period while the temperature further increased in the second illumination period, reaching values of up to C.

2.3.2 Chamber-specific features and observations in the experiments

Experiments in the HELIOS chamber

The photooxidation of -pinene was studied at low NO_x ($NO_x <$ ppbv in the experiment H1, Fig. A.1) and at high NO_x (NO_x ppbv in the experiment H2, Fig. 2.2, Tab. A.3) in the HELIOS chamber (HELIOS, 2023). Before the injections of trace gases in the dark, the clean chamber air was illuminated for min in the experiment H2 (Fig. 2.2), allowing to characterise the emissions of trace gases from the chamber wall. Dark periods, before and after the first illumination phase, are used to determine the wall loss rates.

Emission from the chamber wall is observed for formaldehyde and nitrous acid. A chamber source of formaldehyde with a rate of ppbv h was determined in the experiment H1 (Fig. A.1) from the concentration increase in the dark, while in the experiment H2 (Fig. 2.2), the calculated emission strength was one order of magnitude lower. In the clean, illuminated chamber at the beginning of the experiment H2 (Fig. 2.2), the chamber source of HCHO was ppbv h , which agrees within the -uncertainty with the HCHO chamber source of ppbv h published in the auxiliary mechanism (Tab. 2.1, Eurochamp (2023)). The reason for the differences is not clear, but is likely related to the state of the chamber film.

A HONO production is observed in the dark and in the sunlit chamber. In the dark chamber in the experiment H1 and also in the dark phase preceding the first illumination period in the experiment H2, the HONO concentrations increase, which might be correlated to previous injections of trace gases, such as H O , as this is not observed before trace gases are injected in the experiment H2. A HONO chamber source that depends on the intensity of the radiation can be determined from the increase of the concentration in the clean, illuminated chamber in the experiment H2 (Fig. 2.2). The calculated rate is pptv h , which is much smaller than the value of pptv h published in the auxiliary mechanism (Tab. 2.1, Eurochamp (2023)). Again, this points to a strong dependence of the chamber sources on the history of experiments.

Overall, much higher HONO mixing ratios are reached in the experiment H2 (x_{HONO} pptv, Fig. 2.2) than in the experiment H1 (x_{HONO} pptv, Fig. A.1), conducted at low concentrations of NO_x (NO_x ppbv). The high HONO mixing ratios observed may be related to the presence of NO in the experiment H2, which reacts with OH forming HONO. A good agreement between the measured HONO mixing ratio of pptv and the value of pptv is obtained, if values are calculated from the photostationary state between HONO, NO and OH (NO = ppbv, [OH] = cm). Additional HONO production from the interaction of NO with the chamber wall, as observed in the CESAM, PACS-C3, and ILMARI chambers (Tab. 2.1, Eurochamp (2023)), may also contribute to the high HONO production observed in the experiment H2 in the presence of NO_x.

Losses of formaldeyhde and -pinene on the chamber wall are reported by the chamber providers (Tab. 2.1), however a chamber-related loss of formaldehyde is not observed in this study. In contrast, a decrease of -pinene is observed in the dark periods, when no oxidants are present. Concentrations of -pinene, measured in the experiment H1 in the dark, can only be explained by an additional wall loss with a rate of s , which is more than a factor of 30 larger than reported in the auxiliary mechanism (Tab. 2.1, Eurochamp (2023)). However, in the experiment H2, the decrease in the -pinene concentrations can be explained by only loss due to dilution, indicating that the wall loss may be linked to the state of the chamber film that may depend on the history of previous experiments.

In the experiment H1 (Fig. A.1) at low NO_x conditions, the OH radical concentrations do not exceed cm , despite the injection of ppbv of H_2O_2, which is rapidly lost to the chamber wall with a loss rate of s , being equivalent to a lifetime of only two hours. As a consequence, the loss of -pinene due to OH oxidation was negligible and the measured formaldehyde was mainly produced from the chamber wall. Therefore, no product yield can be determined from this experiment. First model calculations (not shown in this work) confirm that the OH radical production from H_2O_2 and HONO photolysis is of minor importance, and OH radicals are mainly produced from the reaction of HO_2 with NO. Results of the experiment H1 highlight that it is not feasible to carry out phootoxidation experiments without injecting NO_x in the HELIOS chamber, as there are not enough OH radicals formed from the photolysis of injected H_2O_2 and of chamber wall emitted HONO. The addition of more H_2O_2 than in the experiment H1 may help increasing the OH radical concentrations in the absence of NO_x. However, the production of OH radicals will rapidly decline due to the significant loss of $H_2O_2$to the chamber wall.

Experiments in the SAPHIR chamber

Photooxidation experiments of -pinene (S1 and S2, Figs. 2.3, A.7, Tab. A.3), focusing on gas-phase product yields, were conducted in the SAPHIR chamber (SAPHIR, 2023) and have been already analysed by Rolletter et al. (2019), and are only briefly discussed here. Before

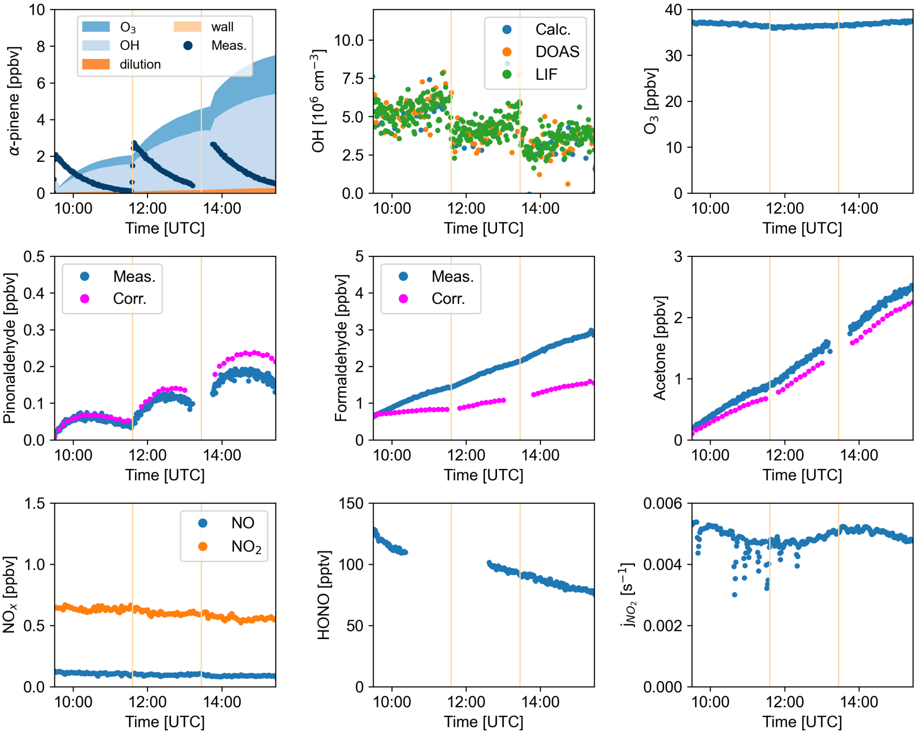

Figure 2.3: Time series of trace gas concentrations measured in the experiment S2 performed in the SAPHIR chamber (Tab. A.3). Different contributions of the loss paths of -pinene are shown by coloured areas, together with the time series of the -pinene concentration. The OH radical concentrations were measured via the DOAS technique (Section 2.2.2), and calculated from the corrected time series of -pinene concentrations according to Eq. (2.8). Injections of -pinene into the chamber are marked by yellow, vertical lines. The relative humidity decreased from % to % throughout the experiment and the temperature increased from C to C during the experiment.

-pinene was added into the chamber, trace gases were measured for two hours in the sunlit, humidified chamber and in the presence of ozone. In this phase, the production of HONO and small oxygenated compounds from the chamber wall are characterised, which can be described by Eqs. (2.2) and (2.3). By scaling the emission strength by factors between 0.08 and 1.2, the observed chamber production of HONO, HCHO, and acetone could be described correctly for the experiments discussed in this section.

The losses of -pinene and pinonaldehyde were investigated in a separate experiment, in which only either one of the two species was injected into the clean air. The concentrations were monitored for several hours. The observed decrease of the -pinene and pinonaldehyde concentrations could be fully explained by dilution, indicating that the loss to the chamber wall is negligible.

Experiments in the EUPHORE chamber

In the EUPHORE chamber (EUPHORE, 2023), six photooxidation experiments with -pinene (two type E1, three type E2 experiments, one type E3, Tab. A.3, Figs. A.5, A.2-A.6) were provided. Zádor et al. (2006) parameterised the wall emissions of HONO and HCHO, which depend on the NO_2 photolysis frequency and the temperature (Eqs. (2.4) and (2.5)). Overall, an emission rate of HONO of pptv h and of HCHO of ppbv h is obtained for the experiments in this study.

The chamber sources are determined from phases, when the oxidation of -pinene is negligible, as it contributes to the formation of HCHO, and dilution dominates the loss of -pinene, such as in the beginning of the experiments E1 (Figs. A.2, A.3) and E2 (Figs. A.5, 2.4, A.4). A HONO production rate on the order of a few hundreds of pptv per hour could be roughly estimated from the experiment E2, before NO was injected, which agrees well with the expectation from the auxiliary mechanism (Eq. 2.4). In contrast, a chamber source of formaldehyde of ppbv h is determined from the experiments E1, which is about a factor of 4 larger than the observed wall emission in the -pinene experiments. In these periods, also an increase of the pinonaldehyde concentration with a rate of ppbv h and of acetone with a rate of ppbv h was observed. A large difference of a factor of two is found between the HCHO chamber source determined in the -pinene experiment and in a reference experiment (not shown in this work), performed before experiments E2 without the addition of -pinene. This could be due to memory effects of the Teflon film and highlights the importance of determining chamber sources for individual experiments.

In the auxiliary mechanism (Tab. 2.1, Eurochamp (2023)), no wall loss of trace gases is reported. However, from the dark phase, following the photooxidation of -pinene in the experiment E2 (Figs. A.5, A.4), a loss of pinonaldehyde and of HCHO on the chamber wall can be determined with rates of s and s , respectively. For acetone, there was no significant wall loss, as its concentration did not decrease in the dark (experiment E3, Fig. A.6).

Particles with diameters between nm and nm observed in the experiments in the

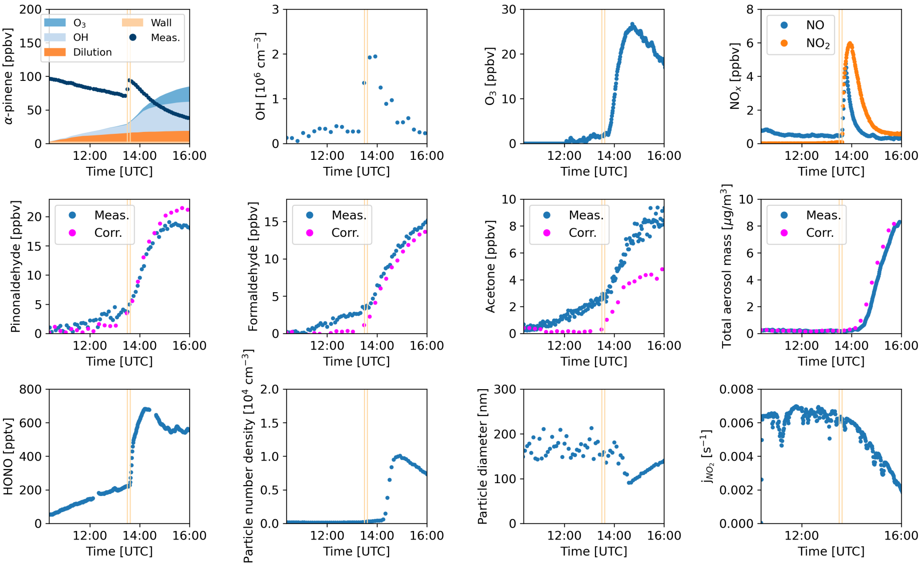

Figure 2.4: Time series of trace gas concentrations measured in the experiment E2 performed on the 14 of January 2019 in the EUPHORE chamber (Tab. A.3). Different contributions of the loss paths of -pinene are shown by coloured areas together with the time series of the -pinene concentration. OH radical concentrations are derived from the corrected time series of -pinene concentrations according to Eq. (2.8). Injections of -pinene into the chamber are marked by yellow, vertical lines. "ND" and "Dia" refer to the particle number density and the mean particle diameter. A relative humidity below % was present during the experiment. The temperature increased from C to C after the roof opening and decreased afterwards to C.

EUPHORE chamber, are expected to be lost on the chamber wall with a rate between s and s , based on the auxiliary mechanism (Eurochamp, 2023). From the experiments in this work, the overall wall loss rate ranges between s and s .

The experiments E1 (Figs. A.2, A.3) and E2 (Figs. A.5, A.4), can be divided into two phases: Phase 1 with low -pinene concentrations (ppbv) in the presence of high NO_x (ppbv, experiment E1) or high -pinene concentrations (ppbv) in the presence of low NO_x (ppbv, experiment E2), and phase 2 with high -pinene concentrations (ppbv) in the presence of high (NO ppbv, experiment E1) or medium NO_x (ppbv, experiment E2). In the first phases, -pinene is mainly lost due to dilution and there is no formation of product species and particle observed, independent of the amount of HONO. This suggests that the OH radicals, which are produced in these phases from the HONO photolysis react with other reactants instead of -pinene. First zero-dimensional box model calculations of the experiment E1 confirm that a faster decay of -pinene would be expected from the measured decrease of NO_x.

For experiments E1 and E2, the first phases are not used for determining product yields as dilution dominated the loss of -pinene. This phase, is still useful for estimating the chamber sources. This, however, can be much easier achieved in a separate phase of the experiment where trace gas concentrations are observed in the clean, illuminated chamber.

Experiments in the PACS-C3 chamber

Gas-phase products as well as the particle size distribution were measured in the experiments performed in the PACS-C3 chamber (PACS-C3, 2023) (P1-P4, Figs. 2.5, A.19-A.21, Tab. A.3). Photolytic chamber sources of HONO and HCHO are reported in the published auxiliary mechanism (Tab. 2.1, Eurochamp (2023)) with emission rates of cm s and cm s , respectively. OH radicals are assumed to be produced by the photolysis of HONO emitted by the chamber wall. OH radical concentrations of cm are observed, indicating a large OH production rate. Due to the lack of HONO and NO_x measurements, the HONO chamber source cannot be estimated. Although there were high ozone mixing ratios of up to ppbv in the presence of water vapour, ozone photolysis alone does not explain the large OH radical concentration. The HCHO chamber source cannot be verified in the provided experiments, as no formaldehyde data are available for a phase of the experiment with light but without -pinene. However, a chamber-related production of formaldehyde with a rate of ppbv h is observed in the dark.

No wall loss rates for trace gases or particles are given in the auxiliary mechanism (Tab. 2.1, Eurochamp (2023)). A HCHO loss rate could be determined from the dark phase following the photooxidation in the experiment P3 (Fig. 2.5), giving a rate of s . Although there is no significant loss of pinonaldehyde in the dark in this experiment, in three other experiments (Figs. A.19-A.21), a loss of pinonaldehyde is observed in the illuminated chamber, which is significantly higher than the loss expected from the OH reaction and photolysis. An additional loss rate between s and s is required to explain the observations, but it is not clear, why this is only the case for the conditions of these experiments. For -pinene, no wall loss can be determined, as it is entirely consumed during the oxidation phase of the experiment P3 (Fig. 2.5).

Particle losses, possibly to the chamber wall, can be determined from the decrease of their mass concentration when the lamps were switched off. During this phase, the average particle diameter is constant, indicating that no further particle formation or coagulation took place. From Eq. (2.1), a loss rate of s is derived.

Experiments in the ILMARI chamber

Three photooxidation experiments (I1s, I2, and I3, Figs. 2.6, A.22, A.23, Tab. A.3) were performed in the ILMARI chamber (ILMARI, 2023). Gas-phase products as well as particle

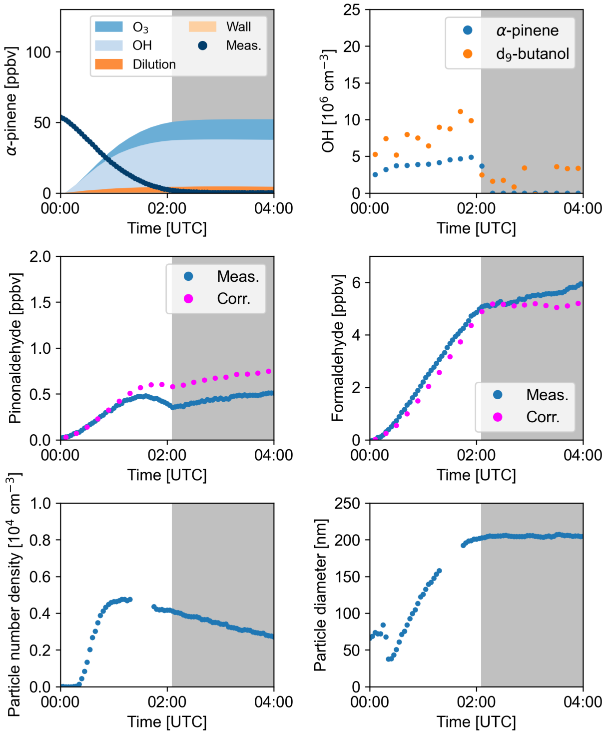

Figure 2.5: Time series of trace gas concentrations measured in the experiment P3 performed in one of the PACS-C3 chambers (Tab. A.3). Different contributions of the loss paths of -pinene are shown by coloured areas together with the time series of the -pinene concentration. OH radical concentrations are derived from the decrease of injected d -butanol and from the corrected time series of -pinene concentrations according to Eq. (2.8). Injections of -pinene into the chamber are marked by yellow, vertical lines and dark conditions are indicated by grey areas. HONO was injected before the start of the photooxidation. “ND” and “Dia” refer to the particle number density and the mean particle diameter. The total aerosol mass concentration was interpolated for its correction for wall loss. A relative humidity of % and a temperature of C were present during the experiment.

properties were measured. In the auxiliary mechanism, wall emission rates of HONO between cm s and cm s are reported (Tab. 2.1, Eurochamp (2023)). Due to the lack of data in the clean, illuminated chamber, no wall emission rates can be derived from experiments in the ILMARI chamber in this study. In all experiments, the OH radical concentration is minimum cm , indicating a strong OH radical production from the photolysis of H_2O_2, which was injected in the experiments, but which concentration was not measured.

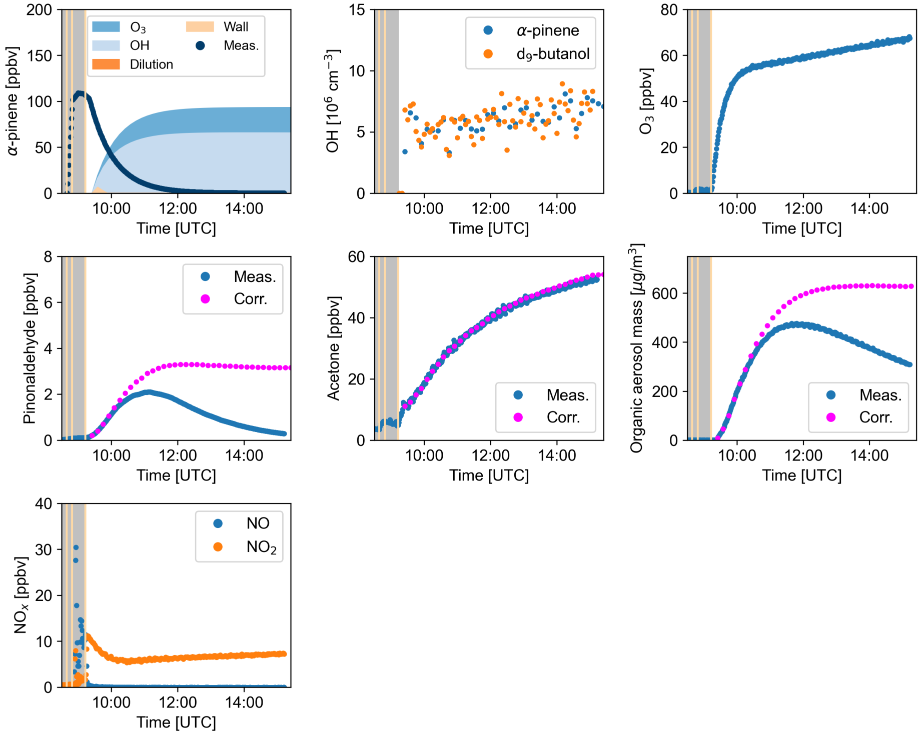

Figure 2.6: Time series of trace gas concentrations measured in the experiment I2 performed in the ILMARI chamber (Tab. A.3). Different contributions of the loss paths of -pinene are shown by coloured areas together with the time series of the -pinene concentration. OH radical concentrations are derived from the decrease of injected d -butanol and from the corrected time series of -pinene concentrations according to Eq. (2.8). Injections of -pinene into the chamber are marked by yellow, vertical lines and dark conditions are indicated by grey areas. “ND” and “Dia” refer to the particle number density and the mean particle diameter. A relative humidity of % and a temperature of C were present during the experiment.

No wall loss of trace gases, but a loss of aerosol on the chamber wall with a rate of s (for a particle diameter of 200 nm) is reported in the auxiliary mechanism (Tab. 2.1, Eurochamp (2023)). In the experiments in this work, the wall loss can be derived for pinonaldehyde, -pinene, and particles. A possible wall loss of acetone cannot be determined, as acetone concentrations increased throughout the experiments.

In the illuminated chamber, a wall loss of pinonaldehyde is observed. This can be seen in the decrease of the pinonaldehyde concentrations, when -pinene was entirely consumed, with a rate that is faster than expected from its photolysis, its reactions with OH and O , and dilution (Figs. 2.6, A.22, and A.23). The pinonaldehyde wall loss rate is s (lifetime of 7 hours) in experiment I2 (Fig. 2.6), using OH radical concentrations determined from the decrease of d -butanol.

Concerning -pinene, no wall needs to be considered (Figs. 2.6, A.23), as no significant decrease in its concentration is observed when the lamps were switched off.

A loss of aerosol was observed in all experiments, as indicated by the concentration decrease, when -pinene was entirely consumed (Figs. A.22, 2.6, and A.23). A wall loss rate of s (lifetime of h) is derived from the total aerosol mass concentration, measured with a SMPS in the experiment I1s, and from the organic aerosol mass, measured by an AMS instrument in the experiments I2 and I3.

Experiments in the CESAM chamber

In the indoor chamber CESAM (CESAM, 2023), only the particle formation from the photooxidation of -pinene was studied (Figs. 2.7, A.8-A.10, Tab. A.3). Chamber sources cannot be evaluated for the experiments performed in the CESAM chamber due to the lack of data in the clean, illuminated chamber. However, the CESAM chamber is made of stainless steel, which may have less memory effects than a polymer like Teflon. The published auxiliary

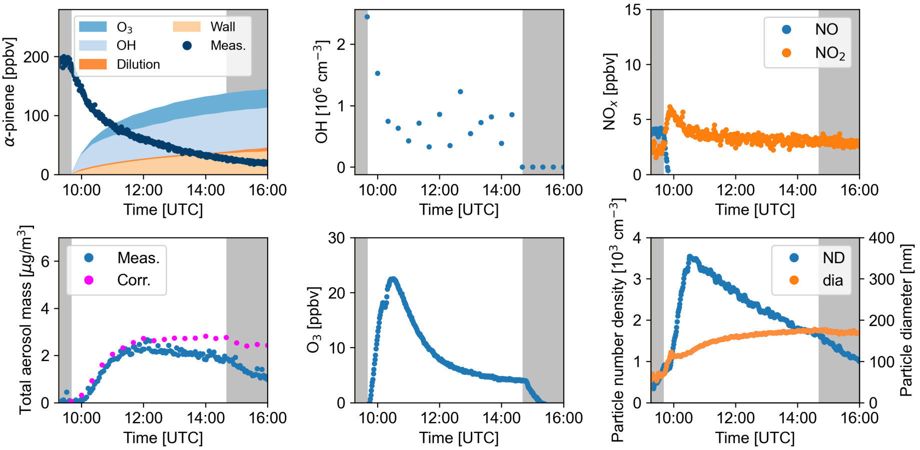

Figure 2.7: Time series of trace gas concentrations measured in the experiment C2 performed on the 15 of February 2019 in the CESAM chamber (Tab. A.3). Different contributions of the loss paths of -pinene are shown by coloured areas together with the time series of the -pinene concentration. OH radical concentrations are derived from the corrected time series of -pinene concentrations according to Eq. (2.8). Injections of -pinene into the chamber are marked by yellow, vertical lines and dark conditions are indicated by grey areas. “ND” and “Dia” refer to the particle number density and the mean particle diameter. A relative humidity between % and % and a temperature of C were present during the experiment.

mechanism (Tab. 2.1, Eurochamp (2023)) includes the conversion of NO to HONO. As no HONO measurements were available, the correlation of NO_2 and HONO could not be investigated.

From the experiment C2 performed on the 15 of February 2019 (Fig. 2.7), the wall loss rates can be determined, using the phase, when the lamps were switched off before and after the photooxidation phase. No loss of -pinene is observed in the dark period until the start of the photooxidation (Figs. 2.7, A.8-A.10). However, a decrease of the -pinene concentrations is observed in the dark phase at the end of the experiment, although the ozone concentrations quickly dropped to zero within half an hour and the OH radical concentrations are expected to decline as well (Fig. 2.7). This suggests that the wall loss rate of -pinene changed over the course of the experiment, possibly due to the passivation of surfaces. A loss of -pinene to the chamber wall with a rate of s is determined.

Beside -pinene, a wall loss of the aerosol with a rate of s is determined from the dark phase following the photooxidation phase of the experiment (Fig. 2.7). For particles with a diameter between 100 and 200 nm, as observed in the experiments in the CESAM chamber in this work, particle loss rates between s and s are reported (Eurochamp, 2023), being in a similar range as observed in this study.

The loss of -pinene on the chamber wall was significant (% of the entire loss) competing with the reaction with OH, as the OH radical concentrations are low in the presence of NO_x ppbv.

Experiments in the FORTH chamber

Aerosol formation and aging from the photooxidation of -pinene (Figs. 2.8, A.11, Tab. A.3) were also studied in the experiments in the FORTH simulation chamber (FORTH-ASC, 2023), in which both, the particle size distributions and their chemical composition, were provided. The release of trace gases from the chamber film of the FORTH chamber cannot be determined in this study, as the experiments do not include appropriate phases with a clean, illuminated chamber. In the auxiliary mechanism, no chamber sources are listed (Tab. 2.1, Eurochamp (2023)). As the FORTH chamber is made of Teflon, a HONO chamber source can be expected. Wall loss rates for -pinene and particles are published in the auxiliary mechanism (Tab. 2.1, Eurochamp (2023)). The experiments started with a dark period, from which the loss rates of trace gases and particles to the chamber wall can be determined. In this period, no wall loss of -pinene is observed. As ammonium sulfate was used as seed aerosol, the aerosol wall loss rates can be determined from the ammonium sulfate fraction of the aerosol, which is expected to change only due to aerosol loss. The time series of sulfate and ammonia aerosol, measured in the experiment F1 (Fig. 2.8), can be correctly described by introducing two different wall loss rates: a loss rate of s before 20:40 UTC and afterwards a wall loss rate of s .

High amounts of NO_2 (ppbv to ppbv) were injected in the experiments to produce

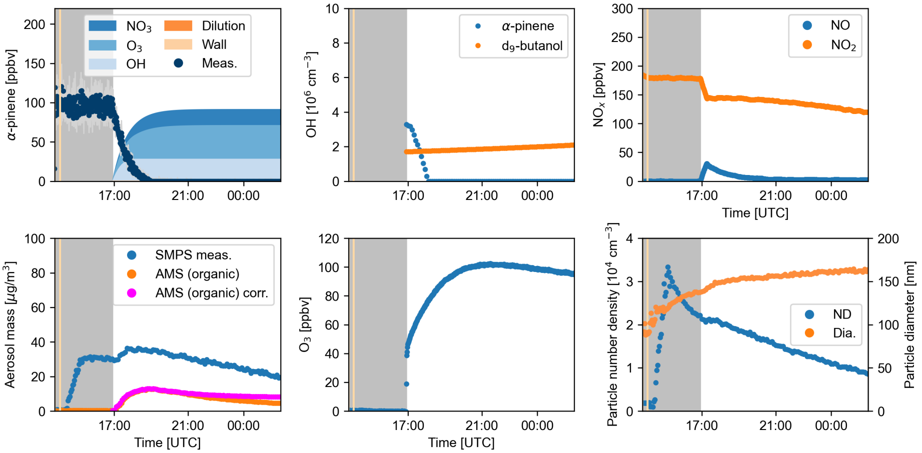

Figure 2.8: Time series of trace gas concentrations measured in the experiment F1s performed in the FORTH chamber (Tab. A.3). Different contributions of the loss paths of -pinene are shown by coloured areas together with the time series of the -pinene concentration. OH radical concentrations are derived from the corrected time series of -pinene concentrations and of d -butanol according to Eq. (2.8). The injection of seed aerosol (ammonium sulfate) into the chamber is marked by a yellow, vertical line and dark conditions are indicated by grey areas. "ND" and "Dia" refer to the particle number density and the mean particle diameter. The relative humidity decreased from % to % and the temperature increased from C to C after the lights had been switched on.

OH radicals from ozone photolysis, as in the illuminated chamber, a photostationary state between NO, NO , and O concentrations was rapidly established, leading to peak NO and O mixing ratios of ppbv and ppbv to ppbv, respectively, one hour after starting the illumination. With the initial -pinene mixing ratios of ppbv to ppbv, ozone concentrations increased further in the photooxidation of -pinene. Consequently, high amounts of ozone and NO were present, leading to a high production rate of NO , which is expected to have contributed maximum % to the oxidation of -pinene. The presence of NO$_3$ makes the simulation of atmospheric daytime processes challenging in the FORTH chamber under these conditions. The production of NO$_3$ could have been lowered by either injecting less NO$_2$, less VOC producing O$_3$ from radical chemistry or choosing a different OH precursor, such as H$_2$O$_2$ or HONO.

Experiments in the MAC chamber

Photooxidation experiments were performed in the MAC chamber (MAC, 2023), focusing on the formation of particles (Figs. 2.9, A.12-A.15, Tab. A.3). Data are only available for the oxidation period, therefore chamber-related loss and wall emission rates are difficult to

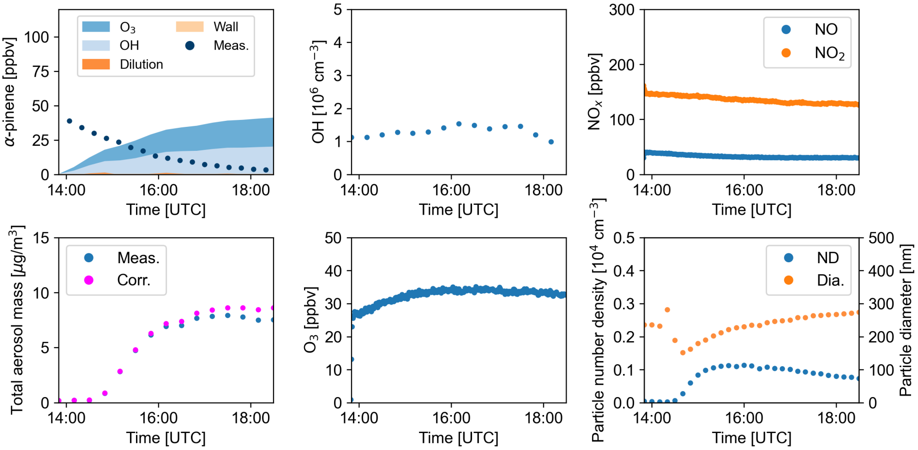

Figure 2.9: Time series of trace gas concentrations measured in the experiment M1 performed in the MAC chamber (Tab. A.3). Different contributions of the loss paths of -pinene are shown by coloured areas together with the time series of the -pinene concentration. OH radical concentrations are derived from the corrected time series of -pinene concentrations according to Eq. (2.8). Injections of -pinene into the chamber are marked by yellow, vertical lines. "ND" and "Dia" refer to the particle number density and the mean particle diameter. A relative humidity of % and a temperature of C were present during the experiment.

determine. A small loss rate of -pinene of s (lifetime of 59 days) is reported in the published auxiliary mechanism (Tab. 2.1, Eurochamp (2023)), but this is not relevant for the time scale of the experiments in this study.

From the experiment M1 (Fig. 2.9), when -pinene was nearly completely consumed (18:00 UTC), a slight decrease of the total aerosol mass is observed, which may indicate a small aerosol wall loss with a rate of s .

As only OH radical concentrations of maximum cm were present in the experiment, the contribution of ozonolysis to the loss of -pinene was significant with %, reaching % at low NO_x (Fig. A.13).

Experiments in the LEAK chamber

Four -pinene oxidation experiments in the LEAK chamber (TROPOS, 2023) are analysed (Figs. 2.10, A.16-A.18, Tab. A.3). No information about chamber sources is given for the LEAK chamber in the auxiliary mechanism (Tab. 2.1, Eurochamp (2023)). In the experiments performed in this study, no OH precursors were injected, however, OH radical concentrations of up to cm were calculated from the consumption of -pinene. As the chamber is made of Teflon, it is likely that HONO is released from the chamber wall, as also observed in the HELIOS, SAPHIR, PACS-C3, and ILMARI chambers (Tab. 2.1). Unfortunately, the chamber sources cannot be studied in this work, as photooxidation started immediately after the illumination started in the experiments in the LEAK chamber.

A loss of -pinene and of particles with rates of s and s (for a particle diameter of 200 nm), respectively, is reported in the auxiliary mechanism (Tab. 2.1, Eurochamp (2023)). As -pinene was only measured in the illuminated chamber, no loss of -pinene to the chamber walls can be estimated. Therefore, the reported value is assumed in the evaluation of all experiments, except for the experiment L4 (Fig. A.18), where no wall loss is assumed as the total loss rate of -pinene is lower than the wall loss rate in this experiment. Hence, the reported wall loss rate of -pinene needs to be regarded as an upper limit.

From a reference experiment (not shown in this work), in which seed aerosol was injected in the dark and subsequently illuminated for three hours, a loss rate of particle to the chamber wall of s is determined, which is more than a factor of 2 lower than reported.

In the experiment L2s (Fig. 2.10), an increase of ozone concentrations, reaching up to ppbv, is observed despite NO mixing ratios of about zero. If a photostationary state is assumed, a NO mixing ratio of ppbv is expected, assuming O_3 ppbv. The reason for the not measurable concentration of NO remains unclear.

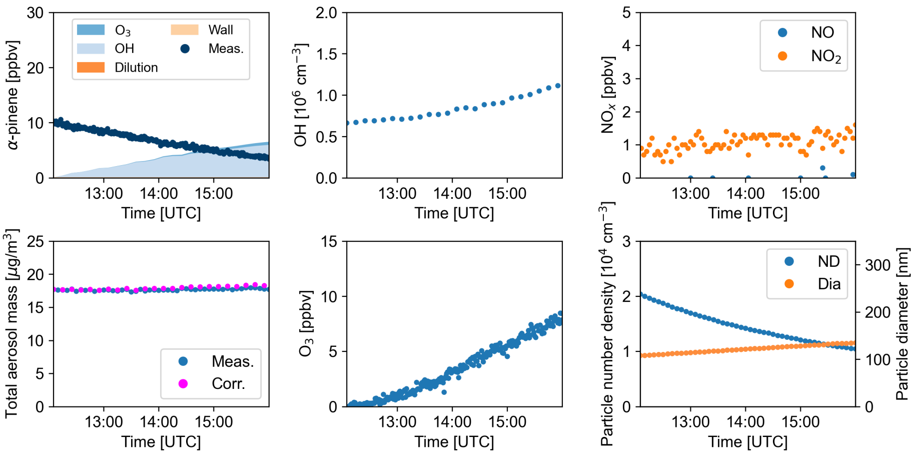

Figure 2.10: Time series of trace gas concentrations measured in the experiment L2s performed in the LEAK chamber (Tab. A.3). Different contributions of the loss paths of -pinene are shown by coloured areas together with the time series of the -pinene concentration. OH radical concentrations aree derived from the corrected time series of -pinene concentrations according to Eq. (2.8). Injections of -pinene into the chamber are marked by yellow, vertical lines. “ND” and “Dia” refer to the particle number density and the mean particle diameter. A relative humidity of % and a temperature of C were present during the experiment.

2.3.3 Comparison of results from the simulation chambers

Yields of pinonaldehyde, formaldehyde, and/or acetone could be determined for the experiments performed in the HELIOS, EUPHORE, SAPHIR, PACS-C3, and ILMARI chambers. In most experiments, -pinene was mainly oxidised by OH with varying contributions of ozone. In the FORTH chamber, the oxidation of -pinene by NO contributed as well. Yields were determined according to Eq. (2.6). The correlation between the corrected product concentrations (Eqs. (A.1)-(A.3)) and the amount of reacted -pinene, oxidised by OH (Eq. (2.7)) are summarised in Section A.1.5 (Figs. A.24-A.28). Overall, a good agreement of product yields is found for similar experimental conditions performed in the same chamber, such as for the experiments E1 and E2, conducted in the EUPHORE chamber (Fig. A.25), or for the experiments I2 and I3, performed in the ILMARI chamber (Fig. A.28).

Yields of pinonaldehyde

Pinonaldehyde was measured in all experiments except for the experiments in the HELIOS chamber. Among the studied gas-phase products, pinonaldehyde is the only one which is solely produced in the first oxidation step of -pinene initiated by OH or O . From the analysed experiments, pinonaldehyde yields from the oxidation by OH range between 0.7 and %. In all experiments, ozonolysis is expected to have contributed approximately between % and % to the oxidation of -pinene, with the exception of the experiments P1, I1s, and I3, in which the contribution of ozonolysis was negligible. In the experiments performed in the PACS-C3, ILMARI, and SAPHIR chambers at relative humidities larger than %, similar small pinonaldehyde yields of % are observed. The lowest yields of % and %, observed in the PACS-C3 and ILMARI chambers, respectively, are obtained from experiments with -pinene mixing ratios of ppbv. A twice as large pinonaldehyde yield is observed in the experiment P2, compared to the experiments P3 and P4 (all in the PACS-C3 chamber), in which NO_x concentrations were likely smaller. In contrast, yields between % and % are determined from experiments, conducted in the EUPHORE chamber performed at dry conditions (relative humidity of less than %), with the exception of the experiment E3.

In the literature, a large variability of the pinonaldehyde yield is reported, with values ranging between % and %. Rolletter et al. (2019) addressed this high variability of yields and highlighted that high pinonaldehyde yields were particularly observed in experiments, in which pinonaldehyde was measured by FT-IR instruments, since these instruments are prone to interferences from carbonyl compounds. Furthermore, lowest yields in the literature are found by Larsen et al. (2001) and Rolletter et al. (2019) (S1, S2), where the latter performed experiments at atmospheric conditions (ppbv, NO pptv).

In the multi-chamber study in this work, highest yields of pinonaldehyde are obtained from the experiments conducted in the EUPHORE chamber, which agree with yields determined by Hatakeyama et al. (1991) and Nozière et al. (1999) within the uncertainties. Similar to

Table 2.2: Gas-phase yields of compounds formed in the oxidation of -pinene by OH determined from experiments in this work and reported in the literature.

Experiments (this work)	Yield PINAL[a] [%]	Yield HCHO [%]	Yield Acetone [%]
H2	-		-
E1.2[b]			
E2.2[b]			
E3			
P1			-
P2			-
P3			-
P4			-
I1s		-	
I2		-	
I3		-	
S1, S2[c]			
Arey et al. (1990)	29	-	-
Hatakeyama et al. (1991)			-
Nozière et al. (1999) (with NO)	[c]		
Nozière et al. (1999) (no NO)			
Orlando et al. (2000)	-		
Jaoui and Kamens (2001)	28	-	-
Larsen et al. (2001)			
Wisthaler et al. (2001)			
Aschmann et al. (2002)		-	-
Lee et al. (2006)		16	6

[a] Pinonaldehyde concentrations are not corrected for the ozonolysis reaction of the ozonolysis reaction, therefore these values correspond to upper limits; [b] Values from E1.2 and E2.2 are derived from the second half of the experiment, initiated by the second injection of -pinene and correspond to an average of calculated values; [c] Taken from Rolletter et al. (2019).

Hatakeyama et al. (1991) and Nozière et al. (1999), pinonaldehyde was measured with a FT-IR in the EUPHORE chamber. In the experiments in the PACS-C3 and the ILMARI chamber, pinonaldehyde yields between 0.7 % and 3.6 % are observed, which agree with values, derived by Rolletter et al. (2019) (S1, S2) and Larsen et al. (2001). Overall, -pinene mixing ratios of up to ppbv were present in the experiments in the PACS-C3 and ILMARI chambers and NO mixing ratios were below ppbv.

Yields of formaldehyde

A span of yields between 6 and % is determined for the formaldehyde yield in the experiments in this work. Formaldehyde yields cannot be determined in the ILMARI chamber due to the lack of formaldehyde measurements. Lowest HCHO yields are determined in the experiments P3 and P4, conducted in the PACS-C3 chamber, in which the initial ozone mixing ratios were below ppbv. In contrast, higher HCHO yields are observed in the same chamber in the experiments P1 and P2, in which ozone mixing ratios were larger than ppb. In the experiment P1, in which the highest HCHO yield among the experiments performed in the PACS-C3 chamber is observed, -pinene mixing ratios were lowest with maximum ppbv. Similar HCHO yields between % and % are derived in the experiments E2.2, E3 (EUPHORE), and P1 (PACS-C3), having however a high variability of the initial -pinene mixing ratios (between ppbv and ppbv). Highest formaldehyde yields are obtained in the experiments E1.2, performed in the EUPHORE chamber, when the initial NO mixing ratios were ppbv, and in the experiment H2 performed in the HELIOS chamber, when the initial NO mixing ratios were ppbv.

Values reported in the literature (Nozière et al., 1999; Larsen et al., 2001; Wisthaler et al., 2001; Lee et al., 2006) for the formaldehyde yield from the OH oxidation of -pinene range between 8 and 23 % with the exception of the results in the work by Hatakeyama et al. (1991), who measured a formaldehyde yield of more than 50 %. HCHO yields, determined from the experiments P3 and P4 (PACS-C3), are in good agreement with the yields observed by Larsen et al. (2001) and Wisthaler et al. (2001). The yields of formaldehyde in the other experiments (experiments H2, E1.2, E2.2, E3, P1) are in a similar range as measured by Nozière et al. (1999) and by Hatakeyama et al. (1991) in the presence of NO.

Yields of acetone

In contrast to pinonaldehyde and formaldehyde, acetone yields determined in the multi-chamber experiments are similar within the uncertainties, giving values between 12 % and 28 % in the experiments conducted in the EUPHORE, ILMARI, and SAPHIR chambers. In the experiments at NO_x ppbv (experiments E2.2, E3, I3), lower acetone yields are observed than in the experiments at higher NO mixing ratios (ppbv, experiments E1.1, I1s, and I2).

Acetone yields agree within their uncertainties with values around 10 % reported in the literature (Nozière et al., 1999; Orlando et al., 2000; Larsen et al., 2001; Wisthaler et al., 2001; Lee et al., 2006). Compared to pinonaldehyde and HCHO yields, acetone yields do not show a large variability in the experiments in the different chambers and/or at different experimental conditions in agreement with results reported in the literature.

Uncertainties in the analysis

Uncertainties in the derivation of the product yields may cause a variability in the product yields, determined in the different simulation chambers. The correction of product and -pinene concentrations for losses due to the reaction with ozone (PACS-C3, ILMARI) or due to dilution (EUPHORE) introduces generally additional uncertainty in the yields. In some cases, the additional uncertainty is rather small, as, for example, the dilution rates, required for the correction due to dilution, can be precicely determined like from the decrease of measured SF_6 in the EUPHORE chamber. In contrast, the correction of measured -pinene concentrations for the ozonolysis reaction is expected to introduce a larger uncertainty, as the rate constant of the reaction of ozone with -pinene has an uncertainty of % (Atkinson et al., 2006). Major loss processes of pinonaldehyde, formaldehyde, and acetone are photolysis and their reactions with OH. The correction for the loss of organic compounds through photolysis requires the appropriate values of their photolysis frequencies and thus well-characterised lamp spectra (indoor chambers) or the measurement of the actinic flux (outdoor chambers). Furthermore, the uncertainties of the absorption cross section and of the quantum yield, being mainly below % and about 10 % to %, add to the total uncertainty (Moortgat et al., 1983; Hallquist et al., 1997; Gierczak et al., 1998; Atkinson et al., 2006; Rolletter et al., 2020).

In the presence of ozone, pinonaldehyde concentrations would also need to be corrected for their formation from the ozonolysis of -pinene. However, for experiments performed in the PACS-C3 and the ILMARI chambers, pinonaldehyde concentrations become negative after correcting for ozonolysis, highlighting the uncertainty of the performed corrections and of the yield of pinonaldehyde from the ozonolysis reaction.

For estimating the amount of organic compounds reacting with OH, OH radical concentrations need to be known. However, in most of the analysed experiments, no OH radical measurements were available and OH radical concentrations were calculated from the time series of -pinene, which are especially uncertain at low -pinene concentrations as the difference of -pinene concentrations within one time step becomes small. Thus, potential systematic errors in the fraction of -pinene reacting with OH can lead to systematic errors in the product yield calculations.

In addition, chamber-related processes may affect the production and loss of trace gases. A loss of pinonaldehyde to the chamber wall was observed in the PACS-C3 and ILMARI chamber, having though a negligible contribution (lifetime > h). Emissions of small oxygenated molecules, such as formaldehyde and acetone, from the chamber walls, were observed in particular for chambers made of Teflon film, having production rates of up to ppbv h . As the emission strength of the chamber sources depends on the history of previous experiments, it needs to be well characterised for each experiment. However, only averaged source strengths could be determined, specifically for the indoor chambers, due to the lack of suitable experimental phases in this work.

Since the analysed gas-phase compounds are not only formed from the oxidation of -pinene by OH, their concentration time series also need to be corrected for secondary chemistry. Overall, the correction of measured product concentrations for chamber-related emissions, losses and secondary chemistry carry high uncertainties because it requires the quantification of corresponding loss or production rates for each compound of interest which may vary from experiment to experiment.

2.4 Summary and conclusions

As part of the EUROCHAMP-2020 project, a multi-chamber study was performed, investigating the oxidation of -pinene by OH. In total, 32 experiments, conducted in nine different simulation chambers, were analysed, focusing on the characterisation of chamber-related processes, and the determination of the yields of organic products. Emission rates of formaldehyde from the chamber walls were observed in the outdoor chambers, ranging between ppbv h and ppbv h . Determined wall loss rates of pinonaldehyde were between s and s and of -pinene between s and s , determined from experiments in two and three chambers, respectively.

Product yields could be determined from the experiments in the HELIOS, EUPHORE, PACS-C3, ILMARI, and SAPHIR chambers. A high variability of the product yields is found for pinonaldehyde (ranging between % and %) and formaldehyde (ranging between % and %). Similarly, yields for these compounds reported in the literature show a wide span of % (pinonaldehyde) and % (formaldehyde). In contrast, the acetone yields, obtained in this work, agree within % with observations reported in the literature.

A complete characterisation of chamber effects is essential for the evaluation of chamber experiments. The analysis of the multi-chamber experiments in this work demonstrates the importance of standard operational procedures, to ensure that chamber effects can be appropriately taken into account in the evaluation. These procedures are preferably integrated in the experimental procedure, but can also be performed right before or after the experiment, to account for possible changes of wall emission or loss rates due to memory effects from preceding experiments. Chamber experiments, performed in this study, highlight the importance of planning experiments using appropriate concentrations of the VOC of interest, of NO_x, and the oxidants, which fit the properties of the chamber, so that the chemistry of interest is dominating and can be properly investigated. In addition, detailed information about the experimental procedure and about the injected amount of trace gases is vital for interpreting experiments and characterising chamber sources. Finally, measurements of trace gases, driving the chemistry, such as the oxidants OH and O_3 and nitrogen oxides (NO_x) are helpful for *e.g.*, performing chemical box model calculations and for quantifying the importance of the competing oxidation pathways.

3 Daytime and nighttime radical chemistry in urban environments

3.1 Methodology

3.1.1 Studying air quality in the atmospheric simulation chamber SAPHIR

In field measurements, many processes affect the chemical composition of the air, making reasonable improvements of atmospheric chemical models difficult. Atmospheric simulation chambers help bridging this gap and are crucial for developing atmospheric chemical models by investigating the kinetics and the products of the atmospheric oxidation of single trace gases under controlled conditions (Doussin et al., 2023).

Experiments focusing on the daytime and nighttime radical chemistry in this work were performed in the outdoor atmospheric simulation chamber SAPHIR (Simulation of Atmospheric PHotochemistry In a large Reaction chamber, Fig. 3.1) (Rohrer et al., 2005; Schlosser et al., 2007; Fuchs et al., 2010), which is cylindrically shaped (diameter = m, length = m) with a total volume of m . Thus, the chamber has a low surface-to-volume ratio ( ), which allows to study chemical processes at atmospheric concentration levels of the trace gases due to often negligible wall losses of the trace gases. Due to the large size of the chamber, two fans are installed to ensure well mixed air within the chamber. To compensate for small leakages and the air volume measured by the instruments, a replenishment flow is required which causes a dilution with a typical rate of less than s . The chamber is confined

Figure 3.1: The outdoor atmospheric simulation chamber SAPHIR located in Jülich, Germany. Copyright “Forschungszentrum Jülich / Sascha Krelau”. Copyright “Florian Monheim”.

Table 3.1: Instrumentation for measuring trace gas and radical concentrations in the atmospheric simulation chamber SAPHIR. Instrumental details are based on experiments performed in Summer 2022.

Species	Technique	Time resolution	1 precision	1 accuracy	Instrument
OH	DOAS[a]	431 s	cm	6.5 %	FZJ DOAS
	FAGE-LIF[b]	45 s	cm	18 %	FZJ ROxLIF
HO	FAGE-LIF[b]	45 s	cm	18 %	FZJ ROxLIF
RO	FAGE-LIF[b]	45 s	cm	18 %	
OH	LP-LIF	142 s	0.1 s	10 %	FZJ KOH
NO	Chemiluminescence	98 s	3 pptv	5 %	Eco Physics TR780
NO			70 pptv	5 %	
O	UV photometry	60 s	90 ppbv	5 %	Ansyco 42M
H O	Cavity ring-down spectroscopy	60 s	0.1 %	5 %	Picarro G2401
CO			1.5 ppbv		
CO			25 ppbv		
CH			1 ppbv		
HCHO	DOAS[a]	431 s	0.2 ppbv	10 %	FZJ DOAS
	Cavity ring-down spectroscopy	120 s	0.1 ppbv	10 %	Picarro G2307
VOCs	PTR-ToF-MS[c]	30 s	ppbv	10 %	Ionicon Analytik PTR-ToF 8000
	GC-FID[d]	42 min	ppbv	5 %	Agilent 7890N
Photolysis frequencies	Spectroradiometer	30 s	s	10 %	Bentham 300

[a] Differential Optical Absorption Spectroscopy; [b] Fluorescence Array by Gas Expansion - Laser Induced Fluorescence; [c] Proton Transfer Reaction Time-of-Flight Mass Spectrometer; [d] Gas Chromatography - Flame Ionisation Detector.

by a double-wall Teflon (FEP) film which has a high transmittance of the solar radiation over the entire solar spectrum. To protect the chamber film from any meteorological influences such as wind or strong precipitation, a shutter system is installed which also allows the investigation of nighttime atmospheric chemistry during daytime. Even though the FEP film is chemically inert, emissions of different compounds such as HONO, HCHO, acetaldehyde, acetone, and NO_x are observed with open shutters, which is a common observation also in other chambers. Chamber sources are typically dependent on sunlight, humidity, and temperature. The photolysis of HONO emitted from the wall acts as an OH source. To avoid any contaminations from ambient air, an overpressure of Pa is present in the chamber compared to ambient pressure. The chamber is provided with ultra-pure synthetic air (% N , % O , Linde, purity > %). In general, trace gases are added into the chamber by adding them to the replenishment flow. The temperature inside SAPHIR cannot be controlled and is thus dependent on ambient conditions. In total, ten instruments are permanently installed at SAPHIR (Tab. 3.1). Most of them are housed in containers below the chamber. Exceptions are the Differential Optical Absorption Spectroscopy (DOAS) instrument and the Laser-Induced Fluorescence (LIF) instrument. The laser system of the DOAS instrument is located in a container attached to one side of the SAPHIR chamber, so that it can be directly guided into the chamber, at which ends mirrors are installed, spanning an optical multiple reflection cell. In contrast, a temperature-controlled box containing the LIF instrument is directly attached underneath the chamber, while the corresponding laser system is situated in a close container.

3.1.2 Detection system for OH, HO , and RO radicals at the atmospheric simulation chamber SAPHIR

The detection system (Holland et al., 2003; Fuchs et al., 2008) for measuring OH, HO , and RO radicals in the SAPHIR chamber is shown in Fig. 3.2. Three detection cells allow the simultaneous measurement of OH, HO , and RO radicals. Air is sampled into each detection cell (hPa) through a conically-shaped nozzle. To reduce wall contact and re-circulation flows of sampled air, a nitrogen flow of slm (1 slm = 1 L min at 1 atm and C) is continuously directed into each detection cell. Furthermore, contributions of laser-induced background is reduced by using baffle arms which are also purged by nitrogen flows of slm.

Laser system and the detection of fluorescence light

The sampled air is irradiated with a pulsed laser beam at a wavelength of nm, a pulse repetition frequency (PRF) of kHz, and a typical UV laser power of mW to mW. The laser beam is generated by pumping a tunable dye laser (Rhodamin 101 in ethanol, nm) with a frequency-doubled Nd:YAG laser (Nd:Y Al O , nm). A laser wavelength of nm is then achieved via frequency doubling, using a barium borate ($Ba(BO_2)_2$) crystal. OH radicals, contained in the sampled air, are excited by the incoming laser photons via the (3) transition of the band (Fig. 1.8). The emitted fluorescence light is focused via an optical system onto a micro-channel plate photomultiplier (MCP) after passing an interference filter (nm, FWHM nm) and a solarblind optical filter. Since the scattered laser photons and the fluorescence light cannot be discriminated by wavelength, a gated photon counting system is used. Before the laser pulse passes the detection cell, the MCP is switched off to protect the MCP from any damage, caused by a high photon load (Fig. 3.3). The fluorescence measurement starts shortly after the laser pulse passed the detection cell, after the MCP has been switched on again and any effect of the gating on the sensitivity of the MCP abated and laser scattering from the laser pulse is reduced (Hofzumahaus and Holland, 1993). The fluorescence is then measured for ns. The measured photon counts ( ) in the fluorescence counter gate can be expressed as:

$$ {}_{\mathrm{OH}} \tag{3.1} $$

with ${}_{\mathrm{OH}}$ being the OH fluorescence photon counts. To quantify any laser-independent noise, the detector noise ( ) and solar light, which is scattered into the detection system and cannot be completely filtered out ( ), a second counter gate starts approximately 20 µs after the fluorescence counter gate, with a duration of 20 µs (Fig. 3.3). At that time, no contributions from laser scattering ( ) or from fluorescence light (${}_{\mathrm{OH}}$) is expected.

Wavelength scanning. The wavelength of the incoming laser light is modulated on and off the absorption peak to determine the contribution of the laser-dependent background signal ( ) to the total measured photon counts (Eq. (3.1)). The OH fluorescence photon counts are then determined according to:

$$ {}_{\mathrm{OH}} \tag{3.2} $$

with the photon counts and , measured on and off resonant, respectively, and being corrected for laser-independent background photon counts. In addition, the wavelength is scanned over the absorption peak at five wavelength positions to correct for possible small thermally-induced spectral drifts of the laser wavelength (Hofzumahaus et al., 1996). This is achieved by observing the OH fluorescence in a reference cell, in which the OH absorption cross section is tracked simultaneously to the OH measurement with a separate low-pressure reference cell, where the pyrolysis of water vapour produces high OH radical concentrations by means of a hot filament (Fig. 3.2). As the OH fluorescence photon counts depend on the line profile of the OH absorption line, they are normalised to the line profile measured in the reference cell in one complete wavelength scan and are subsequently averaged. With a typical integration time of s per wavelength position, resulting in an integration of PRF s laser pulses, overall integration times of the radical and background measurements are s and s, respectively, resulting in a time resolution of

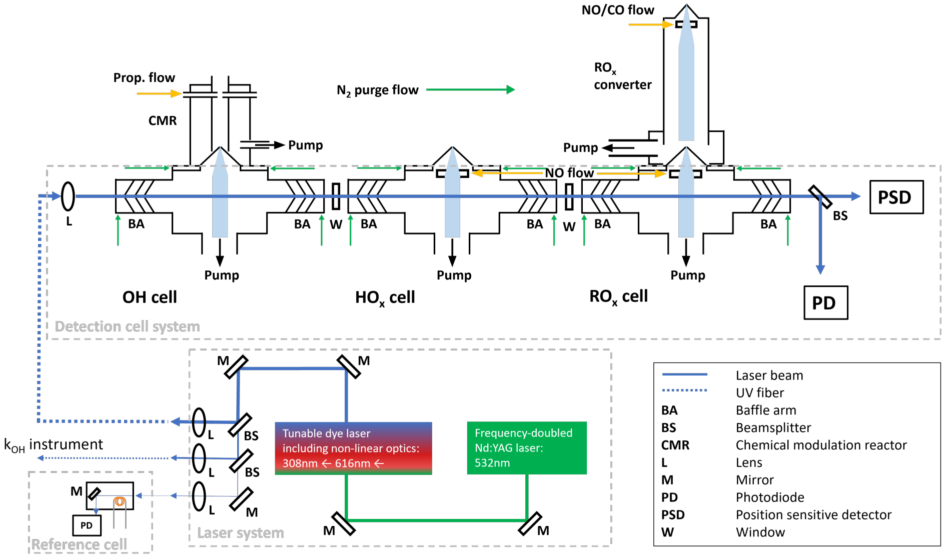

Figure 3.2: Schematic of the LIF detection system installed at the atmospheric simulation chamber SAPHIR, Jülich, adapted from the open access publication by Tan et al. (2017) under the Creative Commons Attribution 3.0 License (https://creativecommons.org/licenses/by/3.0).

radical concentrations measurements of s due to additional electronic processing time.

OH radical concentration measurements

The first detection cell, which the laser passes is the OH detection cell, followed by the HO$_x$ and RO$_x$ detection cells. Air is sucked through a mm orifice with a flow of slm into the low-pressure detection cell and OH radical concentrations are measured as described above. Various potential interferences in the OH radical measurement have been tested in the past, such as impacts from the photolysis of hydrogen peroxide, formaldehyde, nitric acid, and nitrous acid and no measurable OH signal was reported (Ren et al., 2004). Furthermore, the photolysis of acetone as well as the ozonolysis of biogenic and short-chain VOCs are not expected to cause a significant interference for atmospheric conditions (Ren et al., 2004; Fuchs et al., 2016). Another potential interference discussed in literatures (Novelli et al., 2014; Fuchs et al., 2016) is the OH formation from stabilised Criegee intermediates which can decompose forming OH. However, typical ambient concentrations are too small (to cm , Novelli et al. (2014)) to produce a significant interference.

The OH detection cell can be equipped with a chemical modulation reactor (CMR), allowing interference-free OH radical measurements (Cho et al., 2021). A flow of Lmin is sucked through a mm long PTFE Teflon tube (diameter = mm) centered around the inlet nozzle

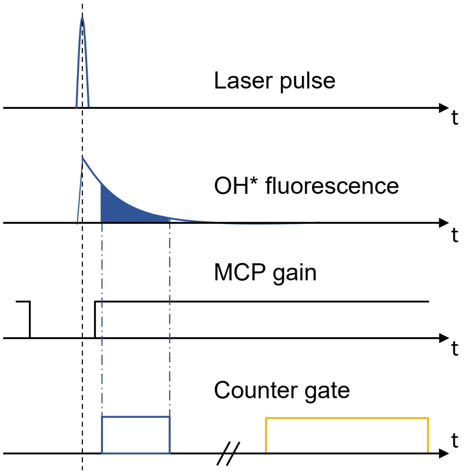

Figure 3.3: Schematic of the gated photon counting for measuring OH radicals with the ROxLIF instrument. The illustration is inspired by Hofzumahaus and Holland (1993).

of the detection cell. The CMR is operated in two modes, with and without the addition of propane (Air Liquide, propane, purity > %, ( ) % mixture in N) to a nitrogen flow of slm (N , purity < %), which is injected into the CMR through two stainless steel tubes (1/8 inch outer diameter with 50 µm inner diameter). In the OH scavenging mode, a propane mixing ratio of ppmv is achieved downstream resulting in an OH scavenging efficiency of % to %. The change from the OH scavenging mode to the pure N mode, in which OH plus possible interferences is measured, is governed by flushing the CMR with an increased N flow of slm for s to purge out any residuals of the OH scavenger within the flow tube. Each mode has a duration of three full wavelength scans (s) and the interference-free OH radical concentration as well as the interference OH radical concentration can be obtained when knowing the OH transmission of the CMR in the N mode.

HO_x radical concentration measurements

In a second detection cell (mm orifice), HO_x (=OH+ HO ,) can be detected by chemically converting HO into OH by adding a small flow of NO from a gas mixture (Air Liquide, % NO in N , purity > %, Reaction (R1.8)) to the sampled slm air flow downstream of the inlet nozzle (Reaction (R1.8)) (Holland et al., 1995, 2003; Fuchs et al., 2008, 2011, 2012). The HO_x detection cell is run at low NO concentrations in the measurement cell of cm , resulting in a conversion efficiency of about %, to minimise possible interferences from specific RO (large alkenes, aromatics, isoprene, among others) radicals which rapidly form HO in their reaction with NO (Fuchs et al., 2011). Furthermore, the HO_x detection cell is typically run in two modes, where the NO concentration is modulated to even

smaller concentrations to check whether RO interferences are present in the measurement. Since the sum of OH and HO (= HO_x) is measured, the HO radical concentration is derived from subtracting the OH radical concentration from the measured HO_x concentration.
Interferences from the photolysis of formaldehyde (Reactions (R1.27)- (R1.29)) can be neglected for atmospheric conditions at which mixing ratios smaller than ppbv can be expected for formaldehyde (Ren et al., 2004). At high NO concentrations (NO ppbv), the decomposition of peroxynitric acid can lead to a % contribution of the interference signal to the measured HO radical concentration (Fuchs et al., 2008).

RO_x radical concentration measurements

The RO_x (=OH+HO +RO) measurement system (Fuchs et al., 2008) includes in addition to the detection cell a RO_x converter (hPa, length = mm, diameter = mm) which is mounted on top of the RO_x detection cell (hPa, Fig. 3.2). An air flow of slm is sampled into the RO_x converter where RO and OH radicals are converted into HO radicals by adding NO (flow = sccm, Air Liquide, ppmv NO in N , purity > %) and excess CO (flow = sccm, Air Liquide, % CO in N , purity > %) according to:

$$HO_2 \quad NO \quad OH \quad NO_2 \tag{R3.3}$$

$$OH \quad CO \quad H \quad CO_2 \tag{R3.4}$$

$$H \quad O_2 \quad HO_2 \tag{R3.5}$$

Due to the high NO and CO conditions in the converter, OH and HO_2 are in a fast equilibrium, which is strongly towards HO_2 (Fuchs et al., 2008). Downstream of the RO_x converter, approximately half of the air is sucked through an inlet nozzle (diameter = mm, flow = slm) into the RO_x detection cell. Similar to the HO_x detection cell, NO (Linde, purity = %) is added to the air stream, however in a much higher concentration (cm) to achieve a high conversion efficiency of HO into OH. In the RO_x detection cell, the interference from potentially remaining RO_2 is wanted as the sum of all radicals (OH+HO_2+RO_2) is aimed to be measured. To determine the RO radical concentration, the measured RO_x radical concentration is subtracted by measured OH and HO radical concentrations, determined from the other two detection systems.
In the RO_x detection cell, interferences from peroxynitrates may appear at high levels of NO (Fuchs et al., 2008). RO radicals can be released through the decomposition of peroxynitrates (Reaction (R1.14)) such as methyl peroxynitrate (CH O NO) which contributes % to the measured CH O concentration for NO ppbv.

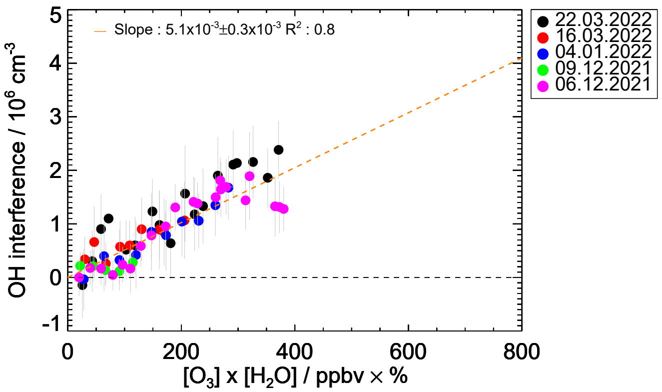

Figure 3.4: Observed ozone-water interference in the OH detection cell, expressed as equivalent ambient OH radical concentration. Measurements were performed with humidified synthetic air and varying water vapour and ozone concentration.

Interferences affecting all measurements

The most important interference is the photolysis of ozone by the excitation laser at nm in the presence of water vapour leading to the formation of OH radicals via Reactions (R1.22) and (R1.23). Since HO and RO radicals are indirectly measured through the conversion to OH and its subsequent laser-induced fluorescence, the ozone-water interference affects all detection cells (Smith and Crosley, 1990; Holland et al., 1995, 2003; Ren et al., 2004). Since ambient HO and RO radical concentrations are typically more than one order of magnitude larger than OH radical concentrations, the O -H O interference typically affects the OH measurement the most. In laboratory studies, this interference can be well characterised by sampling synthetic air with well-known water vapour and ozone concentrations (Holland et al., 2003). Laboratory measurements of the ozone-water interference were performed in this work (Fig. 3.4) and an interference equivalent to cm of OH was determined. In all detection cells in the instrument used in this work, an interference was observed when the sampled air contained NO radicals (Fuchs et al., 2016). An explanation of this interference has not been found yet. It is assumed to be caused by wall reactions of NO with the inlet nozzle or the interaction of possibly formed water clusters with NO (Fuchs et al., 2016). In a previous version of the FZJ ROxLIF instrument, a NO interference was observed which was equivalent to radical concentrations cm , cm and cm of OH, HO , and RO , respectively (Fuchs et al., 2016). In the current version of the FZJ-ROxLIF used in this work, the NO interference has not been fully characterised yet. However, an

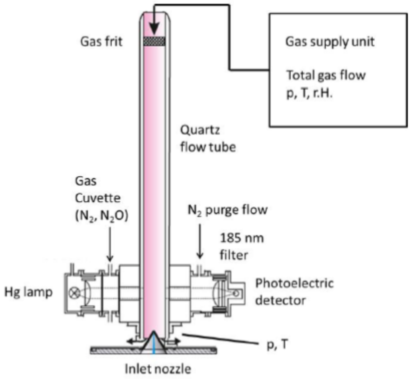

Figure 3.5: Schematic of the calibration source for the LIF instrument, adopted from the open access publications by Cho (2021) and Künstler (2020) under the Creative Commons Attribution 4.0 License (https://creativecommons.org/licenses/by/4.0).

upper limit of the NO interference could be estimated for the RO measurement which is equivalent to a RO radical concentration of cm .

Calibration

The radical measurement via the LIF technique requires a calibration of each detection cell in order to determine the proportionality factor between the radical concentration and the measured signal. Due to the high reactivity of OH radicals, hydroxyl radicals need to be produced during the calibration in a radical source, as for example shown in Fig. 3.5, which can be placed on top of each detection system. There are several methods for calibrating the LIF instrument such as the ozonolysis of alkenes or the photolysis of ozone in the presence of water vapour (Rodgers et al., 1985; Hard et al., 2002; Heard and Pilling, 2003). However, the commonly used technique is based on the photolysis of water vapour, which is described in the following (Heard and Pilling, 2003). In the calibration source used in this work, humid, synthetic (79.1 % N , 20.9 % O) air is flowed with a rate of slm into a cm long flow tube made of quartz glass with an internal diameter of mm. A frit near the entrance of the flow tube (Fig. 3.5) ensures a plug-flow downstream, which is nearly laminar before the air volumes reaches the inlet nozzle of the detection cell. In this region, OH radicals are produced by the photolysis of water vapour at a wavelength of nm, provided by a low-pressure discharge mercury lamp (penray lamp):

$$\mathrm{H_2O} \quad h \qquad \mathrm{nm} \quad \mathrm{H} \quad \mathrm{OH} \tag{R3.6}$$

The OH quantum yield of this reaction is unity. In addition to an OH radical, an HO radical is also produced via the reaction of the hydrogen atom with an oxygen molecule

(Reaction (R3.5)) with the same yield (Fuchs et al., 2011). The produced OH and HO radical concentrations are only dependent on the photolysis frequency of H O and can be expressed by:

$$\mathrm{HO_2} \quad \mathrm{OH} \quad \mathrm{H_2O} \quad {}_{\mathrm{H_2O}} \quad \mathrm{nm} \quad {}_{\mathrm{OH}} \quad \mathrm{nm} \tag{3.7}$$

where d and are the light intensity of the nm emission line of the pen-ray lamp and the irradiation time of the air volume, respectively. The absorption cross section of water vapour is denoted as ${}_{\mathrm{H_2O}}$ (${}_{\mathrm{H_2O}}$ nm cm (Cantrell et al., 1997; Creasey et al., 2000; Holland et al., 2003)) and the OH quantum yield from the water vapour photolysis, ${}_{\mathrm{OH}}$, is unity for nm (Chou et al., 1974; Atkinson et al., 2004).

For determining the value of the product of and , the simultaneous formation of ozone via the photolysis of oxygen molecules is used:

$$\mathrm{O_2} \quad \mathrm{h} \quad \mathrm{nm} \quad \mathrm{O}\ {}^{3}\mathrm{P} \quad \mathrm{O}\ {}^{3}\mathrm{P} \tag{R3.8}$$

$$\mathrm{O}\ {}^{3}\mathrm{P} \quad \mathrm{O_2} \quad \mathrm{O_3} \tag{R3.9}$$

Like in Eq. (3.7), the formed ozone concentration is dependent on the light intensity of the pen-ray lamp:

$$\mathrm{O_3} \quad \mathrm{O_2} \quad {}_{\mathrm{O_2}} \quad \mathrm{nm} \quad {}_{\mathrm{O_3}} \quad \mathrm{nm} \tag{3.10}$$

where the absorption cross section of O is given as an effective cross section ${}_{\mathrm{O_2}}$ ${}_{\mathrm{O_2}}$ d d which accounts for characteristic lines of the Schumann-Runge band that overlap with the spectral width of the nm emission line of the mercury lamp. For the calibration source used in this work, the effective O absorption cross section equals cm , which was determined in previous laboratory experiments (Holland et al., 2003). Since two oxygen atoms are formed in the photolysis of O (Reaction (R3.8)), the O quantum yield amounts to ${}_{\mathrm{O_3}}$ nm . By considering that the irradiation time is antiproportional to the volume flow rate of the humid synthetic air through the radical source, the ozone concentration can be expressed as:

$$\mathrm{O_3} \qquad \overline{} \tag{3.11}$$

such that the proportionality factor can be determined in a separate laboratory experiment by measuring the ozone concentration and the volume flow rate. Corresponding laboratory measurements were performed in this work.

For the calibration of the $\mathrm{HO_x}$ detection cell, CO (Air Liquide, % CO in N , purity > %) is added to the air flow such that the OH radical, formed in the photolysis of water vapour (Reaction (R3.6)) is converted to HO according to Reactions (R3.4) and (R3.5) leading to ${}_{\mathrm{HO_2}}$.

The calibration for peroxy radicals is performed with methyl peroxy radicals (CH O) which are produced by adding methane (Air Liquide, purity > %) to the air volume (Reactions (R1.1) and (R1.2) with R=CH). In the calibration with CH , an HO radical is still formed (Reactions (R3.6) and (R3.5)) such that the sum of HO and RO are measured in the CH calibration mode. Therefore, another calibration measurement of the system needs to be performed with CO addition to determine the sensitivity of the RO_x system for HO and thus the sensitivity for RO can be calculated.

Peroxy radicals which differ significantly in their reaction rate with NO or which alkoxy radicals do not form OH or HO in their unimolecular reaction can have different detection sensitivities than CH O . Examples are iso-butane, isoprene, as well as NO -containing RO , formed in the oxidation of isoprene and in the oxidation short-chain alkenes by NO (Fuchs et al., 2008; Novelli et al., 2021). The deviation of the detection sensitivity relative to CH O can be determined by zero-dimensional box model calculations of the specific RO reactions inside the RO_x detection system, considering the chemical conditions inside the converter and the RO_x detection cell.

3.2 Photooxidation of anthropogenic VOCs and the impact of the alkoxy chemistry on the ozone production

The content of this chapter was published as “Effect of the alkoxy radical chemistry on the ozone formation investigated for organic compounds from anthropogenic emissions in chamber experiments” by M. Färber, H. Fuchs, B. Bohn, P.M.T. Carlsson, G.I. Gkatzelis, A.C. Marcillo Lara, F. Rohrer, S. Wedel, A. Wahner, and A. Novelli in ACS Environmental Science & Technology Air 2024, **1**, 1096-1111 DOI: 10.1021/acsestair.4c00064, under the Creative Commons Attribution 4.0 License (https://creativecommons.org/licenses/by/4.0).

The supplementary material is provided in the Appendix A.2. Data from the experiments in this work are stored on servers at the Institute for Energy and Climate Research, IEK-8: Troposphere at Forschungszentrum Jülich and are accessible on request.

The authors contributed to the article as follows:

MF analysed the data, and wrote the manuscript together with AN. MF, AN, and HF conceptualised the manuscript. AN designed the experiments. MF and AN conducted the RO_x radical measurements and OH reactivity measurements. PMTC performed DOAS measurements and BB was responsible for the radiation measurements. FR performed measurements of NO_x, O_3, and HCHO. SW was together with GIG responsible for operating the PTR-ToF-MS instrument and together with ACML responsible for GC-MS measurements.

ACS ES&T Air

ACCESS | Metrics & More | Article Recommendations | Supporting Information

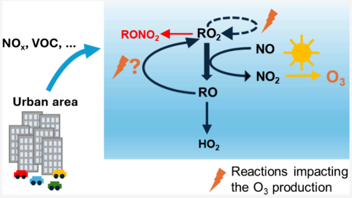

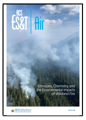

[illegible]

$$RO_2 + NO + M \rightarrow RONO_2 + M$$

$$OH + NO_2 + M \rightarrow HNO_3 + M$$

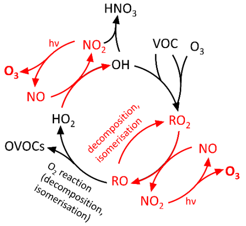

[illegible]

$$RO \rightarrow R^2 + R^3CHO$$

$$RO \rightarrow R^4$$

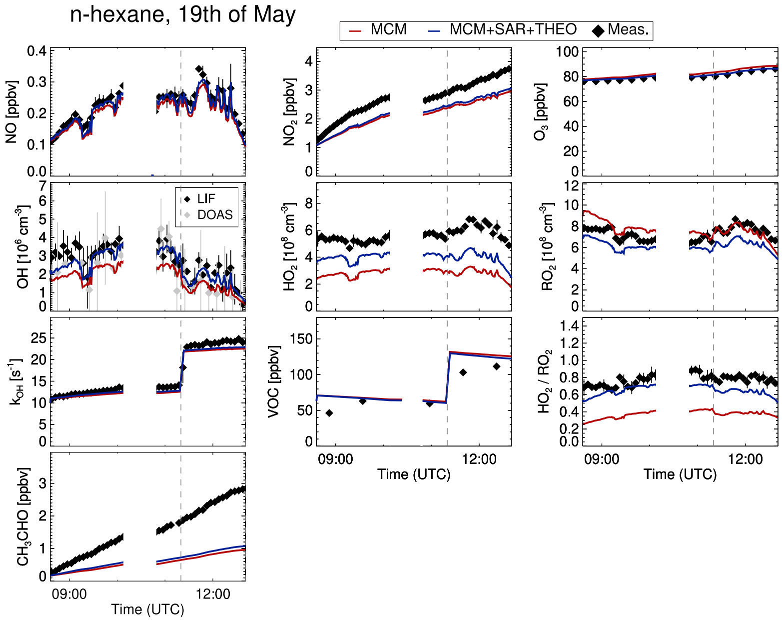

$$HO_2 + O_3 \rightarrow OH + 2O_2$$

$$h\nu + O_3 \rightarrow O(^1D) + O_2$$

$$\text{alkene} + O_3 \rightarrow \text{products}$$

$$\begin{aligned} P(O_x)_{\text{radical}} = {} & k_{RO_2+NO}[RO_2][NO](1 - f_{RONO_2}) \\ & + k_{HO_2+NO}[HO_2][NO] - k_{OH+NO_2} \\ & [OH][NO_2] - k_{HO_2+O_3}[HO_2][O_3] \\ & - f_{O(^1D)+H_2O}\, j_{O(^1D)}[O_3] - k_{O_3+\text{alkene}}[O_3] \\ & [\text{alkene}] \end{aligned}$$

$f_{O(^1D)+H_2O}$

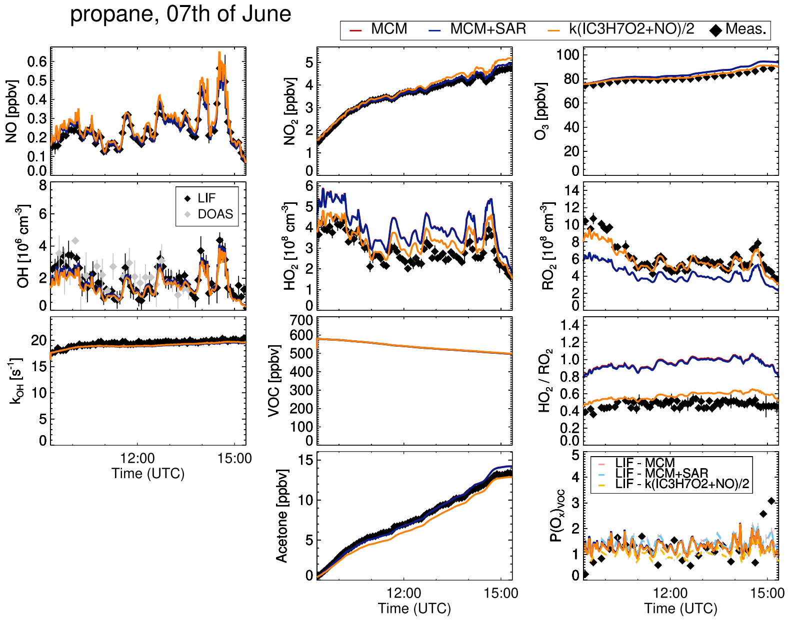

k_{HO_2+NO} $k_{HO_2+O_3}$ 2 k_{RO_2+NO}

$P(O_x)_{radical}$

$P(O_x)_{LIF}$ $P(O_x)_{model}$

$P(O_x)_{LIF}$

% 9 88

F

$$P(O_x)_{O_x} = \frac{d[O_x]}{dt} + k_{dilution}[O_x] + k_{wall}[O_x] \quad 8$$

79 8

$$L(OH + VOC) = (k_{OH} - k_{OH+NO_2}[NO_2] - k_{OH+NO}[NO])\cdot[OH] \quad 8-$$

% 9 8-

$P(O_x)_{VOC}$

$$P(O_x)_{VOC} = P(O_x)/L(OH + VOC) \quad 84$$

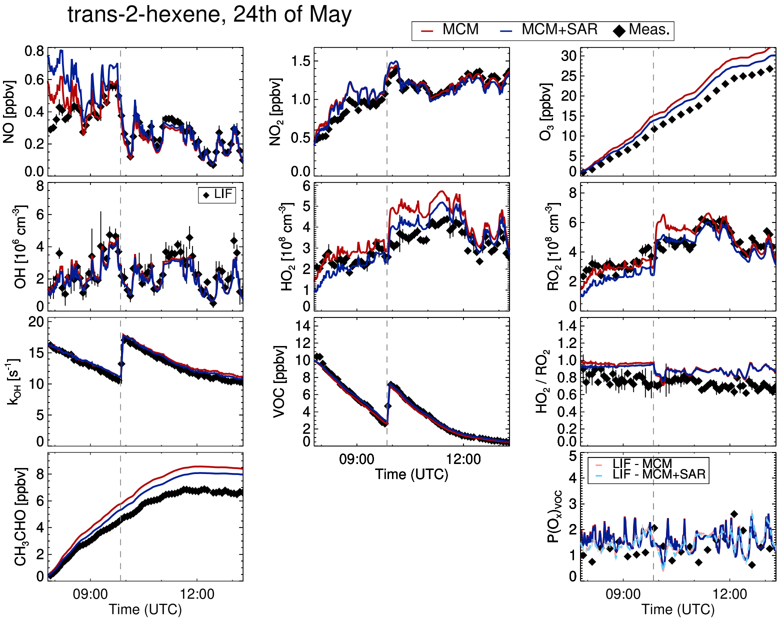
trans-2-hexene, 24th of May
MCM
MCM+SAR
Meas.
NO [ppbv]
0.0
0.2
0.4
0.6
0.8
NO$_2$ [ppbv]
0.0
0.5
1.0
1.5
O$_3$ [ppbv]
0
5
10
15
20
25
30
OH [10^6 cm^{-3}]
LIF
HO$_2$ [10^8 cm^{-3}]
RO$_2$ [10^8 cm^{-3}]
k$_{OH}$ [s^{-1}]
VOC [ppbv]
HO$_2$ / RO$_2$
CH$_3$CHO [ppbv]
P(O$_x$)$_{VOC}$
LIF - MCM
LIF - MCM+SAR
09:00
12:00
Time (UTC)

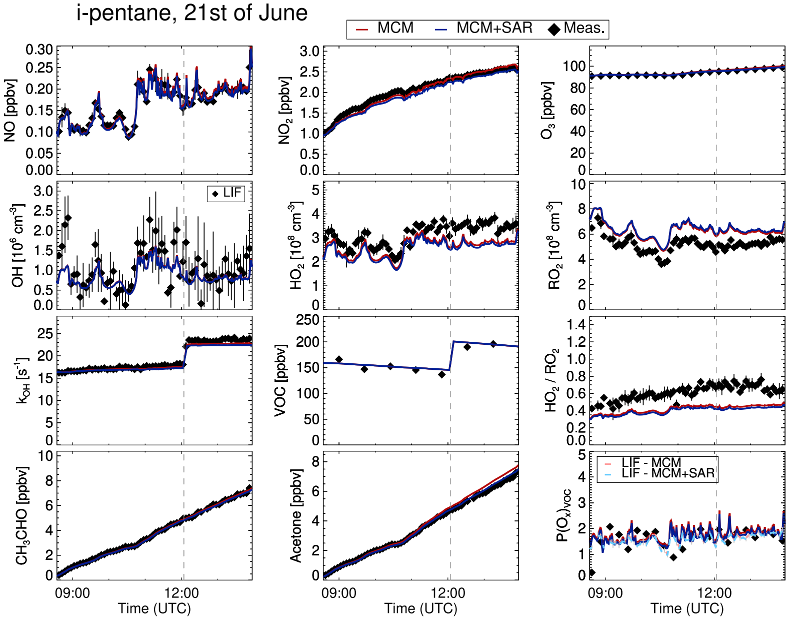

- ☒ 0 , L 8 8)
. ☒ B 6 , ☒

8 D, J ☒ 0 < 8 8. 4 8 8 8. @ 8
0☒ A @ 0☒ @
-☒ .☒ 8. 8 - 8 =☒ 8☒ ☒☒☒ ☒ ☒ 0
8. 8 - 8 0 , -☒ 0 ☒
☒☒ 7 @@ ☒ 0
☒ A @ 0 0 0 0 ☒
20 ☒☒ 0 + , + + , + 1☒☒1 ☒7
☒ @ 0 : . / ☒H
0 ☒@ 0 0
☒ 3 0 ☒☒ 8☒
☒, 0 9 : .
0 + , + 1☒☒1 ☒7 ☒
B ☒
6 , ☒☒ ☒ 8
8=/
☒ 4 ☒@
☒; ☒8. ☒☒ 0 0 0
. =/ 0 8☒ = 8☒
0 0
0 ☒ 4 ☒☒ 0 B 0 8☒ 0 + , + 1☒☒
1 ☒7 ☒%
I =. / 2 0 0 ☒ , ☒
, ☒ , ☒ , ☒ ☒ , ☒ + , + , ☒ , ☒ + , + F ☒7, , ☒ , ☒
F , @ ☒4 , ☒ , ☒ ☒ , ☒ , ☒ + , + , ☒ , ☒ , ☒ + , + F ☒7A
F, @ ☒ = ☒ 0 0
2 0 + , + + , + 1☒☒ ☒☒
8 8. @ 8 -☒ 8. D 8 0
D, J 0☒% (2 0 0
0 0 0
0 ☒ ☒

☒☒(6 ☒

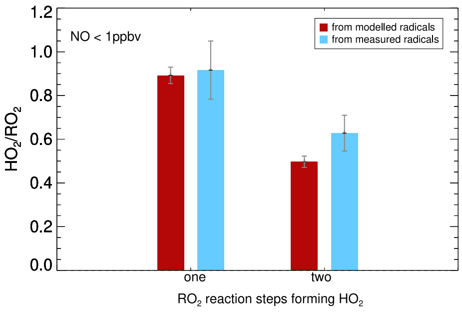

$P(\mathrm{O}_x)_{\mathrm{VOC}}$

$P(\mathrm{O}_x)_{\mathrm{VOC,LIF}}$

$P(\mathrm{O}_x)_{\mathrm{VOC,model}}$

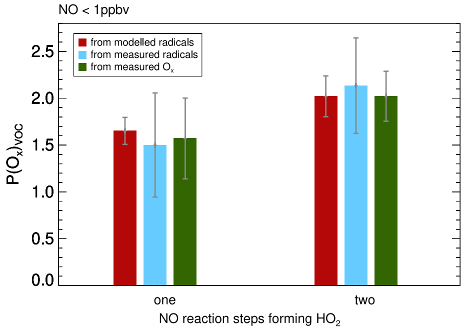

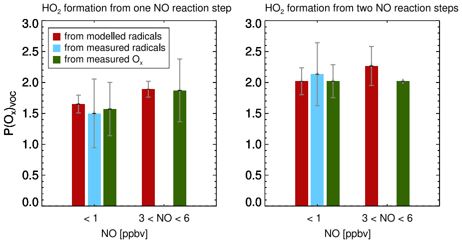

[illegible]

$P(O_x)_{VOC,LIF}$ $P(O_x)_{VOC,model}$

[illegible]

$$OH + X \rightarrow R^1O_2$$

$$R^1O_2 + NO \xrightarrow{k_{RO_2+NO}\times(1-f_{RONO_2})} R^1O + NO_2$$

$$R^1O \xrightarrow{k_{O_2}} HO_2 + R^{1'}CHO$$

$$R^1O \xrightarrow{k_{uni}} R^2O_2$$

$$R^2O_2 + NO \xrightarrow{k_{RO_2+NO}\times(1-f_{RONO_2})} R^2O + NO_2$$

$$R^2O \xrightarrow{k_{O_2}} HO_2 + R^{2'}CHO$$

k_{RO_2+NO}

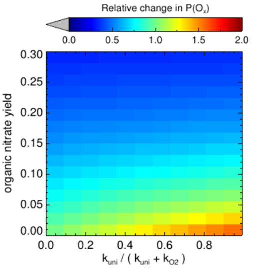

$P(\mathrm{O}_x)_{\mathrm{VOC,model}}$

$P(\mathrm{O}_x)_{\mathrm{VOC,LIF}}$

3.3 Nighttime oxidation chemistry of anthropogenic VOCs and the role of the formation of alkyl peroxynitrates

The content of this chapter was published as “Impact of temperature-dependent non-PAN peroxynitrate formation, RO_2NO_2, on nighttime atmospheric chemistry” by M. Färber, L. Vereecken, H. Fuchs, G.I. Gkatzelis, F. Rohrer, S. Wedel, A. Wahner, and A. Novelli in Physical Chemistry Chemical Physics, 2024, **26**, 5183 DOI: 10.1039/d3cp04163h, under the Creative Commons Attribution 3.0 License (https://creativecommons.org/licenses/by/3.0).
The supplementary material is provided in the Appendix A.3. Data from the experiments in this work are available on the EUROCHAMP data homepage (https://data.eurochamp.org/). Detailed information is provided in the publication.
The authors contributed to the article as follows:
MF analysed the data and wrote the paper. AN and LV designed the experiments and worked closely with MF to conceptualise the paper. MF and AN conducted the RO_x radical measurements and OH reactivity measurements. FR performed measurements of NO_x and O_3. SW and GIG were responsible for operating the PTR-ToF-MS instrument. All co-authors commented on the paper.

PCCP

CORRECTION

View Article Online
View Journal | View Issue

Cite this: *Phys. Chem. Chem. Phys.*, 2024, **26**, 7239

Correction: Impact of temperature-dependent non-PAN peroxynitrate formation, RO_2NO_2, on nighttime atmospheric chemistry

Michelle Färber,[a] Luc Vereecken,[a] Hendrik Fuchs,[ab] Georgios I. Gkatzelis,[a] Franz Rohrer,[a] Sergej Wedel,[a] Andreas Wahner[a] and Anna Novelli*[a]

DOI: 10.1039/d4cp90031f

rsc.li/pccp

Correction for 'Impact of temperature-dependent non-PAN peroxynitrate formation, RO_2NO_2, on nighttime atmospheric chemistry' by Michelle Färber *et al.*, *Phys. Chem. Chem. Phys.*, 2024, **https://doi.org/10.1039/d3cp04163h**.

In the Abstract, 'radicals of up to 2×10 cm^{-3} are predicted at 276 K' should read 'radicals of up to 2×10^{10} cm^{-3} are predicted at 276 K'.

The captions to Fig. 2 and 3 should say:

Model results displayed as FZJ (blue) and FZJ + RO_2NO_2 (brown) models refer to the FZJ mechanism without and with including additional formation of non-acyl RO_2NO_2, respectively.

Throughout the text all characters in the expressions using the MCM notation should be inline.

In several places in the text $CH_3CH(NO_3)CH(CH_3)O$ was incorrectly written as CH_3 $CH(NO_3)CH(CH_3)O$.

In the Summary & conclusions section, the text 'Under the conditions of the experiments in this work, up to 2×10 cm^{-3} of non-acyl RO_2NO_2 are expected at 276 K' should read 'Under the conditions of the experiments in this work, up to 2×10^{10} cm^{-3} of non-acyl RO_2NO_2 are expected at 276 K'.

In the Data availability section the link to the data from the nighttime experiment of *trans*-2-hexene in the presence of NO_2 and CH_4 should be **https://doi.org/10.25326/DSQH-4X71**.

The Royal Society of Chemistry apologises for these errors and any consequent inconvenience to authors and readers.

---

[a] *Institute for Energy and Climate Research, IEK-8: Troposphere, Forschungszentrum Jülich GmbH, 52428 Jülich, Germany. E-mail: m.faerber@fz-juelich.de, a.novelli@fz-juelich.de*

[b] *Department of Physics, University of Cologne, 50932 Cologne, Germany*

PCCP

PAPER

View Article Online
View Journal | View Issue

Check for updates

Impact of temperature-dependent non-PAN peroxynitrate formation, RO_2NO_2, on nighttime atmospheric chemistry†‡

Michelle Färber,[a] Luc Vereecken,[a] Hendrik Fuchs,[ab] Georgios I. Gkatzelis,[a] Franz Rohrer,[a] Sergej Wedel,[a] Andreas Wahner[a] and Anna Novelli*[a]

The formation of peroxynitrates (RO_2NO_2) from the reaction of peroxy radicals (RO_2) and nitrogen dioxide (NO_2) and their subsequent redissociation are typically not included in chemical mechanisms. This is often done to save computational time as the assumption is that the equilibrium is strongly towards the RO_2 + NO_2 reaction for most conditions. Exceptions are the reactions of the methyl peroxy radical due to its abundance in the atmosphere and of acyl-RO_2 radicals due to the long lifetime of peroxyacyl nitrates RO_2NO_2 (PANs). In this study, the nighttime oxidation of *cis*-2-butene and *trans*-2-hexene in the presence of NO_2 is investigated in the atmospheric simulation chamber SAPHIR, Forschungszentrum Jülich, Germany, at atmospherically-relevant conditions at different temperatures ($\approx$276 K, $\approx$293 K, $\approx$305 K). Measured concentrations of peroxy and hydroperoxy radicals as well as other trace gases (ozone, NO_2, volatile organic compounds) are compared to state-of-the-art zero-dimensional box model calculations. Good model-measurement agreement can only be achieved when reversible RO_2 + NO_2 reactions are included for all RO_2 species using literature values available from the latest SAR by [Jenkin *et al.*, *Atmos. Chem. Phys.*, 2019, **19**, 7691]. The good agreement observed gives confidence that the SAR, derived originally for aliphatic RO_2, can be applied to a large range of substituted RO_2 radicals, simplifying generalised implementation in chemical models. RO_2NO_2 concentrations from non-acyl RO_2 radicals of up to $2 \times 10\ cm^{-3}$ are predicted at 276 K, impacting effectively the kinetics of RO_2 radicals. Under these conditions, peroxy radicals are slowly regenerated downwind of the pollution source and may be lost in the atmosphere through deposition of RO_2NO_2. Based on this study, 60% of RO_2 radicals would be stored as RO_2NO_2 at a temperature of 10 °C and in the presence of a few ppbv of NO_2. The fraction increases further at colder temperatures and/or higher NO_2 mixing ratios. This does not only affect the expected concentrations of RO_2 radicals but, as the peroxynitrates can react with OH radicals or photolyse, they could comprise a net sink for RO_2 radicals as well as increase the production of NO_x (= NO + NO_2) in different locations depending on their lifetime. Omitting this chemistry from the kinetic model can lead to misinterpreted product formation and may prevent reconciling observations and model predictions.

Received 29th August 2023,
Accepted 16th January 2024

DOI: 10.1039/d3cp04163h

rsc.li/pccp

1 Introduction

In the atmosphere, volatile organic compounds (VOCs) and volatile inorganic compounds are removed *via* oxidation which drives their chemical degradation. In the lower troposphere, the daytime oxidation processes are driven by ozone (O_3), and the hydroxyl radical (OH), which is often found to be the predominant oxidant. Another tropospheric oxidant is the nitrate radical (NO_3) which plays a major role during the night.[1] NO_3 is formed by the reaction of nitrogen dioxide (NO_2) with O_3:

$$NO_2 + O_3 \rightarrow NO_3 + O_2, \qquad (1)$$

---

[a] *Institute for Energy and Climate Research, IEK-8: Troposphere, Forschungszentrum Jülich GmbH, 52428 Jülich, Germany. E-mail: m.faerber@fz-juelich.de, a.novelli@fz-juelich.de*

[b] *Department of Physics, University of Cologne, 50932 Cologne, Germany*

† The data of the experiments in the SAPHIR chamber used in this work are available on the EUROCHAMP data home page (https://data.eurochamp.org/). More information can be found in the Data availability statement.

‡ Electronic supplementary information (ESI) available: The supplement related to this article is available online, and contains detailed information about the ozonolysis experiment of *trans*-2-hexene, the NO_3 interference of the radical instrument, the modified alkoxy decomposition rate used for *cis*-2-butene-RO, instrumentation details, contributions of NO_3 and O_3 to the VOC oxidation, the time series of measured acetaldehyde concentrations, and the discussion of the nighttime oxidation of trans-2-hexene at medium and hot temperatures. See DOI: https://doi.org/10.1039/d3cp04163h

and is typically in a rapid thermal equilibrium with dinitrogen pentoxide (N_2O_5). The fast photolysis of NO_3 back to NO_2 and O_3 and its loss reaction with nitric oxide (NO) lead to an atmospheric lifetime of a few seconds,[2] preventing substantial daytime concentrations. Still, in forests below the canopy (high VOC concentrations, low NO concentrations (< 0.3 ppbv), among other favourable conditions), the reaction of NO_3 with VOCs might compete with other loss reactions of NO_3 (photolysis, reaction with NO) and contributes to the tropospheric oxidation during the day.[2–4] At night, when there is no OH production from photolytic processes, the oxidation of VOCs is driven by O_3 and NO_3.

In recent field studies utilising the laser-induced-fluorescence (LIF) technique for radical measurements, discrepancies between measured and modelled RO_2 radical concentrations were found at night at moderate O_3 ($\sim$(1–70) ppbv), NO_2 ($\sim$(3–50) ppbv), and low NO ($\sim$(0–0.3) ppbv) mixing ratios in the vicinity of Beijing,[5,6] China, Wangdu,[7] China, and London,[8] UK. Just recently, two studies focussing on investigating the oxidation of isoprene[9] and anthropogenic alkenes[10] by NO_3 resulted in new detailed chemical mechanisms for these compounds as intricate as their oxidation by OH. These studies highlighted the inability of detecting a large fraction of NO_3 -containing isoprene-RO_2[9] as well as NO_3–RO_2 from short-chain alkenes.[10] Both the isomerisation (isoprene)[9] and the decomposition (short-chain alkenes)[10] of the NO_3 -alkoxy radical do not lead to the formation of HO_2 or OH, which is required for the RO_2 measurement by the LIF technique:

$$NO_3 - RO_2 + NO \overset{-NO_2}{\rightarrow} RO \begin{cases} \rightarrow NO_2\ (\text{notdetectable}), \\ \nrightarrow HO_2\ (\text{detectable}). \end{cases} \quad (2)$$

However, for long-chain alkenes such as for example *trans*-2-hexene, all RO_2 are detectable.[10] The discrepancies found at nighttime in the field[5–8] may be partly explainable by the missing detection of the LIF instrument of single short-chain alkenes, contained in the measured air mixture. Still large discrepancies remain between measured and modelled RO_2 radicals for high NO (up to $\sim$100 ppbv) and NO_2 (up to $\sim$70 ppbv).[5–8,11]

Despite improvements in the agreement between measured and modelled RO_2 radicals observed in the experiments in the SAPHIR chamber,[10] discrepancies are still observed in particular right after the injection of the VOC when the RO_2 radical production is the highest, as well as in the time dependence of the RO_2 radical concentrations. The conditions in the chamber were chosen to facilitate the formation of NO_3 radicals, and were characterised by zero NO and medium NO_2 (17–40 ppbv) and ozone (7–30 ppbv). For these conditions, RO_2 radicals formed in the oxidation by either O_3 or NO_3 are assumed to be mainly lost by their reaction with HO_2 or RO_2. NO_2 will be the dominant reaction partner for these RO_2 radicals, producing a short-lived peroxynitrate (RO_2NO_2) which is in a very fast equilibrium ($\tau_{RO_2NO_2} \approx 0.2$ s at 298 K) with its decomposition in the lower troposphere:

$$RO_2 + NO_2(+M) \underset{k_{RO_2NO_2}}{\overset{k_{RO_2+NO_2}}{\rightleftharpoons}} RO_2NO_2(+M). \quad (3)$$

The impact of eqn (3) on the RO_2 radical and the formed RO_2NO_2 is thought to be negligible due to the instability of RO_2NO_2 in lower tropospheric oxidation processes, therefore, the reaction of RO_2 and NO_2 forming RO_2NO_2 is omitted in most atmospheric models for non-acyl RO_2 radicals except for CH_3O_2.[12] For the latter, the formation of alkyl peroxynitrates has been thought to be mostly relevant at cold temperatures in polar regions,[13,14] in the upper troposphere, where Browne *et al.*[14] found that including the methyl peroxynitrate ($CH_3O_2NO_2$) chemistry is relevant at temperatures below 240 K, or in biomass burning plumes that are lofted to high altitudes.[14] In contrast, the reactions of acyl-RO_2 radicals with NO_2 are typically implemented in all chemical models due to the long lifetime ($\sim$40–45 min at 298 K) of the corresponding peroxyacyl nitrate RO_2NO_2 (PANs) and, consequently, their relevance on regional and even global scales.[13]

A recent study by Khan *et al.*[15] investigated the global effect of the reversible formation of RO_2NO_2 on NO_x, *i.e.* NO + NO_2, OH, and O_3, using the generic rate coefficients from Jenkin *et al.*[12] for more than 40 non-acyl RO_2 radicals. Loss rates for the formed RO_2NO_2 species *via* reaction of OH and photolysis were also included. In their study, it was shown that even on the ground, up to 25% more NO_x would be expected at the equator as photolysis and reaction with OH accelerate the consumption of RO_2NO_2. This indicates that their role and importance might need to be reevaluated.

A measure for the ratio of RO_2 and RO_2NO_2 concentrations at equilibrium is given by the equilibrium constant K, the ratio of the forward and backward reaction rate constants $k_{RO_2+NO_2}$ and $k_{RO_2NO_2}$, respectively:

$$K = k_{RO_2+NO_2}/k_{RO_2NO_2}. \quad (4)$$

For the alkyl peroxynitrates $CH_3O_2NO_2$ and ethyl peroxynitrate ($C_2H_5O_2NO_2$), the equilibrium constant is 7×10^{-11} cm^3 at 276 K, respectively (Table 1). In contrast, peroxyacetyl nitrate ($CH_3C(O)O_2$) has an equilibrium constant of 1×10^{-8} cm^3 due to its longer lifetime. While at high temperatures formation of alkyl peroxynitrates is not important, the equilibrium shifts more towards the RO_2NO_2 products at lower temperatures, making it worthwhile to evaluate the impact of RO_2NO_2 formation during winter conditions.

In this work, the impact of the RO_2 + NO_2 reaction on modelled RO_2 radical concentrations is studied for RO_2 radicals from the oxidation of *cis*-2-butene and *trans*-2-hexene by O_3 and NO_3 at different temperatures ($\approx$276 K, $\approx$293 K, $\approx$305 K). Experiments were performed in the atmospheric simulation chamber SAPHIR at Forschungszentrum Jülich, Germany. Nighttime conditions with high NO_2 ($>$20 ppbv) and moderate O_3 ($\sim$10 ppbv) mixing ratios were tested which facilitate the formation of NO_3 and mimic conditions often found at night. Concentrations of HO_2 and RO_2 radicals, as well as of O_3,

Table 1 Temperature-dependent rate coefficients for the formation and decomposition of different alkyl peroxynitrates, adopted from Jenkin *et al.*[12] Rate coefficients are given for ambient pressure (1013 hPa) and T = 276 K, 292 K, and 305 K

RO_2 or RO_2NO_2	k_0	k_∞	F_c	$k_{276\,K}$	$k_{292\,K,1\,atm}$	$k_{305\,K,1\,atm}$
Forward reaction, $k_{RO_2+NO_2}$ [$cm^3\ s^{-1}$]						
CH_3O_2[a]	$1.2 \times 10^{-30}\ (T/300)^{-6.9}[M]$	1.8×10^{-11}	0.36	7.1×10^{-12}	6.2×10^{-12}	5.5×10^{-12}
$C_2H_5O_2$[a]	$1.3 \times 10^{-29}\ (T/300)^{-6.2}\ [M]$	8.8×10^{-12}	0.31	5.6×10^{-12}	5.3×10^{-12}	5.0×10^{-12}
n- and *sec*- $C_4H_9O_2$[b]		9.6×10^{-12}		9.6×10^{-12}	9.6×10^{-12}	9.6×10^{-12}
RO_2[d]		9.0×10^{-12} (=k_{fPN})		9.0×10^{-12}	9.0×10^{-12}	9.0×10^{-12}
Reverse reaction, $k_{RO_2NO_2}$ [s^{-1}]						
$CH_3O_2NO_2$[a]	$9.0 \times 10^{-5}\exp(-9690/T)[M]$	$1.1 \times 10^{16}\exp(-10\,560/T)$	0.36	0.1	0.7	3.2
$C_2H_5O_2NO_2$[a]	$4.8 \times 10^{-4}\exp(-9285/T)[M]$	$8.8 \times 10^{15}\exp(-10\,440/T)$	0.31	0.2	1.7	7.5
n- and *sec*- $C_4H_9O_2NO_2$ *b*		$8.3 \times 10^{15}\exp(-10\,368/T)$		0.4	3.2	14.3
$C_6H_{13}O_2NO_2$ isomers[c]		$7.5 \times 10^{15}\exp(-10\,368/T)$		0.4	2.8	12.9
RO_2NO_2[d]		$7.6 \times 10^{15}\exp(-10\,400/T)$(=$k_{bPN}$)		0.3	2.6	11.8

[a] Recommended by IUPAC.[16] [b] Determined from isomeric mixtures formed from the reaction of chlorine with butane[17,18] and recommended by Jenkin *et al.*[12] [c] Determined from isomeric mixtures formed from the reaction of chlorine with hexane[18] and recommended by Jenkin *et al.*[12] [d] Pressure-independent generic rate coefficient recommended by Jenkin *et al.*[12]

NO_2, and VOCs were measured and are compared to zero-dimensional box model calculations, incorporating state-of-the-art oxidation schemes. The reaction of non-acyl RO_2 radicals with NO_2 forming RO_2NO_2 and its backward reaction are implemented in the chemical mechanisms of *cis*-2-butene and *trans*-2-hexene by using literature values,[12,16–18] and the implications of the findings on the nighttime atmospheric RO_2 chemistry are discussed. The newly introduced ozonolysis scheme and RO_2 isomerisation reactions, suggested by Novelli *et al.*[10] for *cis*-2-butene and *trans*-2-hexene, as well as their temperature dependence are tested and model-measurement comparisons are used to improve the chemical mechanisms for these species.

2 Methodology

2.1 Experiments in the atmospheric simulation chamber SAPHIR

The experiments were conducted in the outdoor atmospheric simulation chamber SAPHIR at Forschungszentrum Jülich, Germany. The 270 m^3 chamber (5 m diameter, 18 m length) allows to study atmospheric processes in a well-characterised system and is confined by an inert double-wall Teflon (FEP) film, enabling high transmittance of impinging solar radiation. A shutter system allows the shielding of the chamber from solar radiation to also mimic nighttime conditions. The temperature inside the chamber is not controlled and thus dependent on ambient conditions. The chamber utilises ultra-pure synthetic air, mixed from ultra-pure nitrogen and oxygen (79.1% N_2, 20.9% O_2, Linde, purity > 99.9999%). Contaminations are prevented from entering the chamber by an over-pressure of ≈33 Pa above ambient pressure. A replenishment flow is applied to account for small leakages and the air sampled by the instruments, causing a dilution for all trace gases with an average first order loss rate of $9.7 \times 10^{-6}\ s^{-1}$ in the experiments in this study. Two fans are installed to mix the air in the chamber, so that all instruments sample the same air. A detailed description of SAPHIR can be found in previous works.[19–22]

Nighttime experiments for *cis*-2-butene and *trans*-2-hexene were performed at different temperatures. The nighttime oxidation of *cis*-2-butene was studied at two different temperatures ($T \approx$ 276 K (cold), 295 K (medium)). The nighttime chemistry of *trans*-2-hexene was investigated at three temperatures ($T \approx$ 276 K (cold), 292 K (medium), 305 K (hot)). At low temperatures ($T \approx$ 280 K), a pure ozonolysis experiment in the absence of NO_2 was also performed for *trans*-2-hexene.

The experimental procedure of the experiments is shown in Fig. 1–3. Before each experiment, the chamber was flushed to remove trace gases from the previous experiment. No detectable OH reactivity, equivalent to the inverse lifetime of OH, was observed in the dark, clean, and dry chamber. *Cis*-2-Butene (Air Liquide, 1% in N_2, purity 99.4%) or *trans*-2-hexene (Sigma Aldrich, purity 97%) were first injected in the clean, dry, and dark chamber, reaching mixing ratios close to atmospheric conditions (<6 ppbv). Afterwards, 170–210 ppmv of carbon monoxide (CO, Air Liquide, purity 99.997%) was added to the chamber acting as OH scavenger by converting OH into HO_2 to avoid its reaction with *cis*-2-butene or *trans*-2-hexene. In one oxidation experiment of *trans*-2-hexene, 142 ppmv of methane (CH_4, Air Liquide, purity 99.5%) were injected instead to aim for lower HO_2 radical concentrations. Since more reactions are involved to form HO_2, a slower production of HO_2 can be achieved, and higher RO_2 radical concentrations are expected due to the formation of CH_3O_2. Nitrogen dioxide (Linde, 500 ppmv in N_2, purity 99.991%) of up to 35 ppbv was then injected in all experiments with the exception of the ozonolysis study. Afterwards, ozone generated by a silent discharge ozoniser (O3onia) was injected to reach mixing ratios between 12 ppbv and 33 ppbv (96 ppbv in the ozonolysis experiment), initiating the production of NO_3 in the reaction with NO_2 (eqn (1)). Due to the fast reaction of *cis*-2-butene and *trans*-2-hexene with O_3 and NO_3, they are consumed on a timescale of ~2–5 hours, and the alkene was injected a second time and third time (experiments with *cis*-2-butene at 295 K and

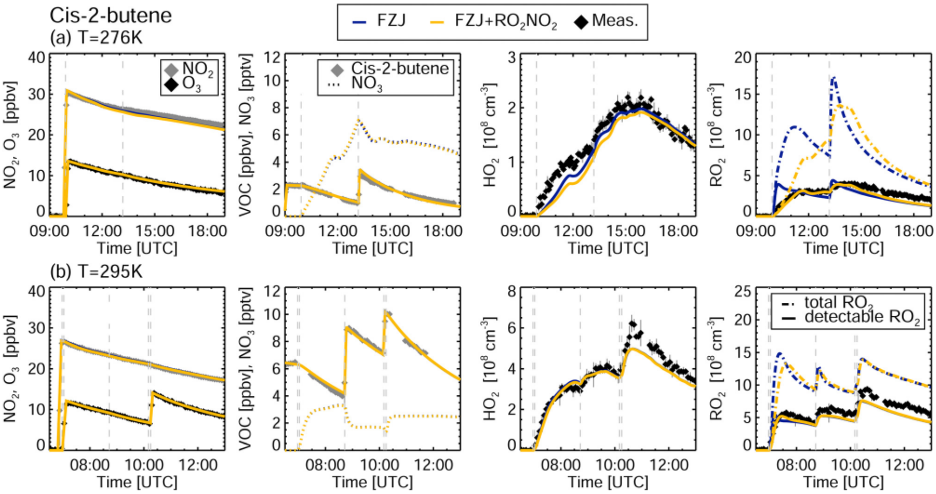

Fig. 1 Comparison of modelled and measured (5 minutes average) trace gases and HO_2 and RO_2 radicals in the experiment with *cis*-2-butene for cold (276 K) and medium (295 K) temperatures. Model results displayed as FZJ (blue) and FZJ + RO_2NO_2 (brown) models refer to the FZJ mechanism without and with including additional formation of non-acyl RO_2NO_2, respectively. Dashed lines indicate the total RO_2 radical concentration predicted by the model, while solid lines are the RO_2 radical concentration predicted to be detectable by the RO_x LIF system, as discussed in Section 2.2. Injections of chemical species into the chamber are marked by vertical lines.

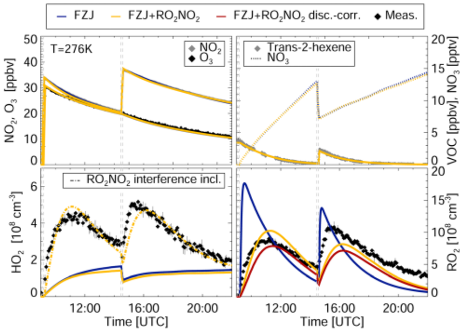

Fig. 2 Comparison between modelled and measured (5 minutes average) trace gases and HO_2 and RO_2 radical concentrations in the *trans*-2-hexene experiment performed at ≈276 K with CO as OH scavenger. Model results displayed as FZJ (blue) and FZJ + RO_2NO_2 (brown) models refer to the FZJ mechanism with and without including additional formation of non-acyl RO_2NO_2, respectively. In addition, FZJ + RO_2NO_2 disc.-corr. (red) denotes the model run considering the overestimation of ozonolysis-generated RO_2 radical concentrations by a factor of 1.7, observed in the ozonolysis of *trans*-2-hexene (see text). Injections of chemical species into the chamber are marked by vertical lines.

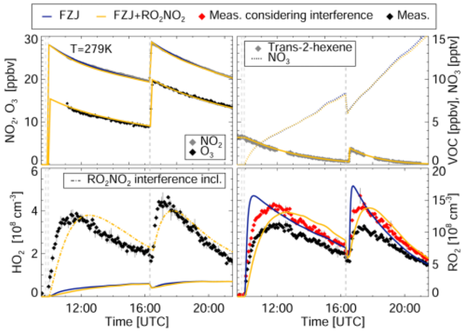

Fig. 3 Comparison between modelled and measured (5 minutes average) trace gases and HO_2 and RO_2 radical concentrations in the nighttime oxidation experiment of *trans*-2-hexene in presence of CH_4. Model results displayed as FZJ (blue) and FZJ + RO_2NO_2 (brown) models refer to the FZJ mechanism with and without including additional formation of non-acyl RO_2NO_2, respectively. Solid lines indicate the total RO_2 radical concentration predicted by the model without the RO_2NO_2 interference, while dashed lines are the RO_2 radical concentration predicted by the model considering a 2% interference by RO_2NO_2. Injections of chemical species into the chamber are marked by vertical lines.

trans-2-hexene at 305 K). To boost the oxidation by NO_3, NO_2 was injected a second time as well. In all experiments, no NO was present in the chamber and OH radical concentrations were below the detection limit, leading to a negligible contribution of OH chemistry. All experiments were conducted in dry conditions (H_2O < 0.07 ppmv) and in complete darkness.

2.2 Instrumentation

Measurements of the radicals OH, HO_2, and RO_2 were conducted with a laser-induced fluorescence (LIF) instrument (RO_x LIF).[23,24] Chamber air is sucked into a low-pressure detection cell ($\approx$ 4 hPa) where OH radicals are excited by a laser pulse (repetition frequency = 8.5 kHz) at a wavelength of 308 nm. The subsequently emitted fluorescence light, which is directly proportional to the sampled OH radical concentration, is detected by gated photon counting.[25–27] By adding NO in a second detection cell, a fraction of HO_2 radicals is chemically converted to OH and, thus, HO_x (= OH + f HO_2, $f < 1$) can be detected.[24–26,28] Possible interferences in the HO_x measurement may appear in the presence of specific RO_2 radicals, when HO_2 is rapidly produced by the RO_2 + NO reaction.[28] By working at lower NO concentrations, RO_2 interferences are minimised and do not play a role in the presented experiments. RO_2 radicals are indirectly measured after they are converted into HO_2 or OH in a converter ($\approx$25 hPa) by adding NO. OH, formed from the reaction of HO_2 with NO, is converted back to HO_2 in the converter by addition of excess CO. The HO_2 radicals are then sampled by a detection cell and converted to OH by a continuous addition of pure NO, which enables a high conversion efficiency of HO_2,[23] so that the sum of OH, HO_2, and RO_2 (=RO_x) is measured, from which [RO_2] can be derived. An interference signal in the presence of NO_3 that is equivalent to a RO_2 radical concentration of 3.6×10^6 cm^{-3} per pptv of NO_3 was observed in the RO_x system. A previous study[29] also reported a NO_3 interference signal equivalent to HO_2 and RO_2 radical concentrations of 1.0×10^6 cm^{-3} and 1.7×10^6 cm^{-3} per pptv of NO_3, respectively. More details can be found in the ESI‡ Section B. Modelled RO_2 radical concentrations were corrected for this interference which only impacted the experiment at highest temperature when very high concentrations of NO_3 were reached. Modelled HO_2 radical concentrations were corrected using the parametrisation determined by Fuchs *et al.*[29] Recently, it was found that -nitrate-alkoxy radicals decompose in the converter of the RO_2 detection system forming NO_2 and therefore these radicals are not detectable with the LIF technique that requires the formation of either OH or HO_2 in the detection system.[9,10] Examples include alkoxy radicals (RO) produced in the oxidation of anthropogenic alkenes by NO_3 such as CH_3 $CH(NO_3)CH(CH_3)O$ (MCM notation: $C_{42}NO_{33}O$) formed in the oxidation of *cis*-2-butene by NO_3. The rate coefficient of the decomposition of CH_3 $CH(NO_3)CH(CH_3)O$ (MCM notation: $C_{42}NO_{33}O$), forming NO_2, was optimised based on the observed RO_2 in the experiments of the nighttime oxidation of *cis*-2-butene, resulting in a decomposition rate of 3.0×10^3 s^{-1} (this work) compared to 9.5×10^3 s^{-1} predicted theoretically[10] at 276 K. Further details can be found in the ESI‡ Section C.

The OH reactivity (k_{OH}) was measured by a pump-and-probe technique utilising LIF to detect the amount of OH reacting with the sampled air in a flow tube.[30,31] Time series of *cis*-2-butene and *trans*-2-hexene and calibrated time series of acetaldehyde were measured by proton-transfer-reaction time-of-flight mass spectrometry (PTR-ToF-MS, Ionicon).[32,33] Normalised counts of *cis*-2-butene and *trans*-2-hexene are converted to parts per billion (ppb) by using the observed OH reactivity at the point in time of the VOC injection. Ozone was detected by UV absorption (Ansyco), and CO, CH_4, formaldehyde, and water vapour were monitored utilising cavity ring-down spectroscopy (CRDS, Picarro). Furthermore, NO and NO_2 were measured by a chemiluminescence instrument (EcoPhysics). More detailed information about the performance of the instruments can be found in the ESI‡ Section D. NO_3 and N_2O_5 measurements were not available for any experiment, therefore corresponding wall loss rates were introduced and adjusted to match the observed VOC decay.

2.3 Model calculations

To compare measurements with model results, a zero-dimensional box model is used, starting from the chemical mechanistic information in the FZJ mechanisms for *cis*-2-butene and *trans*-2-hexene published by Novelli *et al.*[10]; these are themselves built upon the Master Chemical Mechanism (MCM v3.3.1, http://mcm.leeds.ac.uk).[34,35] Dilution is taken into account by considering a first-order loss for all implemented species as described in Section 2.1. Temperature and pressure are constrained to measured data. The injection of O_3, NO_2, *cis*-2-butene, *trans*-2-hexene, CO, and CH_4 into the chamber is reproduced by an active source during the injection period, with a source strength that is matched to the measured increase of the observables. The temperature-dependent reaction rate of *trans*-2-hexene with O_3 is taken from Atkinson and Arey.[1] At medium and high temperatures, the reaction rate of *trans*-2-hexene and NO_3 is taken to be twice as large as the temperature-independent reaction rate used in the MCM; the latter is estimated from the SAR in Jenkin *et al.*[34] The increased rate is consistent with the study by Novelli *et al.*[10] The FZJ mechanisms for *cis*-2-butene and *trans*-2-hexene used here as the base kinetic models differ from the MCM by the following points:

- Ozonolysis scheme for *cis*-2-butene and *trans*-2-hexene including the formation of $O{=}CHCH_2OO^\bullet$ (ethanal-2-peroxy, MCM notation: $HCOCH_2O_2$) and $O{=}CHCHO(OO^\bullet)CH_2CH_3$ (butanal-2-peroxy, MCM notation: BUTALAO2). The subsequent bimolecular chemistry for these radicals follows the MCM.
- Isomerisation reactions for ethanal-2-peroxy and butanal-2-peroxy based on quantum chemical calculations, leading to the formation of $O{=}C(OOH)CH_2OO^\bullet$ (ethyl-1-peracid-2-peroxy) and $O{=}C(OOH)CH(OO^\bullet)C_2H_5$ (butyl-1-peracid-2-peroxy), respectively (Fig. S1, ESI‡).
- Updated alkoxy decomposition rates for RO radicals formed in the oxidation of *cis*-2-butene and *trans*-2-hexene by NO_3 based on quantum chemical calculations.
- Optimised yield of the RO and OH radical from the reaction of RO_2 with HO_2 for the first generation NO_3–RO_2 (MCM notation: $C_{62}NO_{33}O_2$, $C_{63}NO_{32}O_2$) formed in the oxidation of *trans*-2-hexene by NO_3.

The follow-up chemistry for additionally included RO_2 and RO radicals was implemented following the SARs in Jenkin *et al.*,[12] Vereecken *et al.*,[10,36–38] and Novelli *et al.*[10] For the model-measurement comparison when NO_3 chemistry is contributing, the fraction of RO_2 which is not measurable by the radical instrument[10] (Section 2.2) must be taken into account, *i.e.* distinguishing between "total RO_2" and "detectable RO_2".

The effect of the isomerisation reactions of the RO_2 radicals from the ozonolysis reaction, ethanal-2-peroxy and butanal-2-peroxy, on the predicted RO_2 speciation is investigated by comparing model runs using the FZJ mechanisms with and without including RO_2 isomerisation reactions. In another sensitivity model run, not only reactions of methyl peroxy (CH_3O_2) and PAN-like RO_2 ($RC({=}O)OO^\bullet$) with NO_2 are included, as implemented in the FZJ mechanism, but also the reaction of NO_2 with all formed non-acyl RO_2 species. In this sensitivity run, $RO_2 + NO_2$ reactions forming RO_2NO_2 as well as the corresponding backward reactions (eqn (3)) are introduced for all formed RO_2 species. Rate constants for the forward and backward reactions for CH_3O_2, ethyl peroxy ($C_2H_5O_2$), and acetonyl peroxy ($CH_3\,C({=}O)CH_2O_2$) are taken from recommendations by IUPAC.[16] Recommendations in Jenkin *et al.*,[12] partially based on Zabel *et al.*,[18] are used for the forward and backward reaction rate constants for C_4 peroxy radicals, and for the backward reaction rate constant for C_6–RO_2NO_2 in this work. For all RO_2 for which rate constants cannot be taken from literature, such as for n-$C_3H_7O_2$, a pressure-independent generic forward reaction rate constant, k_{fPN}, and a rounded average of reported backward reaction rate constants for C_2 to C_8 alkyl RO_2, k_{bPN}, recommended by Jenkin *et al.*,[12] are used. However, the contribution of n-$C_3H_7O_2$ to the total RO_2 amounts to 2% and is thus negligible. It is important to mention that all the rate coefficients used from literature and SAR are for non-NO_3 substituted RO_2 radicals but are used here due to the lack of specific values for nitrate RO_2 radicals. An overview of temperature-dependent rate coefficients for the formation and decomposition of non-acyl RO_2NO_2 is shown in Table 1, together with the corresponding rate coefficients at T = 276 K, 292 K, and 305 K. We also determined the k_{bPN} and k_{fPN} values by a fitting procedure against the experimental data, retrieving values that are within 30% of the literature data above. This supports applying literature data for alkyl-RO_2 to our NO_3-RO_2 radicals, but the fitted values carry a large uncertainty and are not used in the results and discussion below

3 Results

3.1 Nighttime chemistry of *cis*-2-butene

Measured and modelled time series of HO_2 and RO_2 radical concentrations in the two nighttime experiments investigating the oxidation of *cis*-2-butene are shown in Fig. 1. For the two experiments in this work, injected O_3, NO_2, and *cis*-2-butene concentrations are below 15 ppbv, 30 ppbv and 15 ppbv, respectively, and expected NO_3 concentrations do not exceed 8 pptv. For these conditions, on average, NO_3 contributed about 40% at 276 K and 50% at 295 K to the oxidation of *cis*-2-butene (Table S2, ESI‡). As described in Section 2.2, only 16% and 5% of the most dominant RO_2 that is formed, $CH_3CH(OO^\bullet)CH(ONO_2)CH_3$ (MCM notation: $C42NO33O2$), are detected by the instrument at cold ($T \approx 276$ K) and medium ($T \approx 295$ K) temperatures, respectively. The higher the temperature becomes, the faster the decomposition of the alkoxy radical is. Therefore, the modelled total RO_2 and the modelled detectable RO_2 are discussed separately in the following.

For cold conditions, there is a large difference in the total modelled RO_2 between the FZJ mechanisms with and without including the additional formation of RO_2NO_2, with the latter predicting a much lower concentration (by a factor of 7 on average) in the first two hours of oxidation and a much slower increase. When the detectable modelled RO_2 are compared to the measured RO_2 radical concentrations at low temperatures, the mechanism including non-acyl RO_2NO_2 formation (FZJ + RO_2NO_2 model) reproduces the data very well with a model-to-measurement ratio of 0.84, and excellent reproduction of the time dependence. The mechanism without including $RO_2 + NO_2$ reactions (FZJ model) can reasonably reproduce the detectable RO_2 after one hour after the *cis*-2-butene injections (average model-to-measurement ratio = 0.8). However, their concentration is largely overestimated by up to a factor of 4.5 right after the injection, with a distinctly earlier concentration peak. The smaller difference between the two model results observed for the second injection of *cis*-2-butene is due to a larger contribution of CH_3O_2 (from close to 0% after the first *cis*-2-butene injection to ∼ 20% after the second). As the reaction of CH_3O_2 with NO_2 is included in both the FZJ and MCM mechanisms, the effect of the correction is smaller.

Differences of total RO_2 radical concentrations between the two FZJ mechanisms are also observed in the experiment at medium temperatures. However, the difference is much less pronounced and the average ratio of concentrations obtained between the two FZJ mechanisms is 1.1. A small underestimation of the measured RO_2 (by a factor of 1.2) by both mechanisms can be observed by comparing it to the detectable RO_2. The FZJ mechanism without alkyl-$RO_2 + NO_2$ reactions would predict a small peak of the detectable RO_2, while concentrations are better described if these reactions are considered (Fig. 1). From the second injection on, RO_2 radical concentrations predicted by both mechanisms converge to the same value.

The measured HO_2 radical concentrations are well described by both FZJ mechanisms and agree within 36% (FZJ model) and 21% (FZJ + RO_2NO_2 model) after the first VOC injection and within 5% (both FZJ models) after the second VOC injection in the experiment at cold conditions and within 7% (both FZJ mechanisms) in the experiment at medium temperatures. A comparison of the concentration of acetaldehyde, a major product of the ozonolysis of *cis*-2-butene, obtained by the different models is shown in Fig. S11 (ESI‡) for the experiment at cold conditions. The different mechanisms predict similar product concentrations with a model-to-measurement ratio of 0.7.

3.2 Nighttime chemistry of *trans*-2-hexene

Fig. 2 shows measured HO_2 and RO_2 radical concentrations for the experiment with *trans*-2-hexene performed at ≈276 K.

In contrast to *cis*-2-butene, the amount of RO_2 that cannot be detected is negligible,[10] so that the total RO_2 can be directly compared to the measurements.

The addition of RO_2 + NO_2 reactions leads to a less steep increase of the RO_2 radical concentrations which is in much better agreement with the measurements after the first injection of *trans*-2-hexene (within 2% compared to 20% for the FZJ model). Similar to *cis*-2-butene, at 276 K the FZJ mechanism expects a fast increase of RO_2 radicals, which is not observed in the measurements.

As ozone contributes up to 40% to the oxidation of *trans*-2-hexene, and discrepancies were observed earlier when ozone dominated the oxidation at 292 K in the study by Novelli *et al.*,[10] an ozonolysis experiment was performed for *trans*-2-hexene. Fig. S2 (ESI‡) shows the comparison between measured and modelled HO_2 and RO_2 radicals for the MCM and the FZJ mechanisms. An agreement within 20% and 30% between measured and modelled HO_2 is found for the MCM and the FZJ mechanism, respectively. Although the FZJ mechanism improves the agreement between measured and modelled RO_2 radicals, still a ratio of modelled to measured of 1.7 remains at the point of injection of *trans*-2-hexene. The impact of this discrepancy, in the presence of NO_2, was estimated by assuming an overall overestimation of a factor of 1.7 for RO_2 formed from ozonolysis and correcting their concentrations modelled by the FZJ mechanism including RO_2NO_2 formation by this factor. As a consequence, the total modelled RO_2 radical concentrations would be 25% lower (cold temperatures) at the peak RO_2 after the first injection (Fig. 2) with an average ratio of modelled to measured RO_2 of $\approx$0.7. Although the agreement between measured and modelled RO_2 is decreased when an overestimation of RO_2 of 1.7 is assumed (from 12% to 37% for the first 2.5 hours of oxidation), the modelled RO_2 shows the same behaviour in reaching the peak RO_2 radical concentrations and a worse agreement is found for the mechanism without additional NO_2 reactions (model-to-measurement ratio of 1.9 for the first 2.5 hours of oxidation). More details about the interpretation of the ozonolysis experiment can be found in the ESI‡ Section A.

As compared to *cis*-2-butene (Fig. 1) and to the ozonolysis experiment (Fig. S2, ESI‡), the HO_2 radicals are largely underestimated by both models. HO_2 radicals are mainly formed from the reaction of CO with OH ($\approx$61% of the total production rate) which is formed directly from the ozonolysis of *trans*-2-hexene, among other production pathways such as isomerisation reactions of second-generation RO_2 (30% of the total production rate). A similar discrepancy between measured and modelled HO_2 radicals was observed when performing the same experiment but using CH_4 instead of CO as an OH scavenger (Fig. 3).

The observed model-measurement discrepancy could be due to an artefact in the LIF instrument detecting HO_2, if there was a mechanism artificially producing HO_2 in the HO_x detection cell. An instrumental interference by NO_2 and peroxynitric acid (HNO_4, formed in the reaction of HO_2 with NO_2) can be excluded because this would also impact the HO_2 radical concentration measured in the experiment with *cis*-2-butene, for which no model-measurement discrepancy for HO_2 was observed (Fig. 1). Furthermore, an interference from the contemporary decomposition of RO_2 radicals is minimised by running the HO_x detection cell at reduced NO (Section 2.2) and no indication of an interference was observed when changing the NO concentrations in the HO_x cell. A clear correlation of the model-measurement difference in HO_2 radical concentrations is only found with the modelled non-acyl RO_2NO_2 concentrations (Fig. 4), indicating that the model-measurement discrepancy of HO_2 is likely due to an instrumental interference in the HO_2 measurements from RO_2NO_2. This would be consistent with the good agreement observed for the ozonolysis experiment (Fig. S2, ESI‡). An interference of $\approx$2% of the non-acyl RO_2NO_2 in the HO_x cell would be enough to explain the measured HO_2 radical concentration (Fig. 2 and 3).

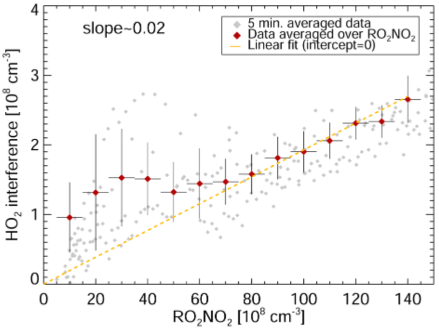

Fig. 4 Correlation between observed model-measurement deviations of HO_2 with modelled non-acyl RO_2NO_2 concentrations. Displayed are NO_3 oxidation experiments of *trans*-2-hexene.

It is currently not clear how the non-acyl RO_2NO_2 would be detected as HO_2 in the HO_x cell of the LIF instrument, especially as no discrepancy was observed for *cis*-2-butene. RO_2 radicals are obtained by subtracting the measured HO_2 and OH radicals from the sum of all three radical species (OH + HO_2 + RO_2), as detected in the RO_x LIF system. Therefore, an interference in the HO_x measurement would result in a lower measured RO_2 radical concentration as compared to the "real" value. Using the modelled HO_2 radical instead of the measured value would increase the RO_2 radical concentrations by 20% and 30% in the experiments at low temperatures with CO (Fig. S15, ESI‡) and CH_4 (Fig. 3) as OH scavenger, respectively. As the HO_2 radical concentrations for the conditions of the experiments in this study are low, their impact is limited and no change in the time profile of the RO_2 radical is observed. More details can be found in Section G of the ESI.‡

Two more experiments at 292 K and 305 K were performed with *trans*-2-hexene (Fig. S12, ESI‡). Although a worse agreement between measured and modelled RO_2 was observed (average model-measurement ratio of 1.5 and 1.2 for 292 K and 305 K, respectively) as compared with the experiment at 276 K, a shift in the peak for measured RO_2 radical concentration could be observed which does not show any "delay" as found in the experiment at cold temperatures (Fig. 2). This is consistent with the faster decomposition rate of the formed RO_2NO_2 at those temperatures and is also reproduced by both models where negligible differences are seen already maximum 30 minutes after the VOC injection.

As compared to the experiment at 276 K (cold), a better agreement between modelled and measured HO_2 radical is obtained. Model calculations tend to overestimate the HO_2 radicals at 276 K. Just recently, a study by McKee *et al.*[39] showed that at high temperatures production of nitryl hydride (HNO_2) from the reaction of HO_2 and NO_2 can be expected. By including this reaction in the model calculations of the experiment at hot conditions (T = 305 K), the comparison of the model with the measurement improves leading to a model-to-measurement ratio of 1.3 on average (compared to 1.6 if the HNO_2 formation is not considered, Fig. S12, ESI‡). More discussion about possible reasons for the observed discrepancies found at 292 K and 305 K for *trans*-2-hexene can be found in the ESI‡ Section G.

The comparison of acetaldehyde concentrations predicted by the mechanisms is shown in Fig. S14 (ESI‡), showing similar concentrations for the different temperatures. The mechanisms overall underestimate the measured acetaldehyde concentrations by a factor of 1.7 and 3 in the experiments at medium and hot temperatures, respectively, but in the experiment at cold conditions a good agreement is achieved (within 15%). The reason for this temperature-dependent discrepancy cannot be easily explained and needs further investigations.

4 Discussion

An overview of the concentrations of non-acyl peroxynitrates, formed in the nighttime oxidation, is shown in Fig. 5 for *cis*-2-butene and in Fig. S13 (ESI‡) for *trans*-2-hexene. Acyl peroxynitrates are excluded here because their formation is implemented identically in both mechanisms, and in the following, RO_2 and RO_2NO_2 refer only to non-acyl peroxy radicals and their respective peroxynitrates, unless noted otherwise.

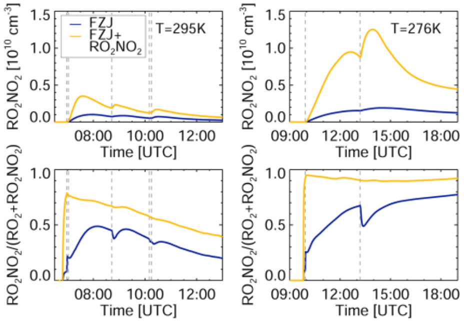

Fig. 5 Formed non-acyl RO_2NO_2 concentrations and the fraction of non-acyl RO_2 stored as RO_2NO_2 ($RO_2NO_2/(RO_2 + RO_2NO_2)$) for the two *cis*-2-butene oxidation experiments in the presence of NO_2 applying the FZJ mechanism either without (FZJ model, blue) or with (FZJ + RO_2NO_2 model, brown) the additional formation of alkyl-RO_2NO_2. Model results of the RO_2NO_2 concentrations, based on the FZJ mechanism without including additional formation of RO_2NO_2 (FZJ model), refer to $CH_3O_2NO_2$ concentrations. Vertical lines refer to the injection of chemical species.

The RO_2NO_2 concentrations expected from the FZJ mechanism are systematically lower than the RO_2NO_2 concentrations expected from the FZJ + RO_2NO_2 mechanism, including non-acyl RO_2NO_2 formation, as only the formation of $CH_3O_2NO_2$ is implemented (Section 2.3). A strong increase of peak RO_2NO_2 concentrations from 140 pptv to up to 480 pptv is observed over the temperature range of 295–276 K. While the main loss path for RO_2 radicals in the FZJ model is the loss in the reaction with HO_2 ($k \sim (2-10) \times 10^{-3}\ s^{-1}$), the reaction with NO_2 ($k \sim (5-9)\ s^{-1}$, Table 1) is the predominant, temporary loss of RO_2 in the FZJ + RO_2NO_2 mechanism, including formation of non-acyl RO_2NO_2, due to the large NO_2 mixing ratios (up to 40 ppbv).

The fraction of RO_2 stored in the reservoir RO_2NO_2 species can be derived from the ratio of corresponding concentrations: $RO_2NO_2/(RO_2 + RO_2NO_2)$ (Table 2, Fig. 5 and Fig. S13, ESI‡). In the experiment at cold conditions, the conversion of RO_2 *via* reaction with NO_2 leads to more than 90% of non-acyl RO_2 that is present in form of the reservoir species RO_2NO_2 throughout the experiment. In comparison, 80% to 40% of the non-acyl RO_2 are stored as RO_2NO_2 throughout the experiment at medium temperatures (Fig. 5), in which the temperature increased from 290 K to 300 K, leading to a shift of equilibrium towards RO_2. When one of the VOCs is injected a large fraction of the RO_2 radicals formed is converted into the reservoir species RO_2NO_2, leading to the slower increase of the free, measurable RO_2 radical concentrations in the FZJ + RO_2NO_2 mechanism, including additional RO_2NO_2 formation, compared to the FZJ mechanism (Fig. 1 and 2). This emphasises the importance of including the formation of peroxynitrates in chemical mechanisms, especially at lower temperatures where the RO_2NO_2/RO_2 ratio can reach a factor of 20.

At temperatures typically reached in mid latitudes, RO_2NO_2 concentrations are expected to be on the order of $1 \times 10^{10}\ cm^{-3}$ at the conditions tested in this work and can therefore impact the fate of RO_x species. In cities as Beijing,[5] China, temperatures around 255 K can be reached in winter, leading to a significant fraction of non-acyl RO_2 stored as reservoir RO_2NO_2 species, and thus to different RO_2 radical concentrations. Low

Table 2 Equilibrium constants of the formation and decomposition of non-acyl RO_2NO_2 (eqn (4)) formed in the oxidation of *trans*-2-hexene by NO_3, derived from the pressure-independent generic forward reaction rate, k_{fPN}, and the backward reaction rate for $C_6H_{13}O_2$ isomers (Table 1), recommended by Jenkin *et al.*[12]

Temperature [K]	K|eqn (3) [cm^3]
305	7.0×10^{-13}
292	3.2×10^{-12}
276	2.5×10^{-11}

temperatures are also present at high altitudes, where biomass burning plumes can introduce polluted conditions, allowing alkyl-RO_2NO_2 other than $CH_3O_2NO_2$ to be formed and impacting the effective RO_2 radical concentration.

One important finding of this study is that the rate coefficients used for forward and backward reactions (Table 1 and 2) do an excellent job in bringing measurements and model results in agreement despite not being derived for the NO_3-substituted RO_2 radicals as investigated here. This indicates that the substituent on the RO_2 radical does not seem to have an impact on the reaction rate. This allows to generalise the finding beyond the molecules and conditions explored in the SAPHIR chamber.

Fig. 6 shows the fraction of $RO_2NO_2/(RO_2 + RO_2NO_2)$ for different temperatures and NO_2 mixing ratios. Conditions observed in different cities[5,6,8,40] are highlighted and are found to favour the formation of non-acyl RO_2NO_2. Especially at wintertime in Beijing, a significant amount of RO_2 is expected to be stored as RO_2NO_2. In contrast, NO_2 and temperature observed in September in a boreal forest[2] do not facilitate the production of RO_2NO_2. Though, for relatively low values of NO_2 of ~1 ppbv and ~10 °C (280 K) that can also be found in forested environments, more than 20% of RO_2 radical is stored as RO_2NO_2. For a mixing ratio of NO_2 up to 10 ppbv, the fraction can increase up to 80%. Although a large part of the RO_2NO_2 will decompose back to RO_2 and NO_2, depending on temperature and lifetime, RO_2NO_2 can be transported and contribute to the NO_x levels further away from their emission sources. In addition, nothing is known about the additional loss rate of RO_2NO_2 by reaction with OH and photolysis. Khan *et al.*[15] introduced these loss reactions based on similarity with other molecules and show they could have an impact in particular at the equator.

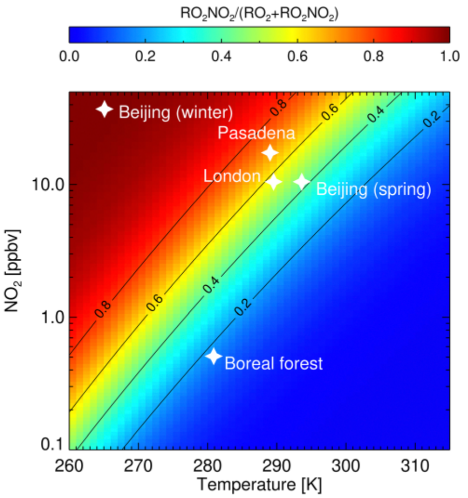

Fig. 6 Fraction of peroxy radicals stored as RO_2NO_2 as a function of temperature and NO_2 mixing ratios. Contour lines mark certain $RO_2NO_2/(RO_2 + RO_2NO_2)$ ratios. Values were determined from a steady-state calculation, assuming the generic forward and backward reaction rate coefficients k_{fPN} and k_{bPN} (Table 1) for reaction (3), respectively. White stars mark regimes that were observed in a boreal forest,[2] in London,[8] Pasadena,[40] and Beijing at cold[5] and medium temperatures.[6]

5 Summary & conclusions

In this study, the nighttime chemistry of *cis*-2-butene and *trans*-2-hexene was investigated under nighttime conditions. Experiments were performed in an outdoor simulation chamber under controlled conditions. The measurements show a clear dependence of the RO_2 radical concentration time profiles on temperature, with the lowest temperatures having a significantly delayed RO_2 peak concentration compared to what would be expected for direct formation of short-lived RO_2 radicals. Measured trace gases and radicals were compared with different chemical mechanisms, implemented in zero-dimensional box model calculations based on the FZJ mechanism.[10] This model improves upon the Master Chemical Mechanism by including a state-of-the-art ozonolysis scheme for *cis*-2-butene and *trans*-2-hexene, updated chemistry for nitrate peroxy radicals (NO_3–RO_2) from NO_3 radical chemistry as well as for oxygenated peroxy radicals from ozonolysis. An extended model, FZJ + RO_2NO_2, additionally includes the reversible reactions of all non-acyl RO_2 radicals with NO_2 forming RO_2NO_2. In addition, the decomposition rate of –NO_3–RO radicals, first introduced by a study by Novelli *et al.*,[10] is adjusted to best match observed radical concentrations.

The measured time profiles of the RO_2 radical concentrations are reproduced best when accounting for the reaction of RO_2 with NO_2 for all RO_2, not solely those for CH_3O_2 and acyl-RO_2 radicals as typically included in atmospheric models. Especially for cold conditions, including the formation of reservoir RO_2NO_2 species significantly improves the modelled RO_2 and an average agreement with the measured RO_2 within 16% is achieved for *cis*-2-butene. This reaction allows reversible formation of alkyl peroxynitrate reservoir species, leading to a reduction of the effective concentration of free RO_2 radicals that is especially pronounced at lower temperatures. In addition, the RO_2 radical concentrations observed are equally (within 20% on average) described by both FZJ mechanisms (FZJ model with and without including additional RO_2NO_2 formation) above 290 K. With decreasing temperatures, including the formation and subsequent decomposition of RO_2NO_2 in the model reduces the predicted total free RO_2 radical concentration and delays peak RO_2 radical concentrations as observed in the experiments, thereby significantly improving the shape of modelled RO_2 time profiles.

A discrepancy between modelled and measured HO_2 radical concentration, which for the low-temperature conditions reached a factor of 3 on average, was observed for *trans*-2-hexene. Sensitivity analyses indicate that this discrepancy correlates best with a measurement interference by non-acyl RO_2NO_2, where an interference of $\approx$2% would be sufficient to reproduce the measured HO_2. However, as this discrepancy does not influence the time-dependence of the RO_2 radical concentration profiles in the chamber experiments, it has no impact on the conclusions.

Under the conditions of the experiments in this work, up to 2×10 cm^{-3} of non-acyl RO_2NO_2 are expected at 276 K, comprising about 95% of RO_2. Under winter conditions in polluted cities such as Beijing, China, where temperatures of 255 K are reached,[5] even higher fractions of the RO_2 present as RO_2NO_2 reservoir species are expected. This will have consequences for radical chemistry, the spatial distribution of RO_2 and NO_2, and the loss of radicals through deposition of RO_2NO_2.[13]

The general forward and backward reaction rates from SAR[12] which refer to non-substituted RO_2 radicals do an excellent job in bringing measured and modelled RO_2 radicals in agreement for the conditions of this study (NO_3–RO_2). This suggests that substituents on the RO_2 radical have a small effect on the reaction rates making the implementation in global models easier. Although the largest impact of these reactions can be expected for cold temperatures (higher altitudes), already for NO_2 mixing ratios as low as few ppbv and a temperature of 280 K, a fraction of $RO_2NO_2/(RO_2 + RO_2NO_2)$ of 20% can be expected (Fig. 6). Given the large uncertainties of the follow-up chemistry of RO_2NO_2, it is not easy to assess, a priori, their effect in different environments and more studies are needed to shed light on their chemistry. Generally, the impact of the formation of RO_2NO_2 manifests likely as a time delay in the response of the chemical mixture to changes in VOC emission and oxidation, NO_x levels, temperature, and other environmental factors.

Discrepancies remain between modelled and measured RO_2 radicals in the ozonolysis experiment of *trans*-2-hexene and for $NO_2 + O_3$ experiments of *trans*-2-hexene at higher temperatures (292 K and 305 K). Uncertainties in the ozonolysis may be related to the chemistry of peracid-substituted RO_2 radicals formed in RO_2H-migration reactions. Insufficient data are available to resolve this issue at this time, but it is shown that the discrepancy is too small to significantly affect the $O_3 + NO_3$ nighttime experiments in this work.

Data availability

Data from the experiments in the SAPHIR chamber used in this work are available on the EUROCHAMP data home page (https://data.eurochamp.org/). Experiments with *cis*-2-butene performed at $T \approx 276$ K and $T \approx 295$ K are available at https://doi.org/10.25326/MBQ2-QY95[41] and https://doi.org/10.25326/6BV7-MR14,[42] respectively. Experimental data from the nighttime oxidation experiments of *trans*-2-hexene in the presence of NO_2 and CO conducted at $T \approx 276$ K, $T \approx 292$ K, and $T \approx 305$ K are accessible at https://doi.org/10.25326/DV74-3P36,[43] https://doi.org/10.25326/E63B-9J58,[44] and https://doi.org/10.25326/5CDB-Q698,[45] respectively. Data from the nighttime experiment of *trans*-2-hexene in the presence of NO_2 and CH_4 as well as from the ozonolysis experiment of *trans*-2-hexene are available at https://doi.org/10.25326/DSQH-4 × 71[46] and https://doi.org/10.25326/89B1-GR69,[47] respectively.

Conflicts of interest

The authors declare that they have no conflict of interest.

References

1 R. Atkinson and J. Arey, *Chem. Rev.*, 2003, **103**, 4605–4638.
2 J. Liebmann, E. Karu, N. Sobanski, J. Schuladen, M. Ehn, S. Schallhart, L. Quéléver, H. Hellen, H. Hakola, T. Hoffmann, J. Williams, H. Fischer, J. Lelieveld and J. N. Crowley, *Atmos. Chem. Phys.*, 2018, **18**, 3799–3815.
3 J. M. Liebmann, J. B. A. Muller, D. Kubistin, A. Claude, R. Holla, C. Plass-Dülmer, J. Lelieveld and J. N. Crowley, *Atmos. Chem. Phys.*, 2018, **18**, 12045–12059.
4 P. M. Edwards, K. C. Aikin, W. P. Dube, J. L. Fry, J. B. Gilman, J. A. De Gouw, M. G. Graus, T. F. Hanisco, J. Holloway, G. Hübler, J. Kaiser, F. N. Keutsch, B. M. Lerner, J. A. Neuman, D. D. Parrish, J. Peischl, I. B. Pollack, A. R. Ravishankara, J. M. Roberts, T. B. Ryerson, M. Trainer, P. R. Veres, G. M. Wolfe, C. Warneke and S. S. Brown, *Nat. Geosci.*, 2017, **10**, 490–495.
5 Z. Tan, F. Rohrer, K. Lu, X. Ma, B. Bohn, S. Broch, H. Dong, H. Fuchs, G. I. Gkatzelis, A. Hofzumahaus, F. Holland, X. Li, Y. Liu, Y. Liu, A. Novelli, M. Shao, H. Wang, Y. Wu, L. Zeng, M. Hu, A. Kiendler-Scharr, A. Wahner and Y. Zhang, *Atmos. Chem. Phys.*, 2018, **18**, 12391–12411.
6 L. K. Whalley, E. J. Slater, R. Woodward-Massey, C. Ye, J. D. Lee, F. Squires, J. R. Hopkins, R. E. Dunmore, M. Shaw, J. F. Hamilton, A. C. Lewis, A. Mehra, S. D. Worrall, A. Bacak, T. J. Bannan, H. Coe, C. J. Percival, B. Ouyang, R. L. Jones, L. R. Crilley, L. J. Kramer, W. J. Bloss, T. Vu, S. Kotthaus, S. Grimmond, Y. Sun, W. Xu, S. Yue, L. Ren, W. J. F. Acton, C. N. Hewitt, X. Wang, P. Fu and D. E. Heard, *Atmos. Chem. Phys.*, 2021, **21**, 2125–2147.
7 Z. Tan, H. Fuchs, K. Lu, A. Hofzumahaus, B. Bohn, S. Broch, H. Dong, S. Gomm, R. Häseler, L. He, F. Holland, X. Li, Y. Liu, S. Lu, F. Rohrer, M. Shao, B. Wang, M. Wang, Y. Wu, L. Zeng, Y. Zhang, A. Wahner and Y. Zhang, *Atmos. Chem. Phys.*, 2017, **17**, 663–690.
8 L. K. Whalley, D. Stone, R. Dunmore, J. Hamilton, J. R. Hopkins, J. D. Lee, A. C. Lewis, P. Williams, J. Kleffmann, S. Laufs, R. Woodward-Massey and D. E. Heard, *Atmos. Chem. Phys.*, 2018, **18**, 2547–2571.
9 L. Vereecken, P. T. M. Carlsson, A. Novelli, F. Bernard, S. S. Brown, C. Cho, J. N. Crowley, H. Fuchs, W. Mellouki, D. Reimer, J. Shenolikar, R. Tillmann, L. Zhou, A. Kiendler-Scharr and A. Wahner, *Phys. Chem. Chem. Phys.*, 2021, **23**, 5496–5515.
10 A. Novelli, C. Cho, H. Fuchs, A. Hofzumahaus, F. Rohrer, R. Tillmann, A. Kiendler-Scharr, A. Wahner and L. Vereecken, *Phys. Chem. Chem. Phys.*, 2021, **23**, 5474–5495.

11 E. J. Slater, L. K. Whalley, R. Woodward-Massey, C. Ye, J. D. Lee, F. Squires, J. R. Hopkins, R. E. Dunmore, M. Shaw, J. F. Hamilton, A. C. Lewis, L. R. Crilley, L. Kramer, W. Bloss, T. Vu, Y. Sun, W. Xu, S. Yue, L. Ren, W. J. F. Acton, C. N. Hewitt, X. Wang, P. Fu and D. E. Heard, *Atmos. Chem. Phys.*, 2020, **20**, 14847–14871.

12 M. E. Jenkin, R. Valorso, B. Aumont and A. R. Rickard, *Atmos. Chem. Phys.*, 2019, **19**, 7691–7717.

13 J. J. Orlando and G. S. Tyndall, *Chem. Soc. Rev.*, 2012, **41**, 6294–6317.

14 E. C. Browne, A. E. Perring, P. J. Wooldridge, E. Apel, S. R. Hall, L. G. Huey, J. Mao, K. M. Spencer, J. M. S. Clair, A. J. Weinheimer, A. Wisthaler and R. C. Cohen, *Atmos. Chem. Phys.*, 2011, **11**, 4209–4219.

15 M. A. H. Khan, B. Miles, M. E. Jenkin, R. G. Derwent, C. J. Percival and D. E. Shallcross, *ACS Earth Space Chem.*, 2020, **4**, 1201–1212.

16 R. Atkinson, D. L. Baulch, R. A. Cox, J. N. Crowley, R. F. Hampson, R. G. Hynes, M. E. Jenkin, M. J. Rossi, J. Troe and I. Subcommittee, *Atmos. Chem. Phys.*, 2006, **6**, 3625–4055.

17 K. McKee, M. A. Blitz and M. J. Pilling, *J. Phys. Chem. A*, 2016, **120**, 1408–1420.

18 F. Zabel, A. Reimer, K. H. Becker and E. H. Fink, *J. Phys. Chem.*, 1989, **93**, 5500–5507.

19 F. Rohrer, B. Bohn, T. Brauers, D. Brüning, F.-J. Johnen, A. Wahner and J. Kleffmann, *Atmos. Chem. Phys.*, 2005, **5**, 2189–2201.

20 E. Schlosser, B. Bohn, T. Brauers, H.-P. Dorn, H. Fuchs, R. Hässler, A. Hofzumahaus, F. Holland, F. Rohrer, L.-O. Rupp, M. Siese, R. Tillmann and A. Wahner, *J. Atmos. Chem.*, 2007, **56**, 187–205.

21 H. Fuchs, T. Brauers, H.-P. Dorn, H. Harder, R. Häseler, A. Hofzumahaus, F. Holland, Y. Kanaya, Y. Kajii, D. Kubistin, S. Lou, M. Martinez, K. Miyamoto, S. Nishida, M. Rudolf, E. Schlosser, A. Wahner, A. Yoshino and U. Schurath, *Atmos. Chem. Phys.*, 2010, **10**, 12233–12250.

22 E. C. Apel, T. Brauers, R. Koppmann, B. Bandowe, J. BoÃŸmeyer, C. Holzke, R. Tillmann, A. Wahner, R. Wegener, A. Brunner, M. Jocher, T. Ruuskanen, C. Spirig, D. Steigner, R. Steinbrecher, E. Gomez Alvarez, K. Müller, J. P. Burrows, G. Schade, S. J. Solomon, A. Ladstätter-WeiÃŸenmayer, P. Simmonds, D. Young, J. R. Hopkins, A. C. Lewis, G. Legreid, S. Reimann, A. Hansel, A. Wisthaler, R. S. Blake, A. M. Ellis, P. S. Monks and K. P. Wyche, *J. Geophys. Res. Atmos.*, 2008, **113**, D20307.

23 H. Fuchs, F. Holland and A. Hofzumahaus, *Rev. Sci. Instrum.*, 2008, **79**, 084104.

24 F. Holland, A. Hofzumahaus, J. Schäfer, A. Kraus and H.-W. Pätz, *J. Geophys. Res. Atmos.*, 2003, **108**, 2–23.

25 F. Holland, M. Hessling and A. Hofzumahaus, *J. Atmos. Sci.*, 1995, **52**, 3393–3401.

26 H. Fuchs, H.-P. Dorn, M. Bachner, B. Bohn, T. Brauers, S. Gomm, A. Hofzumahaus, F. Holland, S. Nehr, F. Rohrer, R. Tillmann and A. Wahner, *Atmos. Meas. Tech.*, 2012, **5**, 1611–1626.

27 C. Cho, A. Hofzumahaus, H. Fuchs, H.-P. Dorn, M. Glowania, F. Holland, F. Rohrer, V. Vardhan, A. Kiendler-Scharr, A. Wahner and A. Novelli, *Atmos. Meas. Tech.*, 2021, **14**, 1851–1877.

28 H. Fuchs, B. Bohn, A. Hofzumahaus, F. Holland, K. D. Lu, S. Nehr, F. Rohrer and A. Wahner, *Atmos. Meas. Tech.*, 2011, **4**, 1209–1225.

29 H. Fuchs, Z. Tan, A. Hofzumahaus, S. Broch, H.-P. Dorn, F. Holland, C. Künstler, S. Gomm, F. Rohrer, S. Schrade, R. Tillmann and A. Wahner, *Atmos. Meas. Tech.*, 2016, **9**, 1431–1447.

30 S. Lou, F. Holland, F. Rohrer, K. Lu, B. Bohn, T. Brauers, C. C. Chang, H. Fuchs, R. Häseler, K. Kita, Y. Kondo, X. Li, M. Shao, L. Zeng, A. Wahner, Y. Zhang, W. Wang and A. Hofzumahaus, *Atmos. Chem. Phys.*, 2010, **10**, 11243–11260.

31 H. Fuchs, A. Novelli, M. Rolletter, A. Hofzumahaus, E. Y. Pfannerstill, S. Kessel, A. Edtbauer, J. Williams, V. Michoud, S. Dusanter, N. Locoge, N. Zannoni, V. Gros, F. Truong, R. Sarda-Esteve, D. R. Cryer, C. A. Brumby, L. K. Whalley, D. Stone, P. W. Seakins, D. E. Heard, C. Schoemaecker, M. Blocquet, S. Coudert, S. Batut, C. Fittschen, A. B. Thames, W. H. Brune, C. Ernest, H. Harder, J. B. A. Muller, T. Elste, D. Kubistin, S. Andres, B. Bohn, T. Hohaus, F. Holland, X. Li, F. Rohrer, A. Kiendler-Scharr, R. Tillmann, R. Wegener, Z. Yu, Q. Zou and A. Wahner, *Atmos. Meas. Tech.*, 2017, **10**, 4023–4053.

32 A. Jordan, S. Haidacher, G. Hanel, E. Hartungen, L. Märk, H. Seehauser, R. Schottkowsky, P. Sulzer and T. D. Märk, *Int. J. Mass Spectrom.*, 2009, **286**, 122–128.

33 W. Lindinger, A. Hansel and A. Jordan, *Int. J. Mass Spectrom. Ion Processes*, 1998, **173**, 191–241.

34 M. E. Jenkin, S. M. Saunders and M. J. Pilling, *Atmos. Environ.*, 1997, **31**, 81–104.

35 S. M. Saunders, M. E. Jenkin, R. G. Derwent and M. J. Pilling, *Atmos. Chem. Phys.*, 2003, **3**, 161–180.

36 L. Vereecken and J. Peeters, *Phys. Chem. Chem. Phys.*, 2009, **11**, 9062–9074.

37 L. Vereecken and B. Nozière, *Atmos. Chem. Phys.*, 2020, **20**, 7429–7458.

38 L. Vereecken and J. Peeters, *Phys. Chem. Chem. Phys.*, 2010, **12**, 12608–12620.

39 K. McKee, M. A. Blitz, R. J. Shannon and M. J. Pilling, *J. Phys. Chem. A*, 2022, **126**, 7514–7522.

40 S. M. Griffith, R. F. Hansen, S. Dusanter, V. Michoud, J. B. Gilman, W. C. Kuster, P. R. Veres, M. Graus, J. A. De Gouw, J. Roberts, C. Young, R. Washenfelder, S. S. Brown, R. Thalman, E. Waxman, R. Volkamer, C. Tsai, J. Stutz, J. H. Flynn, N. Grossberg, B. Lefer, S. L. Alvarez, B. Rappenglueck, L. H. Mielke, H. D. Osthoff and P. S. Stevens, *J. Geophys. Res.: Atmos.*, 2016, **121**, 4211–4232.

41 M. Färber, H. Fuchs, G. Gkatzelis, F. Rohrer, S. Wedel and A. Novelli, *Atmospheric simulation chamber study: cis-2-butene + NO3 - Gas-phase oxidation - kinetic study - 2022-02-11*, 2023, (Version 1.0) [Data set]. AERIS.

42 A. Novelli, C. Cho, H. Fuchs, A. Hofzumahaus, F. Rohrer and R. Tillmann, *Atmospheric simulation chamber study: cis-2-butene + NO3 - Gas-phase oxidation - product study - 2020-05-19*, 2021, (Version 1.0) [Data set]. AERIS.

43 M. Färber, H. Fuchs, G. Gkatzelis, F. Rohrer, S. Wedel and A. Novelli, *Atmospheric simulation chamber study: trans-2-hexene +* NO*3 - Gas-phase oxidation - kinetic study - 2022-01-26*, 2023, (Version 1.0) [Data set]. AERIS.

44 A. Novelli, C. Cho, H. Fuchs, A. Hofzumahaus, F. Rohrer and R. Tillmann, *Atmospheric simulation chamber study: trans-2-hexene +* NO*3 - Gas-phase oxidation - product study - 2020-05-23*, 2021, (Version 1.0) [Data set]. AERIS.

45 M. Färber, H. Fuchs, G. Gkatzelis, F. Rohrer, S. Wedel and A. Novelli, Atmospheric simulation chamber study: *trans*-2-hexene + NO3 - Gas-phase oxidation - kinetic study - 2022-07-20, 2023, (Version 1.0) [Data set]. AERIS.

46 M. Färber, H. Fuchs, G. Gkatzelis, F. Rohrer, S. Wedel and A. Novelli, *Atmospheric simulation chamber study: trans-2-hexene +* NO*3 - Gas-phase oxidation - kinetic study - 2022-02-21*, 2023, (Version 1.0) [Data set]. AERIS.

47 M. Färber, H. Fuchs, G. Gkatzelis, F. Rohrer, S. Wedel and A. Novelli, *Atmospheric simulation chamber study: trans-2-hexene + O3 - Gas-phase oxidation - kinetic study - 2021-12-08*, 2023, (Version 1.0) [Data set]. AERIS.

4 | Conclusions

This thesis aimed to investigate the atmospheric radical chemistry of anthropogenic VOCs in simulation chambers and to test available chemical mechanisms. In field studies, discrepancies were observed in the comparison of measured radical concentrations with results from chemical box model calculations, resulting in a significant disagreement between measured and modelled ozone production rates, especially at high NO mixing ratios (ppbv) (Tan et al., 2017, 2018; Whalley et al., 2018; Slater et al., 2020; Whalley et al., 2021; Woodward-Massey et al., 2023). As ozone is harmful to human health and is a greenhouse gas, understanding its formation is crucial for mitigating air pollution and thus improving air quality.

In the multi-chamber study, performed as part of the EUROCHAMP-2020 project, experiments investigating the oxidation of -pinene were performed in nine different European simulation chambers. The analysis shows the need to carefully characterise chamber-related processes to derive reproducible results. The comparison of gas-phase product yields (formaldehyde, acetone, and pinonaldehyde), derived from the photooxidation of -pinene, yielded an overall agreement with literature values, although a large variability was observed for pinonaldehyde and formaldehyde in the different chambers. Chemical conditions varied between different experiments and even more between different chambers, making a direct comparison challenging.

Chamber effects, such as the release of small oxygenated compounds and the loss of trace gases to the chamber wall, were identified and accounted for when possible. To further facilitate the evaluation of chamber experiments within the EUROCHAMP-2020 consortium, extended investigations of chamber effects, especially of the chamber production of species such as HONO, would be helpful.

This multi-chamber study emphasises the importance of standard procedures for characterising chamber effects as these can vary with time due to memory effects of the chamber wall from previously performed experiments. In addition, chamber effects were observed to dominate measured trace gas concentrations in few experiments, stressing the need of a careful design of the experimental procedures to ensure that the oxidation of the VOC of interest is dominating the observed chemistry. Furthermore, the simulation chamber should be chosen according to the chemical conditions of interest.

Among the different simulation chambers within the EUROCHAMP-2020 consortium, the SAPHIR chamber is the only one providing measurements of OH, HO_2, and RO_2 radicals, utilising the laser-induced fluorescence (LIF) technique. As part of this thesis, oxidation experiments were performed in the SAPHIR chamber, focusing on daytime (oxidation by OH radicals) and nighttime (oxidation by NO and O) oxidation processes of anthropogenic VOCs. Model-measurement comparison of HO_2 and RO_2 radicals in the photooxidation experiments showed an overall good agreement of observations and model calculations for

anthropogenic alkanes and alkenes C_6 molecules. The model is based on the commonly used Master Chemical Mechanism (MCM). However, for the C_6 molecules n-hexane and trans-2-hexene, measured HO_2 and RO_2 radical concentrations were better reproduced by complementing the MCM with an updated radical chemistry scheme from structure-activity relationships (SARs). This highlights the validity of the MCM mechanisms for small/short alkenes and alkanes and the importance of investigating larger molecules to test and improve chemical models.
In addition to testing chemical mechanisms, the experiments in the chamber allowed to investigate the ozone formation from the oxidation of linear and branched alkanes and alkenes at current and future NO_x levels in urban environments. The ozone production per oxidised VOC was obtained from modelled and measured radical concentrations, as well as from measured O_x (O_3 NO_2) concentrations. The investigated VOC differed in the type of the chemistry of the alkoxy radicals obtained from the reaction of RO with NO. Either they form HO_2 directly (propane, propene, trans-2-hexene) or in a multi-step reaction, which proceeds via the formation of another RO_2 radical (iso-pentane, n-hexane). The multi-step HO_2 formation can increase the O_x production per oxidised VOC molecule. However, the overall effect is highly sensitive to the organic nitrate yield of involved RO_2 radicals. For the study in the chamber, measured and modelled O_x production agree well and an increase of % of the produced ozone was observed in the experiments with VOCs producing RO radicals forming HO_2 in a multi-step reaction compared to VOCs producing RO radicals forming HO_2 in one reaction step. This is much less than the increase in the ozone production that would be needed to explain model-measurement discrepancies found in different urban and rural environments with ratios of up to a factor of 10 in London (Whalley et al., 2018) and of 100 in Beijing (Whalley et al., 2021). The authors of the study in London suggested that the discrepancy could be reduced if a large fraction of RO radicals would undergo multi-step formation of HO radicals. To test their hypothesis the CH C(=O)CHCH CH(CH OO)C(CH)C -RO_2 was included in the model. Its alkoxy chemistry involves three RO_2 regeneration steps before HO_2 is eventually formed. This work, however, demonstrates that the MCM overestimates the organic nitrate yields of n-hexane RO_2 and underestimates the organic nitrate yields of CH C(=O)CHCH CH(CH OO)C(CH)C and the subsequently formed RO_2, when comparing it with SAR. As a consequence, the improvement in the model-measurement agreement of radical concentrations, observed by Whalley et al. (2021), is expected to be quite reduced, when considering updated organic nitrate yields from SAR. This emphasises the need for further measurements of the organic nitrate yields to test the available SAR and to update the chemical mechanisms such as the MCM.

In addition, experiments in the dark using O and NO as oxidants were performed at different temperatures (K to K), studying the nighttime oxidation of cis-2-butene and trans-2-hexene. The study highlights that the formation of non-acyl peroxynitrates (RO_2NO_2) from the reaction of alkyl peroxy radicals with NO_2 affects the RO_2 radical concentrations at low temperatures (K). In commonly used chemical models, such as the MCM, the formation of most non-acyl peroxynitrates is not implemented, as it is thought to be negligible in the lower troposphere due to the short lifetimes of peroxynitrate of approximately s even at 298 K. In addition, a recent model study by Khan et al. (2020) found that up to % more NO_x can be expected in the equatorial regions, if the formation of non-acyl peroxynitrates is included in the model. This work shows that % of the RO_2 radicals are expected to be stored as peroxynitrate already at low NO_2 mixing ratios of a few ppbv and at a temperature of K, emphasising the need of further investigations regarding the formation of alkyl-RO_2NO_2 and its effect on RO_2 radical concentrations at different chemical conditions. In addition, a model-measurement discrepancy of the HO_2 radical concentrations was observed in the experiment with trans-2-hexene particularly at low temperatures, demonstrating a possible interference of non-acyl RO_2NO_2 in the HO_x measurement of the LIF system. As no discrepancy was observed for cis-2-butene, it is likely that this model-measurement deviation is caused from RO_2, formed in the oxidation of trans-2-hexene. However, further investigations will be required to test this hypothesis. In addition, a deviation between modelled and measured RO_2 radical concentrations was observed, when ozonolysis dominated the loss of trans-2-hexene. This discrepancy was also observed in a separate ozonolysis experiment, hinting towards an incomplete understanding of the chemistry of peracid peroxy radicals (RC(OO)C(=O)OOH).

Overall, findings in this thesis support current atmospheric research and encourage new research questions. Despite efforts to reduce the emission of anthropogenic VOCs, they still play a major role in urban air quality, leading to the production of secondary pollutants, including particulate matter or ozone. Understanding their atmospheric oxidation is crucial for handling upcoming challenges, regionally and globally.

Bibliography

Akimoto, H. and Hirokawa, J.: Atmospheric Multiphase Chemistry: Fundamentals of Secondary Aerosol Formation, John Wiley & Sons, Inc., 1 edn., 2020.

Arey, J., Atkinson, R., and Aschmann, S. M.: Product study of the gas-phase reactions of monoterpenes with the OH radical in the presence of NO_x, J. Geophys. Res. Atmos., 95, 18 539–18 546, doi:10.1029/JD095iD11p18539, 1990.

Arey, J., Aschmann, S. M., Kwok, E. S. C., and Atkinson, R.: Alkyl Nitrate, Hydroxyalkyl Nitrate, and Hydroxycarbonyl Formation from the NO_x—Air Photooxidations of C_5 $-C_8$ *n*-Alkanes, J. Phys. Chem. A, 105, 1020–1027, doi:10.1021/jp003292z, 2001.

Aschmann, S. M., Atkinson, R., and Arey, J.: Products of reaction of OH radicals with -pinene, J. Geophys. Res. Atmos., 107, doi:10.1029/2001JD001098, 2002.

Asif, Z., Chen, Z., Haghighat, F., Nasiri, F., and Dong, J.: Estimation of Anthropogenic VOCs Emission Based on Volatile Chemical Products: A Canadian Perspective, Environ. Manage., 71, 685–703, doi:10.1007/s00267-022-01732-6, 2023.

Atkins, P. W. and de Paula, J.: Kurzlehrbuch Physikalische Chemie für natur- und ingenieurwissenschaftliche Studiengänge, WILEY-VCH, 5 edn., 2020.

Atkinson, R.: Gas-Phase Tropospheric Chemistry of Volatile Organic Compounds: 1. Alkanes and Alkenes, J. Phys. Chem. Ref. Data, 26, 215–290, doi:10.1063/1.556012, 1997.

Atkinson, R.: Rate constants for the atmospheric reactions of alkoxy radicals: An updated estimation method, Atmos. Environ., 41, 8468–8485, doi:10.1016/j.atmosenv.2007.07.002, 2007.

Atkinson, R. and Arey, J.: Atmospheric Degradation of Volatile Organic Compounds, Chem. Rev., 103, 4605–4638, doi:10.1021/cr0206420, 2003.

Atkinson, R., Baulch, D. L., Cox, R. A., Crowley, J. N., Hampson, R. F., Hynes, R. G., Jenkin, M. E., Rossi, M. J., and Troe, J.: Evaluated kinetic and photochemical data for atmospheric chemistry: Volume I - gas phase reactions of O_x, HO_x, NO_x and SO_x species, Atmos. Chem. Phys., 4, 1461–1738, doi:10.5194/acp-4-1461-2004, 2004.

Atkinson, R., Baulch, D. L., Cox, R. A., Crowley, J. N., Hampson, R. F., Hynes, R. G., Jenkin, M. E., Rossi, M. J., Troe, J., and Subcommittee, I.: Evaluated kinetic and photochemical data for atmospheric chemistry: Volume II - gas phase reactions of organic species, Atmos. Chem. Phys., 6, 3625–4055, doi:10.5194/acp-6-3625-2006, 2006.

Aumont, B., Szopa, S., and Madronich, S.: Modelling the evolution of organic carbon during its gas-phase tropospheric oxidation: development of an explicit model based on a self generating approach, Atmospheric Chemistry and Physics, 5, 2497–2517, doi:10.5194/acp-5-2497-2005, 2005.

Barmet, P., Dommen, J., DeCarlo, P. F., Tritscher, T., Praplan, A. P., Platt, S. M., Prévôt, A. S. H., Donahue, N. M., and Baltensperger, U.: OH clock determination by proton transfer reaction mass spectrometry at an environmental chamber, Atmos. Meas. Tech., 5, 647–656, doi:10.5194/amt-5-647-2012, 2012.

Berndt, T.: Peroxy Radical and Product Formation in the Gas-Phase Ozonolysis of -Pinene under Near-Atmospheric Conditions: Occurrence of an Additional Series of Peroxy Radicals O,O–$C_{10}H_{15}O(O_2)_yO_2$ with y = 1–3, J. Phys. Chem. A, 126, 6526–6537, doi:10.1021/acs.jpca.2c05094, 2022.

Bianchi, F., Kurtén, T., Riva, M., Mohr, C., Rissanen, M. P., Roldin, P., Berndt, T., Crounse, J. D., Wennberg, P. O., Mentel, T. F., Wildt, J., Junninen, H., Jokinen, T., Kulmala, M., Worsnop, D. R., Thornton, J. A., Donahue, N., Kjaergaard, H. G., and Ehn, M.: Highly Oxygenated Organic Molecules (HOM) from Gas-Phase Autoxidation Involving Peroxy Radicals: A Key Contributor to Atmospheric Aerosol, Chem. Rev., 119, 3472–3509, doi:10.1021/acs.chemrev.8b00395, 2019.

Bohn, B., Rohrer, F., Brauers, T., and Wahner, A.: Actinometric measurements of NO_2 photolysis frequencies in the atmosphere simulation chamber SAPHIR, Atmospheric Chemistry and Physics, 5, 493–503, doi:10.5194/acp-5-493-2005, 2005.

Briffa, K. R., Jones, P. D., Schweingruber, F. H., and Osborn, T. J.: Influence of volcanic eruptions on Northern Hemisphere summer temperature over the past 600 years, Nature, 393, 450–455, doi:10.1038/30943, 1998.

Brown, S. S. and Stutz, J.: Nighttime radical observations and chemistry, Chem. Soc. Rev., 41, 6405–6447, doi:10.1039/C2CS35181A, 2012.

Browne, E. C., Perring, A. E., Wooldridge, P. J., Apel, E., Hall, S. R., Huey, L. G., Mao, J., Spencer, K. M., Clair, J. M. S., Weinheimer, A. J., Wisthaler, A., and Cohen, R. C.: Global and regional effects of the photochemistry of $CH_3O_2NO_2$: evidence from ARCTAS, Atmos. Chem. Phys., 11, 4209–4219, doi:10.5194/acp-11-4209-2011, 2011.

Brune, W. H., Stevens, P. S., and Mather, J. H.: An aircraft instrument design for in situ tropospheric OH measurements by laser induced fluorescence at low pressures, in: Environmental Sensing '92, edited by Schiff, H. I. and Platt, U., pp. 413–424, Berlin, Federal Republic of Germany, doi:10.1117/12.140194, 1993.

Brune, W. H., Baier, B. C., Thomas, J., Ren, X., Cohen, R. C., Pusede, S. E., Browne, E. C., Goldstein, A. H., Gentner, D. R., Keutsch, F. N., Thornton, J. A., Harrold, S., Lopez-Hilfiker, F. D., and Wennberg, P. O.: Ozone production chemistry in the presence of urban plumes, Faraday Discuss., 189, 169–189, doi:10.1039/C5FD00204D, 2016.

Camredon, M., Aumont, B., Lee-Taylor, J., and Madronich, S.: The SOA/VOC/NO_x system: an explicit model of secondary organic aerosol formation, Atmospheric Chemistry and Physics, 7, 5599–5610, doi:10.5194/acp-7-5599-2007, 2007.

Cantrell, C. A., Zimmer, A., and Tyndall, G. S.: Absorption cross sections for water vapor from 183 to 193 nm, Geophys. Res. Lett., 24, 2195–2198, doi:10.1029/97GL02100, 1997.

Carter, W. P. L. and Atkinson, R.: Alkyl nitrate formation from the atmospheric photoxidation of alkanes; a revised estimation method, J. Atmos. Chem., 8, 165–173, doi:10.1007/BF00053721, 1989.

CESAM: CESAM homepage, `https://www.cesam.cnrs.fr/`, 2023.

Chan, C. Y., Hard, T. M., Mehrabzadeh, A. A., George, L. A., and O'Brien, R. J.: Third-generation FAGE instrument for tropospheric hydroxyl radical measurement, J. Geophys. Res. Atmos., 95, 18 569–18 576, doi:10.1029/JD095iD11p18569, 1990.

Cho, C.: Investigations of the atmospheric OH, HO_2 and RO_2 radical chemical budgets and their impact on tropospheric ozone formation in a rural area in West-Germany in the JULIAC 2019 campaign, vol. 575 of *Schriften des Forschungszentrums Jülich / Reihe Energie & Umwelt: Reihe Energie & Umwelt*, Forschungszentrum Jülich GmbH Zentralbibliothek, Verlag, 2021.

Cho, C., Hofzumahaus, A., Fuchs, H., Dorn, H.-P., Glowania, M., Holland, F., Rohrer, F., Vardhan, V., Kiendler-Scharr, A., Wahner, A., and Novelli, A.: Characterization of a chemical modulation reactor (CMR) for the measurement of atmospheric concentrations of hydroxyl radicals with a laser-induced fluorescence instrument, Atmos. Meas. Tech., 14, 1851–1877, doi:10.5194/amt-14-1851-2021, 2021.

Chou, C. C., Lo, J. G., and Rowland, F. S.: Primary processes in the photolysis of water vapor at 174 nm, J. Chem. Phys., 60, 1208–1210, doi:10.1063/1.1681183, 1974.

Coggon, M. M., McDonald, B. C., Vlasenko, A., Veres, P. R., Bernard, F., Koss, A. R., Yuan, B., Gilman, J. B., Peischl, J., Aikin, K. C., DuRant, J., Warneke, C., Li, S.-M., and De Gouw, J. A.: Diurnal Variability and Emission Pattern of Decamethylcyclopentasiloxane (D_5) from the Application of Personal Care Products in Two North American Cities, Environ. Sci. Technol., 52, 5610–5618, doi:10.1021/acs.est.8b00506, 2018.

Creasey, D. J., Heard, D. E., and Lee, J. D.: Absorption cross-section measurements of water vapour and oxygen at 185 nm. Implications for the calibration of field instruments to measure OH, HO_2 and RO_2 radicals, Geophys. Res. Lett., 27, 1651–1654, doi:10.1029/1999GL011014, 2000.

Crosley, D. R.: The Measurement of OH and HO_2 in the Atmosphere, J. Atmos. Sci., 52, 3299–3314, doi:10.1175/1520-0469(1995)052<3299:TMOOAH>2.0.CO;2, 1995.

Diem, M.: Quantum Mechanical Foundations of Molecular Spectroscopy, WILEY-VCH, 2021.

Donahue, N. M., Henry, K. M., Mentel, T. F., Kiendler-Scharr, A., Spindler, C., Bohn, B., Brauers, T., Dorn, H. P., Fuchs, H., Tillmann, R., Wahner, A., Saathoff, H., Naumann, K.-H., Möhler, O., Leisner, T., Müller, L., Reinnig, M.-C., Hoffmann, T., Salo, K., Hallquist, M., Frosch, M., Bilde, M., Tritscher, T., Barmet, P., Praplan, A. P., DeCarlo, P. F., Dommen, J., Prévôt, A. S., and Baltensperger, U.: Aging of biogenic secondary organic aerosol via gas-phase OH radical reactions, Proceedings of the National Academy of Sciences, 109, 13 503–13 508, doi:10.1073/pnas.1115186109, 2012.

Dorn, H., Neuroth, R., and Hofzumahaus, A.: Investigation of OH absorption cross sections of rotational transitions in the band under atmospheric conditions: Implications for tropospheric long-path absorption measurements, J. Geophys. Res. Atmos., 100, 7397–7409, doi:10.1029/94JD03323, 1995.

Doussin, J.-F., Fuchs, H., Kiendler-Scharr, A., Seakins, P., and Wenger, J.: A Practical Guide to Atmospheric Simulation Chambers, Springer, 2023.

Eddingsaas, N. C., Loza, C. L., Yee, L. D., Chan, M., Schilling, K. A., Chhabra, P. S., Seinfeld, J. H., and Wennberg, P. O.: -pinene photooxidation under controlled chemical conditions – Part 2: SOA yield and composition in low- and high-NO_x environments, Atmos. Chem. Phys., 12, 7413–7427, doi:10.5194/acp-12-7413-2012, 2012a.

Eddingsaas, N. C., Loza, C. L., Yee, L. D., Seinfeld, J. H., and Wennberg, P. O.: -pinene photooxidation under controlled chemical conditions - Part 1: Gas-phase composition in low- and high-NO_x environments, Atmos. Chem. Phys., 12, 6489–6504, doi:10.5194/acp-12-6489-2012, 2012b.

Ehlers, C., Klemp, D., Rohrer, F., Mihelcic, D., Wegener, R., Kiendler-Scharr, A., and Wahner, A.: Twenty years of ambient observations of nitrogen oxides and specified hydrocarbons in air masses dominated by traffic emissions in Germany, Faraday Discuss., 189, 407–437, doi:10.1039/C5FD00180C, 2016.

Ehn, M., Thornton, J. A., Kleist, E., Sipilä, M., Junninen, H., Pullinen, I., Springer, M., Rubach, F., Tillmann, R., Lee, B., Lopez-Hilfiker, F., Andres, S., Acir, I.-H., Rissanen, M., Jokinen, T., Schobesberger, S., Kangasluoma, J., Kontkanen, J., Nieminen, T., Kurtén, T., Nielsen, L. B., Jørgensen, S., Kjaergaard, H. G., Canagaratna, M., Maso, M. D., Berndt, T., Petäjä, T., Wahner, A., Kerminen, V.-M., Kulmala, M., Worsnop, D. R., Wildt, J., and Mentel, T. F.: A large source of low-volatility secondary organic aerosol, Nature, 506, 476–479, doi:10.1038/nature13032, 2014.

Ehn, M., Berndt, T., Wildt, J., and Mentel, T.: Highly Oxygenated Molecules from Atmospheric Autoxidation of Hydrocarbons: A Prominent Challenge for Chemical Kinetics Studies, Int. J. Chem. Kinet., 49, 821–831, doi:10.1002/kin.21130, 2017.

EUPHORE: EUPHORE homepage, `http://www.ceam.es/WWWEUPHORE/home.htm`, 2023.

Eurochamp: Eurochamp-2020 homepage, `https://www.eurochamp.org/`, 2023.

Fei, J., Zhang, D. D., and Lee, H. F.: 1600 AD Huaynaputina Eruption (Peru), Abrupt Cooling, and Epidemics in China and Korea, Adv. Meteorol., 2016, 1–12, doi:10.1155/2016/3217038, 2016.

Finlayson-Pitts, B. J. and Pitts, J. N. J.: Chemistry of the Upper and Lower Atmosphere: Theory, Experiments, and Applications, Academic Press, 2000.

FORTH-ASC: FORTH-ASC homepage, `http://cstacc.iceht.forth.gr/research-facilities/experimental-facilities/laboratories`, 2023.

Fuchs, H., Holland, F., and Hofzumahaus, A.: Measurement of tropospheric RO_2 and HO_2 radicals by a laser-induced fluorescence instrument, Rev. Sci. Instrum., 79, 084 104, doi:10.1063/1.2968712, 2008.

Fuchs, H., Brauers, T., Dorn, H.-P., Harder, H., Häseler, R., Hofzumahaus, A., Holland, F., Kanaya, Y., Kajii, Y., Kubistin, D., Lou, S., Martinez, M., Miyamoto, K., Nishida, S., Rudolf, M., Schlosser, E., Wahner, A., Yoshino, A., and Schurath, U.: Technical Note: Formal blind intercomparison of HO_2 measurements in the atmosphere simulation chamber SAPHIR during the HOxComp campaign, Atmos. Chem. Phys., 10, 12 233–12 250, doi:10.5194/acp-10-12233-2010, 2010.

Fuchs, H., Bohn, B., Hofzumahaus, A., Holland, F., Lu, K. D., Nehr, S., Rohrer, F., and Wahner, A.: Detection of HO_2 by laser-induced fluorescence: calibration and interferences from RO_2 radicals, Atmos. Meas. Tech., 4, 1209–1225, doi:10.5194/amt-4-1209-2011, 2011.

Fuchs, H., Dorn, H.-P., Bachner, M., Bohn, B., Brauers, T., Gomm, S., Hofzumahaus, A., Holland, F., Nehr, S., Rohrer, F., Tillmann, R., and Wahner, A.: Comparison of OH concentration measurements by DOAS and LIF during SAPHIR chamber experiments at high OH reactivity and low NO concentration, Atmos. Meas. Tech., 5, 1611–1626, doi:10.5194/amt-5-1611-2012, 2012.

Fuchs, H., Tan, Z., Hofzumahaus, A., Broch, S., Dorn, H.-P., Holland, F., Künstler, C., Gomm, S., Rohrer, F., Schrade, S., Tillmann, R., and Wahner, A.: Investigation of potential interferences in the detection of atmospheric RO_x radicals by laser-induced fluorescence under dark conditions, Atmos. Meas. Tech., 9, 1431–1447, doi:10.5194/amt-9-1431-2016, 2016.

Gaffney, J. S. and Marley, N. A.: Chemistry of environmental systems: fundamental principles and analytical methods, John Wiley & Sons Ltd, first edition edn., 2020.

Galloway, M. M., Huisman, A. J., Yee, L. D., Chan, A. W. H., Loza, C. L., Seinfeld, J. H., and Keutsch, F. N.: Yields of oxidized volatile organic compounds during the OH radical initiated oxidation of isoprene, methyl vinyl ketone, and methacrolein under high-NO_x conditions, Atmos. Chem. Phys., 11, 10 779–10 790, doi:10.5194/acp-11-10779-2011, 2011.

Gaudel, A., Cooper, O. R., Chang, K.-L., Bourgeois, I., Ziemke, J. R., Strode, S. A., Oman, L. D., Sellitto, P., Nédélec, P., Blot, R., Thouret, V., and Granier, C.: Aircraft observations since the 1990s reveal increases of tropospheric ozone at multiple locations across the Northern Hemisphere, Sci. Adv., 6, eaba8272, doi:10.1126/sciadv.aba8272, 2020.

Gierczak, T., Burkholder, J. B., Bauerle, S., and Ravishankara, A. R.: Photochemistry of acetone under tropospheric conditions, Chem. Phys., 231, 229–244, doi:10.1016/S0301-0104(98)00006-8, 1998.

Gkatzelis, G. I., Coggon, M. M., McDonald, B. C., Peischl, J., Gilman, J. B., Aikin, K. C., Robinson, M. A., Canonaco, F., Prevot, A. S. H., Trainer, M., and Warneke, C.: Observations Confirm that Volatile Chemical Products Are a Major Source of Petrochemical Emissions in U.S. Cities, Environ. Sci. Technol., 55, 4332–4343, doi:10.1021/acs.est.0c05471, 2021.

Gligorovski, S., Strekowski, R., Barbati, S., and Vione, D.: Environmental Implications of Hydroxyl Radicals ($^{\bullet}OH$), Chem. Rev., 115, 13 051–13 092, doi:10.1021/cr500310b, 2015.

Goodhill, V.: Maimonides–modern medical relevance, Transactions of the American Academy of Ophthalmology and Otolaryngology, p. 463, 1971.

Griffith, S. M., Hansen, R. F., Dusanter, S., Michoud, V., Gilman, J. B., Kuster, W. C., Veres, P. R., Graus, M., De Gouw, J. A., Roberts, J., Young, C., Washenfelder, R., Brown, S. S., Thalman, R., Waxman, E., Volkamer, R., Tsai, C., Stutz, J., Flynn, J. H., Grossberg, N., Lefer, B., Alvarez, S. L., Rappenglueck, B., Mielke, L. H., Osthoff, H. D., and Stevens, P. S.: Measurements of hydroxyl and hydroperoxy radicals during CalNex-LA: Model comparisons and radical budgets, J. Geophys. Res. Atmos., 121, 4211–4232, doi:10.1002/2015JD024358, 2016.

Guenther, A. B., Jiang, X., Heald, C. L., Sakulyanontvittaya, T., Duhl, T., Emmons, L. K., and Wang, X.: The Model of Emissions of Gases and Aerosols from Nature version 2.1 (MEGAN2.1): an extended and updated framework for modeling biogenic emissions, Geoscientific Model Development, 5, 1471–1492, doi:10.5194/gmd-5-1471-2012, 2012.

Hakola, H., Arey, J., Aschmann, S., and Atkinson, R.: Product Formation from the Gas-Phase Reactions of OH Radicals and O_3 with a Series of Monoterpenes, J. Atmos. Chem., 18, 75–102, doi:10.1007/BF00694375, 1994.

Hallquist, M., WÄngberg, I., and LjungstrÖm, E.: Atmospheric Fate of Carbonyl Oxidation Products Originating from -Pinene and $_3$-Carene: Determination of Rate of Reaction with OH and NO_3 Radicals, UV Absorption Cross Sections, and Vapor Pressures, Environ. Sci. Technol., 31, 3166–3172, doi:10.1021/es970151a, 1997.

Hallquist, M., Wenger, J. C., Baltensperger, U., Rudich, Y., Simpson, D., Claeys, M., Dommen, J., Donahue, N. M., George, C., Goldstein, A. H., Hamilton, J. F., Herrmann, H., Hoffmann, T., Iinuma, Y., Jang, M., Jenkin, M. E., Jimenez, J. L., Kiendler-Scharr, A., Maenhaut, W., McFiggans, G., Mentel, T. F., Monod, A., Prévôt, A. S. H., Seinfeld, J. H., Surratt, J. D., Szmigielski, R., and Wildt, J.: The formation, properties and impact of secondary organic aerosol: current and emerging issues, Atmos. Chem. Phys., 9, 5155–5236, doi:10.5194/acp-9-5155-2009, 2009.

Hard, T. M., O'Brien, R. J., Cook, T. B., and Tsongas, G. A.: Interference suppression in HO fluorescence detection, Appl. Opt., 18, 3216–3217, doi:10.1364/AO.18.003216, 1979.

Hard, T. M., O'Brien, R. J., Chan, C. Y., and Mehrabzadeh, A. A.: Tropospheric free radical determination by fluorescence assay with gas expansion, Environ. Sci. Technol., 18, 768–777, doi:10.1021/es00128a009, 1984.

Hard, T. M., George, L. A., and O'Brien, R. J.: An Absolute Calibration for Gas-Phase Hydroxyl Measurements, Environ. Sci. Technol., 36, 1783–1790, doi:10.1021/es015646l, 2002.

Hatakeyama, S., Izumi, K., Fukuyama, T., Akimoto, H., and Washida, N.: Reactions of OH with -pinene and -pinene in air: Estimate of global CO production from the atmospheric oxidation of terpenes, J. Geophys. Res. Atmos., 96, 947–958, doi:10.1029/90JD02341, 1991.

Heard, D. E. and Pilling, M. J.: Measurement of OH and HO_2 in the Troposphere, Chem. Rev., 103, 5163–5198, doi:10.1021/cr020522s, 2003.

HELIOS: HELIOS homepage, `https://helios-cnrs.org/`, 2023.

Hoesly, R. M., Smith, S. J., Feng, L., Klimont, Z., Janssens-Maenhout, G., Pitkanen, T., Seibert, J. J., Vu, L., Andres, R. J., Bolt, R. M., Bond, T. C., Dawidowski, L., Kholod, N., Kurokawa, J.-i., Li, M., Liu, L., Lu, Z., Moura, M. C. P., O'Rourke, P. R., and Zhang, Q.: Historical (1750–2014) anthropogenic emissions of reactive gases and aerosols from the Community Emissions Data System (CEDS), Geosci. Model Dev., 11, 369–408, doi:10.5194/gmd-11-369-2018, 2018.

Hofzumahaus, A. and Holland, F.: Laser-induced fluorescence based detection system for measurement of tropospheric OH using 308 nm excitation at low pressure, in: Environmental Sensing '92, edited by Schiff, H. I. and Platt, U., pp. 163–173, Berlin, Federal Republic of Germany, doi:10.1117/12.140228, 1993.

Hofzumahaus, A., Dorn, H.-P., and Platt, U.: Tropospheric OH Radical Measurement Techniques: Recent Developments, in: Physico-Chemical Behaviour of Atmospheric Pollutants, edited by Restelli, G. and Angeletti, G., pp. 103–108, Springer Netherlands, Dordrecht, doi:10.1007/978-94-009-0567-2_16, 1990.

Hofzumahaus, A., Aschmutat, U., Heßling, M., Holland, F., and Ehhalt, D. H.: The measurement of tropospheric OH radicals by laser-induced fluorescence spectroscopy during the POPCORN Field Campaign, Geophys. Res. Lett., 23, 2541–2544, doi:10.1029/96GL02205, 1996.

Holland, F., Hessling, M., and Hofzumahaus, A.: In Situ Measurement of Tropospheric OH Radicals by Laser-Induced Fluorescence—A Description of the KFA Instrument, J. Atmos. Sci., 52, 3393 – 3401, doi:10.1175/1520-0469(1995)052<3393:ISMOTO>2.0.CO;2, 1995.

Holland, F., Hofzumahaus, A., Schäfer, J., Kraus, A., and Pätz, H.-W.: Measurements of OH and HO_2 radical concentrations and photolysis frequencies during BERLIOZ, J. Geophys. Res. Atmos., 108, PHO 2–1–PHO 2–23, doi:10.1029/2001JD001393, 2003.

ILMARI: ILMARI homepage, `https://sites.uef.fi/ilmari/`, 2023.

Intergovernmental Panel On Climate Change: Climate Change 2021 – The Physical Science Basis: Working Group I Contribution to the Sixth Assessment Report of the Intergovernmental Panel on Climate Change, Cambridge University Press, 1 edn., ISBN 978-1-00-915789-6, doi:10.1017/9781009157896, `https://www.cambridge.org/core/product/identifier/9781009157896/type/book`, 2023.

Isaksen, I. S. A. and Dalsøren, S. B.: Getting a Better Estimate of an Atmospheric Radical, Science, 331, 38–39, doi:10.1126/science.1199773, 2011.

Jaoui, M. and Kamens, R. M.: Mass balance of gaseous and particulate products analysis from -pinene/NO_x /air in the presence of natural sunlight, J. Geophys. Res. Atmos., 106, 12 541–12 558, doi:10.1029/2001JD900005, 2001.

Jenkin, M. E., Saunders, S. M., and Pilling, M. J.: The tropospheric degradation of volatile organic compounds: a protocol for mechanism development, Atmos. Environ., 31, 81–104, doi:10.1016/S1352-2310(96)00105-7, 1997.

Jenkin, M. E., Valorso, R., Aumont, B., and Rickard, A. R.: Estimation of rate coefficients and branching ratios for reactions of organic peroxy radicals for use in automated mechanism construction, Atmos. Chem. Phys., 19, 7691–7717, doi:10.5194/acp-19-7691-2019, 2019.

Jiang, Z., McDonald, B. C., Worden, H., Worden, J. R., Miyazaki, K., Qu, Z., Henze, D. K., Jones, D. B. A., Arellano, A. F., Fischer, E. V., Zhu, L., and Boersma, K. F.: Unexpected slowdown of US pollutant emission reduction in the past decade, Proc. Natl. Acad. Sci. U.S.A., 115, 5099–5104, doi:10.1073/pnas.1801191115, 2018.

Jokinen, T., Sipilä, M., Richters, S., Kerminen, V., Paasonen, P., Stratmann, F., Worsnop, D., Kulmala, M., Ehn, M., Herrmann, H., and Berndt, T.: Rapid Autoxidation Forms Highly Oxidized RO_2 Radicals in the Atmosphere, Angew. Chem. Int. Ed., 53, 14 596–14 600, doi:10.1002/anie.201408566, 2014.

Jørgensen, S., Knap, H. C., Otkjær, R. V., Jensen, A. M., Kjeldsen, M. L. H., Wennberg, P. O., and Kjaergaard, H. G.: Rapid Hydrogen Shift Scrambling in Hydroperoxy-Substituted Organic Peroxy Radicals, J. Phys. Chem. A, 120, 266–275, doi:10.1021/acs.jpca.5b06768, 2016.

Kaminski, M., Fuchs, H., Acir, I.-H., Bohn, B., Brauers, T., Dorn, H.-P., Häseler, R., Hofzumahaus, A., Li, X., Lutz, A., Nehr, S., Rohrer, F., Tillmann, R., Vereecken, L., Wegener, R., and Wahner, A.: Investigation of the -pinene photooxidation by OH in the atmosphere simulation chamber SAPHIR, Atmos. Chem. Phys., 17, 6631–6650, doi:10.5194/acp-17-6631-2017, 2017.

Kanakidou, M., Tsigaridis, K., Dentener, F. J., and Crutzen, P. J.: Human-activity-enhanced formation of organic aerosols by biogenic hydrocarbon oxidation, J. Geophys. Res. Atmos., 105, 9243–9354, doi:10.1029/1999JD901148, 2000.

Khan, M. A. H., Miles, B., Jenkin, M. E., Derwent, R. G., Percival, C. J., and Shallcross, D. E.: Investigating the Impacts of Nonacyl Peroxy Nitrates on the Global Composition of the Troposphere Using a 3-D Chemical Transport Model, STOCHEM-CRI, ACS Earth Space Chem., 4, 1201–1212, doi:10.1021/acsearthspacechem.0c00133, 2020.

Kim, S., McDonald, B. C., Seo, S., Kim, K., and Trainer, M.: Understanding the Paths of Surface Ozone Abatement in the Los Angeles Basin, J. Geophys. Res. Atmos., 127, e2021JD035 606, doi:10.1029/2021JD035606, 2022.

Künstler, C.: Measurements of Atmospheric OH and HO$_2$ Radicals by Laser-induced Fluorescence on the HALO Aircraft During the OMO-ASIA 2015 Campaign, vol. 495 of *Schriften des Forschungszentrums Jülich / Reihe Energie & Umwelt: Reihe Energie & Umwelt*, Forschungszentrum Jülich GmbH Zentralbibliothek, Verlag, ISBN 978-3-95806-477-5, `https://books.google.de/books?id=KVMDzgEACAAJ`, 2020.

Lamarque, J.-F., Bond, T. C., Eyring, V., Granier, C., Heil, A., Klimont, Z., Lee, D., Liousse, C., Mieville, A., Owen, B., Schultz, M. G., Shindell, D., Smith, S. J., Stehfest, E., Van Aardenne, J., Cooper, O. R., Kainuma, M., Mahowald, N., McConnell, J. R., Naik, V., Riahi, K., and Van Vuuren, D. P.: Historical (1850–2000) gridded anthropogenic and biomass burning emissions of reactive gases and aerosols: methodology and application, Atmos. Chem. Phys., 10, 7017–7039, doi:10.5194/acp-10-7017-2010, 2010.

Larsen, B. R., Di Bella, D., Glasius, M., Winterhalter, R., Jensen, N. R., and Hjorth, J.: Gas-Phase OH Oxidation of Monoterpenes: Gaseous and Particulate Products, J. Atmos. Chem., 38, 231–276, doi:10.1023/A:1006487530903, 2001.

Laughner, J. L. and Cohen, R. C.: Direct observation of changing NO$_x$ lifetime in North American cities, Science, 366, 723–727, doi:10.1126/science.aax6832, 2019.

Lee, A., Goldstein, A. H., Kroll, J. H., Ng, N. L., Varutbangkul, V., Flagan, R. C., and Seinfeld, J. H.: Gas-phase products and secondary aerosol yields from the photooxidation of 16 different terpenes, J. Geophys. Res. Atmos., 111, 2006JD007 050, doi:10.1029/2006JD007050, 2006.

Lee, B. H., Iyer, S., Kurtén, T., Varelas, J. G., Luo, J., Thomson, R. J., and Thornton, J. A.: Ring-opening yields and auto-oxidation rates of the resulting peroxy radicals from OH-oxidation of -pinene and -pinene, Environ. Sci.: Atmos., 3, 399–407, doi:10.1039/D2EA00133K, 2023.

Lengel, R. K. and Crosley, D. R.: Energy transfer in $A^2\Sigma^+$ OH. I. Rotational, J. Chem. Phys., 67, 2085–2101, doi:10.1063/1.435095, 1977.

Lengel, R. K. and Crosley, D. R.: Energy transfer in $A^2\Sigma^+$ OH. II. Vibrational, J. Chem. Phys., 68, 5309–5324, doi:10.1063/1.435707, 1978.

Li, K., Jacob, D. J., Liao, H., Shen, L., Zhang, Q., and Bates, K. H.: Anthropogenic drivers of 2013–2017 trends in summer surface ozone in China, Proc. Natl. Acad. Sci. U.S.A., 116, 422–427, doi:10.1073/pnas.1812168116, 2019a.

Li, K., Jacob, D. J., Liao, H., Zhu, J., Shah, V., Shen, L., Bates, K. H., Zhang, Q., and Zhai, S.: A two-pollutant strategy for improving ozone and particulate air quality in China, Nat. Geosci., 12, 906–910, doi:10.1038/s41561-019-0464-x, 2019b.

Liebmann, J., Karu, E., Sobanski, N., Schuladen, J., Ehn, M., Schallhart, S., Quéléver, L., Hellen, H., Hakola, H., Hoffmann, T., Williams, J., Fischer, H., Lelieveld, J., and Crowley, J. N.: Direct measurement of NO_3 radical reactivity in a boreal forest, Atmos. Chem. Phys., 18, 3799–3815, doi:10.5194/acp-18-3799-2018, 2018.

MAC: The Manchester Aerosol Chamber homepage, `http://www.cas.manchester.ac.uk/restools/aerosolchamber/`, 2023.

Martinez, M.: OH and HO_2 concentrations, sources, and loss rates during the Southern Oxidants Study in Nashville, Tennessee, summer 1999, J. Geophys. Res., 108, 4617, doi:10.1029/2003JD003551, 2003.

McDonald, B. C., De Gouw, J. A., Gilman, J. B., Jathar, S. H., Akherati, A., Cappa, C. D., Jimenez, J. L., Lee-Taylor, J., Hayes, P. L., McKeen, S. A., Cui, Y. Y., Kim, S.-W., Gentner, D. R., Isaacman-VanWertz, G., Goldstein, A. H., Harley, R. A., Frost, G. J., Roberts, J. M., Ryerson, T. B., and Trainer, M.: Volatile chemical products emerging as largest petrochemical source of urban organic emissions, Science, 359, 760–764, doi:10.1126/science.aaq0524, 2018.

McGee, T. and McIlrath, T.: Absolute OH absorption cross sections (for lidar measurements), J. Quant. Spectrosc. Radiat. Transf., 32, 179–184, doi:10.1016/0022-4073(84)90082-7, 1984.

McHugh, K., Cummins, T., and Aherne, J.: Distribution and Long-Term Trends of Tropospheric Ozone Concentrations in Ireland, Atmosphere, 14, 569, doi:10.3390/atmos14030569, 2023.

McVay, R. C., Zhang, X., Aumont, B., Valorso, R., Camredon, M., La, Y. S., Wennberg, P. O., and Seinfeld, J. H.: SOA formation from the photooxidation of -pinene: systematic exploration of the simulation of chamber data, Atmos. Chem. Phys., 16, 2785–2802, doi:10.5194/acp-16-2785-2016, 2016.

Mentel, T. F., Wildt, J., Kiendler-Scharr, A., Kleist, E., Tillmann, R., Dal Maso, M., Fisseha, R., Hohaus, T., Spahn, H., Uerlings, R., Wegener, R., Griffiths, P. T., Dinar, E., Rudich, Y., and Wahner, A.: Photochemical production of aerosols from real plant emissions, Atmospheric Chemistry and Physics, 9, 4387–4406, doi:10.5194/acp-9-4387-2009, 2009.

Miyoshi, A.: Molecular size dependent falloff rate constants for the recombination reactions of alkyl radicals with O_2 and implications for simplified kinetics of alkylperoxy radicals, Int. J. Chem. Kinet., 44, 59–74, doi:10.1002/kin.20623, 2012.

Moortgat, G. K., Seiler, W., and Warneck, P.: Photodissociation of HCHO in air: CO and H_2 quantum yields at 220 and 300 K, J. Chem. Phys., 78, 1185–1190, doi:10.1063/1.444911, 1983.

Mutzel, A., Zhang, Y., Böge, O., Rodigast, M., Kolodziejczyk, A., Wang, X., and Herrmann, H.: Importance of secondary organic aerosol formation of -pinene, limonene, and m-cresol comparing day- and nighttime radical chemistry, Atmos. Chem. Phys., 21, 8479–8498, doi:10.5194/acp-21-8479-2021, 2021.

Newland, M. J., Nelson, B. S., Muñoz, A., Ródenas, M., Vera, T., Tárrega, J., and Rickard, A. R.: Trends in stabilisation of Criegee intermediates from alkene ozonolysis, Phys. Chem. Chem. Phys., 22, 13 698–13 706, doi:10.1039/D0CP00897D, 2020.

Newland, M. J., Mouchel-Vallon, C., Valorso, R., Aumont, B., Vereecken, L., Jenkin, M. E., and Rickard, A. R.: Estimation of mechanistic parameters in the gas-phase reactions of ozone with alkenes for use in automated mechanism construction, Atmos. Chem. Phys., 22, 6167–6195, doi:10.5194/acp-22-6167-2022, 2022.

Ng, N. L., Kroll, J. H., Keywood, M. D., Bahreini, R., Varutbangkul, V., Flagan, R. C., Seinfeld, J. H., Lee, A., and Goldstein, A. H.: Contribution of First- versus Second-Generation Products to Secondary Organic Aerosols Formed in the Oxidation of Biogenic Hydrocarbons, Environ. Sci. Technol., 40, 2283–2297, doi:10.1021/es052269u, 2006.

Ng, N. L., Chhabra, P. S., Chan, A. W. H., Surratt, J. D., Kroll, J. H., Kwan, A. J., McCabe, D. C., Wennberg, P. O., Sorooshian, A., Murphy, S. M., Dalleska, N. F., Flagan, R. C., and Seinfeld, J. H.: Effect of NO_x level on secondary organic aerosol (SOA) formation from the photooxidation of terpenes, Atmos. Chem. Phys., 7, 5159–5174, doi:10.5194/acp-7-5159-2007, 2007.

Novelli, A., Hens, K., Tatum Ernest, C., Kubistin, D., Regelin, E., Elste, T., Plass-Dülmer, C., Martinez, M., Lelieveld, J., and Harder, H.: Characterisation of an inlet pre-injector laser-induced fluorescence instrument for the measurement of atmospheric hydroxyl radicals, Atmos. Meas. Tech., 7, 3413–3430, doi:10.5194/amt-7-3413-2014, 2014.

Novelli, A., Cho, C., Fuchs, H., Hofzumahaus, A., Rohrer, F., Tillmann, R., Kiendler-Scharr, A., Wahner, A., and Vereecken, L.: Experimental and theoretical study on the impact of a nitrate group on the chemistry of alkoxy radicals, Phys. Chem. Chem. Phys., 23, 5474–5495, doi:10.1039/D0CP05555G, 2021.

Nozière, B. and Vereecken, L.: Direct Observation of Aliphatic Peroxy Radical Autoxidation and Water Effects: An Experimental and Theoretical Study, Angew. Chem. Int. Ed., 58, 13 976–13 982, doi:10.1002/anie.201907981, 2019.

Nozière, B., Barnes, I., and Becker, K.: Product study and mechanisms of the reactions of -pinene and of pinonaldehyde with OH radicals, J. Geophys. Res. Atmos., 104, 23 645–23 656, doi:10.1029/1999JD900778, 1999.

Nölscher, A. C., Williams, J., Sinha, V., Custer, T., Song, W., Johnson, A. M., Axinte, R., Bozem, H., Fischer, H., Pouvesle, N., Phillips, G., Crowley, J. N., Rantala, P., Rinne, J., Kulmala, M., Gonzales, D., Valverde-Canossa, J., Vogel, A., Hoffmann, T., Ouwersloot, H. G., Vilà-Guerau De Arellano, J., and Lelieveld, J.: Summertime total OH reactivity measurements from boreal forest during HUMPPA-COPEC 2010, Atmos. Chem. Phys., 12, 8257–8270, doi:10.5194/acp-12-8257-2012, 2012.

Orlando, J. J. and Tyndall, G. S.: Laboratory studies of organic peroxy radical chemistry: an overview with emphasis on recent issues of atmospheric significance, Chem. Soc. Rev., 41, 6294–6317, doi:10.1039/C2CS35166H, 2012.

Orlando, J. J., Nozière, B., Tyndall, G. S., Orzechowska, G. E., Paulson, S. E., and Rudich, Y.: Product studies of the OH- and ozone-initiated oxidation of some monoterpenes, J. Geophys. Res. Atmos., 105, 11 561–11 572, doi:10.1029/2000JD900005, 2000.

Orlando, J. J., Tyndall, G. S., and Wallington, T. J.: The Atmospheric Chemistry of Alkoxy Radicals, Chem. Rev., 103, 4657–4690, doi:10.1021/cr020527p, 2003.

PACS-C3: PACS homepage, `https://www.psi.ch/en/lac/smog-chamber`, 2023.

Pathak, R. K., Presto, A. A., Lane, T. E., Stanier, C. O., Donahue, N. M., and Pandis, S. N.: Ozonolysis of -pinene: parameterization of secondary organic aerosol mass fraction, Atmospheric Chemistry and Physics, 7, 3811–3821, doi:10.5194/acp-7-3811-2007, 2007.

Peeters, J., Fantechi, G., and Vereecken, L.: A Generalized Structure-Activity Relationship for the Decomposition of (Substituted) Alkoxy Radicals, J. Atmos. Chem., 48, 59–80, doi:10.1023/B:JOCH.0000034510.07694.ce, 2004.

Piletic, I. R. and Kleindienst, T. E.: Rates and Yields of Unimolecular Reactions Producing Highly Oxidized Peroxy Radicals in the OH-Induced Autoxidation of -Pinene, -Pinene, and Limonene, J. Phys. Chem. A, 126, 88–100, doi:10.1021/acs.jpca.1c07961, 2022.

Pollack, I. B., Ryerson, T. B., Trainer, M., Neuman, J. A., Roberts, J. M., and Parrish, D. D.: Trends in ozone, its precursors, and related secondary oxidation products in Los Angeles, California: A synthesis of measurements from 1960 to 2010, J. Geophys. Res. Atmos., 118, 5893–5911, doi:10.1002/jgrd.50472, 2013.

Presto, A. A., Huff Hartz, K. E., and Donahue, N. M.: Secondary Organic Aerosol Production from Terpene Ozonolysis. 2. Effect of NO_x Concentration, Environ. Sci. Technol., 39, 7046–7054, doi:10.1021/es050400s, 2005.

Ren, X.: HOx concentrations and OH reactivity observations in New York City during PMTACS-NY2001, Atmos. Environ., 37, 3627–3637, doi:10.1016/S1352-2310(03)00460-6, 2003.

Ren, X., Harder, H., Martinez, M., Faloona, I. C., Tan, D., Lesher, R. L., Di Carlo, P., Simpas, J. B., and Brune, W. H.: Interference Testing for Atmospheric HO_x Measurements by Laser-induced Fluorescence, J. Atmos. Chem., 47, 169–190, doi:10.1023/B:JOCH.0000021037.46866.81, 2004.

Ren, X., Van Duin, D., Cazorla, M., Chen, S., Mao, J., Zhang, L., Brune, W. H., Flynn, J. H., Grossberg, N., Lefer, B. L., Rappenglück, B., Wong, K. W., Tsai, C., Stutz, J., Dibb, J. E., Thomas Jobson, B., Luke, W. T., and Kelley, P.: Atmospheric oxidation chemistry and ozone production: Results from SHARP 2009 in Houston, Texas, J. Geophys. Res. Atmos., 118, 5770–5780, doi:10.1002/jgrd.50342, 2013.

Rissanen, M.: Anthropogenic Volatile Organic Compound (AVOC) Autoxidation as a Source of Highly Oxygenated Organic Molecules (HOM), J. Phys. Chem. A, 125, 9027–9039, doi:10.1021/acs.jpca.1c06465, 2021.

Rodgers, M. O., Bradshaw, J. D., Sandholm, S. T., KeSheng, S., and Davis, D. D.: A 2-laser-induced fluorescence field instrument for ground-based and airborne measurements of atmospheric OH, J. Geophys. Res. Atmos., 90, 12 819–12 834, doi:10.1029/JD090iD07p12819, 1985.

Rohrer, F., Bohn, B., Brauers, T., Brüning, D., Johnen, F.-J., Wahner, A., and Kleffmann, J.: Characterisation of the photolytic HONO-source in the atmosphere simulation chamber SAPHIR, Atmos. Chem. Phys., 5, 2189–2201, doi:10.5194/acp-5-2189-2005, 2005.

Rolletter, M., Kaminski, M., Acir, I.-H., Bohn, B., Dorn, H.-P., Li, X., Lutz, A., Nehr, S., Rohrer, F., Tillmann, R., Wegener, R., Hofzumahaus, A., Kiendler-Scharr, A., Wahner, A., and Fuchs, H.: Investigation of the -pinene photooxidation by OH in the atmospheric simulation chamber SAPHIR, Atmospheric Chemistry and Physics, 19, 11 635–11 649, doi:10.5194/acp-19-11635-2019, 2019.

Rolletter, M., Blocquet, M., Kaminski, M., Bohn, B., Dorn, H.-P., Hofzumahaus, A., Holland, F., Li, X., Rohrer, F., Tillmann, R., Wegener, R., Kiendler-Scharr, A., Wahner, A., and Fuchs, H.: Photooxidation of pinonaldehyde at ambient conditions investigated in the atmospheric simulation chamber SAPHIR, Atmospheric Chemistry and Physics, 20, 13 701–13 719, doi:10.5194/acp-20-13701-2020, 2020.

Russell, A. G., Winner, D. A., Harley, R. A., McCue, K. F., and Cass, G. R.: Mathematical modeling and control of the dry deposition flux of nitrogen-containing air pollutants, Environ. Sci. Technol., 27, 2772–2782, doi:10.1021/es00049a016, 1993.

Saathoff, H., Naumann, K.-H., Möhler, O., Jonsson, M., Hallquist, M., Kiendler-Scharr, A., Mentel, T. F., Tillmann, R., and Schurath, U.: Temperature dependence of yields of secondary organic aerosols from the ozonolysis of -pinene and limonene, Atmos. Chem. Phys., 9, 1551–1577, doi:10.5194/acp-9-1551-2009, 2009.

SAPHIR: SAPHIR homepage, `https://www.fz-juelich.de/de/iek/iek-8/wissenschaftliche-infrastruktur/saphir`, 2023.

Saunders, S. M., Jenkin, M. E., Derwent, R. G., and Pilling, M. J.: Protocol for the development of the Master Chemical Mechanism, MCM v3 (Part A): tropospheric degradation of non-aromatic volatile organic compounds, Atmos. Chem. Phys., 3, 161–180, doi:10.5194/acp-3-161-2003, 2003.

Schlosser, E., Bohn, B., Brauers, T., Dorn, H.-P., Fuchs, H., Hässler, R., Hofzumahaus, A., Holland, F., Rohrer, F., Rupp, L.-O., Siese, M., Tillmann, R., and Wahner, A.: Intercomparison of Two Hydroxyl Radical Measurement Techniques at the Atmosphere Simulation Chamber SAPHIR, J. Atmos. Chem., 56, 187–205, doi:10.1007/s10874-006-9049-3, 2007.

Seinfield, J. H. and Pandis, S. N.: Atmospheric chemistry and physics: from air pollution to climate change, John Wiley & Sons, Inc., 2nd ed. edn., 2006.

Shilling, J. E., Chen, Q., King, S. M., Rosenoern, T., Kroll, J. H., Worsnop, D. R., McKinney, K. A., and Martin, S. T.: Particle mass yield in secondary organic aerosol formed by the dark ozonolysis of -pinene, Atmospheric Chemistry and Physics, 8, 2073–2088, doi:10.5194/acp-8-2073-2008, 2008.

Sicard, P., Paoletti, E., Agathokleous, E., Araminienė, V., Proietti, C., Coulibaly, F., and De Marco, A.: Ozone weekend effect in cities: Deep insights for urban air pollution control, Environ. Res., 191, 110 193, doi:10.1016/j.envres.2020.110193, 2020.

Skeie, R. B., Hodnebrog, and Myhre, G.: Trends in atmospheric methane concentrations since 1990 were driven and modified by anthropogenic emissions, Commun. Earth Environ., 4, 317, doi:10.1038/s43247-023-00969-1, 2023.

Skyttä, A., Gao, J., Cai, R., Ehn, M., Ahonen, L. R., Kurten, T., Wang, Z., Rissanen, M. P., and Kangasluoma, J.: Isomer-Resolved Mobility-Mass Analysis of -Pinene Ozonolysis Products, J. Phys. Chem. A, 126, 5040–5049, doi:10.1021/acs.jpca.2c03366, 2022.

Slater, E. J., Whalley, L. K., Woodward-Massey, R., Ye, C., Lee, J. D., Squires, F., Hopkins, J. R., Dunmore, R. E., Shaw, M., Hamilton, J. F., Lewis, A. C., Crilley, L. R., Kramer, L., Bloss, W., Vu, T., Sun, Y., Xu, W., Yue, S., Ren, L., Acton, W. J. F., Hewitt, C. N., Wang, X., Fu, P., and Heard, D. E.: Elevated levels of OH observed in haze events during wintertime in central Beijing, Atmos. Chem. Phys., 20, 14 847–14 871, doi:10.5194/acp-20-14847-2020, 2020.

Smith, G. P. and Crosley, D. R.: A photochemical model of ozone interference effects in laser detection of tropospheric OH, J. Geophys. Res. Atmos., 95, 16 427–16 442, doi:10.1029/JD095iD10p16427, 1990.

Somnitz, H. and Zellner, R.: Theoretical studies of unimolecular reactions of C_2–C_5 alkoxyl radicals. Part III. A microscopic structure activity relationship (SAR), Phys. Chem. Chem. Phys., 2, 4319–4325, doi:10.1039/b004022n, 2000.

Stauffer, H. U., Roy, S., Kulatilaka, W. D., and Gord, J. R.: Detailed calculation of hydroxyl (OH) radical two-photon absorption via broadband ultrafast excitation, J. Opt. Soc. Am. B, 29, 40–52, doi:10.1364/JOSAB.29.000040, 2012.

Stothers, R. B.: The Great Tambora Eruption in 1815 and Its Aftermath, Science, 224, 1191–1198, doi:10.1126/science.224.4654.1191, 1984.

Taatjes, C. A., Shallcross, D. E., and Percival, C. J.: Research frontiers in the chemistry of Criegee intermediates and tropospheric ozonolysis, Phys. Chem. Chem. Phys., 16, 1704, doi:10.1039/c3cp52842a, 2014.

Tan, Z., Fuchs, H., Lu, K., Hofzumahaus, A., Bohn, B., Broch, S., Dong, H., Gomm, S., Häseler, R., He, L., Holland, F., Li, X., Liu, Y., Lu, S., Rohrer, F., Shao, M., Wang, B., Wang, M., Wu, Y., Zeng, L., Zhang, Y., Wahner, A., and Zhang, Y.: Radical chemistry at a rural site (Wangdu) in the North China Plain: observation and model calculations of OH, HO_2 and RO_2 radicals, Atmos. Chem. Phys., 17, 663–690, doi:10.5194/acp-17-663-2017, 2017.

Tan, Z., Rohrer, F., Lu, K., Ma, X., Bohn, B., Broch, S., Dong, H., Fuchs, H., Gkatzelis, G. I., Hofzumahaus, A., Holland, F., Li, X., Liu, Y., Liu, Y., Novelli, A., Shao, M., Wang, H., Wu, Y., Zeng, L., Hu, M., Kiendler-Scharr, A., Wahner, A., and Zhang, Y.: Wintertime photochemistry in Beijing: observations of RO_x radical concentrations in the North China Plain during the BEST-ONE campaign, Atmos. Chem. Phys., 18, 12 391–12 411, doi:10.5194/acp-18-12391-2018, 2018.

Tan, Z., Lu, K., Hofzumahaus, A., Fuchs, H., Bohn, B., Holland, F., Liu, Y., Rohrer, F., Shao, M., Sun, K., Wu, Y., Zeng, L., Zhang, Y., Zou, Q., Kiendler-Scharr, A., Wahner, A., and Zhang, Y.: Experimental budgets of OH, HO_2, and RO_2 radicals and implications for ozone formation in the Pearl River Delta in China 2014, Atmos. Chem. Phys., 19, 7129–7150, doi:10.5194/acp-19-7129-2019, 2019.

Teng, A. P., Crounse, J. D., Lee, L., St. Clair, J. M., Cohen, R. C., and Wennberg, P. O.: Hydroxy nitrate production in the OH-initiated oxidation of alkenes, Atmos. Chem. Phys., 15, 4297–4316, doi:10.5194/acp-15-4297-2015, 2015.

Tillmann, R., Hallquist, M., Jonsson, A. M., Kiendler-Scharr, A., Saathoff, H., Iinuma, Y., and Mentel, T. F.: Influence of relative humidity and temperature on the production of pinonaldehyde and OH radicals from the ozonolysis of -pinene, Atmos. Chem. Phys., 10, 7057–7072, doi:10.5194/acp-10-7057-2010, 2010.

TROPOS: ACD-C homepage, `https://www.tropos.de/forschung/grossprojekte-infrastruktur-technologie/technologie-am-tropos/aerosolversuchsanlagen/leak`, 2023.

US Department of Commerce, N.: Global Monitoring Laboratory, `https://gml.noaa.gov/ccgg/trends/weekly.html`, 2024.

Vereecken, L.: The reaction of Criegee intermediates with acids and enols, Phys. Chem. Chem. Phys., 19, 28 630–28 640, doi:10.1039/C7CP05132H, 2017.

Vereecken, L. and Nozière, B.: H migration in peroxy radicals under atmospheric conditions, Atmos. Chem. Phys., 20, 7429–7458, doi:10.5194/acp-20-7429-2020, 2020.

Vereecken, L. and Peeters, J.: Decomposition of substituted alkoxy radicals—part I: a generalized structure–activity relationship for reaction barrier heights, Phys. Chem. Chem. Phys., 11, 9062–9074, doi:10.1039/B909712K, 2009.

Vereecken, L. and Peeters, J.: A structure–activity relationship for the rate coefficient of H-migration in substituted alkoxy radicals, Phys. Chem. Chem. Phys., 12, 12 608–12 620, doi:10.1039/C0CP00387E, 2010.

Vereecken, L., Nguyen, T., Hermans, I., and Peeters, J.: Computational study of the stability of -hydroperoxyl- or -alkylperoxyl substituted alkyl radicals, Chem. Phys. Lett., 393, 432–436, doi:10.1016/j.cplett.2004.06.076, 2004.

Vereecken, L., Müller, J.-F., and Peeters, J.: Low-volatility poly-oxygenates in the OH-initiated atmospheric oxidation of -pinene: impact of non-traditional peroxyl radical chemistry, Phys. Chem. Chem. Phys., 9, 5241–5248, doi:10.1039/B708023A, 2007.

Vereecken, L., Harder, H., and Novelli, A.: The reactions of Criegee intermediates with alkenes, ozone, and carbonyl oxides, Phys. Chem. Chem. Phys., 16, 4039, doi:10.1039/c3cp54514h, 2014.

Vereecken, L., Novelli, A., and Taraborrelli, D.: Unimolecular decay strongly limits the atmospheric impact of Criegee intermediates, Phys. Chem. Chem. Phys., 19, 31 599–31 612, doi:10.1039/C7CP05541B, 2017.

Vereecken, L., Carlsson, P. T. M., Novelli, A., Bernard, F., Brown, S. S., Cho, C., Crowley, J. N., Fuchs, H., Mellouki, W., Reimer, D., Shenolikar, J., Tillmann, R., Zhou, L., Kiendler-Scharr, A., and Wahner, A.: Theoretical and experimental study of peroxy and alkoxy radicals in the NO_3-initiated oxidation of isoprene, Phys. Chem. Chem. Phys., 23, 5496–5515, doi:10.1039/D0CP06267G, 2021.

Verosub, K. L. and Lippman, J.: Global Impacts of the 1600 Eruption of Peru's Huaynaputina Volcano, EoS Transactions, 89, 141–142, doi:10.1029/2008EO150001, 2008.

Visconti, G.: Fundamentals of Physics and Chemistry of the Atmospheres, Springer, 2nd edn., 2016.

Wallington, T. J., Anderson, J. E., Dolan, R. H., and Winkler, S. L.: Vehicle Emissions and Urban Air Quality: 60 Years of Progress, Atmosphere, 13, 650, doi:10.3390/atmos13050650, 2022.

Wang, C. C. and Davis, L. I.: Measurement of Hydroxyl Concentrations in Air Using a Tunable uv Laser Beam, Phys. Rev. Lett., 32, 349–352, doi:10.1103/PhysRevLett.32.349, 1974.

Wang, W., Fang, H., Zhang, Y., Ding, Y., Hua, F., Wu, T., and Yan, Y.: Characterizing sources and ozone formations of summertime volatile organic compounds observed in a medium-sized city in Yangtze River Delta region, Chemosphere, 328, 138 609, doi:10.1016/j.chemosphere.2023.138609, 2023.

Warneke, C., De Gouw, J. A., Holloway, J. S., Peischl, J., Ryerson, T. B., Atlas, E., Blake, D., Trainer, M., and Parrish, D. D.: Multiyear trends in volatile organic compounds in Los Angeles, California: Five decades of decreasing emissions, J. Geophys. Res. Atmos., 117, D00V17, doi:10.1029/2012JD017899, 2012.

Whalley, L. K., Stone, D., Dunmore, R., Hamilton, J., Hopkins, J. R., Lee, J. D., Lewis, A. C., Williams, P., Kleffmann, J., Laufs, S., Woodward-Massey, R., and Heard, D. E.: Understanding in situ ozone production in the summertime through radical observations and modelling studies during the Clean air for London project (ClearfLo), Atmos. Chem. Phys., 18, 2547–2571, doi:10.5194/acp-18-2547-2018, 2018.

Whalley, L. K., Slater, E. J., Woodward-Massey, R., Ye, C., Lee, J. D., Squires, F., Hopkins, J. R., Dunmore, R. E., Shaw, M., Hamilton, J. F., Lewis, A. C., Mehra, A., Worrall, S. D., Bacak, A., Bannan, T. J., Coe, H., Percival, C. J., Ouyang, B., Jones, R. L., Crilley, L. R., Kramer, L. J., Bloss, W. J., Vu, T., Kotthaus, S., Grimmond, S., Sun, Y., Xu, W., Yue, S., Ren, L., Acton, W. J. F., Hewitt, C. N., Wang, X., Fu, P., and Heard, D. E.: Evaluating the sensitivity of radical chemistry and ozone formation to ambient VOCs and NO_x in Beijing, Atmos. Chem. Phys., 21, 2125–2147, doi:10.5194/acp-21-2125-2021, 2021.

Wisthaler, A., Jensen, N., Winterhalter, R., Lindinger, W., and Hjorth, J.: Measurements of acetone and other gas phase product yields from the OH-initiated oxidation of terpenes by proton-transfer-reaction mass spectrometry (PTR-MS), Atmos. Environ., 35, 6181–6191, doi:10.1016/S1352-2310(01)00385-5, 2001.

Wong, K. W., Oh, H.-J., Lefer, B. L., Rappenglück, B., and Stutz, J.: Vertical profiles of nitrous acid in the nocturnal urban atmosphere of Houston, TX, Atmos. Chem. Phys., 11, 3595–3609, doi:10.5194/acp-11-3595-2011, 2011.

Woodward-Massey, R., Sommariva, R., Whalley, L. K., Cryer, D. R., Ingham, T., Bloss, W. J., Ball, S. M., Cox, S., Lee, J. D., Reed, C. P., Crilley, L. R., Kramer, L. J., Bandy, B. J., Forster, G. L., Reeves, C. E., Monks, P. S., and Heard, D. E.: Radical chemistry and ozone production at a UK coastal receptor site, Atmos. Chem. Phys., 23, 14 393–14 424, doi:10.5194/acp-23-14393-2023, 2023.

Wu, K., Zhu, S., Mac Kinnon, M., and Samuelsen, S.: Unexpected deterioration of O_3 pollution in the South Coast Air Basin of California: The role of meteorology and emissions, Environ. Pollut., 330, 121 728, doi:10.1016/j.envpol.2023.121728, 2023.

Zhao, D., Schmitt, S. H., Wang, M., Acir, I.-H., Tillmann, R., Tan, Z., Novelli, A., Fuchs, H., Pullinen, I., Wegener, R., Rohrer, F., Wildt, J., Kiendler-Scharr, A., Wahner, A., and Mentel, T. F.: Effects of NO_x and SO_2 on the secondary organic aerosol formation from photooxidation of -pinene and limonene, Atmos. Chem. Phys., 18, 1611–1628, doi:10.5194/acp-18-1611-2018, 2018.

Zádor, J., Turányi, T., Wirtz, K., and Pilling, M. J.: Measurement and investigation of chamber radical sources in the European Photoreactor (EUPHORE), J Atmos Chem, 55, 147–166, doi:10.1007/s10874-006-9033-y, 2006.

List of Figures

List of Tables

Acknowledgments

Many people have accompanied and supported me during my time in Jülich, and I would like to take this opportunity to deeply thank them. Without you, this work would not have been possible.

First of all, I would like to thank Prof. Dr. Andreas Wahner and Prof. Dr. Hendrik Fuchs for giving me the opportunity of writing my PhD thesis at the Institute for Energy and Climate Research, IEK-8: Troposphere at Forschungszentrum Jülich.

I would like to deeply thank my Doktorvater Prof. Dr. Hendrik Fuchs for his enduring support, his patience, and his trust in me. Despite his full schedule, he took his time introducing me to the LIF instrument, and he always had time for discussing my work, which I am very grateful for. Furthermore, I would like to thank him for his guidance and his effort in improving this work.

I am grateful to Prof. Dr. Peter Wiesen for acting as a second reviewer of my thesis. Furthermore, I would like to thank Prof. Dr. Andreas Zilges for supporting me throughout my studies and for accepting to act as chair of my thesis defence committee.

A special thank you goes to Dr. Anna Novelli. Her endless motivation, her patience, and her positive attitude helped me throughout my PhD. No matter how often I came up with a spontaneous idea or forgot another one, she supported me and tried to keep me on track. Even though we sometimes talked past each other, our discussions were always entertaining and eventually we agreed on one perspective. It was a pleasure working with you together on the LIF instrument and on the papers.

Furthermore, I would like to thank Dr. Luc Vereecken for fruitful discussions and his valuable ideas, which improved this work.

For helping me realising the numerous experiments in SAPHIR, I would like to thank the entire SAPHIR team.

I also like to thank the entire LIF group who warmly welcomed me at the IEK-8. A special thanks goes to Dr. Frank Holland who was always very supportive whenever I could not find something or needed help with IDL. I also would like to thank Mathias Bachner for introducing me to the data processing of the LIF instrument and for his help in solving software problems. In addition, I would like to thank Aaron Stainsby for the harmonious atmosphere in our office.

A special thanks goes to Tobias Schuldt and Patrick Weber, who made my time in Jülich even more enjoyable.

I am very grateful to my friends and family for your enduring support. Danke Elena und Jojo für eure langjährige Freundschaft. Des Weiteren möchte ich Lukas für seine Unterstützung und sein großartiges Verständnis für meine Arbeitseinstellung danken. Mein größter Dank gilt Mama, Papa, Niklas und Nathalie für eure endlose Unterstützung und Begleitung auf meinem Lebensweg, eure verrückten Ideen und für eure ablenkenden Steuergespräche. Ich

würde euch um nichts in der Welt eintauschen wollen. Ein großer Dank geht insbesondere an Nathalie, die mich auch an den schlimmsten Tagen ertragen musste und mich stetig umsorgt. Um diese Arbeit mit ihren Worten abzuschließen: Dies war “Michelles Reise in die Welt der Umweltphysik: Ein Ausschnitt aus vier lehrreichen und experimentellen Jahren der Forschung”.

A | Appendix

A.1 Supplementary materials to Chapter 2

A.1.1 Detailed information about the participating simulation chambers

Table A.1: Overview of the properties of the outdoor simulation chambers, which participated in the presented multi-chamber study. The dilution rates and the wall effects correspond to mean values determined in the analysed experiments, if not otherwise noted. The general properties are taken from the EUROCHAMP webpage (Eurochamp, 2023).

Chamber	HELIOS[a]	EUPHORE[b]	SAPHIR[c]
Institution	CNRS[d]-Orléans	CEAM[e]	FZJ[f]
Geometry	hemisphere	hemisphere	cylinder
Volume [m]	90	200	270
S/V ratio [m]	1.2	1	1
Wall material	FEP	FEP	FEP
OH precursors	H O , HONO (wall)	HONO (wall)	O , HONO (wall)
Dilution rate [s]	^{g}	^{g}	^{h}
Wall loss rate [s]			
HCHO			
Pinonaldehyde			
Aerosol			
Wall emission rate [ppbv h]			
HONO (dark)			
HONO (light)	0.017[i]	^{i}	0.16
HCHO (dark)	0.35		
HCHO (light)	0.58		
Acetone			
Pinonaldeyhde:			

[a] cHambrE de simuLation atmosphérique à Irradiation naturel d'OrléanS; [b] EUropean PHOtoREactor; [c] Simulation of Atmospheric PHotochemistry In a large Reaction chamber; [d] Centre National de la Recherche Scientifique; [e] Mediterranean Centre for Environmental Studies; [f] Research Centre Jülich; [g] Determined from measured decrease of SF concentration; [h] Derived from the measured replenishment flow; [i] Taken from the auxiliary mechanism, provided by the chambers (Eurochamp, 2023).

Table A.2: Overview of indoor simulation chambers, which participated in the presented multi-chamber study, and their individual properties. Dilution rates and wall effects correspond to mean values determined in the analysed experiments, otherwise noted. General properties were taken from the EUROCHAMP webpage (Eurochamp, 2023).

Chamber	CESAM[a]	FORTH-ASC[b]	MAC[c]	LEAK[d]	PACS-C3[e]	ILMARI[f]
Institution	CNRS[g]-LISA	FORTH[h]	UMAN[i]	TROPOS[j]	PSI[k]	UEF[l]
Geometry	cylinder	cube	cube	cylinder	cube	cube
Volume [m]	4.2	10	18	19	27	29.4
S/V ratio [m]	4.3	2.7	2.3	2	2	2
Wall material	stainless steel	FEP	FEP	FEP	FEP	FEP
OH source in the experiment	NO ,	NO	NO	(H O /HONO)	HONO, HONO (wall)	H O , HONO (wall)
Temperature control	C	C	C	C	C	C
Artificial light source	Xe arc lamps	blacklight lamps	arc lamps, halogen bulbs	UV lamps, blacklight lamps, mercury lamps	Xe arc lamps, blacklight lamps	blacklight lamps
$_{\mathrm{NO}_2}$ [s]						
Dilution rate [s]		_^{m}	_^{m}	_^{m}	^{o}	_^{m}
Wall loss rate [s]						
-pinene				2.0^{p}		
Pinonaldehyde						

Continued.

Chamber	CESAM[a]	FORTH-ASC[b]	MAC[c]	LEAK[d]	PACS-C3[e]	ILMARI[f]
Aerosol						
Wall emission rate [ppbv h]						
HCHO (dark)						
HCHO (light)					2[p]	

[a] cHambrE de simuLation atmosphérique à Irradiation naturel d'OrléanS - Laboratoire Interuniversitaire des Systèmes Atmosphériques; [b] FORTH-Atmospheric Simulation Chamber; [c] Manchester Aerosol Chamber; [d] LEipziger AErosolKammer; [e] PSI Atmospheric Chemistry Simulation Chambers; [f] Aersol physics, chemistry and toxicology research unit; [g] Centre National de la Recherche Scientifique; [h] FOundation for Research and Technology Hellas; [i] University of Manchester; [j] Leibniz institute for TROPOSpheric research; [k] Paul Scherrer institute; [l] University of Eastern Finland; [m] Collapsible bag; [o] Determined from decrease of the water vapour concentration; [p] Taken from the auxiliary mechanism, provided by the chambers (Eurochamp, 2023).

A.1.2 List of experimental conditions for each experiment

Table A.3: Experimental, chemical conditions in the different chamber experiments. The maximum concentrations of -pinene, NO_x (NO, NO), OH, O , H O , and HONO are listed. Entries marked with mark species that were injected. Labels of experiments including “s” indicate experiments with seed aerosol. No data were provided if no value is listed. OH radical concentrations were determined from the decreasing concentration of -pinene in most experiments. If more than one value is given, more than one injection of the species was done.

Chamber	Experiment (date)	-pinene [ppbv]	NO [ppbv]	NO [ppbv]	OH [cm]	O [ppbv]	H O [ppbv]	HONO [ppbv]	RH [%]
HELIOS	H1 (21.10.2018)	10	0.2	0.2	1.6	0.7	300	0.05	
	H2 (22.10.2018)	10	15	6	2.4	6	290	0.35	dry
EUPHORE	E1.1 (19.02.2019)	12	200	37	0.9	22	-	4.5	
	E1.2 (19.02.2019)	92	200	37	0.9	22	-	4.5	
	E1.1 (20.02.2019)	12	200	7	2	3.5	-	4.5	
	E1.2 (20.02.2019)	96	183	34	0.9	96	-	4.7	
	E2.1 (14.01.2019)	100	0.8	0	0.4	2	-	0.2	
	E2.2 (14.01.2019)	100	5	6	2	27	-	0.7	
	E2.1 (15.01.2019)	105	0.7	0	0.4	2	-	0.2	
	E2.2 (15.01.2019)	103	7	6.5	2	28	-	0.6	
	E2.1 (16.01.2019)	105	0.7	0.2	0.4	3	-	0.2	
	E2.2 (16.01.2019)	105	6.6	7	1.7	30	-	778	
	E3 (18.01.2019)	105	8	5.5	1.8	24	-	5.1	36
SAPHIR	S1 (30.08.2012)		0.2	0.8	4	53	-	0.3	
	S2 (02.07.2014)		0.2	0.7	4	44	-	0.2	
CESAM	C1 (13.02.2019)	116	200	75	7	72	-	-	
	C2 (14.02.2019)	184	8	24	3	26	-	-	50
	C2 (15.02.2019)	200	6	6	2	23	-	-	50

Continued.

Chamber	Experiment (date)	-pinene [ppbv]	NO [ppbv]	NO [ppbv]	OH [cm]	O [ppbv]	H O [ppbv]	HONO [ppbv]	RH [%]
	C3 (19.03.2019)	113	160	62	4	37	-	-	
FORTH-ASC	F1s (24.07.2018)	120	31	262	11	102	-	-	27
	F2s (11.07.2018)	162	49	176	3	140	-	-	14
MAC	M1 (23.10.2018)	45	41	162	2	35	-	-	50
	M2 (02.11.2018)	80	70	133	1	62	-	-	15
	M3 (31.10.2018)	80	5	7	1	26	-	-	40
	M4 (30.10.2018)	90	100	120	1	28	-	-	50
	M5 (01.11.2018)	70	70	130	3	40	-	-	55
LEAK	L1s (01.08.2018)	10	33	33	2	33	-	-	50
	L2s (15.08.2018)	10	0.4	1.6	2	9	-	-	50
	L3 (16.08.2018)	3.5	9	6	4.5	14	-	-	50
	L4 (18.07.2018)	100	0.6	1	0.4	4	-	-	0
PACS-C3	P1 (03.01.2019)	6	-	-	10	245	-	-	45
	P2 (01.01.2019)	55	-	-	6	320	-	-	40
	P3 (05.01.2019)	55	-	-	4	135	-	-	50
	P4 (02.01.2019)	75	-	-	6	160	-	-	50
ILMARI	I1s (19.03.2018)	10	11	14	8	110	-	-	65
	I2 (27.03.2018)	110	30	11	6	68	-	-	55
	I3 (26.03.2018)	110	0	4	4	26	-	-	55

A.1.3 Correction of time series of gas-phase products for the calculation of product yields

Similar to -pinene, measured concentrations of the gas-phase products pinonaldehyde (PINAL), formaldehyde (HCHO), and acetone (ACETONE) were corrected for other destruction and production path than their production by the oxidation of -pinene by OH (Galloway et al., 2011; Kaminski et al., 2017):

$$\frac{\mathrm{d\ PINAL}}{\mathrm{d}} \qquad \mathrm{PINAL} \qquad \mathrm{PINAL} \quad {}_{\mathrm{PINAL}}\ \mathrm{PINAL}$$

$${}_{\mathrm{OH}}\ {}_{\mathrm{PINAL}}\ \mathrm{OH}\ \ \mathrm{PINAL} \tag{A.1}$$

$$\frac{\mathrm{d\ ACETONE}}{\mathrm{d}} \qquad \mathrm{ACETONE} \quad {}_{\mathrm{OH}}\ {}_{\mathrm{ACETONE}}\ \mathrm{OH}\ \ \mathrm{ACETONE}$$

$${}_{\mathrm{ACETONE}}\ \mathrm{ACETONE} \tag{A.2}$$

$$\frac{\mathrm{d\ HCHO}}{\mathrm{d}} \qquad \mathrm{HCHO} \qquad \mathrm{HCHO} \quad {}_{\mathrm{HCHO}}\ \mathrm{HCHO}$$

$${}_{\mathrm{OH}}\ {}_{\mathrm{HCHO}}\ \mathrm{OH}\ \ \mathrm{HCHO} \tag{A.3}$$

Rate constants for the reaction of OH with the products (X = PINAL, HCHO, ACETONE) are denoted as ${}_{\mathrm{OH}}\ {}_{\mathrm{X}}$. Furthermore, the loss of the organic species by photolysis is accounted for by the photolysis frequencies ${}_{\mathrm{PINAL}}$, ${}_{\mathrm{ACETONE}}$, and ${}_{\mathrm{HCHO}}$.

Photolysis frequencies were derived from the measured actinic flux (outdoor chambers) or from lamp spectra (indoor chambers) according to:

$$\mathrm{d} \tag{A.4}$$

with being the photon flux, the absorption cross section, and the quantum yield . For indoor chambers the photon flux was given by the chambers providers while values of the absorption cross sections and the quantum yield were taken from Atkinson et al. (2006). The absorption cross section and the quantum yield for the photolysis of pinonaldehyde were taken from Hallquist et al. (2009) and Rolletter et al. (2020). For the HELIOS and EUPHORE outdoor chambers, only photolysis frequency of NO were provided and no actinic flux measurements were available. Therefore, for these chambers the photolysis frequency of pinonaldehyde was approximated by scaling the measured ${}_{\mathrm{NO_2}}$ with the same factor as calculated from photolysis frequencies in the SAPHIR outdoor chamber (${}_{\mathrm{PINAL}}$ ${}_{\mathrm{NO_2}}$). This neglects the differences in the absorption spectra.

A.1.4 Further experiments analysed in the multi-chamber study

HELIOS

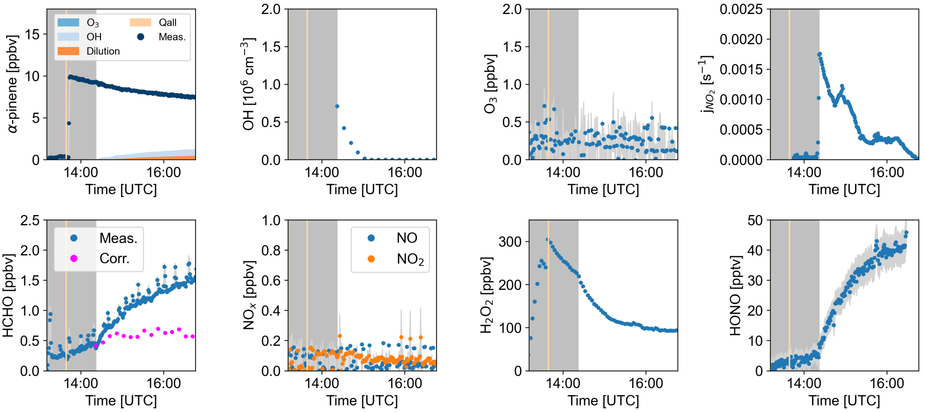

Figure A.1: Time series of trace gas concentrations measured in the experiment H1 (Tab. A.3) performed in the HELIOS chamber. Different contributions of the loss paths of -pinene are shown by coloured areas together with the time series of the -pinene concentration. OH radical concentrations are derived from the corrected time series of -pinene concentrations according to Eq. (2.8). Injections of -pinene into the chamber are marked by yellow, vertical lines. A relative humidity of % and temperatures between C and C were present during the experiment.

EUPHORE

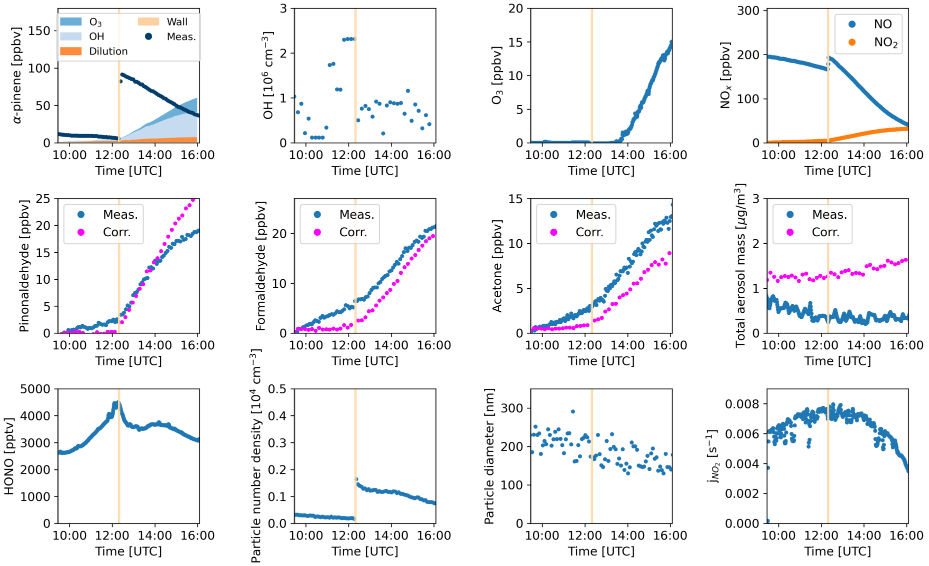

Figure A.2: Time series of trace gas concentrations measured in the experiment E1 performed on the 19 of February 2019 in the EUPHORE chamber (Tab. A.3). Different contributions of the loss paths of -pinene are shown by coloured areas together with the time series of the -pinene concentration. OH radical concentrations are derived from the corrected time series of -pinene concentrations according to Eq. (2.8). Injections of -pinene into the chamber are marked by yellow, vertical lines. "ND" and "Dia" refer to the particle number density and the mean particle diameter. A relative humidity of less than % and temperatures between C and C were present during the experiment.

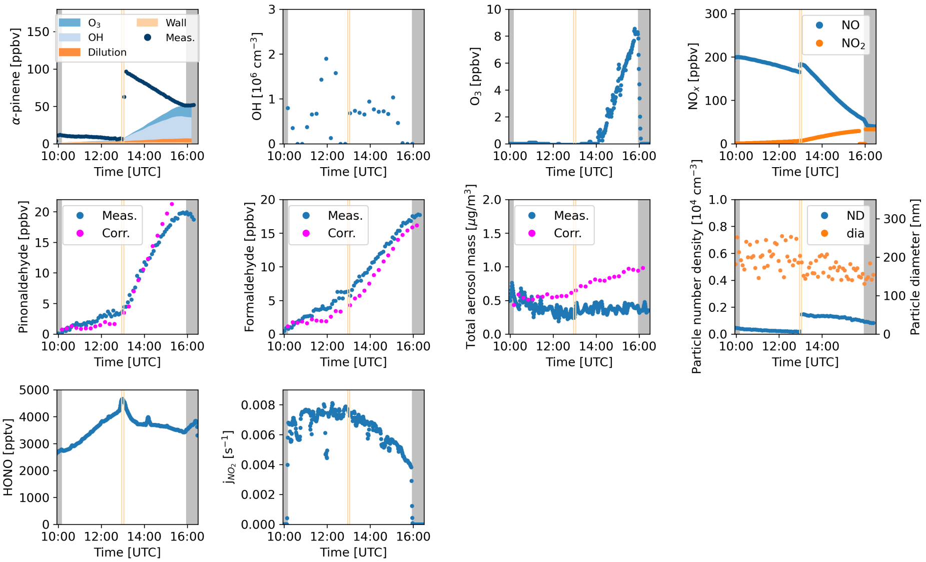

Figure A.3: Time series of trace gas concentrations measured in the experiment E1 performed on the 20 of February 2019 in the EUPHORE chamber (Tab. A.3). Different contributions of the loss paths of -pinene are shown by coloured areas together with the time series of the -pinene concentration. OH radical concentrations are derived from the corrected time series of -pinene concentrations according to Eq. (2.8). Injections of -pinene into the chamber are marked by yellow, vertical lines and dark conditions are indicated by grey areas. “ND” and “Dia” refer to the particle number density and the mean particle diameter. A relative humidity below % was present during the experiment. The temperature increased from C to C at about 13:00 UTC and decreased afterwards to C.

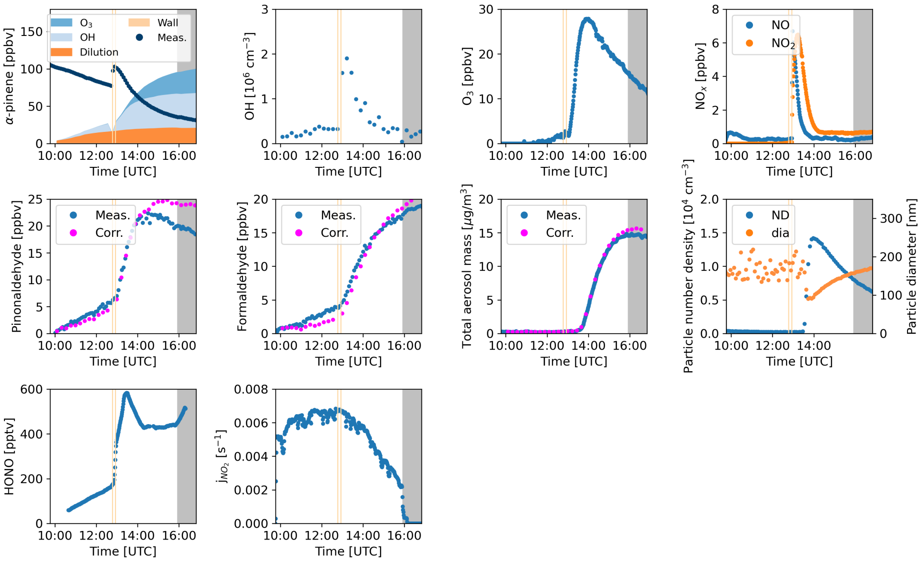

Figure A.4: Time series of trace gas concentrations measured in the experiment E2 performed on the 15 of January 2019 in the EUPHORE chamber (Tab. A.3). Different contributions of the loss paths of -pinene are shown by coloured areas, together with the time series of the -pinene concentration. OH radical concentrations were derived from the corrected time series of -pinene concentrations according to Eq. (2.8). Injections of -pinene into the chamber are marked by yellow, vertical lines. "ND" and "Dia" refer to the particle number density and the mean particle diameter. A relative humidity below % was present during the experiment. The temperature increased from C to C after the roof opening and decreased afterwards to C.

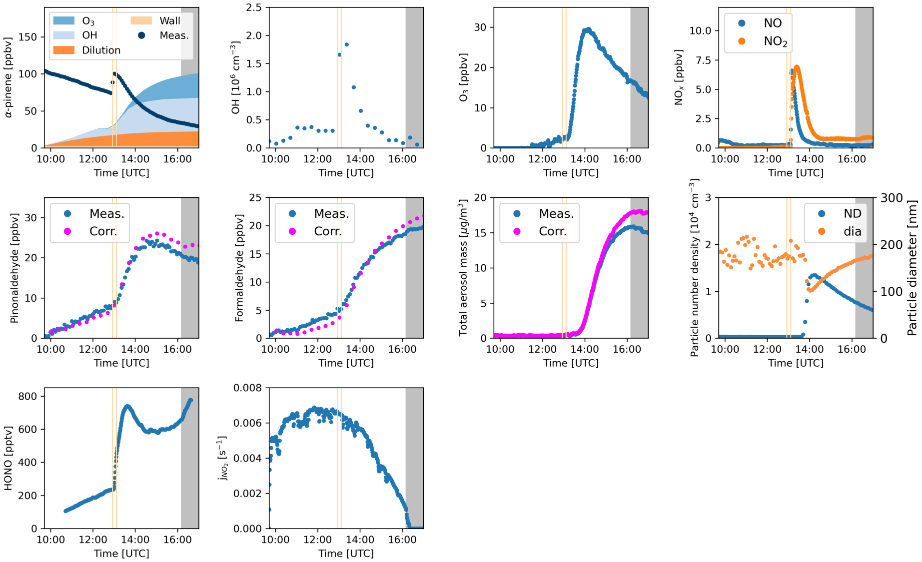

Figure A.5: Time series of trace gas concentrations measured in the experiment E2 performed on the 16 of January 2019 in the EUPHORE chamber (Tab. A.3). Different contributions to the loss of -pinene are shown by coloured areas together with the time series of the -pinene concentration. OH radical concentrations are derived from the corrected time series of -pinene concentrations according to Eq. (2.8). Injections of -pinene into the chamber are marked by yellow, vertical lines. “ND” and “Dia” refer to the particle number density and the mean particle diameter. A relative humidity below % was present during the experiment. The temperature increased from C to C after the roof opening and decreased afterwards to C.

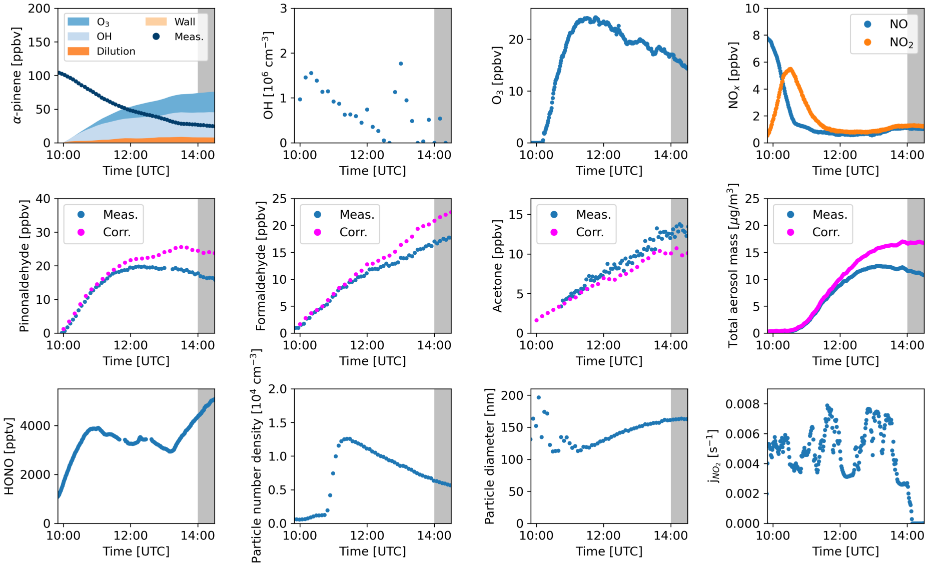

Figure A.6: Time series of trace gas concentrations measured in the experiment E3 performed on the 18 of January 2019 in the EUPHORE chamber (Tab. A.3). Different contributions of the loss paths of -pinene are shown by coloured areas together with the time series of the -pinene concentration. OH radical concentrations are derived from the corrected time series of -pinene concentrations according to Eq. (2.8). Injections of -pinene into the chamber are marked by yellow, vertical lines. “ND” and “Dia” refer to the particle number density and the mean particle diameter. A relative humidity was between % and %, while the temperature increased from C to C after the roof opening and decreased afterwards to C.

SAPHIR

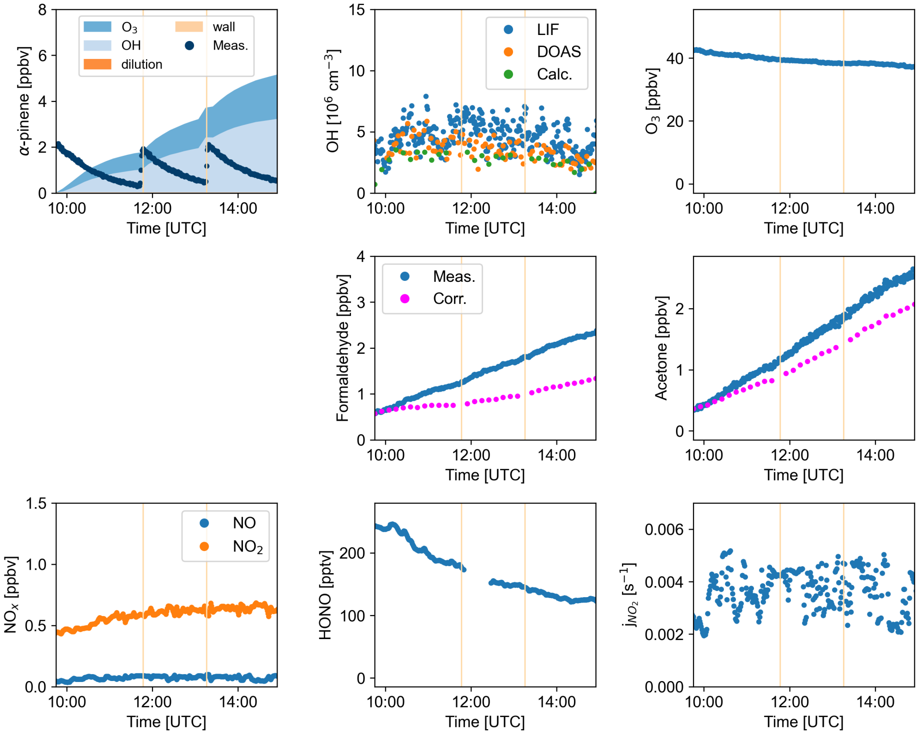

Figure A.7: Time series of trace gas concentrations measured in the experiment S1 performed in the SAPHIR chamber (Tab. A.3). Different contributions of the loss paths of -pinene are shown by coloured areas together with the time series of the -pinene concentration. OH radical concentrations were measured by the LIF and DOAS instruments (Section 2.2.2), and calculated from the corrected time series of -pinene concentrations according to Eq. (2.8). Injections of -pinene into the chamber are marked by yellow, vertical lines. The relative humidity decreased from % to % throughout the experiment and the temperature increased from C to C during the experiment.

CESAM

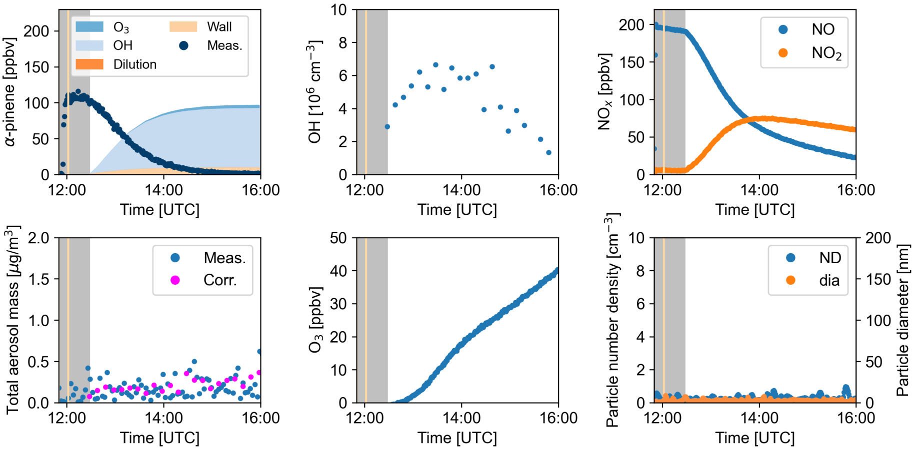

Figure A.8: Time series of trace gas concentrations measured in the experiment C1 performed on the 13 of February 2019 in the CESAM chamber (Tab. A.3). Different contributions of the loss paths of -pinene are shown by coloured areas together with the time series of the -pinene concentration. OH radical concentrations are derived from the corrected time series of -pinene concentrations according to Eq. (2.8). Injections of -pinene into the chamber are marked by yellow, vertical lines and dark conditions are indicated by grey areas. “ND” and “Dia” refer to the particle number density and the mean particle diameter. A relative humidity of less than % and a temperature of C were present during the experiment.

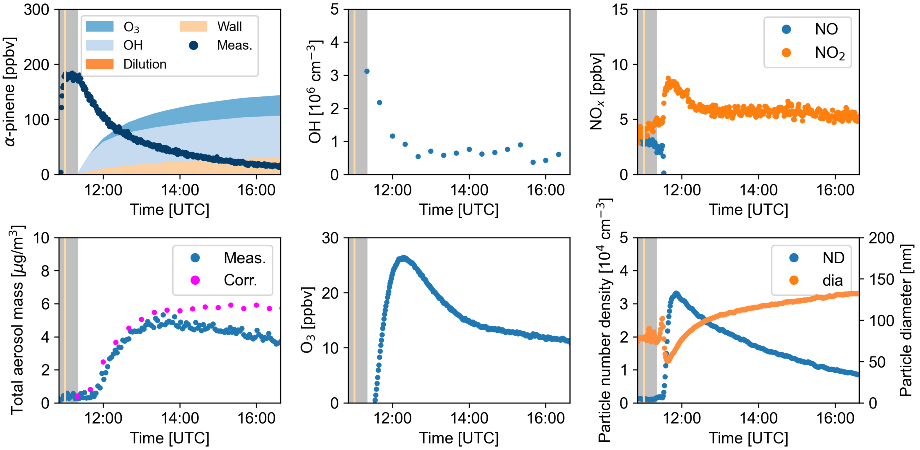

Figure A.9: Time series of trace gas concentrations measured in the experiment C2 performed on the 14 of February 2019 in the CESAM chamber (Tab. A.3). Different contributions of the loss paths of -pinene are shown by coloured areas together with the time series of the -pinene concentration. OH radical concentrations arederived from the corrected time series of -pinene concentrations according to Eq. (2.8). Injections of -pinene into the chamber are marked by yellow, vertical lines and dark conditions are indicated by grey areas. “ND” and “Dia” refer to the particle number density and the mean particle diameter. A relative humidity of about % and a temperature of C were present during the experiment.

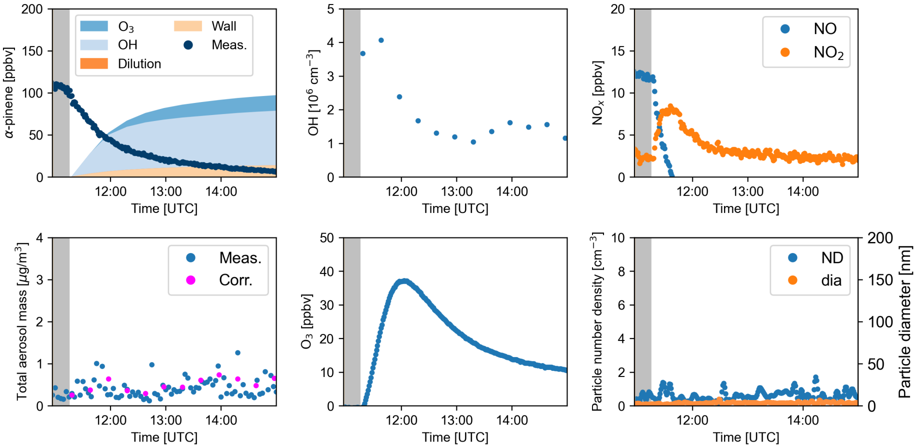

Figure A.10: Time series of trace gas concentrations measured in the experiment C3 performed in the CESAM chamber (Tab. A.3). Different contributions of the loss paths of -pinene are shown by coloured areas together with the time series of the -pinene concentration. OH radical concentrations are derived from the corrected time series of -pinene concentrations according to Eq. (2.8). Injections of -pinene into the chamber are marked by yellow, vertical lines and dark conditions are indicated by grey areas. "ND" and "Dia" refer to the particle number density and the mean particle diameter. A relative humidity of less than % and a temperature of C were present during the experiment.

FORTH-ASC

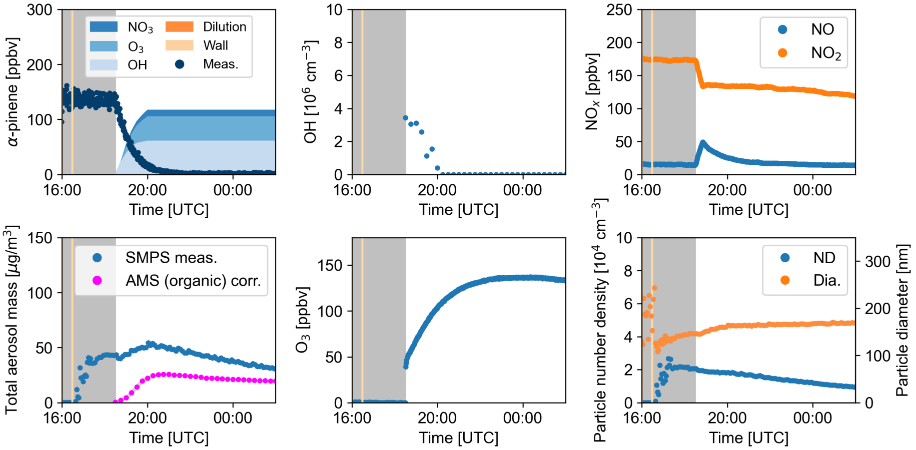

Figure A.11: Time series of trace gas concentrations measured in the experiment F2s performed in the FORTH chamber (Tab. A.3). Different contributions of the loss paths of α-pinene are shown by coloured areas together with the time series of the α-pinene concentration. OH radical concentrations are derived from the corrected time series of α-pinene concentrations according to Eq. (2.8). The injection of seed aerosol (ammonium sulfate) into the chamber is marked by a yellow, vertical line and dark conditions are indicated by grey areas. “ND” and “Dia” refer to the particle number density and the mean particle diameter. The relative humidity decreased from % to % and the temperature increased from C to C after the light had been switched on.

MAC

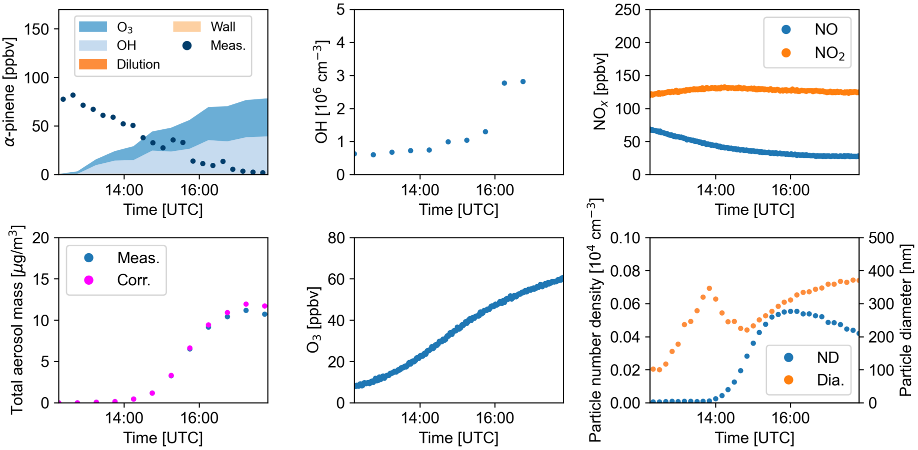

Figure A.12: Time series of trace gas concentrations measured in the experiment M2 performed in the MAC chamber (Tab. A.3). Different contributions of the loss paths of -pinene are shown by coloured areas together with the time series of the -pinene concentration. OH radical concentrations are derived from the corrected time series of -pinene concentrations according to Eq. (2.8). Injections of -pinene into the chamber are marked by yellow, vertical lines. “ND” and “Dia” refer to the particle number density and the mean particle diameter. A relative humidity of % and a temperature of C were present during the experiment.

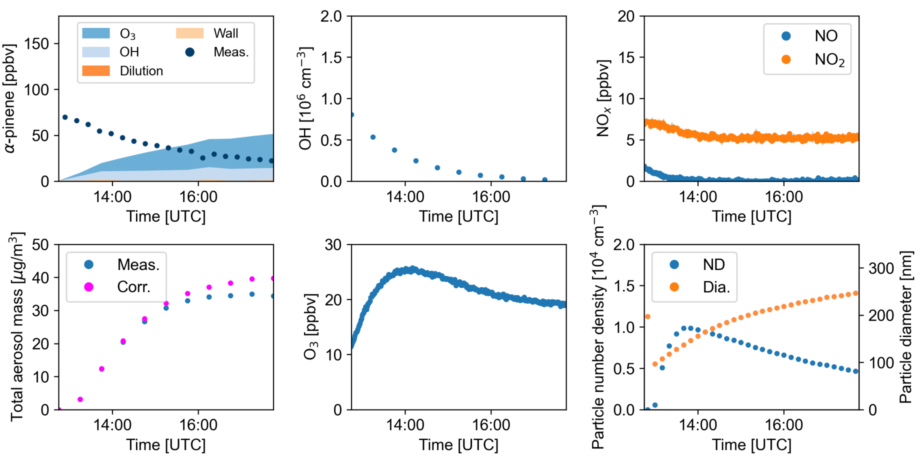

Figure A.13: Time series of trace gas concentrations measured in the experiment M3 performed in the MAC chamber (Tab. A.3). Different contributions of the loss paths of -pinene are shown by coloured areas together with the time series of the -pinene concentration. OH radical concentrations are derived from the corrected time series of -pinene concentrations according to Eq. (2.8). Injections of -pinene into the chamber are marked by yellow, vertical lines. "ND" and "Dia" refer to the particle number density and the mean particle diameter. A relative humidity of % and a temperature of C were present during the experiment.

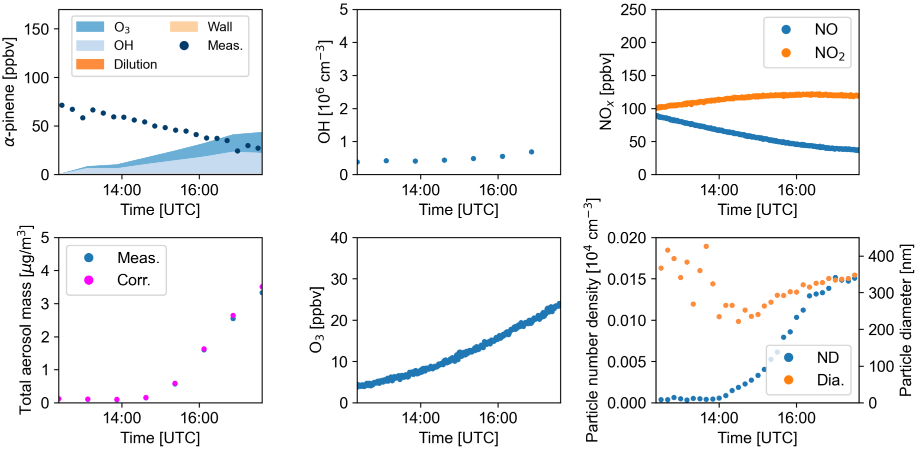

Figure A.14: Time series of trace gas concentrations measured in the experiment M4 performed in the MAC chamber (Tab. A.3). Different contributions of the loss paths of -pinene are shown by coloured areas together with the time series of the -pinene concentration. OH radical concentrations are derived from the corrected time series of -pinene concentrations according to Eq. (2.8). Injections of -pinene into the chamber are marked by yellow, vertical lines. “ND” and “Dia” refer to the particle number density and the mean particle diameter. A relative humidity of % and a temperature of C were present during the experiment.

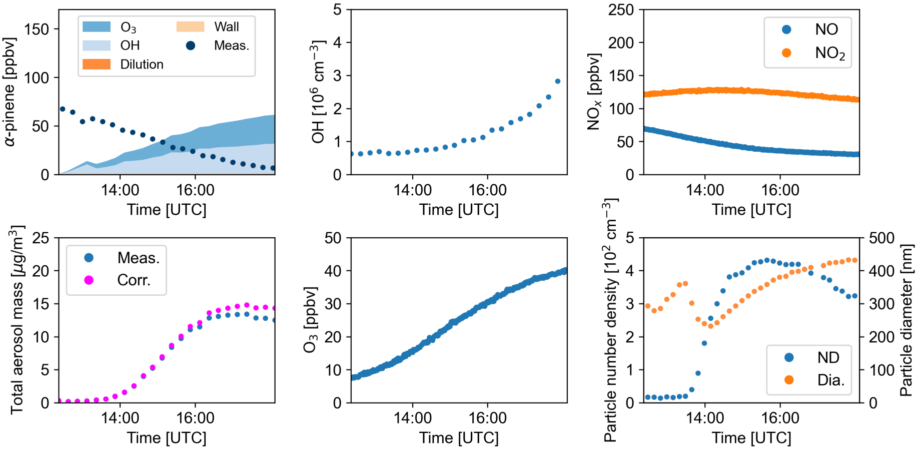

Figure A.15: Time series of trace gas concentrations measured in the experiment M5 performed in the MAC chamber (Tab. A.3). Different contributions of the loss paths of -pinene are shown by coloured areas together with the time series of the -pinene concentration. OH radical concentrations are derived from the corrected time series of -pinene concentrations according to Eq. (2.8). Injections of -pinene into the chamber are marked by yellow, vertical lines. "ND" and "Dia" refer to the particle number density and the mean particle diameter. A relative humidity of % and a temperature of C were present during the experiment.

LEAK

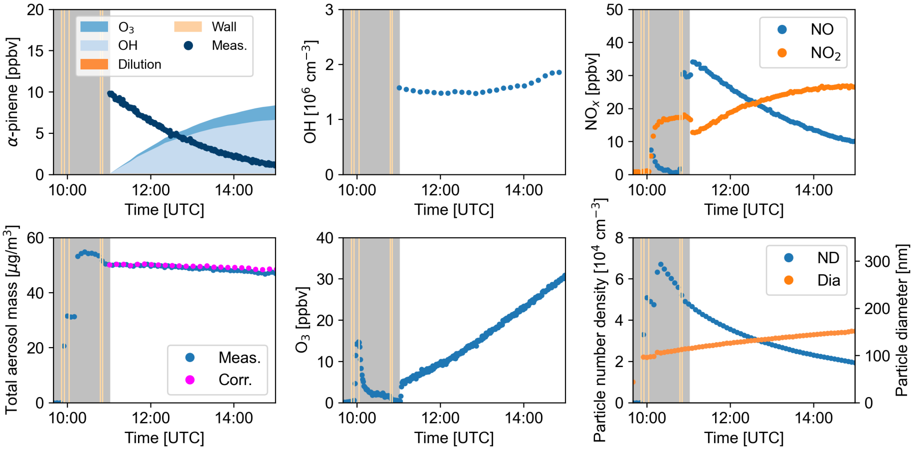

Figure A.16: Time series of trace gas concentrations measured in the experiment L1s performed in the LEAK chamber (Tab. A.3). Different contributions of the loss paths of -pinene are shown as coloured areas together with the time series of the -pinene concentration. OH radical concentrations are derived from the corrected time series of -pinene concentrations according to Eq. (2.8). Injections of -pinene into the chamber are marked by yellow, vertical lines and dark conditions are indicated by grey areas. “ND” and “Dia” refer to the particle number density and the mean particle diameter. A relative humidity of % and a temperature of C were present during the experiment.

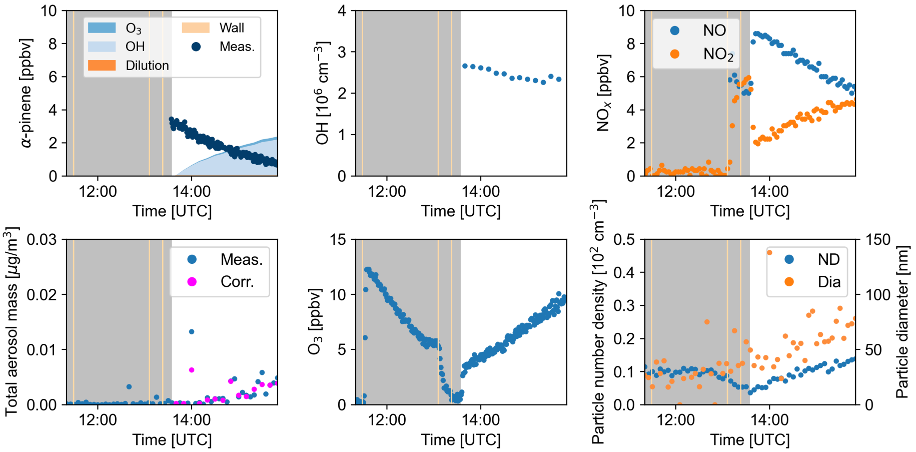

Figure A.17: Time series of trace gas concentrations measured in the experiment L3 performed in the LEAK chamber (Tab. A.3). Different contributions of the loss paths of -pinene are shown by coloured areas together with the time series of the -pinene concentration. OH radical concentrations are derived from the corrected time series of -pinene concentrations according to Eq. (2.8). Injections of -pinene into the chamber are marked by yellow, vertical lines and dark conditions are indicated by grey areas. “ND” and “Dia” refer to the particle number density and the mean particle diameter. A relative humidity of % and a temperature of C were present during the experiment.

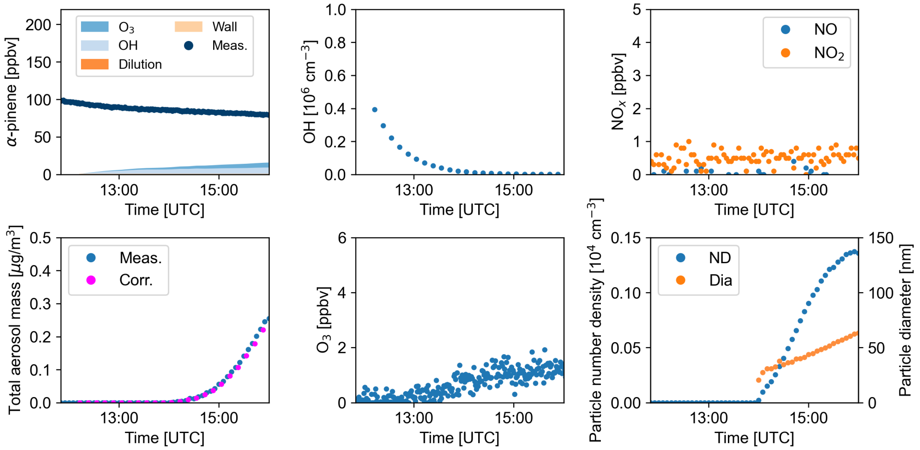

Figure A.18: Time series of trace gas concentrations measured in the experiment L4 performed in the LEAK chamber (Tab. A.3). Different contributions of the loss paths of -pinene are shown by coloured areas together with the time series of the -pinene concentration. OH radical concentrations are derived from the corrected time series of -pinene concentrations according to Eq. (2.8). Injections of -pinene into the chamber are marked by yellow, vertical lines and dark conditions are indicated by grey areas. “ND” and “Dia” refer to the particle number density and the mean particle diameter. A relative humidity of % and a temperature of C were present during the experiment.

PACS-C3

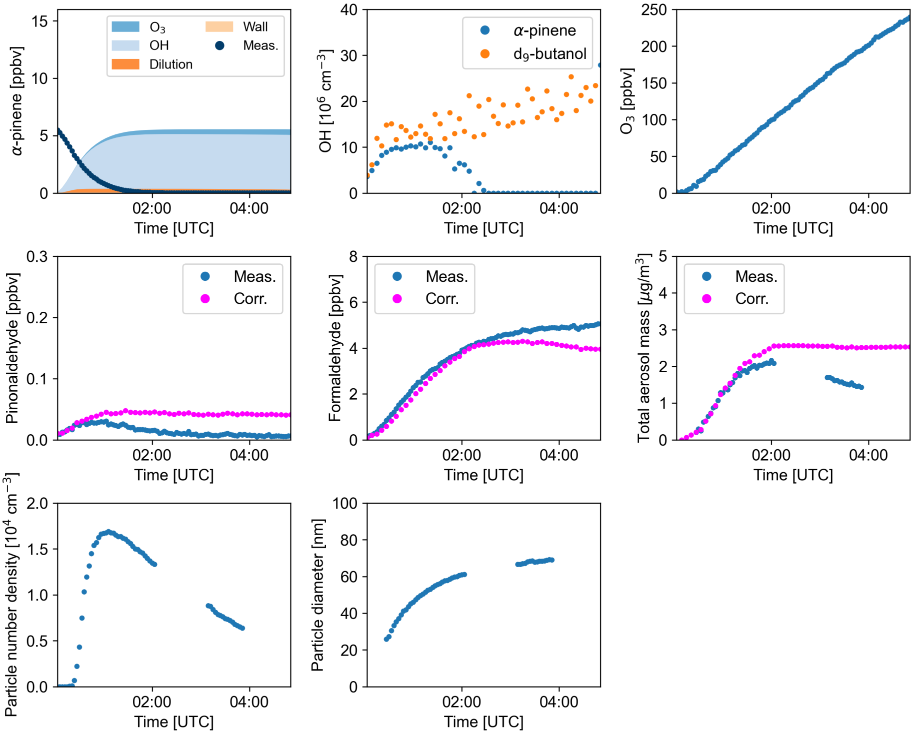

Figure A.19: Time series of trace gas concentrations measured in the experiment P1 performed in one of the PACS-C3 chambers (Tab. A.3). Different contributions of the loss paths of -pinene are shown by coloured areas together with the time series of the -pinene concentration. OH radical concentrations are derived from the decrease of injected d -butanol and from the corrected time series of -pinene concentrations according to Eq. (2.8). Injections of -pinene into the chamber are marked by yellow, vertical lines. HONO was injected before the start of the photooxidation. “ND” and “Dia” refer to the particle number density and the mean particle diameter. The total aerosol mass concentration was interpolated for its correction for wall loss. A relative humidity of % and a temperature of C were present during the experiment.

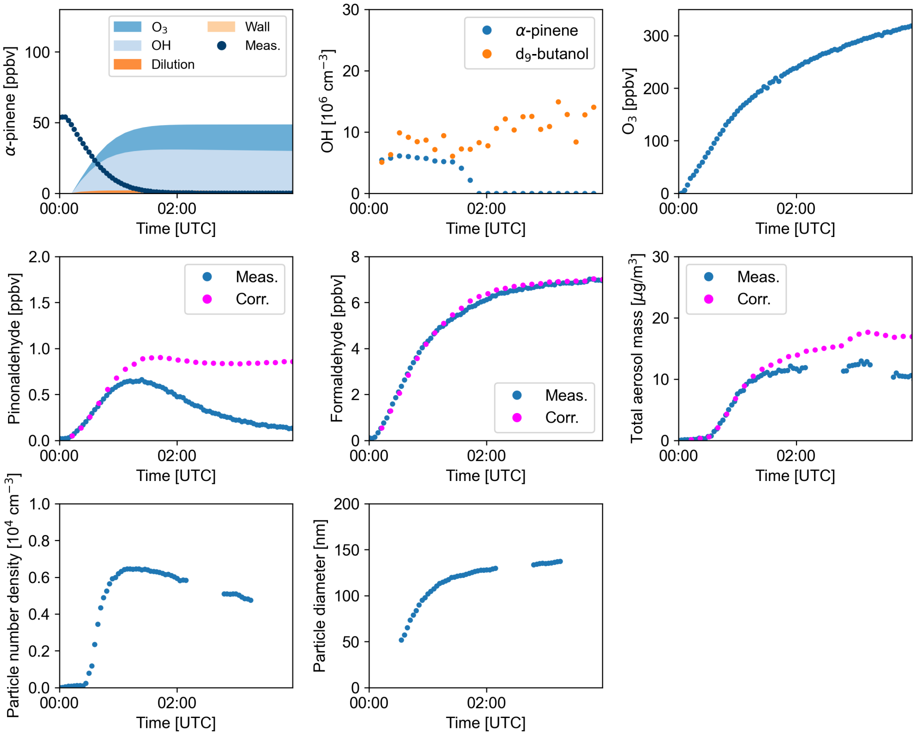

Figure A.20: Time series of trace gas concentrations measured in the experiment P2 performed in one of the PACS-C3 chambers (Tab. A.3). Different contributions of the loss paths of -pinene are shown by coloured areas together with the time series of the -pinene concentration. OH radical concentrations are derived from the decrease of injected d -butanol and from the corrected time series of -pinene concentrations according to Eq. (2.8). Injections of -pinene into the chamber are marked by yellow, vertical lines. NO_2 was added before the start of the photooxidation. “ND” and “Dia” refer to the particle number density and the mean particle diameter. The total aerosol mass concentration was interpolated for its correction for wall loss. A relative humidity of % and a temperature of C were present during the experiment.

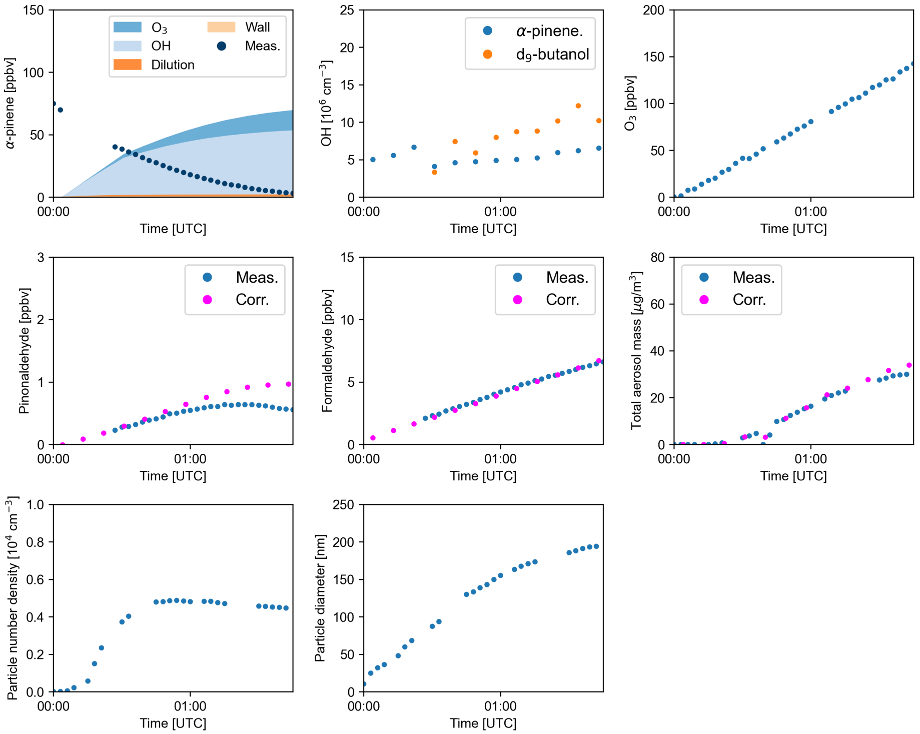

Figure A.21: Time series of trace gas concentrations measured in the experiment P4 performed in one of the PACS-C3 chambers (Tab. A.3). Different contributions of the loss paths of -pinene are shown by coloured areas together with the time series of the -pinene concentration. OH radical concentrations are derived from the decrease of injected d -butanol and from the corrected time series of -pinene concentrations according to Eq. (2.8). Injections of -pinene into the chamber are marked by yellow, vertical lines. HONO was added before the start of the photooxidation. “ND” and “Dia” refer to the particle number density and the mean particle diameter. The total aerosol mass concentration was interpolated for its correction for wall loss. A relative humidity of % and a temperature of C were present during the experiment.

ILMARI

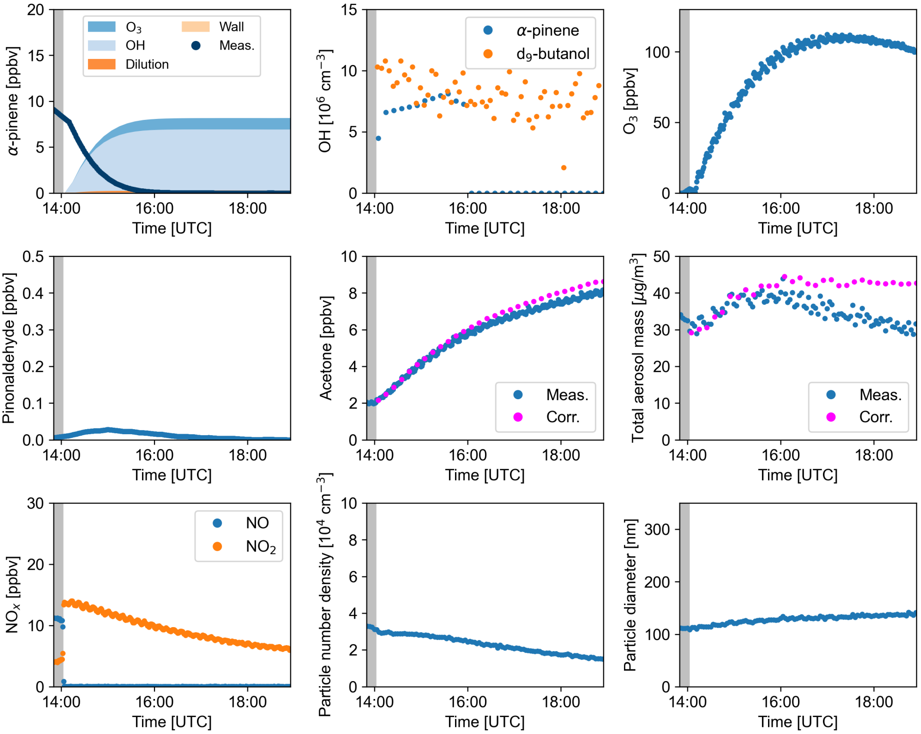

Figure A.22: Time series of trace gas concentrations measured in the experiment I1s performed in the ILMARI chamber (Tab. A.3). Different contributions of the loss paths of -pinene are shown by coloured areas together with the time series of the -pinene concentration. OH radical concentrations are derived from the decrease of injected d -butanol and from the corrected time series of -pinene concentrations according to Eq. (2.8). Injections of -pinene into the chamber are marked by yellow, vertical lines and dark conditions are indicated by grey areas. “ND” and “Dia” refer to the particle number density and the mean particle diameter. A relative humidity of % and a temperature of C were present during the experiment.

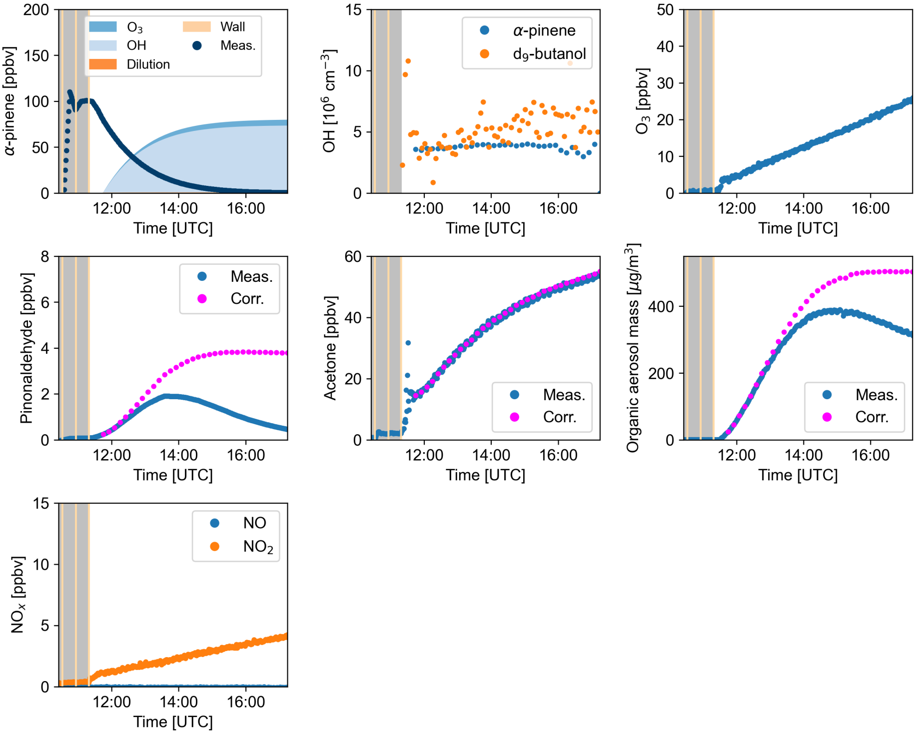

Figure A.23: Time series of trace gas concentrations measured in the experiment I3 performed in the ILMARI chamber (Tab. A.3). Different contributions of the loss paths of -pinene are shown by coloured areas together with the time series of the -pinene concentration. OH radical concentrations are derived from the decrease of injected d -butanol and from the corrected time series of -pinene concentrations according to Eq. (2.8). Injections of -pinene into the chamber are marked by yellow, vertical lines and dark conditions are indicated by grey areas. "ND" and "Dia" refer to the particle number density and the mean particle diameter. A relative humidity between % and % and a temperature of C were present during the experiment.

A.1.5 Relation between consumed -pinene and formed gas-phase products

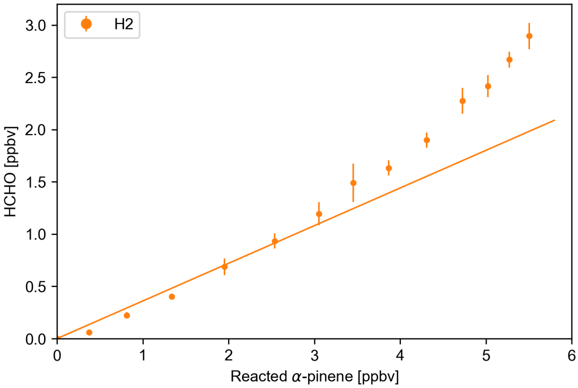

Figure A.24: Mixing ratios of formaldehyde in dependence on the amount of -pinene that reacted with OH for experiments performed in the outdoor simulation chamber HELIOS. Formaldehyde concentrations were corrected for chamber effects and chemical losses. Furthermore, lines illustrate the linear correlation of product and -pinene concentrations and their slope correspond to the obtained product yield (Tab. 2.2).

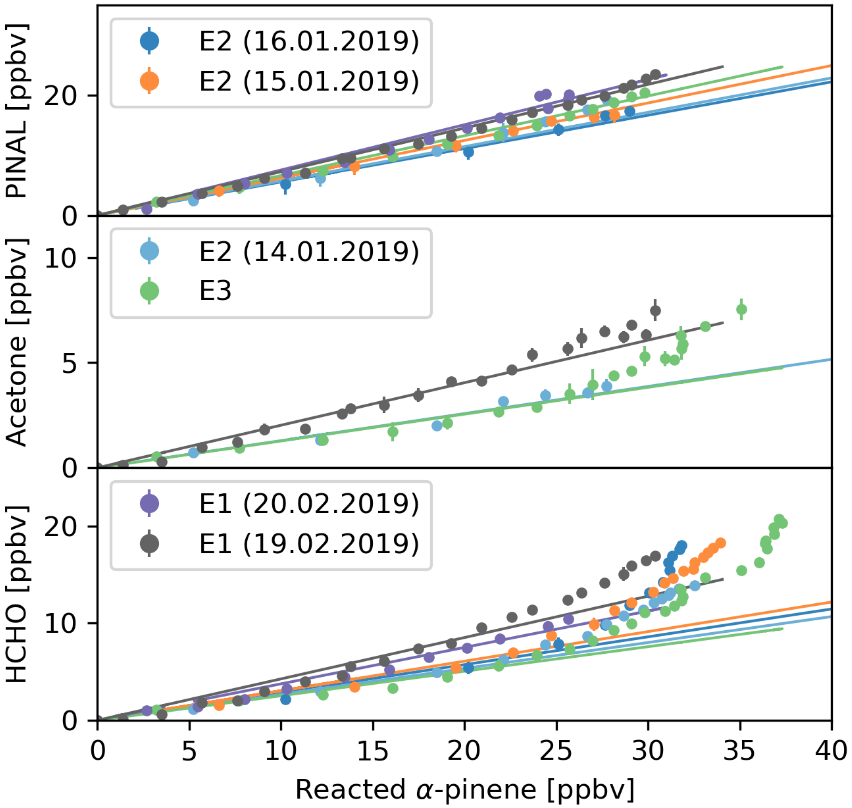

Figure A.25: Mixing ratios of pinonaldehyde, acetone, and formaldehyde in dependence on the amount of α-pinene that reacted with OH for the experiments performed in the simulation chamber EUPHORE. The organic products are corrected for chamber effects and chemical losses. Furthermore, lines illustrate the linear correlation of product and α-pinene concentrations and their slope correspond to the obtained product yield (Tab. 2.2).

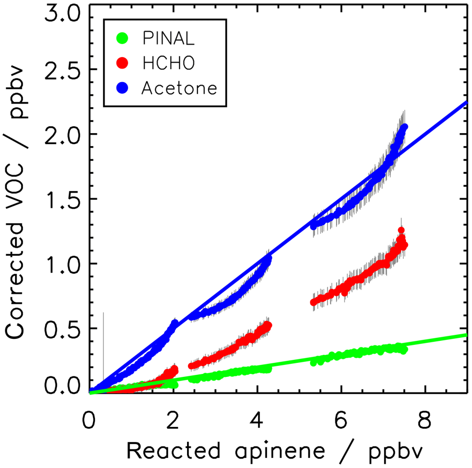

Figure A.26: Mixing ratios of pinonaldehyde, acetone, and formaldehyde in dependence on the amount of α-pinene that reacted with OH for the experiments performed in the simulation chamber SAPHIR. The organic products are corrected for chamber effects and chemical losses. Furthermore, lines illustrate the linear correlation of product and α-pinene concentrations and their slope correspond to the obtained product yield (Tab. 2.2). The figure was adopted from Rolletter et al. (2019) under the CCA 4.0 license.

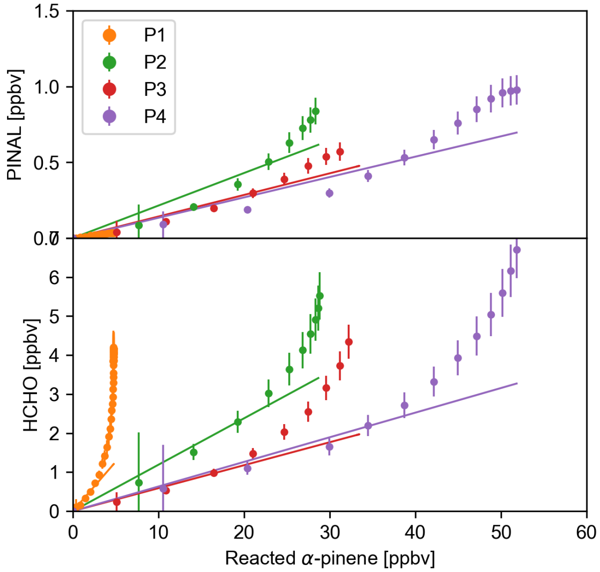

Figure A.27: Mixing ratios of pinonaldehyde and formaldehyde in dependence on the amount of -pinene that reacted with OH for the experiments performed one of the PACS-C3 simulation chambers. The organic products are corrected for chamber effects and chemical losses. Furthermore, lines illustrate the linear correlation of product and -pinene concentrations and their slope correspond to the obtained product yield (Tab. 2.2).

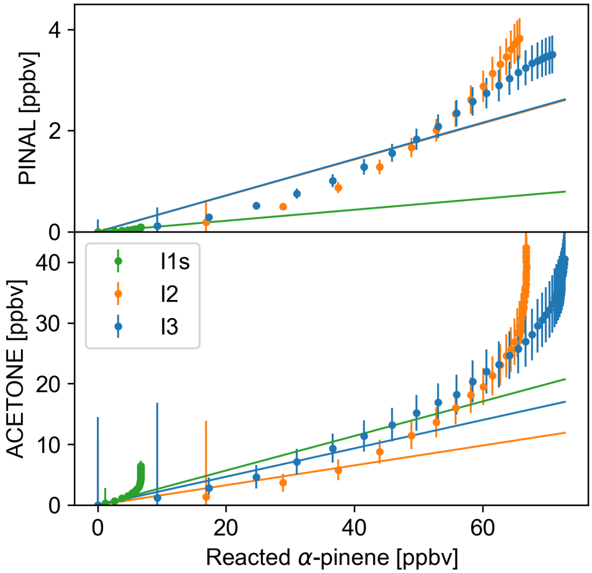

Figure A.28: Mixing ratios of pinonaldehyde and acetone in dependence on the amount of -pinene that reacted with OH for the experiments performed in the ILMARI chamber. The organic products are corrected for chamber effects and chemical losses. Furthermore, lines illustrate the linear correlation of product and -pinene concentrations and their slope correspond to the obtained product yield (Tab. 2.2).

A.2 Supplementary materials to Section 3.2

Effect of the alkoxy radical chemistry on the ozone formation from anthropogenic organic compounds investigated in chamber experiments

– *Supporting information* –

Michelle Färber,[†] Hendrik Fuchs, ,[†,‡] Birger Bohn,[†] Philip T.M. Carlsson,[†] Georgios I. Gkatzelis,[†] Andrea C. Marcillo Lara,[†] Franz Rohrer,[†] Luc Vereecken,[†] Sergej Wedel,[†] Andreas Wahner,[†] and Anna Novelli ,[†]

†*Institute for Energy and Climate Research, IEK-8: Troposphere, Forschungszentrum Jülich GmbH, Jülich, Germany*

‡*Department of Physics, University of Cologne, Cologne, Germany*

E-mail: h.fuchs@fz-juelich.de; a.novelli@fz-juelich.de

Contents

A OH reaction schemes of compounds investigated in this work

A.1 Propane

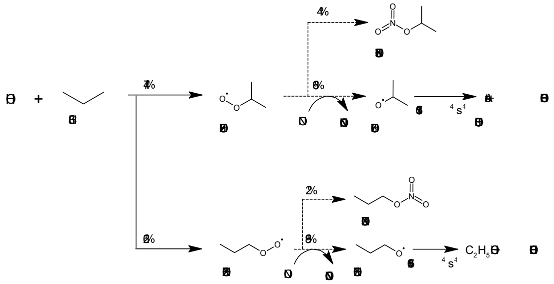

Figure S1: Simplified reaction scheme of the oxidation of propane by OH, when the reaction with NO is the dominant loss for RO_2 radicals. HO_2 radicals are formed after one RO_2 reaction step. Under these conditions, 1.93 NO molecules are oxidised to NO_2 by either RO_2 or HO_2 radicals, leading to a net ozone production. Dashed lines indicate reaction of RO_2 with NO. Values and names are taken from the MCM.[1,2]

A.2 Propene

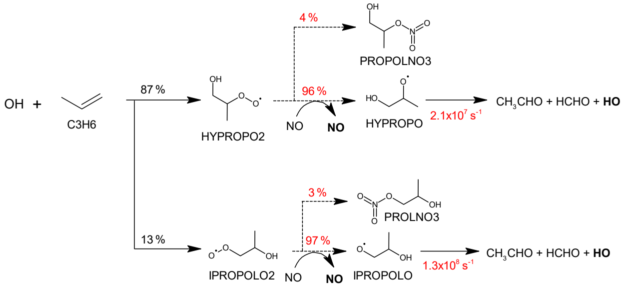

Figure S2: Simplified reaction scheme of the oxidation of propene by OH, when the reaction with NO is the dominant loss for RO$_2$ radicals. HO$_2$ radicals are formed after one RO$_2$ reaction step. Under these conditions, 1.92 NO molecules are oxidised to NO$_2$ by either RO$_2$ or HO$_2$ radicals, leading to a net ozone production. Dashed lines indicate reaction of RO$_2$ with NO. Red arrows and red values mark pathways and reaction rate constants, derived from SAR,[3–6] while black arrows and values are taken from the MCM.[1,2] Names correspond to the MCM notation.

A.3 iso-Pentane

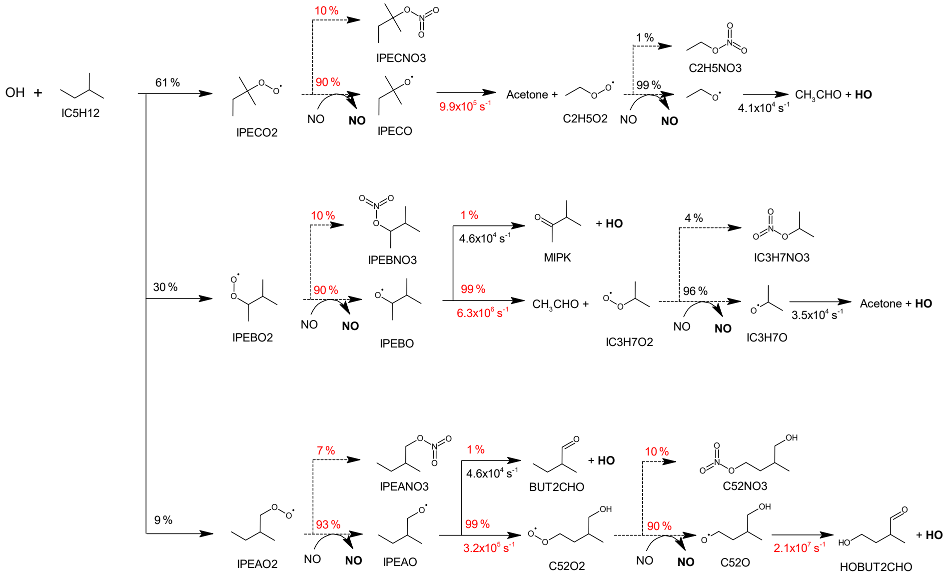

Figure S3: Simplified reaction scheme of the oxidation of iso-pentane by OH, when the reaction with NO is the dominant loss for RO$_2$ radicals. HO$_2$ radicals are formed after two RO$_2$ reaction steps for 87 % of the RO$_2$ radicals initially formed in the reaction of iso-pentane with OH. Under these conditions, 2.66 NO molecules are oxidised to NO$_2$ by either RO$_2$ or HO$_2$ radicals, leading to a net ozone production. Dashed lines indicate reaction of RO$_2$ with NO. Red arrows and red values mark pathways and reaction rate constants, derived from SAR,[3–6] while black arrows and values are taken from the MCM.[1,2] Names correspond to the MCM notation.

A.4 n-Hexane

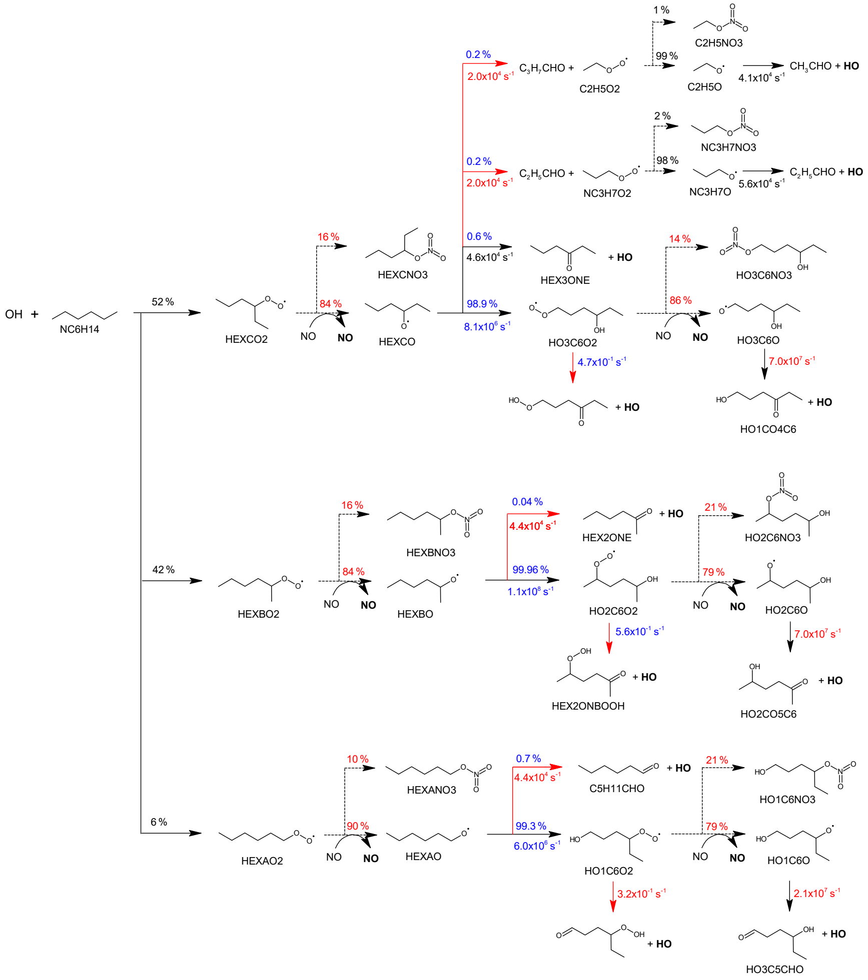
OH +
NC6H14
52 %
42 %
6 %
HEXCO2
16 %
84 %
NO
NO
HEXCNO3
HEXCO
0.2 %
2.0x10⁴ s⁻¹
C₃H₇CHO +
C2H5O2
1 %
99 %
C2H5NO3
C2H5O
4.1x10⁴ s⁻¹
CH₃CHO + HO
0.2 %
2.0x10⁴ s⁻¹
C₂H₅CHO +
NC3H7O2
2 %
98 %
NC3H7NO3
NC3H7O
5.6x10⁴ s⁻¹
C₂H₅CHO + HO
0.6 %
4.6x10⁴ s⁻¹
HEX3ONE
+ HO
98.9 %
8.1x10⁶ s⁻¹
HO3C6O2
14 %
86 %
NO
NO
HO3C6NO3
HO3C6O
4.7x10⁻¹ s⁻¹
+ HO
7.0x10⁷ s⁻¹
+ HO
HO1CO4C6
HEXBO2
16 %
84 %
NO
NO
HEXBNO3
HEXBO
0.04 %
4.4x10⁴ s⁻¹
HEX2ONE
+ HO
99.96 %
1.1x10⁸ s⁻¹
HO2C6O2
21 %
79 %
NO
NO
HO2C6NO3
HO2C6O
5.6x10⁻¹ s⁻¹
+ HO
HEX2ONBOOH
7.0x10⁷ s⁻¹
+ HO
HO2CO5C6
HEXAO2
10 %
90 %
NO
NO
HEXANO3
HEXAO
0.7 %
4.4x10⁴ s⁻¹
C5H11CHO
+ HO
99.3 %
6.0x10⁶ s⁻¹
HO1C6O2
21 %
79 %
NO
NO
HO1C6NO3
HO1C6O
3.2x10⁻¹ s⁻¹
+ HO
2.1x10⁷ s⁻¹
+ HO
HO3C5CHO

Figure S4 *(previous page)*: Simplified oxidation scheme of the oxidation of n-hexane by OH, when the reaction with NO and isomerisation reactions are the dominant loss for RO_2 radicals. HO_2 radicals are formed after two RO_2 reaction steps for 84 % of the RO_2 radicals initially formed in the reaction of n-hexane with OH. Under these conditions, 1.75 (NO < 1 ppbv) and 2.09 (NO = 6 ppbv) NO molecules are oxidised to NO_2 by either RO_2 or HO_2 radicals, leading to a net ozone production. Dashed lines indicate reaction of RO_2 with NO. Red arrows and red values mark pathways and reaction rate constants, derived from SAR,[3–6] while black arrows and values are taken from the MCM.[1,2] Theoretically calculated reaction rate constants (Tab. S3) are shown in blue. Names correspond to the MCM notation.

A.5 trans-2-Hexene

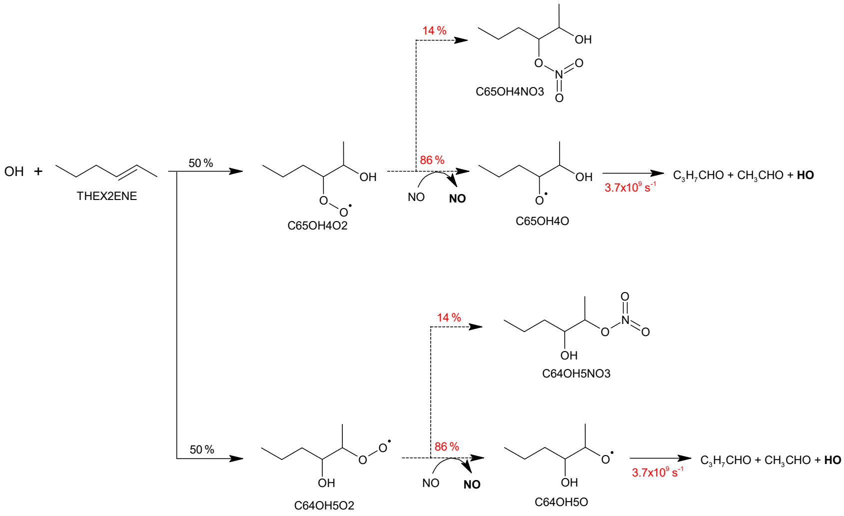

Figure S5: Simplified oxidation scheme of the oxidation of trans-2-hexene by OH, when the reaction with NO is the dominant loss for RO_2 radicals. HO_2 radicals are formed after one RO_2 reaction steps. Under these conditions, 1.72 NO molecules are oxidised to NO_2 by either RO_2 or HO_2 radicals, leading to a net ozone production. Dashed lines indicate reaction of RO_2 with NO. Red arrows and red values mark pathways and reaction rate constants, derived from SAR,[3–6] while black arrows and values are taken from the MCM.[1,2] Names correspond to the MCM notation.

B Model-measurement comparisons

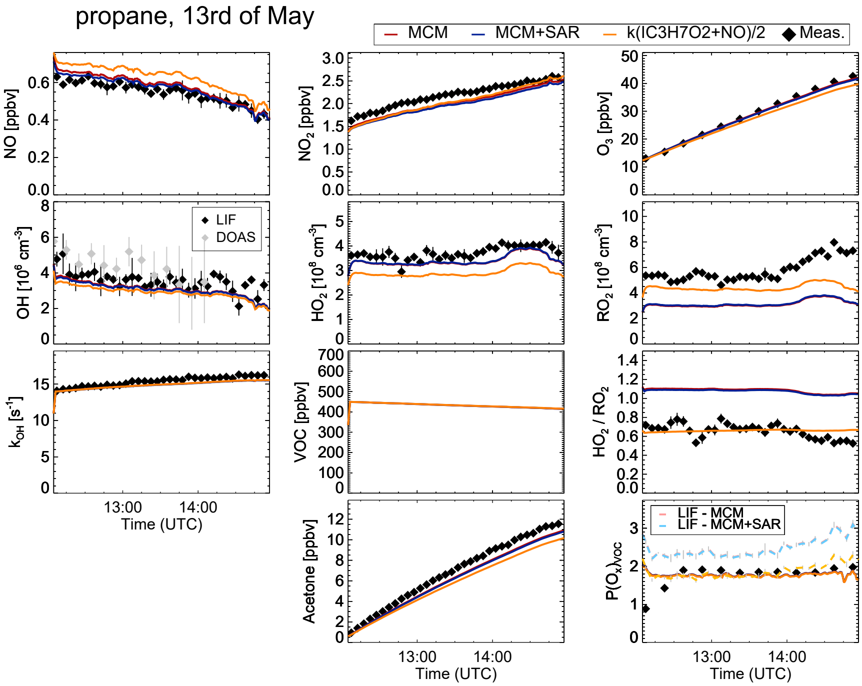

Figure S6: Comparison of measured and modelled trace gas concentrations for the experiment with propane at NO < 1 ppbv, performed on 13 May 2022. Orange lines illustrate model results from a test mechanism assuming a factor of two lower rate coefficient of the reaction of the RO_2 iso-C_3H_7OO (MCM notation: IC3H7O2) with NO.

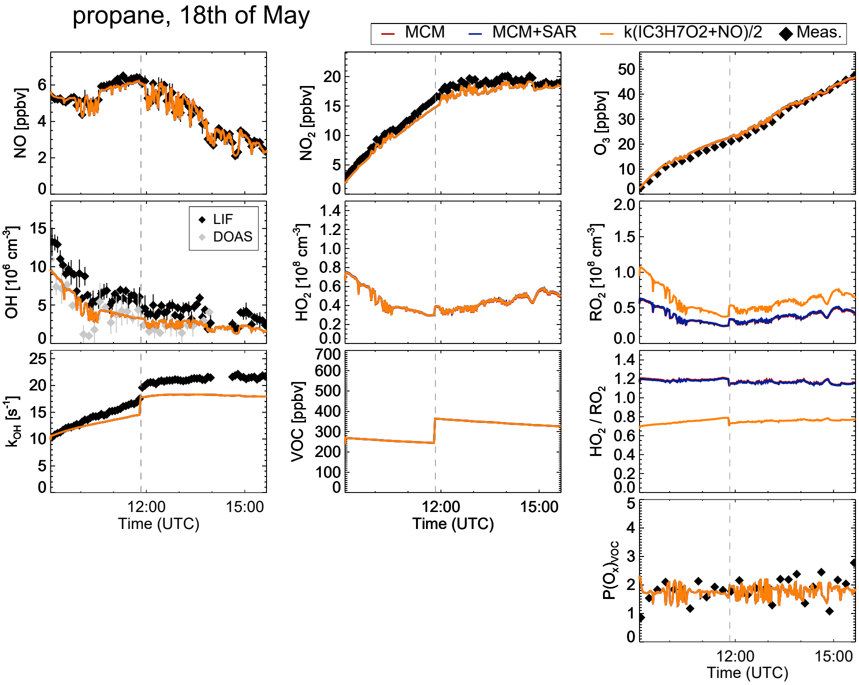

Figure S7: Comparison of measured and modelled trace gas concentrations for the experiment with propane at NO > 1 ppbv, performed on 18 May 2022. The vertical line indicates the second injection of the VOC into the chamber. Orange lines illustrate model results from a test mechanism assuming a factor of two lower rate coefficient of the reaction of the RO$_2$ iso-C_3H_7OO (MCM notation: IC3H7O2) with NO.

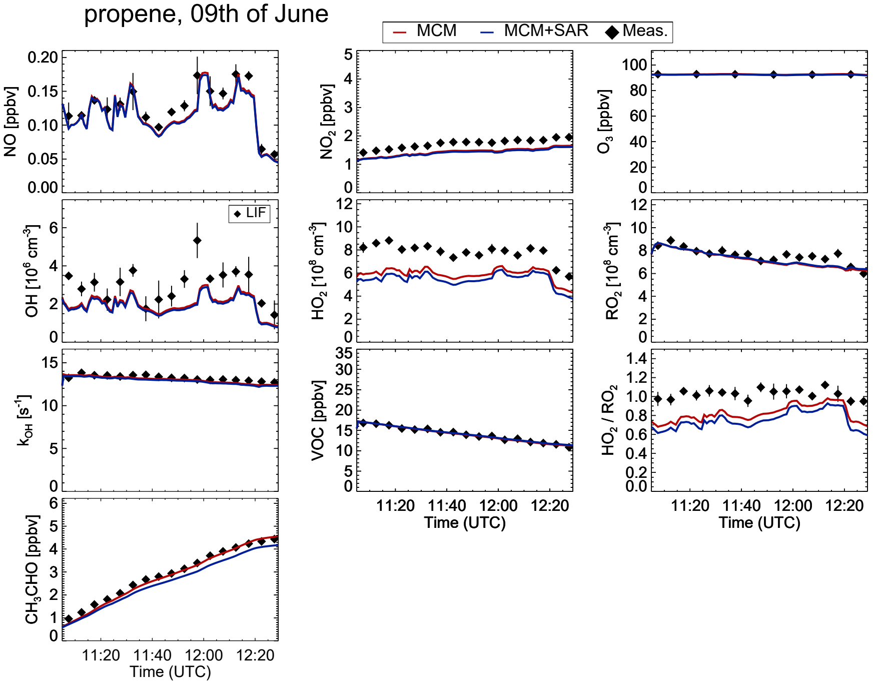

Figure S8: Comparison of measured and modelled trace gas concentrations for the experiment with propene at NO < 1 ppbv, performed on 9 June 2022.

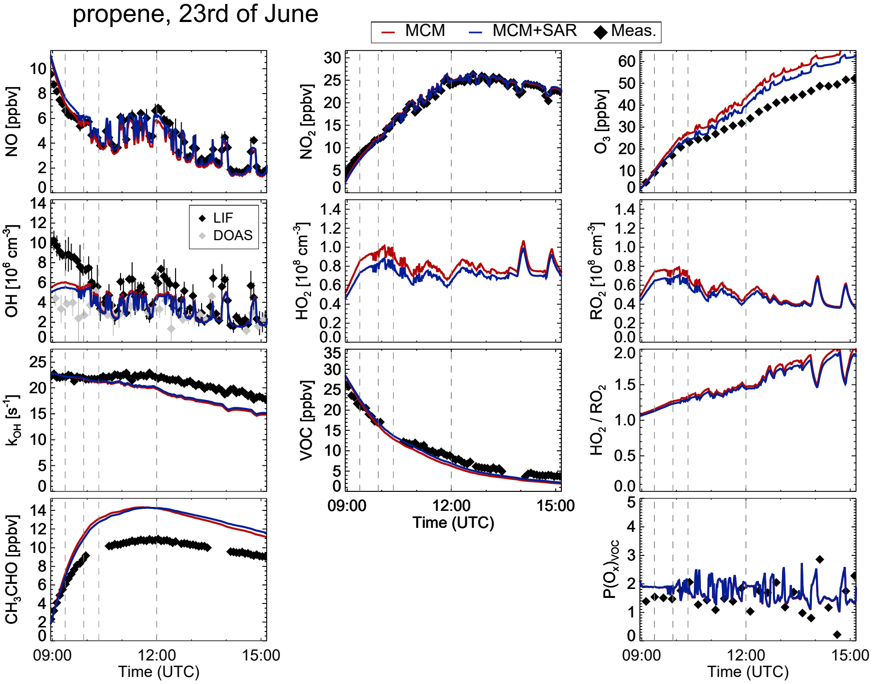

Figure S9: Comparison of measured and modelled trace gas concentrations for the experiment with propene at NO > 1 ppbv, performed on 23 June 2022. Vertical lines indicate a changing flow of the continuous NO injection into the chamber. The first injection of the VOC was performed at the start of the displayed time series.

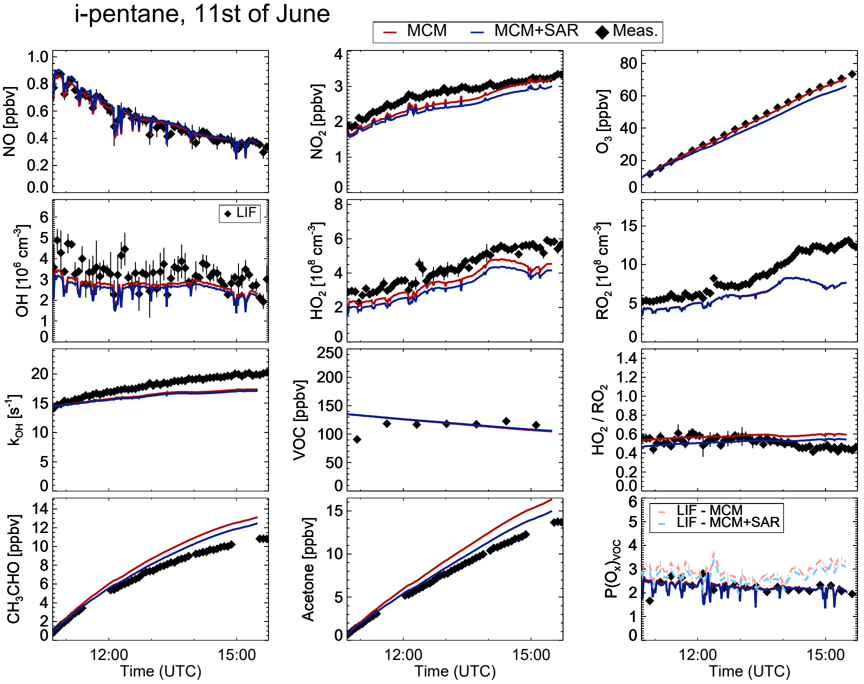

Figure S10: Comparison of measured and modelled trace gas concentrations for the experiment with iso-pentane at NO < 1 ppbv, performed on 11 June 2022.

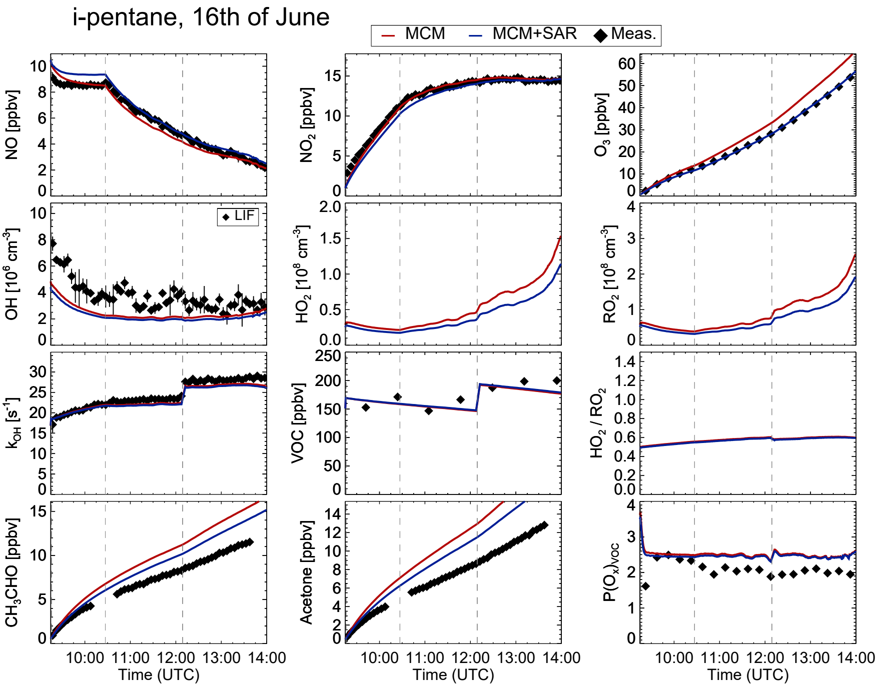

Figure S11: Comparison of measured and modelled trace gas concentrations for the experiment with iso-pentane at NO > 1 ppbv, performed on 16 June 2022. Vertical lines indicate the stop of the continuous NO injection and the second injection of the VOC into the chamber.

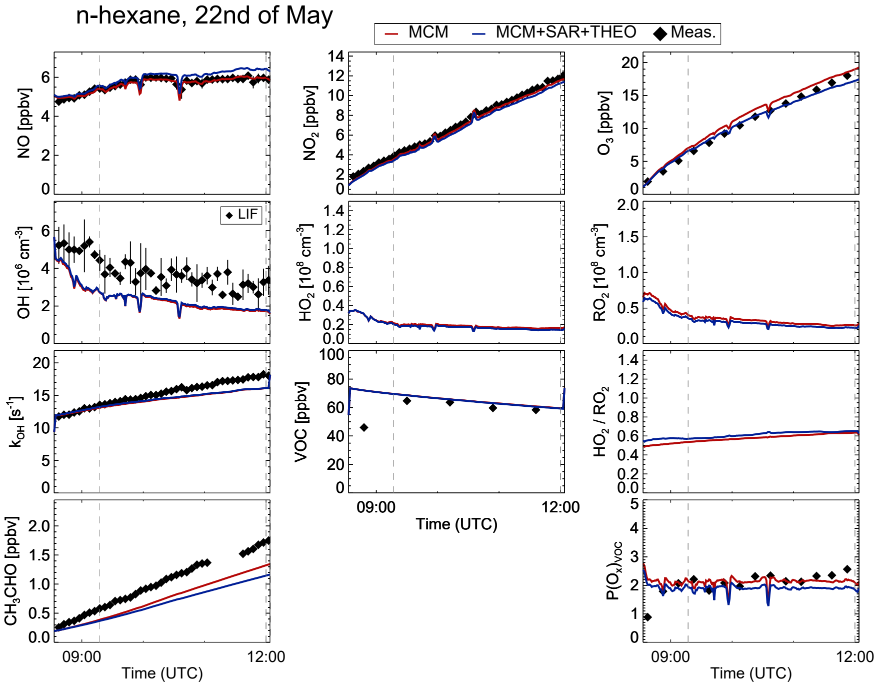

Figure S12: Comparison of measured and modelled trace gas concentrations for the experiment with n-hexane at NO > 1 ppbv, performed on 22 May 2022. The vertical line indicates a change in the amount of continuously added NO into the chamber. Blue lines illustrate model results based on the MCM+SAR+THEO mechanism including theoretically calculated isomerisation reaction rate coefficients for the first-generation alkoxy radicals and the isomerisation products $C_2H_5CH(OH)C_2H_4CH_2OO$ (MCM notation: HO3C6O2) and $CH_3CH(OH)C_2H_4CH(OO\ )CH_3$ (MCM notation: HO2C6O2). More information about the theoretically calculated reaction rate coefficients can be found in Section D.

C Overview of modelled and measured observables

Table S1: Summary of measured HO_2/RO_2 radical concentration ratios, derived from measured and modelled radical concentrations. Values correspond to weighted means of the corresponding experiment(s).

HO_2 formation	VOC	$(HO_2/RO_2)_{meas}$		$(HO_2/RO_2)_{model}$	
		NO < 1 ppbv			
Single-step	propane[a]	0 65	0 01	1 08	0 01
	propene	1 04	0 01	0 84	0 08
	trans-2-hexene	0 77	0 01	0 91	0 04
Two-step	iso-pentane[a]	0 580	0 004	0 49	0 01
	n-hexane	0 766	0 007	0 59	0 05

[a] Determined from multiple experiments.

Table S2: Summary of the O_x production per oxidised VOC, derived from measured O_x (= NO_2 + O_3) concentrations and from measured and modelled radical concentrations. Values correspond to weighted means of the corresponding experiment(s).

HO_2 formation	VOC	$P\ O_x\ {}_{\text{VOC LIF}}$	$P\ O_x\ {}_{\text{VOC } O_x}$	$P\ O_x\ {}_{\text{VOC model}}$	$P\ O_x\ {}_{\text{VOC } O_x}$	$P\ O_x\ {}_{\text{VOC model}}$
		NO < 1 ppbv		NO < 1 ppbv	NO > 1 ppbv	
Single-step	propane	1 89 0 02[a]	1 88 0 08[a]	1 75 0 03[a]	1 9 0 5	1 9 0 1
	propene	-[b]	-[b]	-[b]	-[c]	-[c]
	trans-2-hexene	1 4 0 1	1 3 0 3	1 5 0 4	-[d]	-[d]
Two-step	iso-pentane	2 13 0 02[a]	2 0 0 4[a]	2 02 0 1[a]	2 0 0 1	2 5 0 1
	n-hexane	-[e]	-[e]	-[e]	2 0 0 2	2 1 0 1

[a] Determined from multiple experiments; [b] Not determined due to too small O_x production; [c] Contribution of propene to the total OH reactivity is less than 50 % for 3 ppbv < NO < 6 ppbv; [d] No experiment for NO > 1 ppbv; [e] HO_2 is mainly formed from the isomerisation of the regenerated RO_2, leading, at low NO, to an only small amount of peroxy radicals forming HO_2 in two NO reaction steps (Fig. S4) and thus it cannot be grouped together with iso-pentane at these conditions.

D Theoretical study of alkoxy and alkylperoxy radicals formed from n-hexane

D.1 Methodology

For all intermediates and transition states (TSs) an exhaustive characterisation of all conformers was done first at the M06-2X/cc-pVDZ level of theory,[7,8] where TSs were verified by running IRC calculations at this level. The IRC end points were also used to optimise the properties of the reaction product, as needed for tunneling calculations (see below). Further refinement was then done for all geometries at the M06-2X-D3/aug-cc-pVTZ level of theory.[9,10] The vibrational wavenumbers were likewise characterised at this level, using a scaling factor of 0.971.[11,12] The relative energies between the lowest energy reactant and transition state conformers were then refined at the CCSD(T)/aug-cc-pVTZ level of theory.[13] All T1 diagnostics are below the 0.044 cut-off suggested by Rienstra-Kiracofe et al.[14]The expected uncertainty on the reaction barrier heights at this level of theory is $0\ 5\,\mathrm{kcal\,mol}^{1}$.

The high-pressure thermal rate coefficients were calculated using multi-conformer transition state theory, MC-TST, including all conformers characterised as above.[15] Tunneling is accounted for using asymmetric Eckart tunneling.[16,17] The reactions characterised in this work are not expected to be pressure-dependent under atmospheric conditions, and the estimated accuracy of the rate coefficients is a factor 2 to 3.

D.2 Reaction Mechanism and rate coefficients

Of the systems studied in this work, the n-hexane system is most sensitive to the fate of the intermediate alkoxy and alkylperoxy radicals, where H-migration in the primary alkoxy $C_6H_{13}O$

Table S3: Theoretically calculated rate coefficients based on CCSD(T)/aug-cc-pVTZ//M06-2X-D3/aug-cc-pVTZ quantum chemical data. Shown are the barrier height (E_b, kcal mol$^{\ 1}$), rate coefficients at 298 K (s$^{\ 1}$), and the parameters for the temperature-dependent rate coefficient between 200 and 450 K given as $k\ T \quad A \quad T\ \mathrm{K}^{\ n} \quad exp \quad E_a\ T$ with A in s$^{\ 1}$ and E_a in K.

Reactant	Reaction	E_b	k 298 K	A	n	E_a
$CH_2(O\ )$-CH_2-CH_2-CH_2-CH_2-CH_3	1,5-H-shift	7.7	6 0 $\ 10^6$	2.56E-10	6-77	263
	1,6-H-shift	7.9	7 5 $\ 10^5$	6.80E-10	6.45	623
	1,7-H-shift	12.8	4 0 $\ 10^2$	1.69E-40	16.32	-1370
CH_3-$CH(O\ )$-CH_2-CH_2-CH_2-CH_2-CH_3	1,5-H-shift	6.8	1 1 $\ 10^8$	1.59E-06	5.84	404
	1,6-H-shift	9.4	8 6 $\ 10^5$	6.60E-20	9.99	-273
CH_3-CH_2-$CH(O\ )$-CH_2-CH_2-CH_3	1,5-H-shift	9.2	8 1 $\ 10^6$	2.00E-17	9.42	-205
CH_3-$CH(OO\ )$-CH_2-CH_2-$CH(OH)$-CH_3	1,5-H-shift	21.8	1 1 $\ 10^{\ 3}$	2.25E-22	10.67	5278
	1,6-H-shift (-OH)	17.0	5 6 $\ 10^{\ 1}$	4.63E-25	11.13	2365
	1,7-H-shift	24.0	4 3 $\ 10^{\ 6}$	4.46E-28	12.11	5472
$CH_2(OO\ )$-CH_2-CH_2-$CH(OH)$-CH_2-CH_3	1,5-H-shift	22.4	3 4 $\ 10^{\ 4}$	2.81E-26	11.82	4921
	1,6-H-shift (-OH)	16.9	4 7 $\ 19^{\ 1}$	4.99E-28	12.12	2065
	1,7-H-shift	20.8	3 4 $\ 10^{\ 4}$	1.02E-34	14.20	3155
	1,8-H-shift	25.3	4 9 $\ 10^{\ 7}$	2.13E-23	10.42	6467

radicals can lead to formation of secondary $HOC_6H_{12}OO$ hydroxyalkyl peroxy radicals:

$$C_6H_{14} \quad OH \quad O_2 \quad C_6H_{13}OO \quad H_2O \tag{S1}$$

$$C_6H_{13}OO \quad NO \quad C_6H_{13}O \quad NO_2 \tag{S2}$$

$$C_6H_{13}O \quad O_2 \quad HOC_6H_{12}OO \tag{S3}$$

The n-hexane + OH reaction proceeds by H-abstraction, where the secondary H-atoms on the inner carbons are strongly favoured compared to abstraction of the primary H-atoms on the terminal carbons (see Figure S4). The primary peroxy radicals can be converted to the primary alkoxy radicals by reaction with NO, or by the alkoxy channel of the RO_2 + RO_2 reaction.[6] All three alkoxy radicals have access to fast H-migration pathways, where the rate coefficients depend on the migration span, as well as the order of the migrating H-atom (primary or secondary). In all cases, an H-migration is accessible with a rate of $\ 5 \quad 10^6$ s$^{\ 1}$ at ambient temperatures (see Table S3), which exceeds the rate of reaction with O_2, $k \quad 5 \quad 10^4$ s$^{\ 1}$,[18] as well as the decomposition reaction to a carbonyl + an alkyl radical, k 2 10^{4} s ^{1}.[5]

The resulting hydroxy-alkyl radical, HOC_6H_{12}, rapidly reacts with O_2, k 5 10^{7} s ^{1}, forming a hydroxyalkyl peroxy radical, $HOC_6H_{12}OO$ (see Figure S4); no other competing reactions are expected. Here, we discuss only the dominant $HOC_6H_{12}OO$ radicals, where primary alkylperoxy radicals are neglected due to the low contribution of abstraction of the primary H-atoms in n-hexane, and only the products of the dominant 1,5-H-shift in the secondary parent alkoxy radicals are retained. The HO-hexylperoxy radicals readily undergo an H-migration shift of the -OH H-atom(s), with rates exceeding 0 1 s ^{1} (see Table S3). These autoxidation reactions occur mainly in competition with other RO_2 loss processes such as the reaction with NO or HO_2 (see main text and modeling); the contribution of other H-migration reactions is negligible, with k 1 10 ^{3} s ^{1}. The dominant products of the autoxidation is then an -OH alkyl radical, which are known to react rapidly with O_2 to form a carbonyl compound and HO_2.

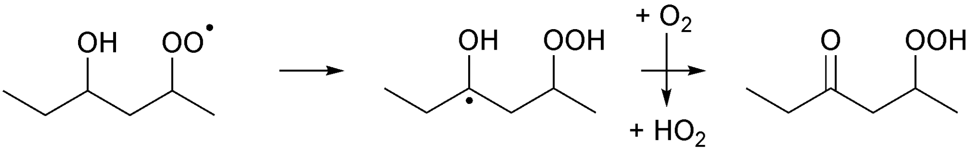

Overall, this mechanism then constitutes a 2-step mechanism for the formation of HO_2 from the n-hexane reactant.

D.3 Comparison of the theoretical data with SAR predictions

It is useful to compare the theoretical predictions obtained above, against the available Structure-Activity Relationships (SARs), where the SAR by Vereecken and Peeters[4] is the most advanced available for alkoxy H-migration reactions, as far as we are aware, and the SAR by Vereecken and Nozière[3] for alkylperoxy radicals H-migrations.

For the primary alkoxy radical, $CH_2(O\ )$-CH_2-CH_2-CH_2-CH_2-CH_3, the SAR predictions by Vereecken and Peeters[4] are in excellent agreement, within a factor 2 for k(298 K). The theory used in this work has been validated to work well for this type of reactions, and the SAR itself is based on rates relative to experimental observations for primary alkoxy radicals even if the level of theory is somewhat outdated by current standards, so the good agreement is encouraging. For the secondary alkoxy radicals (i.e. 2-hexoxy and 3-hexoxy), on the other hand, the agreement is significantly less good, with the SAR underpredicting the rate coefficients by about a factor 10. The main reason seems to be that the SAR, and its underlying experimental data, does not account for the impact of alkyl substitutions around the alkoxy radical site. For alkylperoxy radicals (Vereecken and Nozière[3]), going from a primary to a tertiary radical site was shown to affect the rates by over an order of magnitude. The current results suggest that the Vereecken and Peeters SAR needs to be updated to account for the order of the radical site as well.

The rate coefficients for H-migration in hydroxyperoxy radicals predicted by the Vereecken and Nozière SAR[3] compare well with the calculations in this work, within a factor 3 for the fast migration of -OH H-atoms. For migration of the aliphatic H-atoms, the SAR prediction is too low by about an order of magnitude; this suggests that the prediction correction by a factor 6 for -OH substitution may need to be updated from its current estimate, which is based only on a few lower-level theoretical results.

The differences between the high-level theoretical rate predictions in this work, and the values obtained from the SARs by Vereecken and Peeters,[4] and Vereecken and Nozière,[3] do not have a large impact on the modeling predictions in this work. Figure S13 shows the difference when the MCM model is enhanced purely on SAR predictions (MCM+SAR), or when the direct theoretical calculations in this work are used instead of the Vereecken SARs[3,4] (MCM+SAR+THEO). The difference is smaller than the uncertainties on the model predictions, and a comparison against the experimental data does not allow selection of the optimal result.

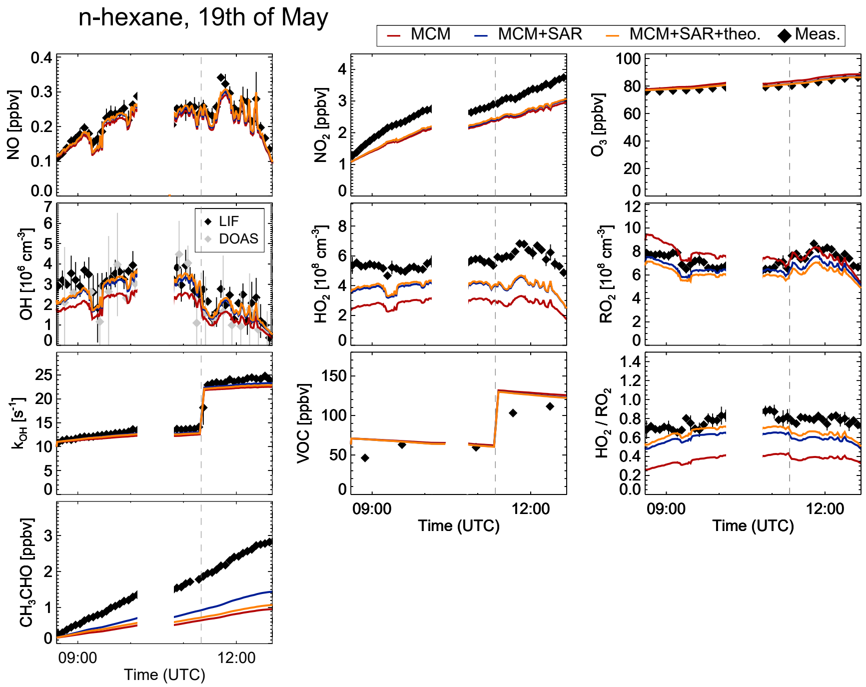

Figure S13: Comparison of measured and modelled radical and trace gas concentrations for the experiment with n-hexane at NO < 1 ppbv, performed on 19 May 2022. The vertical line indicates the second injection of the VOC into the chamber. Blue lines illustrate model results based on the MCM+SAR mechanism, while orange lines illustrate results from MCM+SAR+THEO model calculations including theoretically calculated isomerisation reaction rate coefficients (Tab. S3).

D.4 Additional supporting information

The raw quantum chemical data is available under the following repository: Vereecken, Luc, 2024, “Replication Data for: Effect of the alkoxy radical chemistry on the ozone formation from anthropogenic organic compounds investigated in chamber experiments”, https://doi.org/10.26165/JUELICH-DATA/J2LHTQ.

References

(1) Jenkin, M. E.; Saunders, S. M.; Pilling, M. J. The tropospheric degradation of volatile organic compounds: a protocol for mechanism development. *Atmos. Environ.* **1997**, *31*, 81–104, DOI: `10.1016/S1352-2310(96)00105-7`.

(2) Saunders, S. M.; Jenkin, M. E.; Derwent, R. G.; Pilling, M. J. Protocol for the development of the Master Chemical Mechanism, MCM v3 (Part A): tropospheric degradation of non-aromatic volatile organic compounds. *Atmos. Chem. Phys.* **2003**, *3*, 161–180, DOI: `10.5194/acp-3-161-2003`.

(3) Vereecken, L.; Nozière, B. H migration in peroxy radicals under atmospheric conditions. *Atmos. Chem. Phys.* **2020**, *20*, 7429–7458, DOI: `10.5194/acp-20-7429-2020`.

(4) Vereecken, L.; Peeters, J. A structure–activity relationship for the rate coefficient of H-migration in substituted alkoxy radicals. *Phys. Chem. Chem. Phys.* **2010**, *12*, 12608–12620, DOI: `10.1039/C0CP00387E`.

(5) Vereecken, L.; Peeters, J. Decomposition of substituted alkoxy radicals—part I: a generalized structure–activity relationship for reaction barrier heights. *Phys. Chem. Chem. Phys.* **2009**, *11*, 9062–9074, DOI: `10.1039/B909712K`.

(6) Jenkin, M. E.; Valorso, R.; Aumont, B.; Rickard, A. R. Estimation of rate coefficients and branching ratios for reactions of organic peroxy radicals for use in automated mechanism construction. *Atmos. Chem. Phys.* **2019**, *19*, 7691–7717, DOI: `10.5194/acp-19-7691-2019`.

(7) Dunning, T. H. Gaussian basis sets for use in correlated molecular calculations. I. The atoms boron through neon and hydrogen. *J. Chem. Phys.* **1989**, *90*, 1007–1023, DOI: `10.1063/1.456153`.

(8) Zhao, Y.; Truhlar, D. G. The M06 suite of density functionals for main group thermochemistry, thermochemical kinetics, noncovalent interactions, excited states, and transition ele-

ments: two new functionals and systematic testing of four M06-class functionals and 12 other functionals. *Theor. Chem. Acc.* **2008**, *120*, 215–241, DOI: `10.1007/s00214-007-0310-x`.

(9) Goerigk, L.; Hansen, A.; Bauer, C.; Ehrlich, S.; Najibi, A.; Grimme, S. A look at the density functional theory zoo with the advanced GMTKN55 database for general main group thermochemistry, kinetics and noncovalent interactions. *Phys. Chem. Chem. Phys.* **2017**, *19*, 32184–32215, DOI: `10.1039/C7CP04913G`.

(10) Grimme, S.; Ehrlich, S.; Goerigk, L. Effect of the damping function in dispersion corrected density functional theory. *J. Comput. Chem.* **2011**, *32*, 1456–1465, DOI: `10.1002/jcc.21759`.

(11) Alecu, I. M.; Zheng, J.; Zhao, Y.; Truhlar, D. G. Computational Thermochemistry: Scale Factor Databases and Scale Factors for Vibrational Frequencies Obtained from Electronic Model Chemistries. *J. Chem. Theory Comput.* **2010**, *6*, 2872–2887, DOI: `10.1021/ct100326h`.

(12) Kanchanakungwankul, S.; Bao, J. L.; Zheng, J.; Alecu, I. M.; Lynch, B. J.; Zhao, Y.; Truhlar, D. G. Database of Frequency Scale Factors for Electronic Model Chemistries. 2021; `http://comp.chem.umn.edu/freqscale/index.html`.

(13) Bartlett, R. J.; Purvis, G. D. Many-body perturbation theory, coupled-pair many-electron theory, and the importance of quadruple excitations for the correlation problem. *Int. J. Quantum Chem.* **1978**, *14*, 561–581, DOI: `10.1002/qua.560140504`.

(14) Rienstra-Kiracofe, J. C.; Allen, W. D.; Schaefer, H. F. The C_2H_5 + O_2 Reaction Mechanism: High-Level ab Initio Characterizations. *J. Phys. Chem. A* **2000**, *104*, 9823–9840, DOI: `10.1021/jp001041k`.

(15) Vereecken, L.; Peeters, J. The 1,5-H-shift in 1-butoxy: A case study in the rigorous implementation of transition state theory for a multirotamer system. *The Journal of Chemical Physics* **2003**, *119*, 5159–5170, DOI: `10.1063/1.1597479`.

(16) Eckart, C. The Penetration of a Potential Barrier by Electrons. *Phys. Rev.* **1930**, *35*, 1303–1309, DOI: `10.1103/PhysRev.35.1303`.

(17) Johnston, H. S.; Heicklen, J. Tunneling corrections for unsymmetrical Eckart potential energy barriers. *J. Phys. Chem.* **1962**, *66*, 532–533, DOI: `10.1021/j100809a040`.

(18) Orlando, J. J.; Tyndall, G. S.; Wallington, T. J. The Atmospheric Chemistry of Alkoxy Radicals. *Chem. Rev.* **2003**, *103*, 4657–4690, DOI: `10.1021/cr020527p`.

A.3 Supplementary materials to Section 3.3

Temperature-dependent impact of non-PAN peroxy nitrate formation, RO_2NO_2, on nighttime atmospheric chemistry[†]

– Supporting information –

Michelle Färber, Luc Vereecken, Hendrik Fuchs, Georgios I. Gkatzelis, Franz Rohrer, Sergej Wedel, Andreas Wahner, and Anna Novelli

Contents

A Investigation of the ozonolysis of trans-2-hexene

The FZJ mechanism includes among other modifications an updated ozonolysis and isomerisation scheme compared to the MCM (Section 2.3). Since ozonolysis also contributes to the nighttime chemistry (Tab. S3) the validity of this mechanism was separately tested with an ozonolysis experiment with trans-2-hexene (T 280 K).

Measured species are compared with model results using either the FZJ mechanism or the MCM. The measured time series of trans-2-hexene and ozone are very well described by all mechanisms within the uncertainties (Fig. S2). Measured HO_2 radical concentrations agree with the MCM and FZJ mechanisms within 20 % and 30 %, respectively. Predicted HO_2 radical concentrations are similar for all models; the HO_2 production is predominantly driven by the OH + CO reaction, contributing to about 83 % to the total HO_2 production, while HO_2 is lost via its reactions with RO_2 and O_3, contributing to about 50 % and 35 % to the total HO_2 loss, respectively.

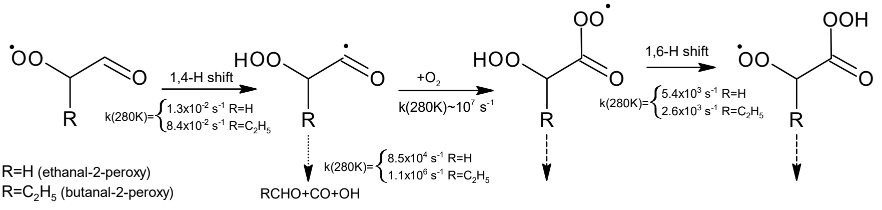

Figure S1: Generalised isomerisation scheme of ethanal-2-peroxy and butanal-2-peroxy based on quantum mechanical calculations by Novelli *et al.*[1]. Dashed lines indicate the loss of RO_2 through reaction with NO, NO_2, HO_2, and R'O_2, while dotted lines display decomposition reactions.

For the MCM mechanism, a model-to-measurement ratio of up to 2.8 is found for RO_2 radicals formed. In comparison, the FZJ mechanism substantially improves the agreement (agreement within 27 % on average, and a maximum deviation of a factor 1.7), since less RO_2 are expected to be formed in the FZJ mechanism than in the MCM due to a lower RO_2 yield from ozonolysis (59 % in the FZJ mechanism, 70 % in the MCM). However, modelled RO_2 radical concentrations remain up to a factor of 1.7 higher than measured values, particularly after the first injection. This was also observed by Novelli *et al.*[1] for RO_2 formed in the nighttime oxidation of trans-2-hexene when ozonolysis dominated the chemistry.

For this reason, the isomerisation scheme (Fig. S1) of the RO_2 radicals from the ozonolysis, ethanal-2-peroxy and butanal-2-peroxy, was tested separately by comparing model results when their isomerisation reactions are included or not (Figs. S2 and S3). The impact of the isomerisation of ethanal-2-peroxy and butanal-2-peroxy on the total RO_2 is small, and results from the models with and without RO_2 isomerisation reactions agree within 10 % (Fig. S2). However, including isomerisation reactions does influence the RO_2 speciation, displayed in Fig. S3. While the FZJ mechanisms yield similar contributions of methyl and propyl peroxy radical concentrations to the total RO_2 radical concentration (approximately 36 % combined), differences emerge in the allocation of the remaining RO_2 species. In the FZJ model without RO_2 isomerisation, these RO_2 are distributed among oxygenated peroxy radicals like ethanal-2-peroxy and butanal-2-peroxy. In contrast, in the FZJ model including RO_2 isomerisation, they are apportioned between their respective isomerisation products, ethyl-1-peracid-2-peroxy and butyl-1-peracid-2-peroxy, with a minor contribution from ethanal-2-peroxy and butanal-2-peroxy. Due to

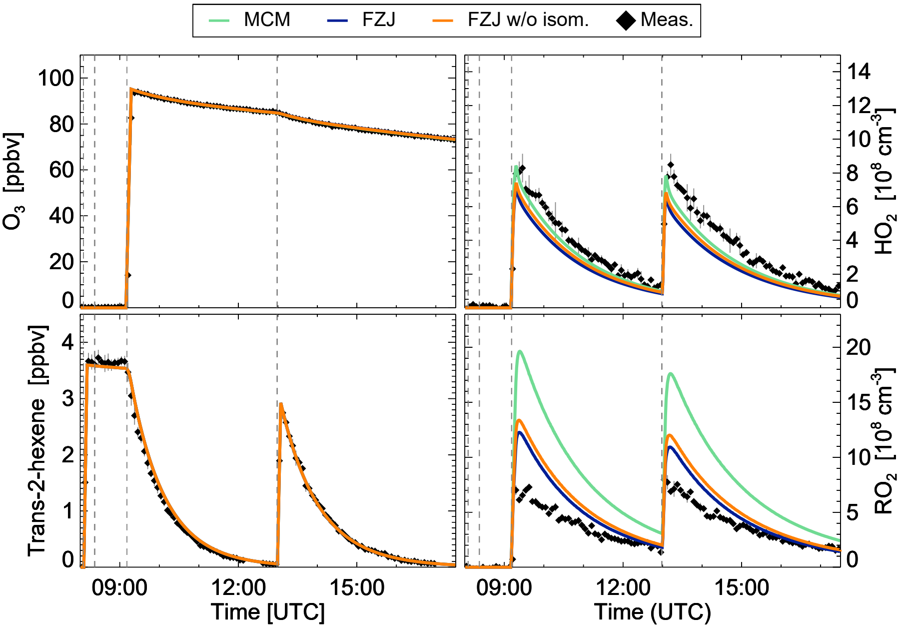

Figure S2: Comparison between modelled and measured (5 minutes average) trace gases and HO_2 and RO_2 radical concentrations for three different mechanisms for the ozonolysis experiment of trans-2-hexene at 280 K. Model results displayed as FZJ and FZJ w/o isom models refer to the FZJ mechanism with and without RO_2 isomerisation reactions, respectively. Injections of chemical species into the chamber are marked by vertical lines.

similar lifetimes of all these RO_2, the total RO_2 radical concentration does not significantly change whether isomerisation reactions are included in the model or not. Measurements of speciated RO_2 would be necessary to validate the isomerisation scheme.

An updated ozonolysis scheme following the recent recommendation by Newland *et al.*[2] was also tested. In short, the main difference comprises a yield of 40 % towards the C_3 carbonyl compounds as compared to 50 % as used in this study. The major impact is on the modelled acetaldehyde (increase of 40 % as compared to the FZJ mechanism) with negligible differences for the radicals. To bring measured and modelled RO_2 radicals in agreement a total yield of RO_2 as low as 20 % would be needed. Although there is a lack of studies focusing directly on trans-2-hexene ozonolysis, this would be in stark disagreement with the molecules used to develope the SAR (1 and 3-hexene).

In the following, the remaining discrepancy between modelled and measured RO_2 is further discussed, examining the potential impact of the peracidic functionality on the RO_2 chemistry and detection. A partial detection of RO_2 by the FZJ-RO_xLIF instrument due to the formation of organic nitrites (RONO) or carbonyl compounds (RC=O) in the reaction of RO with NO can be excluded. Table S1 shows pseudo-first order loss rates of the main RO radicals in the ozonolysis reaction with trans-2-hexene. For all listed RO radicals, the reaction of RO with NO does not compete with the other RO loss reactions. The fate of the peracid-substituted RO_2 radicals was mostly estimated from the SAR in Jenkin *et al.*[3], which does not consider peracid substituents explicitly. Due to the large contribution of peracidic peroxy radicals to the total RO_2 the modelled total RO_2 is sensitive to their

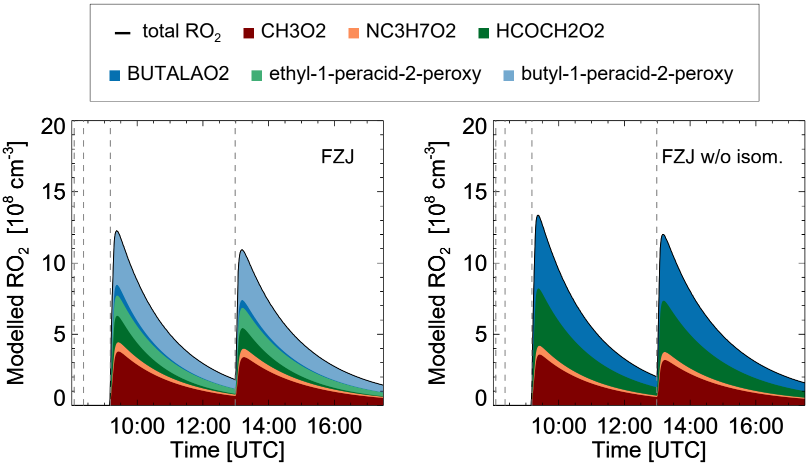

Figure S3: Model results of time-dependent speciation of RO_2 radicals obtained for the FZJ mechanism with (FZJ) and without (FZJ w/o isom) RO_2 isomerisation reactions. Contributions of butanal-2-peroxy, ethanal-2-peroxy, and the RO_2 formed subsequently their isomerisation are shown. Injections of chemical species into the chamber are marked by vertical lines.

chemistry (Fig. S4).

Removing the fraction of RO_2 stored in form of butyl-1-peracid-2-peroxy from the observable RO_2 would improve the agreement between modelled and measured RO_2 significantly (model-to-measurement ratio improved from 1.38 to 0.92 for the first injection period), but the exclusion of both, ethyl-1-peracid-2-peroxy and butyl-1-peracid-2-peroxy, would result in an underestimation of the measured RO_2 (model-to-measurement ratio of 0.7 for the first injection period). This observation is consistent with the systematic study performed by Novelli *et al.*[1] who observed a good agreement between measured and modelled (FZJ model) nighttime RO_2 for cis-2-butene but a discrepancy for 1-pentene and trans-2-hexene. While only ethanal-2-peroxy and thus ethyl-1-peracid-2-peroxy are formed in the ozonolysis of cis-2-butene, butanal-2-peroxy and thus butyl-1-peracid-2-peroxy are predicted for 1-pentene and trans-2-hexene. The presence of an alkyl moiety may have an impact on the respective RO_2 chemistry that we are currently not aware of. However, as we are lacking speciated RO_2 measurements in this work, we cannot unam-

Table S1: Comparison of the pseudo-first order loss rates of main RO radicals formed in the ozonolysis of trans-2-hexene. The loss rates were determined for conditions present inside the FZJ-RO$_x$LIF reactor (25 hPa, 3 10^{11} cm ^{3} of NO, 6 s residence time). k_{dec} and k_{isom} refer to unimolecular reaction rate coefficients for the decomposition and isomerisation of RO radicals, respectively. Rate coefficients for the bimolecular reactions of RO with O_2 (H abstraction reaction) and with NO are denoted as $k_{\mathrm{H}abstr}$ and $k_{\mathrm{RO\ \ NO}}$, respectively.

RO radical	k_{dec} [s ^{1}]	k_{isom} [s ^{1}]	$k_{\mathrm{H}abstr}$ O_2 [s ^{1}]	$k_{\mathrm{RO\ \ NO}}$ NO [s ^{1}]
CH_3O			183	4
$C_2H_5CH(OH)C(=O)O$	5 3 10^{12}			14
$CH_2(O\ )C(=O)OOH$	0.6	2 8 10^{3}	1 1 10^{3}	14

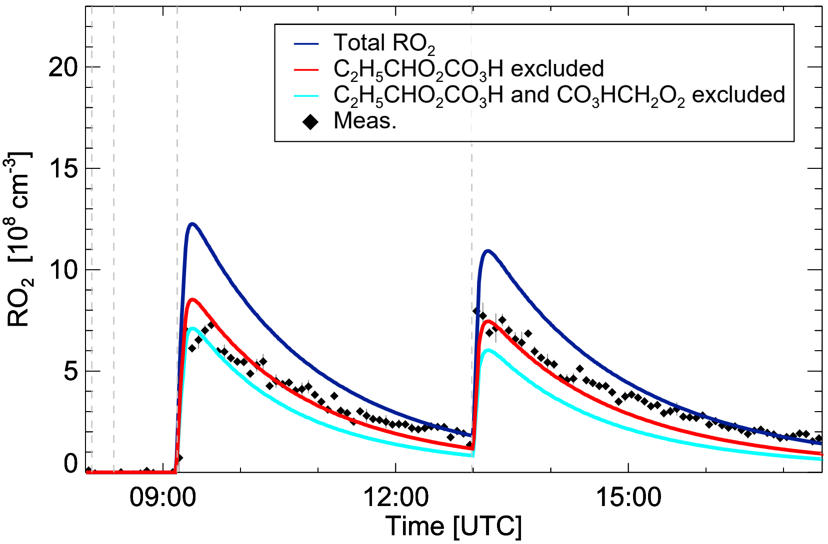

Figure S4: Comparison of modelled and measured (5 minutes average) total RO_2 concentrations in the ozonolysis experiment of trans-2-hexene. Model results are based on the FZJ mechanism. Displayed modelled RO_2 show the total RO_2 and total RO_2 excluding either butyl-1-peracid-2-peroxy or ethyl-1-peracid-2-peroxy and butyl-1-peracid-2-peroxy.

biguously decide which RO_2 is aberrant, making speculations on the exact nature of the missing chemistry complex.

For the nighttime trans-2-hexene experiments, ozonolysis is contributing most in the experiment performed at low temperatures (T 276 K), but less so for the higher temperatures (Tab. S3). Figure S5 shows total RO_2 modelled by the FZJ mechanism including non-acyl RO_2NO_2 formation, but with and without including butyl-1-peracid-2-peroxy in the observable RO_2. For hot and medium temperatures, the modelled total RO_2 improves somewhat when ignoring the contribution of butyl-1-peracid-2-peroxy, however, for cold conditions, measured RO_2 radical concentrations are now underestimated by a factor of 1.5. Such behaviour could be consistent with a loss process that is temperature dependent and becomes less important at lower temperatures, *e.g.* a unimolecular reaction of butyl-1-peracid-2-peroxy not forming a new RO_2 radical. However, some unimolecular reactions have been considered by Novelli *et al.*[1], and none are competitive. Simulations adding dummy bimolecular reactions with the typical co-reactants, HO_2 and RO_2, likewise did not suggest any suitable pathways.

Overall, at the present time the cause for the RO_2 discrepancy observed in the ozonolysis experiment remains unknown. Further investigations of the RO_2 chemistry of peracid

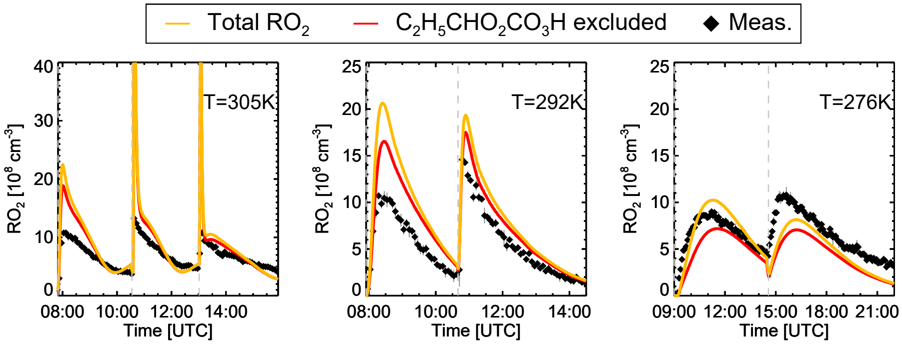

Figure S5: Comparison of modelled and measured (5 minutes average) total RO_2 concentrations for the nighttime experiments of trans-2-hexene. Model results are based on the FZJ mechanism including additional formation of non-acyl RO_2NO_2. Displayed modelled RO_2 show the total RO_2 and total RO_2 excluding butyl-1-peracid-2-peroxy.

peroxy radicals would be required as well as measurements of speciated RO_2. Important, though, is that the impact of the discrepancy in the ozonolysis chemistry remains rather limited in the nighttime experiments (Fig. S5), such that the main conclusions on the impact of peroxynitrate formation are robust against the uncertainties on the fate of butyl-1-peracid-2-peroxy.

B Estimation of the NO_3 interference in the RO_x system

In the NO_3-oxidation experiment of trans-2-hexene at high temperatures, a NO_3 interference was observed in the RO_x cell. The RO_x system of the LIF instrument is run in two modes, with and without addition of NO in the converter, enabling the measurement of RO_x (= OH + HO_2 + RO_2) or $HO_2(RO_x)$ (= HO_2 + interfering RO_2), respectively. $HO_2(RO_x)$ is not further evaluated but it can be used as an indicator for possible interferences. If no interference is present, the following is valid:

$$HO_2 \; RO_x \qquad RO_x \tag{S1}$$

The two observables are shown in Fig. S6, together with the modelled NO_3 mixing ratio for the aforementioned experiment of interest. For NO_3 20 pptv, $HO_2(RO_x)$ starts to deviate from RO_x such that Eq. (S1) no longer holds. As there is no evidence for a change

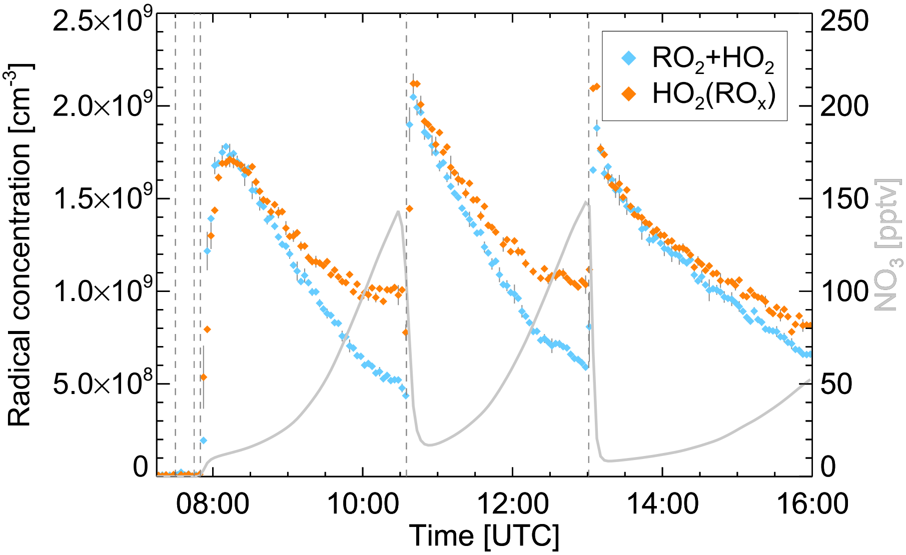

Figure S6: Comparison between RO_x and $HO_2(RO_x)$ radical concentrations, measured with the RO_xLIF radical instrument (3 minutes average) in the nighttime oxidation of trans-2-hexene at hot conditions. Injections of chemical species into the chamber are marked by vertical lines.

in the sensitivity of the instrument between the two modes, this discrepancy can only be explained by an interference. A lower limit of the interference signal in the RO_x system, without adding NO in the converter, is given by the difference of $HO_2(RO_x)$ and RO_x since it is assumed that all RO_2 are converted to OH or HO_2 in the RO_x detection cell. According to Fuchs *et al.*[4], the interference signal in the RO_x system, when adding NO in the converter, is two times smaller, therefore, it can be treated as an estimate for the NO_3 interference in the RO_x measurement.

By performing a linear regression, a NO_3 interference of 3 6 10^6 cm ^{3} per pptv of

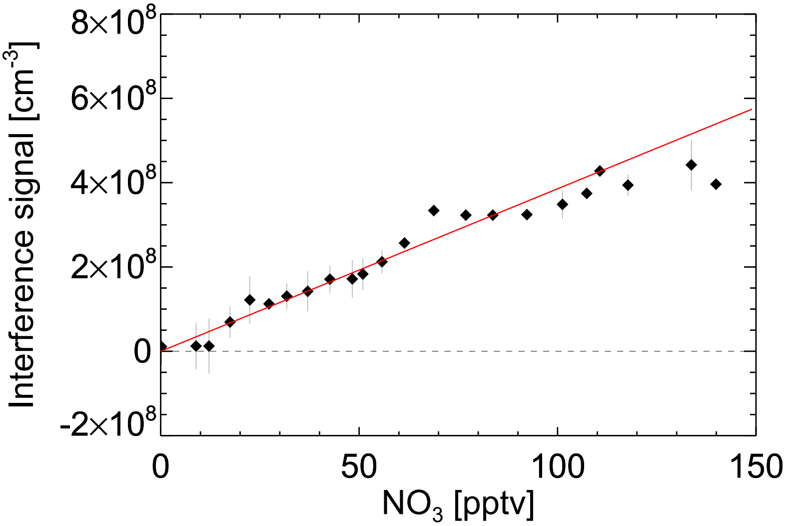

Figure S7: Correlation plot of the estimated NO_3 interference. The interference signal is derived from the difference of HO_2RO_x and the sum of HO_2 and RO_2 radicals.

NO_3 could be estimated (see Fig. S7). Figures S8 and S9 display the impact of the NO_3 interference on the measured HO_2 and RO_2 radical concentrations. Overall, the NO_3 interference in the RO_2 radical measurement only affects the trans-2-hexene experiment at high temperatures where the interference decreases the RO_2 by approximately a factor of 1.5.

The NO_3 interference in the HO_2 radical measurement could not be determined in this study, therefore, a recently reported value for the previous SAPHIR-RO_xLIF system of 1 10^6 cm ^{3} per pptv NO_3 was taken from Fuchs *et al.*[4]. Corresponding interference-corrected HO_2 radical concentrations are lowered by 25 % relative to the measured HO_2 for the trans-2-hexene experiment at high temperatures (Fig. S8). Similarly to RO_2, the NO_3 interference in the HO_2 radical measurement is only important for hot conditions, therefore it is not considered for the remaining experiments. For the experiment at high temperatures, the interference is taken into account in the mechanisms by adding it to the modelled HO_2 and RO_2 radicals.

For the cis-2-butene experiments, including the NO_3 interference does not affect the HO_2 and RO_2 radical.

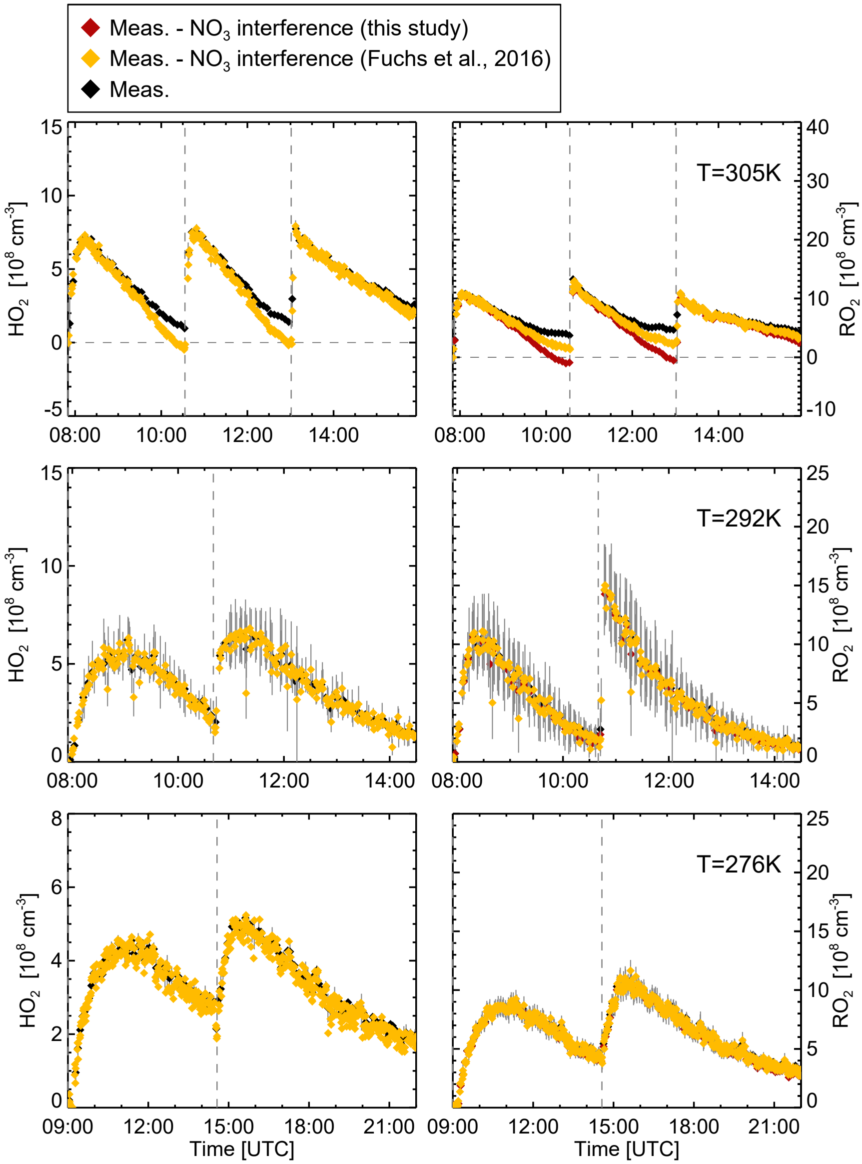

Figure S8: Measured (5 minutes average) HO_2 and RO_2 radical concentrations in the trans-2-hexene experiments at cold, medium, and hot temperatures, with and without including the NO_3 interference, derived from this work for RO_2 and taken from Fuchs *et al.*[4] for HO_2. Injections of chemical species into the chamber are marked by vertical lines.

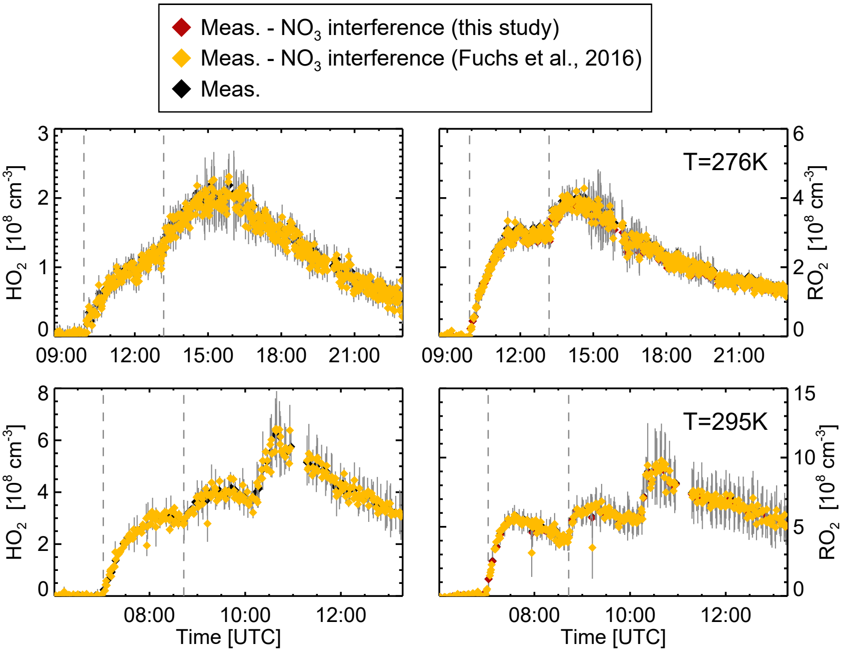

Figure S9: Measured (5 minutes average) HO_2 and RO_2 radical concentrations in the cis-2-butene experiment at cold and medium temperatures, with and without the NO_3 interference, derived from this work for RO_2 and taken from Fuchs *et al.*[4] for HO_2. Injections of chemical species into the chamber are marked by vertical lines.

C Modified $CH_3CH(NO_3)CH(CH_3)O$ decomposition rate

A previous study on -nitrate alkoxy radicals by Novelli *et al.*[1] showed that specific -nitrate alkoxy radicals, >C(ONO_2)C(O)<, decompose with a rate of about 4 5 10^4 s ^{1} at 298 K. The reaction with O_2 or isomerisation are not competitive in the RO_x converter at room temperature. Since the RO_2 detection relies on the formation of OH or HO_2 in the process of the reaction of RO_2 with NO, the detectability of the according peroxy radical $CH_3CH(OO\ )CH(ONO_2)CH_3$ (MCM notation: C42NO33O2) is affected.

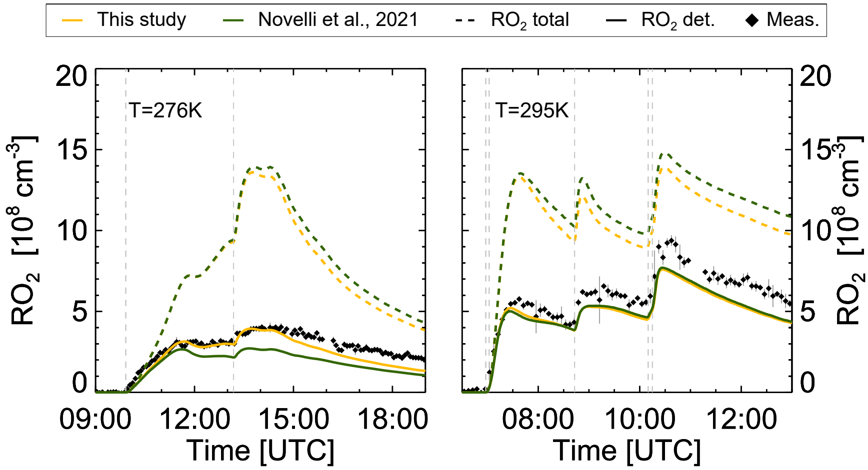

Figure S10: Comparison of modelled time series with measurements for the decomposition rates of $CH_3CH(NO_3)CH(CH_3)O$ (MCM notation: C42NO33O) used by Novelli *et al.*[1] (Eq. (S2)) and in this work (Eq. (S3)) for the cis-2-butene experiments. Model results are based on the FZJ mechanism including additional formation of non-acyl RO_2NO_2. Injections of chemical species into the chamber are marked by vertical lines.

The decomposition rate of $CH_3CH(NO_3)CH(CH_3)O$ (MCM notation: C42NO33O) was calculated theoretically in the study by Novelli *et al.*[1] and was modified within its uncertainty to improve the agreement between model and measurement for cold conditions. Figure S10 displays the comparison of the modelled RO_2 radical concentrations with the decomposition rate as used in the study by Novelli *et al.*[1] and with the new one:

$$k_{dec\ \text{Novelli}\ et\ al.} \quad 2\ 94 \quad 10^9 \quad T^{1\ 32} \quad \exp \quad \frac{5542}{T} \qquad \text{(S2)}$$

$$k_{dec\ \text{this study}} \quad 2\ 94 \quad 10^9 \quad T^{1\ 32} \quad \exp \quad \frac{5860}{T} \qquad \text{(S3)}$$

In the tested temperature range (from 276 K to 305 K), the decomposition rate, used in this work, is deviating by maximum a factor of 3 from the decomposition rate used by Novelli *et al.*[1]. This is on the higher end of the expected uncertainty (factor of 2 to 3) of the theoretically calculated rate in Novelli *et al.*[1], but remains comparable to the variability between the various stereo-specific RO_2 isomers and the uncertainty on the rate predictions.

The decomposition rate, as used in this study, results in a detectability of 16 % at 279 K (increasing from 5 % with the decomposition rate from Novelli *et al.*[1]) and of 5 % at 295 K (increasing from 1 7 % with the decomposition rate from Novelli *et al.*[1]).

For the analogous $CH_3CH(NO_3)CH(C_3H_7)O$ (MCM notation: C62NO33O), formed in the NO_3-oxidation scheme of trans-2-hexene, the decomposition reaction rate should likely be adjusted by a similar amount. However, its dominant loss is isomerisation by H-migration, such that we are not sensitive to the rate coefficient for decomposition for this compound.

D Instrumentation details

Table S2: Instrumentation for radical and trace-gas measurements during the presented experiments.

Species	Technique	Time resolution	1 precision	1 accuracy
OH	LIF	45 s	2 8 10^5 cm 3	18 %
HO_2	LIF	45 s	2 9 10^7 cm 3	18 %
RO_2	LIF	45 s	5 6 10^7 cm 3	18 %
k_{OH}	Laser photolysis+LIF	132 s	0 4 s 1	10 %
O_3	UV absorption	60 s	1 ppbv	5 %
CO	CRDS	60 s	1 5 ppbv	1 %
Acetaldehyde	PTR-TOF-MS	30 s	>15 pptv	10 %
NO	Chemiluminescence	45 s	10 pptv	5 %
NO_2	Chemiluminescence	97 s	2 pptv	5 %

E Contribution of NO_3 and O_3 to the oxidation of cis-2-butene and trans-2-hexene

Table S3: Overview of performed cis-2-butene and trans-2-hexene experiments. The contributions of ozonolysis and reaction with NO_3 to the oxidation of the VOCs are listed.

Temperature [K]	Experimental description	Contribution O_3 [%]	Contribution NO_3 [%]
Cis-2-butene			
295	CO addition	54	46
276	CO addition	38	63
Trans-2-hexene			
305	CO addition	14	86
292	CO addition	22	78
279	CH_4 addition	46	54
276	CO addition	45	55

F Comparison of modelled and measured acetaldehyde from the oxidation of cis-2-butene by NO_3

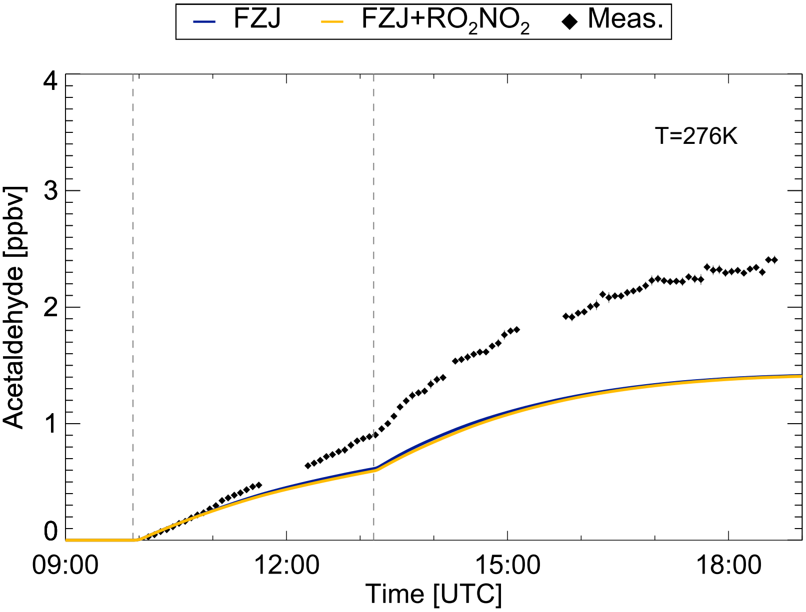

Figure S11: Comparison of modelled and measured (5 minutes average) acetaldehyde in the nighttime experiments of cis-2-butene at cold conditions. Model results displayed as FZJ (blue) and FZJ+RO_2NO_2 (brown) models refer to the FZJ mechanism without and with the additional formation of non-acyl RO_2NO_2, respectively. Injections of chemical species into the chamber are marked by vertical lines.

G Nighttime oxidation of trans-2-hexene at different temperatures

Experiments focussing on the nighttime oxidation of trans-2-hexene were performed at three different temperatures: at cold temperatures of 276 K (Fig. 2) and 279 K (Fig. 3), and at medium (T 292 K) and hot (T 305 K) temperatures (Fig. S12). In the main paper, the experiment conducted at T 276 K was already presented. Here, we discuss the experiments at medium and hot temperatures, and compare them to the experiment performed at cold temperatures.

For hot conditions, the FZJ mechanisms, with and without additional RO_2NO_2 formation, overestimate the measured RO_2 radical concentration by a factor of up to 1.5, after 0.5 h after the VOC was (re-)injected. Directly after the VOC injections, especially after the second and third injection, a very large peak concentration of RO_2 (up to 6 10^9 cm ^{3}) is predicted by all mechanisms which is not observed in the measurements. Since trans-2-hexene was completely consumed before it was re-injected the second or third time, the mechanisms predict NO_3 concentrations to build up, reaching up to 150 pptv. The high NO_3 concentration then reacts rapidly with the newly injected trans-2-hexene, generating the very large concentration of modelled RO_2 radicals until a new equilibrium between NO_3 and N_2O_5 is reached. However, these large RO_2 radical concentrations are not observed, suggesting unknown chamber reactions for NO_3 when trans-2-hexene is not dominating, which cannot be described correctly in the presented experiments due to missing NO_3 and N_2O_5 measurements.

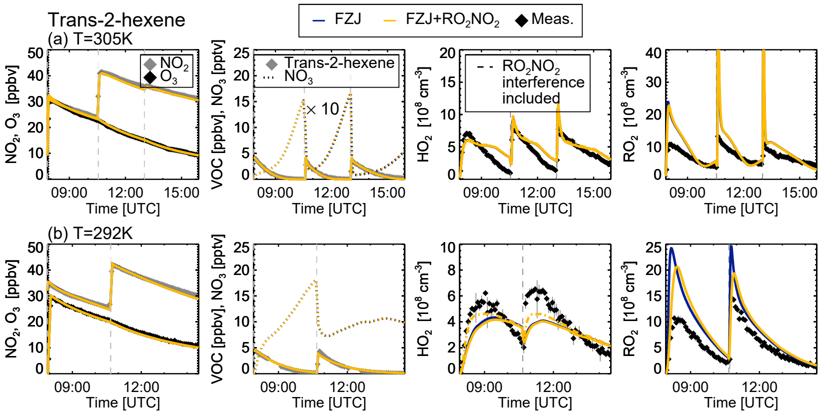

Figure S12: Comparison between modelled and measured (5 minutes average) trace gases and HO_2 and RO_2 radical concentrations in the trans-2-hexene experiments with CO as OH scavenger. Model results displayed as FZJ (blue) and FZJ+RO_2NO_2 (brown) models refer to the FZJ mechanism with and without the additional formation of non-acyl RO_2NO_2, respectively. For the experiment conducted at 305 K, the formation of HNO_2 was considered according to Eq. (S4). Injections of chemical species into the chamber are marked by vertical lines.

In the experiment at medium temperatures, the FZJ mechanisms overestimate the measured RO_2 radical concentrations on average by a factor of 1.5, where the FZJ+RO_2NO_2 model, including non-acyl RO_2NO_2 formation, predicts a time-dependence that better agrees with the observations.

The agreement between measured and modelled HO_2 radical concentrations differs significantly in the experiments at the three temperatures. At low temperatures (cold), the measured HO_2 is highly underestimated by a factor of 3. The underestimation is only a factor of 1.1 in the experiment at medium temperatures. In the experiment at high temperatures (hot), an overestimation of the detected HO_2 is observed with an average model-to-measurement ratio of 1.4.

At higher temperatures, the isomerisation of RO_2 radicals, with rates derived from the SAR from Vereecken and Nozière[5], increasingly contributes to the HO_2 production rate (from 23 % for cold to 34 % for hot conditions) and thus leads to higher HO_2 radical concentrations. Through the reaction of HO_2 with RO_2, the HO_2 radical can be recycled by forming OH which will subsequently react with CO producing HO_2 again. Therefore, it is difficult to understand why the measured HO_2 radical concentrations in the experiment at cold conditions are so similar as in the experiment at medium temperatures when the source strength should have increased substantially at a similar HO_2 loss rate. In contrast to the NO_3 experiment performed at cold conditions, a good agreement between modelled and measured HO_2 is observed in the ozonolysis experiment, which was performed at cold conditions as well (Fig. S2, Section E.2). Therefore, the observed model-measurement discrepancy in the HO_2 radical concentrations is unlikely to be caused by the oxidation of trans-2-hexene by O_3 and, thus, arises either from the contribution of the oxidation of trans-2-hexene by NO_3 or by the presence of NO_2.

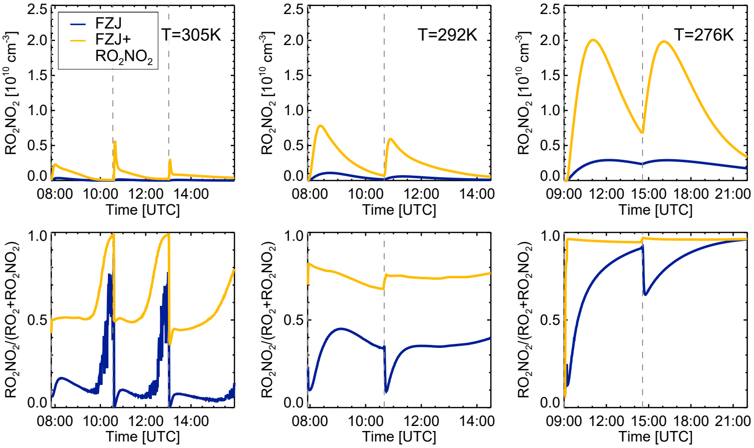

Figure S13: Formed non-acyl RO_2NO_2 concentrations and the fraction of non-acyl RO_2 stored as RO_2NO_2 ($RO_2NO_2/(RO_2+RO_2NO_2)$) for the three trans-2-hexene oxidation experiments in the presence of NO_2 applying the FZJ mechanism either without (FZJ model, blue) or with (FZJ+RO_2NO_2 model, brown) the additional formation of alkyl-RO_2NO_2. Model results of the RO_2NO_2 concentrations, based on the FZJ mechanism without additional formation of RO_2NO_2 (FZJ model), refer to $CH_3O_2NO_2$ concentrations. Vertical lines refer to the injection of chemical species.

The amount of RO_2NO_2 reservoir species formed in the experiments with trans-2-hexene at the different tested temperatures is shown in Fig. S13, together with the fraction of non-acyl RO_2 radicals stored as RO_2NO_2. RO_2NO_2 mixing ratios are predicted to increase from 100 pptv to up to 750 pptv over a temperature range of 305 K to 276 K, resulting in 50 % to 95 % less non-acyl RO_2 radicals, respectively. The impact of this high amount of non-acyl RO_2 radicals stored as RO_2NO_2 reservoir species is discussed in Sections 3.2

and 4 in the main paper.

Concentrations of acetaldehyde observed in the experiments with trans-2-hexene are shown in Fig. S14. The comparison between measured and modelled acetaldehyde is discussed in Section 3.2 in the main paper.

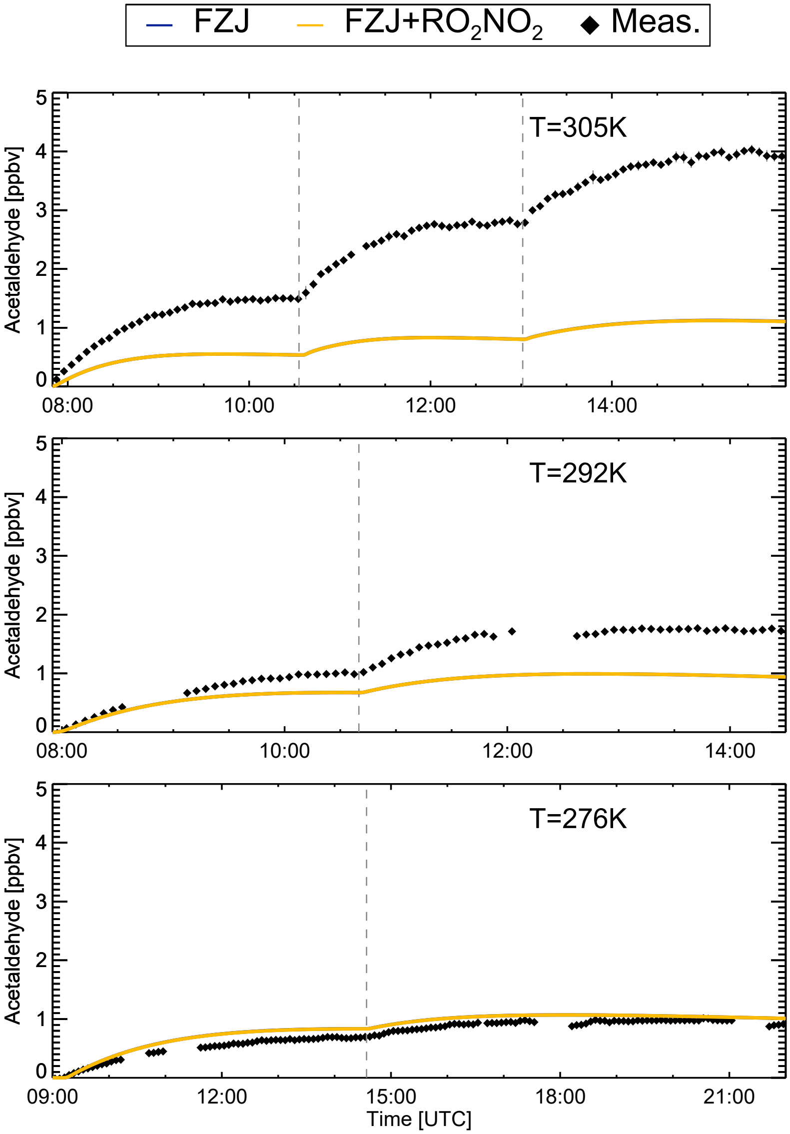

Figure S14: Comparison of modelled and measured (5 minutes average) acetaldehyde in the trans-2-hexene NO_3 experiments. Model results displayed as FZJ (blue) and FZJ+RO_2NO_2 (brown) models refer to the FZJ mechanism without and with the additional formation of non-acyl RO_2NO_2, respectively. Injections of chemical species into the chamber are marked by vertical lines.

G.1 Overestimation of HO_2 radical concentrations observed for hot conditions

For hot conditions, an overestimation of the measured HO_2 radical concentration by both, the FZJ and FZJ+RO_2NO_2 mechanisms, is observed. The discrepancy could be improved by accounting for the formation of nitryl hydride (HNO_2) from the reaction of HO_2 with NO_2[6]:

$$HO_2 + NO_2 \rightarrow HNO_2 + O_2, \tag{S4}$$

which rate coefficient can be described by the following Arrhenius expression: $k_{Eq.\ (S4)} = 1 \times 10^{-10} \times \exp(-(27.4 \pm 0.4)\,\mathrm{kJ\,mol^{-1}}/(RT))$[6]. Reactions of nitryl hydride are typically investigated at temperatures relevant in combustion processes, *i.e.* temperatures much larger than 305 K. At these temperatures, HNO_2 was observed to undergo bimolecular reactions with a number of radicals such as the hydrogen atom or the methyl radical[7–10]. Also unimolecular reactions forming HONO or OH + NO were studied[9–11], which were found to not impact the model results at the given temperatures. Including the formation of HNO_2 improves the model-measurement agreement for HO_2 by $\sim 30\,\%$ leading to an agreement within $\sim 30\,\%$.

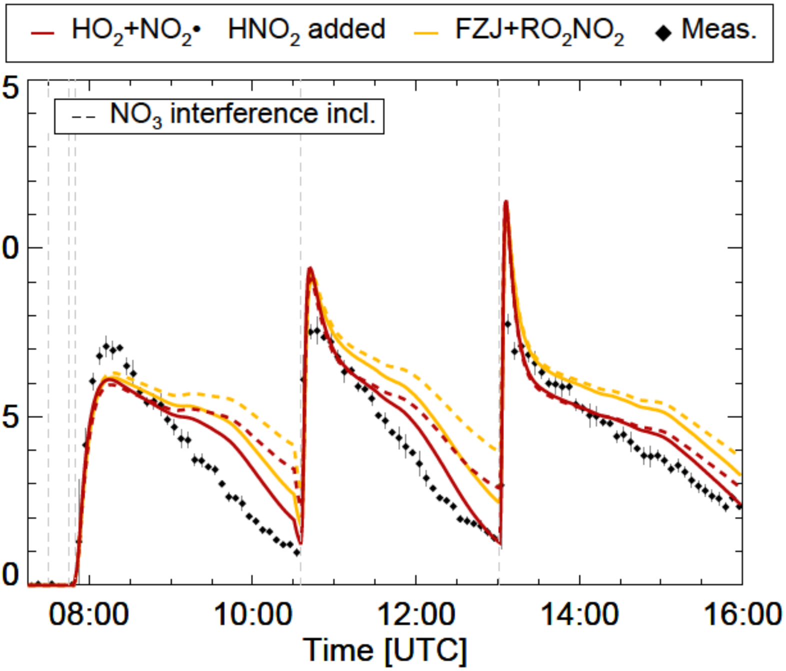

Figure S15: Modelled and measured (5 minutes average) HO_2 radical concentrations for the FZJ mechanism including additional formation of non-acyl RO_2NO_2 (FZJ+RO_2NO_2 model), with and without the formation of HNO_2 from the reaction of HO_2 with NO_2. Injections of chemical species into the chamber are marked by vertical lines.

G.2 Further analysis of the remaining uncertainties

Measured values of acetaldehyde are well reproduced in the experiment with trans-2-hexene at cold conditions but are underestimated by the FZJ mechanisms in the experiments at medium and hot conditions (Fig. S14). In both FZJ mechanisms, acetaldehyde is mainly produced (> 93 %) directly from the ozonolysis of trans-2-hexene and is lost via dilution. An erroneous rate constant of the ozonolysis reaction is unlikely to be the reason for the observed model-measurement differences since the time series of trans-2-hexene is well reproduced at all probed temperatures. Therefore, it is likely that the yield of acetaldehyde in the chemical mechanism is too small or, given that a good model-measurement agreement is found at the low temperatures, that the temperature-dependence of the yield is incorrect. Indeed, the updated ozonolysis scheme in Novelli *et al.*[1] as well as the ozonolysis SAR from Newland *et al.*[2] do not provide temperature-dependent product yields, and further experiments at higher temperatures would be useful to improve the product yields.

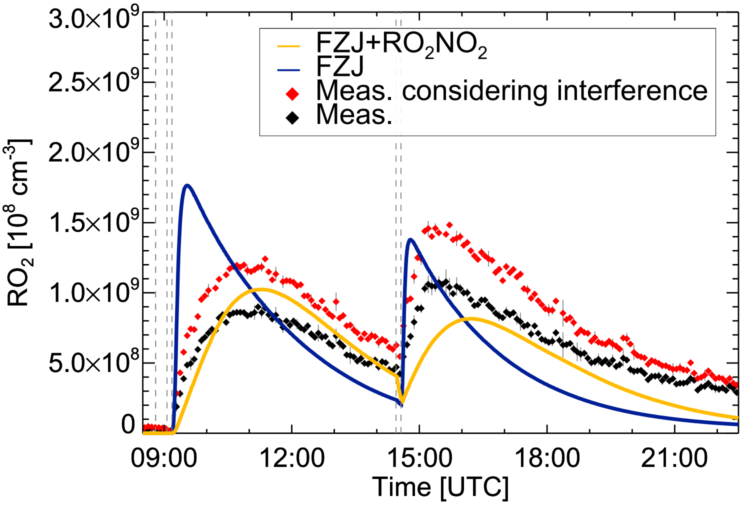

Figure S16: Comparison of the time series of RO_2 radical concentrations with and without considering a possible interference in the HO_x measurement in the trans-2-hexene experiment with CO as OH scavenger at 276 K. Model results from the FZJ mechanism with (FZJ+RO_2NO_2 model, brown) and without (FZJ model, blue) the additional formation of non-acyl RO_2NO_2 are shown as well. Injections of chemical species into the chamber are marked by vertical lines.

References

[1] A. Novelli, C. Cho, H. Fuchs, A. Hofzumahaus, F. Rohrer, R. Tillmann, A. Kiendler-Scharr, A. Wahner and L. Vereecken, *Phys. Chem. Chem. Phys.*, 2021, **23**, 5474–5495.

[2] M. J. Newland, C. Mouchel-Vallon, R. Valorso, B. Aumont, L. Vereecken, M. E. Jenkin and A. R. Rickard, *Atmos. Chem. Phys.*, 2022, **22**, 6167–6195.

[3] M. E. Jenkin, R. Valorso, B. Aumont and A. R. Rickard, *Atmos. Chem. Phys.*, 2019, **19**, 7691–7717.

[4] H. Fuchs, Z. Tan, A. Hofzumahaus, S. Broch, H.-P. Dorn, F. Holland, C. Künstler, S. Gomm, F. Rohrer, S. Schrade, R. Tillmann and A. Wahner, *Atmos. Meas. Tech.*, 2016, **9**, 1431–1447.

[5] L. Vereecken and B. Nozière, *Atmos. Chem. Phys.*, 2020, **20**, 7429–7458.

[6] K. McKee, M. A. Blitz, R. J. Shannon and M. J. Pilling, *J. Phys. Chem. A*, 2022, **126**, 7514–7522.

[7] M. E. Fuller and C. F. Goldsmith, *Proc. Combust. Inst.*, 2019, **37**, 695–702.

[8] O. Mathieu, B. Giri, A. Agard, T. Adams, J. Mertens and E. Petersen, *Fuel*, 2016, **182**, 597–612.

[9] Y. Zhang, O. Mathieu, E. L. Petersen, G. Bourque and H. J. Curran, *Combust. Flame*, 2017, **182**, 122–141.

[10] S. F. Ahmed, J. Santner, F. L. Dryer, B. Padak and T. I. Farouk, *Energy Fuels*, 2016, **30**, 7691–7703.

[11] X. Chen, M. E. Fuller and C. Franklin Goldsmith, *React. Chem. Eng.*, 2019, **4**, 323–333.

B Anhänge gemäß Prüfungsordnung

B.1 Own contributions to publications and manuscripts

The two publications forming the basis of Chapter 3 and the unpublished report used as inspiration for Chapter 2 include author contributions, which are summarised in the following.

1. **Färber, M.**, Vereecken, L., Fuchs, H., Gkatzelis, G.I., Rohrer, F., Wedel, S., Wahner, A., and Novelli, A.: Impact of temperature-dependent non-PAN peroxynitrate formation, RO_2NO_2, on nighttime atmospheric chemistry, Phys. Chem. Chem. Phys., 2024, **26**, 5183, DOI: 10.1039/D3CP04163H.

   MF analysed the data and wrote the paper. AN and LV designed the experiments and worked closely with MF to conceptualise the paper. MF and AN conducted the RO_x radical measurements and OH reactivity measurements. FR performed measurements of NO_x and O_3. SW and GIG were responsible for operating the PTR-ToF-MS instrument. All co-authors commented on the paper.

2. **Färber, M.**, Fuchs, H., Bohn, B., Carlsson, P.M.T., Gkatzelis, G.I., Marcillo Lara, A.C., Rohrer, F., Wedel, S., Wahner, A., and Novelli, A.: Effect of the Alkoxy Radical Chemistry on the Ozone Formation investigated from Anthropogenic Organic Compounds Investigated in Chamber Experiments, ACS ES&T Air 2024, **1**, 1096-1111, DOI: 10.1021/acsestair.4c00064.

   MF analysed the data, and wrote the manuscript together with AN. MF, AN, and HF conceptualised the manuscript. AN designed the experiments. MF and AN conducted the RO_x radical measurements and OH reactivity measurements. PMTC performed DOAS measurements and BB was responsible for the radiation measurements. FR performed measurements of NO_x, O_3, and HCHO. SW was together with GIG responsible for operating the PTR-ToF-MS instrument and together with ACML responsible for GC-MS measurements. The manuscript was sent to all co-authors for feedback.

3. **Färber, M.**, Fuchs, H., Bell, D., Herrmann, H., McFiggans, G., Mellouki, W., Munoz, A., Pandis, S., Picquet-Varrault, B., Saathoff, H., Virtanen, A.: Report -pinene multi-chamber experiment, “Work Package 2” of the EUROCHAMP-2020 project.

   HF and MF wrote the report. HF provided MF scripts for the data processing of the individual chamber data. MF analysed the data. DB, HH, GM, WM, AM, SP, BP-V, HS, AV were responsible for chamber experiments performed in the PACS-C3, LEAK, MAC, HELIOS, EUPHORE, FORTH, CESAM, AIDA, and ILMARI chambers, respectively.

B.2 | Erklärung zur Dissertation

Hiermit versichere ich an Eides statt, dass ich die vorliegende Dissertation selbstständig und ohne die Benutzung anderer als der angegebenen Hilfsmittel und Literatur angefertigt habe. Alle Stellen, die wörtlich oder sinngemäß aus veröffentlichten und nicht veröffentlichten Werken dem Wortlaut oder dem Sinn nach entnommen wurden, sind als solche kenntlich gemacht. Ich versichere an Eides statt, dass diese Dissertation noch keiner anderen Fakultät oder Universität zur Prüfung vorgelegen hat; dass sie - abgesehen von unten angegebenen Teilpublikationen und eingebundenen Artikeln und Manuskripten - noch nicht veröffentlicht worden ist sowie, dass ich eine Veröffentlichung der Dissertation vor Abschluss der Promotion nicht ohne Genehmigung des Promotionsausschusses vornehmen werde. Die Bestimmungen dieser Ordnung sind mir bekannt. Darüber hinaus erkläre ich hiermit, dass ich die Ordnung zur Sicherung guter wissenschaftlicher Praxis und zum Umgang mit wissenschaftlichem Fehlverhalten der Universität zu Köln gelesen und sie bei der Durchführung der Dissertation zugrundeliegenden Arbeiten und der schriftlich verfassten Dissertation beachtet habe und verpflichte mich hiermit, die dort genannten Vorgaben bei allen wissenschaftlichen Tätigkeiten zu beachten und umzusetzen. Ich versichere, dass die eingereichte elektronische Fassung der eingereichten Druckfassung vollständig entspricht.

Teilpublikationen

1. **Färber, M.**, Vereecken, L., Fuchs, H., Gkatzelis, G.I., Rohrer, F., Wedel, S., Wahner, A., and Novelli, A.: Impact of temperature-dependent non-PAN peroxynitrate formation, RO_2NO_2, on nighttime atmospheric chemistry, Phys. Chem. Chem. Phys., 2024, **26**, 5183, DOI: 10.1039/D3CP04163H.
2. **Färber, M.**, Fuchs, H., Bohn, B., Carlsson, P.M.T., Gkatzelis, G.I., Marcillo Lara, A.C., Rohrer, F., Wedel, S., Wahner, A., and Novelli, A.: Effect of the Alkoxy Radical Chemistry on the Ozone Formation investigated from Anthropogenic Organic Compounds Investigated in Chamber Experiments, ACS ES&T Air 2024, **1**, 1096-1111, DOI: 10.1021/acsestair.4c00064.

Die Dissertation beinhaltet die Gewinnung und Analyse von Primärdaten. Diese sind auf den Servern des Instituts für Energie- und Klimaforschung, IEK-8: Troposphäre des Forschungszentrums Jülich gesichert und auf Anfrage zugänglich.

Köln, den 05. Februar 2024

(Michelle Färber)

Band / Volume 643
Multi-dimensional GPR full-waveform inversion for small-scale hydrogeophysical soil characterization
D. Hoven (2024), IX, 163 pp
ISBN: 978-3-95806-781-3

Band / Volume 644
Analyse des Gastransports in komplexen Membransystemen durch Modellierung und multiskalige Simulation
K. Wilkner (2024), VIII, 122 pp
ISBN: 978-3-95806-784-4

Band / Volume 645
Deployment of Fuel Cell Vehicles in Road Transport and the Expansion of the Hydrogen Refueling Station Network: 2024 Update
T. Grube; M. Rex (2024), iii, 26 pp
ISBN: 978-3-95806-786-8

Band / Volume 646
Modellgestützte Analyse treibhausgasneutraler Transformationsstrategien für Deutschland
T. F. Schöb (2024), XII, 228 pp
ISBN: 978-3-95806-789-9

Band / Volume 647
Future Distribution Grids Using Geo-Referenced Synthetic Network Topologies
A. Bandam (2024), ix, 237 pp
ISBN: 978-3-95806-790-5

Band / Volume 648
Multi-scenario, high-resolution Lagrangian transport modeling for the analysis of the Asian tropopause aerosol layer
J. H. Clemens (2024), 143 pp
ISBN: 978-3-95806-792-9

Band / Volume 649
Prospektive Lebenszyklusanalysen von Power-to-Gas-Optionen
J. C. Koj (2024), XVIII, 197 pp
ISBN: 978-3-95806-794-3

Band / Volume 650
Assimilation of groundwater level and cosmic-ray neutron sensor soil moisture measurements into integrated terrestrial system models for better predictions
F. Li (2024), xvii, 172 pp
ISBN: 978-3-95806-796-7

Band / Volume 651
Integration of a rib-channel design to improve air-side contacting in solid oxide cell (SOC) stacks
Y. S. Ayhan (2024), 82 pp
ISBN: 978-3-95806-797-4

Band / Volume 652
Modelling Secondary Circulation in Convective Boundary Layer Using Large Eddy Simulation
L. Zhang (2024), 84 pp
ISBN: 978-3-95806-799-8

Band / Volume 653
Optionen zur Umsetzung der Klimaschutzziele im Verkehrssektor
S. Kraus (2025), XI, 317 pp
ISBN: 978-3-95806-802-5

Band / Volume 654
Modellierung der flächendifferenzierten Grundwasserneubildung für Schleswig-Holstein im Beobachtungszeitraum 1961 – 2021 und für Klimaszenarien bis 2100
I. McNamara, B. Tetzlaff, F. Wendland, T. Wolters (2025), 191 pp
ISBN: 978-3-95806-803-2

Band / Volume 655
Entwicklung alternativer Brenngaselektroden für die Hochtemperatur-Elektrolyse
F. E. Winterhalder (2025), vii, 161 pp
ISBN: 978-3-95806-805-6

Band / Volume 656
Oxide-based All-Solid-State Batteries for and from Recycling Processes
V. M. Kiyek (2025), viii, 128 pp, xix
ISBN: 978-3-95806-806-3

Band / Volume 657
Investigation of current and future anthropogenic chemical regimes in simulation chamber experiments
M. Färber (2025), 213 pp
ISBN: 978-3-95806-809-4

Weitere ***Schriften des Verlags im Forschungszentrum Jülich*** unter
http://wwwzb1.fz-juelich.de/verlagextern1/index.asp

Energie & Umwelt / Energy & Environment
Band / Volume 657
ISBN 978-3-95806-809-4

Mitglied der Helmholtz-Gemeinschaft

JÜLICH
Forschungszentrum